MID-INFRARED SENSORS FOR HYDROCARBON ANALYSIS IN EXTREME ENVIRONMENTS

A Dissertation
Presented To
The Academic Faculty

By

Yuliya Luzinova

In Partial Fulfillment
Of the Requirements for the Degree
Doctor of Philosophy in Chemistry

Georgia Institute of Technology

August, 2010

MID-INFRARED SENSORS FOR HYDROCARBON ANALYSIS IN EXTREME ENVIRONMENTS

Approved by:

Dr. Boris Mizaikoff, Advisor
School of Chemistry and Biochemistry
Georgia Institute of Technology

Dr. Thomas Orlando
School of Chemistry and Biochemistry
Georgia Institute of Technology

Dr. Jiri Janata
School of Chemistry and Biochemistry
Georgia Institute of Technology

Dr. Facundo Fernandez
School of Chemistry and Biochemistry
Georgia Institute of Technology

Dr. Oliver Brand
School of Electrical and Computer Engineering
Georgia Institute of Technology

Dr. Seong-soo Kim
School of Electrical and Computer Engineering
Georgia Institute of Technology

Date Approved: June 1, 2010

ACKNOWLEDGEMENTS

I would like to thank my research advisor Dr. Boris Mizaikoff for his optimism and the endless opportunities he has provided me throughout by PhD studies.

Dr. Facundo Fernandez, Dr. Thomas Orlando, Dr. Jiři Janata, Dr. Seong-oo Kim, Dr. Oliver Brand are gratefully acknowledged for serving as committee members and for the scientific discussions and advice.

In addition, this work has been facilitated by many colleagues and collaborative partners, and I wish to thank all the individuals who helped make this possible. I would like to thank Dr. Orlando and the EPICS (Electron and Photon Induced Chmistry on Surfaces) group for providing me with support and scientific advice throughout my thesis work. Thanks to the past and present members of the Applied Sensors Laboratory at Georgia Tech for their help and support throughout the work. A special thanks goes to Dr. Gary Dobbs for his endless effort to help throughout my thesis work, and to Dr. Dr. Seong-soo Kim for his ongoing support in the field of optics during the final phase of the thesis.

The Gulf of Mexico Gas Hydrate Research Consortium has provided an excellent platform for the interaction and exchange of ideas with many scientists and professionals. I would like to specifically thank Dr. Carol Lutken, Dr. Bob Woolsey, Dr. Jeff Chanton, and Dr. Laura Lapham. Special thanks are extended to Dr. Roger Sassen for the exciting collobaration on diamondoids, for providing diamondoid samples, and for scientific advice.

At Georgia Tech, I would like to thank my collaborators Dr. Oliver Brand, Luke Beardslee, Sefak Demirci, Dr. Ching-Hua Huang, Dr. Lokesh Padhye, Dr. Dennis Hess, and Dr. Balamurali Balu. My collaborators at Clemson University, Dr. Bogdan Zdyrko and Dr. Igor Luzinov, are thanked for scientific discussions and assistance with preparation and characterization of polymer coatings at the surface of optical fibers.

I am also grateful for funding, scientific support, and discussions provided by ExxonMobil Research and Engineering Company (EMRE). Special thanks are extended to Dr. Mark. M. Disko, Dr. John Szobota, and Dr. Clifford Walters for the great collaboration, numerous scientific discussions, and advice during this thesis.

I would like to thank my undergraduate research advisors from Clemson Univeristy, Dr. Michael Kilbey, Dr. George Chumanov, and Dr. Stephen Foulger for the introduction to scientific research, direction, and guidance.

At last, this would not have been possible without the unconditional love and support from my family.

Table of Contents

LIST OF TABLES

LIST OF FIGURES

LIST OF ABBREVIATIONS

°C	Degrees Celsius
A/V	Audio-Visual
AgX	Silver Halide
ATR	Attenuated Total Reflection
cm	Centimeter(s)
cm^{-1}	Wavenumber(s)
cmbsf	Centimeters-Below-Seafloor
de	Effective Evanescent Field Penetration Depth
DI	Deionized
dp	Evanescent Field Penetration Depth where E = 1/e
E	Energy of Evanescent Field
EPB	Epoxidized polybutadiene
FT-IR	Fourier Transform-Infrared
g	Gram(s)
GPS	Global Positioning System
IR-ATR	Infrared-Attenuated Total Reflection
kPa	Kilopascal
l.	Length
L	Liter(s)
Lib.	Libration
LN2	Liquid Nitrogen
μ m	Micrometer(s)
m	Meter(s)
MC118	Mississippi Canyon Block 118
MCT	Mercury-Cadmium-Telluride
mg	Milligram(s)
Mg-calcite	Magnesian Calcite
min	Minute(s)
MIR	Mid-Infrared
mL	Milliliter(s)
mm	Millimeter(s)
MPa	Megapascal
nD	Refractive Index
PA	Peak Area
ppb	Parts per Billion
ppm	Parts per Million
psi	Pounds per Square Inch
PAA	Polyacrylic Acid
R/V	Research Vessel
s	Second(s)
sI	structure-I
sII	structure-II
sH	structure-H
SS	Stainless Steel
STP	Standard Temperature and Pressure
UV	Ultraviolet
VOC	Volatile Organic Compound(s)
ZnSe	Zinc Selenide

SUMMARY

A number of MIR sensing platforms and methods were developed in this research work demonstrating potential applicability of MIR spectroscopy for studying hydrocarbon systems in extreme environments.

First of all, the quantitative determination of the diamondoid compound adamantane in organic media utilizing IR-ATR spectroscopy at waveguide surfaces was established. The developed analytical strategy further enabled the successful detection of adamantane in real world crude oil samples. These reported efforts provide a promising outlook for detection and monitoring of diamondoid constituents in naturally occurring crudes and petroleum samples.

IR-ATR spectroscopy was further utilized for evaluating and characterizing distribution, variations, and origin of carbonate minerals within sediment formations surrounding a hydrocarbon seep site - MC 118 in the Gulf of Mexico. An analytical model for direct detection of ^{13}C-depleted authigenic carbonates associated with cold seep ecosystems was constructed. Potential applicability of IR-ATR spectroscopy as direct on-ship – and in future in-situ - analytical tool for characterizing hydrocarbon seep sites was demonstrated.

MIR evanescent field absorption spectroscopy was also utilized to expand the understanding on the role of surfactants during gas hydrate formation at surfaces. This experimental method allowed detailed spectroscopic observations of detergent-related surface processes during SDS mediated gas hydrate formation. The obtained IR data

enabled proposing a mechanism by which SDS decreases the induction time for hydrate nucleation, and promotes hydrate formation. Potential of MIR fiberoptic evanescent field spectroscopy for studying surface effects during gas hydrate nucleation and growth was demonstrated.

Next, quantifying trace amounts of water content in hexane using MIR evanescent field absorption spectroscopy is presented. The improvement in sensitivity and of limit of detection was obtained by coating an optical fiber with layer of a hydrophilic polymer. The application of the polymer layer has enabled the on-line MIR detection of water in hexane at low ppm levels. These results indicate that the MIR evanescent filed spectroscopy method shows potential for in-situ detection and monitoring of water in industrial oils and petroleum products.

Finally, quantification of trace amounts of oil content in water using MIR evanescent field absorption spectroscopy is reported. Unmodified and modified with grafted hydrophobic polymer layer silver halide optical fibers were employed for the measurements. The surface modification of the fiber has enabled the on-line MIR analysis of crude oil in water at the low ppb level. Potential application of MIR fiber-optic evanescent field spectroscopy using polymer modified waveguides toward in-situ low level detection of crude oil in open waters was demonstrated.

CHAPTER 1

Introduction

Thesis Objective: The objective of this thesis was the design and application of mid-infrared (MIR) chemical sensor platforms for the analysis of hydrocarbon containing systems in extreme environments. Specifically, this thesis was focused on the potential of MIR spectroscopy for studying hydrocarbon seep ecosystems and hazardous scenarios associated with oil/gas production, storage, and transportation.

Original Contributions of this Thesis:

- **Infrared attenuated total reflection (IR-ATR) spectroscopy for the quantitative determination of the diamondoid compound adamantane in organic media.** Application of the developed analytical strategy for the successful detection and quantification of adamantane in crude oil matrices was shown.
- **IR-ATR spectroscopy on gravity core marine sediment samples collected around hydrocarbon seeps.** IR-ATR spectroscopy was demonstrated as a potential rapid and cost-effective on-ship identification and characterization method for active or previously active hydrocarbon seepage areas.
- **Establishment of an IR indicator parameter suitable for the detection of microbially mediated authigenic carbonate precipitations around cold seep ecosystems.** A straightforward method was developed and utilized to instantly differentiate between biogenic and hydrocarbon derived antigenic carbonate formation in marine sediments.

- **In-situ monitoring of propane gas hydrate formation.** Gas hydrate formation in the presence of sodium dodecyl sulfate (SDS) surfactant in a pressure cell utilizing fiberoptic MIR evanescent field spectroscopy was observed and mechanistically studied for explaining surface processes during SDS driven gas hydrate formation.
- **Quantification of low water content in hexane.** As a model for oil/petroleum products, the utility of MIR evanescent field absorption spectroscopy for detecting water in hexane was studied using silver halide MIR waveguides with/without surface modification based on polyacrylic acid membranes.
- **Quantification of trace amounts of oil in water.** MIR evanescent field absorption spectroscopy using silver halide MIR waveguides with/without grafted epoxidized polybutadiene layers was applied for determining trace amounts of oil in water.

1.1 Motivation and chapter summary

Hydrocarbons derived from petroleum, natural gas, or coal play a major role in modern life [1], and are among the Earth's most important energy resources [2]. The bulk of globally retrievable hydrocarbons is used for fuels, electrical power generation, and heating. Additionally, chemical, petrochemical, plastics, and rubber industries are dependent on hydrocarbons as raw materials for their products. In fact, the majority of industrially significant synthetic chemicals are derived from petroleum sources (i.e., plastics, paraffin, waxes, solvents, and lubricants). Presently, the overall oil usage of the world exceeds ten million metric tons a day [1]. While hydrocarbons play a major role in our everyday life, there are also certain negative effects associated with them. Refinement, transportation, storage, and other industrial processes involving

hydrocarbons frequently result in an increased loading of hydrocarbons in water and necessitate remediation before release [3]. Accidental releases can cause extensive damage to marine life, terrestrial life, human health, and natural resources [3, 4].

Thus, the need to understand the role of hydrocarbons in aqueous matrices is of increasing importance. Therefore, it is important to study natural (i.e., origin, environment, role in nature, etc.) and industrial (i.e., refinery, production, storage, transportation, etc.) processes involving hydrocarbons in order to maximize their potential in energy applications, while minimizing environmental contamination effects. However, for analytical assessment of diverse hydrocarbon incarnations in aqueous environments, it should be noted that "hydrocarbon environments"—natural or industrial—maybe considered extreme environments. Extreme environments are identified as areas of low/high temperatures, high pressures, subsea/subearth locations, etc.; that is, extreme environments are considered locations difficult to study with conventional laboratory analytical techniques. Hence, there is an ongoing need to develop robust analytical procedures and technologies capable of operating in these environments**.** A variety of optical chemical sensors has been applied to studies at environmentally challenging conditions [5-10]. To this end, Chapter 2 of this thesis presents an overview of optical sensors, and their advantages over other sensing techniques for such applications [7, 11-14]. Particular attention is paid to optical sensors operating in the mid-infrared (MIR) spectral regime, which appear well suited for studies in extreme environments, as described in Chapter 2 [15-17].

Other chapters of this thesis experimentally investigate the potential of MIR evanescent field absorption spectroscopy utilizing either MIR transparent fiberoptic

waveguides as active transducer or crystalline ATR sensing elements for studying hydrocarbon related processes in extreme environments, as summarized in **Figure 1.1**.

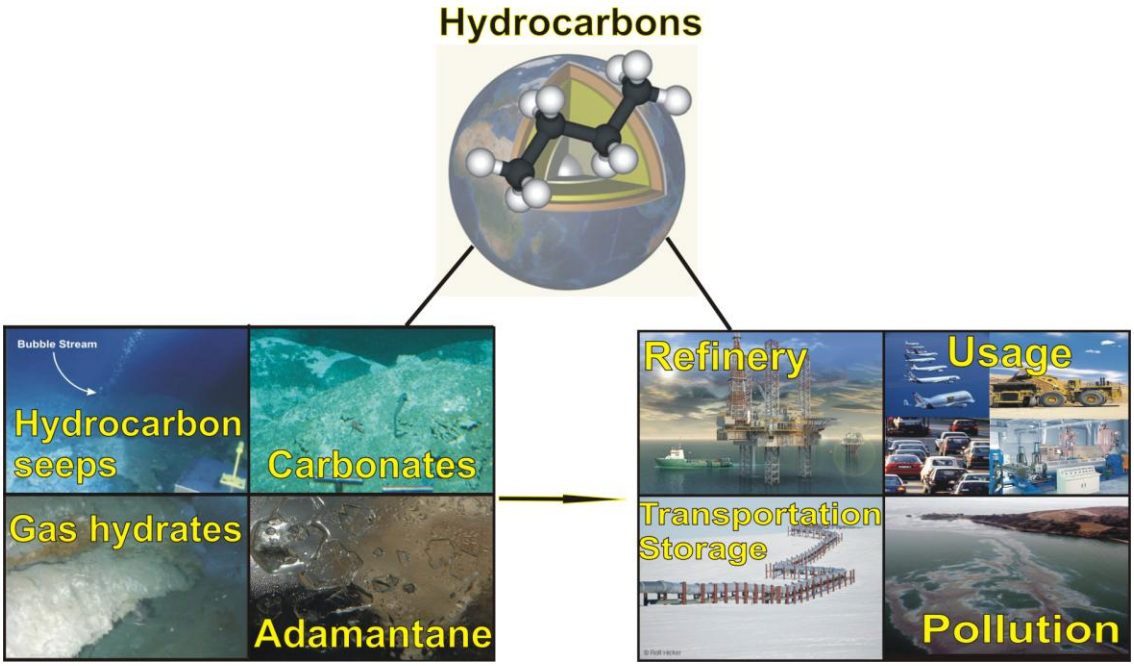

Figure 1.1: Diagram presenting the topics covered in this thesis.

(Individual images are taken from Google images)

First, MIR evanescent field absorption spectroscopy was used as a technique for studying diamandoid compounds that are found in virtually all crude oils. Then, carbonates and gas hydrates have been investigated, which are components of hydrocarbon seep ecosystems. Additionally, MIR sensor platforms capable of monitoring the water content in hydrocarbon matrices are described, which are of crucial interest for oil/petroleum industries. Finally, this thesis wraps up with research on the application of MIR sensors in monitoring hydrocarbon contaminations in open waters.

1.1.1 *Adamantane*

The smallest member of the diamondoid family of molecules, adamantane, is the simplest polycyclic saturated hydrocarbon. Adamantane and higher diamondoids occur naturally in nearly all crude oils, intermediate petroleum distillates, and finished petroleum products [18]. Characterization of diamondoids properties in geosystems, and their geographic distribution may facilitate a better understanding of the thermal maturity, migration history, source rock type, and age of condensates from wells worldwide [19]. Additionally, these compounds are considered hazardous materials in the petroleum industry, as they have a tendency to segregate during production and transportation of natural gas, gas condensates, and light crude oils [20]. Therefore, it is important to rapidly assess whether or not diamondoids occur in a reservoir fluid at concentrations that may potentially affect production operations.

To this end, Chapter 3 of this thesis discusses the application of IR-ATR spectroscopy for the quantitative determination of adamantane in organic matrices including dichloromethane, hexane, and carbon tetrachloride, for the direct evaluation of adamantane in crude oil standards. Additionally, the feasibility of this analytical technique for analyzing real-world crude oil samples was demonstrated. Finally, the potential capability of IR-ATR spectroscopy for low-level detection and monitoring of diamondoid constituents in naturally occurring crudes and petroleum samples was established.

1.1.2 *Carbonates*

Carbonates are naturally occurring minerals, and are ubiquitous features of hydrocarbon seep areas at the seafloor. Hydrocarbon seeps are also referred to as methane or cold seeps, and represent discrete sites where fluids rich in methane and other hydrocarbons seep from deeper sediment depth to the sediment–water interface [21]. Natural gas and crude oil deposits have frequently been found in the proximity of hydrocarbon seeps [22]. Authigenic (formed in place) carbonates derived from hydrocarbon seeps are identified by unique carbon isotopic ratios (depletion in ^{13}C carbon). Thus, by locating these authigenic carbonates in marine sediment, it would be possible to indirectly locate passive or active hydrocarbon seeps, which potentially may lead to the discovery of gas and/or crude oil deposits.

Consequently, Chapter 4 describes IR-ATR spectroscopy studies on gravity core marine sediment samples collected around hydrocarbon seeps in the Gulf of Mexico. IR-ATR spectroscopic study revealed that carbonates formed from different sources of carbon may be identified by diverse IR absorption profiles of the ν_3 asymmetric carbonate stretching vibration. This enabled deriving an analytical model based on IR spectra for directly detecting ^{13}C-depleted authigenic carbonates associated with cold seep ecosystems. Furthermore, there is potential for the application of IR-ATR spectroscopy as a direct on-ship and in future in-situ analytical tool for detecting and characterizing hydrocarbon seep sites.

1.1.3 *Gas hydrates*

Gas hydrates are naturally occurring ice-like structures primarily composed of water molecules oriented in solid cage structures filled with small guest molecules (i.e., methane, ethane, propane, carbon dioxide, adamantine, etc.) [23, 24]. Gas hydrate deposits are considered to be potentially highly hazardous in oil-gas industries causing, for example, blocking of oil and gas flow lines [25]. Since the discovery of naturally occurring gas hydrates, their potential as an alternative energy source has been driving much of the current natural hydrate research. Furthermore, gas hydrates are drawing attention because of their ability to serve as a high-capacity gas storage medium [26, 27]. Recently, several studies have indicated that addition of some surfactants to water prior to gas hydrate formation accelerates the nucleation time and the growth rate of hydrates, thus rendering the application of gas hydrates as a gas storage medium an economically feasible process.

To this end, Chapter 5 describes in-situ monitoring of propane gas hydrate formation in the presence of sodium dodecyl sulfate (SDS) surfactant using surface sensitive MIR fiberoptic evanescent field absorption spectroscopy. Following detailed spectroscopic observations of SDS-related surface processes during gas hydrate formation, a mechanism describing the role of SDS in decreasing hydrate nucleation times and in promoting hydrate growth is discussed. Elucidation of these surface effects may provide a significant step forward for hydrate-based industrial applications.

1.1.4 *Water in hydrocarbons*

As mentioned above (**Section 1.1.3**), gas hydrates are considered potentially highly volatile and even explosive hazards [28]. Water trapped in gas/oil pipelines at low temperatures and high pressures may form gas hydrates, which can block gas/oil flow through the pipelines causing serious disruptions. Therefore, it is important to monitor the water level within gas/oil matrices contained in pipelines. Additionally, water is the most common contaminant in a wide variety of industrial oils and petroleum products. Even small amounts of emulsified water in industrial oils and petroleum products may be detrimental to refinery equipment, heavy equipment, and automotive parts [29, 30]. It is, therefore, immediately evident that the quantification of water in various industrial oils/petroleum products is crucial.

In Chapter 6, an innovative MIR evanescent field fiberoptic sensor platform for the detection and semi-quantification of low water content in hexane was developed. In this work, both unmodified and surface modified silver halide MIR waveguides using hydrophilic polyacrylic acid layers were tested. Limits of detection (LOD) and limits of quantification (LOQ) for water in hexane utilizing crosslinked polyacrylic acid modified fiber were significantly better than the figures-of-merit for unmodified fibers. Water content as low as 10 parts per million (ppm) was identified with this method. Thus far, the results obtained provide a promising outlook for low-level detection and monitoring of water content in industrial oils and petroleum products.

1.1.5 *Hydrocarbons and crude oil in water*

Hydrocarbon spills are reported daily on a global scale [3]. These spills are most frequently caused by failed infrastructure, human error, or natural hazards. Spills of oil and related petroleum products in the marine environment may have serious impacts on human health, and to terrestrial and aquatic ecosystems [3, 4]. Hence, early detection of trace amounts of hydrocarbons in water is of substantial importance, particularly for sensitive ecosystems [31].

Consequently, Chapter 7 reports on the quantitative determination of crude oil content in water at parts per billion (ppb) concentration levels via MIR evanescent field fiberoptic sensor platforms. The measurements are conducted with unmodified and surface modified silver halide MIR waveguides utilizing grafted hydrophobic (epoxidized polybutadiene) sensing layers. The sensitivity and limit of detection were significantly improved using polymer-modified fibers, detecting 46 ppb of crude oil in water. To the best of our knowledge, this is the smallest amount of crude oil reported in literature using MIR based sensing techniques without prior sample preparation, separation, or solvent extraction.

Concluding remarks and an outlook toward future studies derived from the results obtained in this thesis are summarized in Chapter 8 followed by an appendix section comprising supplemental information.

1.2 REFERENCES:

(1) Olah, G.A., "Hydrocarbons for the 21st Century - The Work of the Loker Hydrocarbon Research Institute", **1999**.

(2) Hall, C.; Tharakan, P.; Hallock, J.; Cleveland, C.; Jefferson, M. "Hydrocarbons and the evolution of human culture", *Nature* **2003**, *426*, 318-322.

(3) Wang, Z. D.; Fingas, M. F. "Development of oil hydrocarbon fingerprinting and identification techniques", *Mar. Pollut. Bull.* **2003**, *47*, 423-452.

(4) Perez-Caballero, G.; Andrade, J. M.; Muniategui, S.; Prada, D. "Comparison of single-reflection near-infrared and attenuated total reflection mid-infrared spectroscopies to identify and monitor hydrocarbons spilled in the marine environment", *Anal. Bioanal. Chem.* **2009**, *395*, 2335-2347.

(5) McDonagh, C.; Burke, C. S.; MacCraith, B. D. "Optical chemical sensors", *Chem. Rev.* **2008**, *108*, 400-422.

(6) Holst, G.; Mizaikoff, B. In *Handbook of Optical Fibre Sensing Technology*, 2002, pp 729-755.

(7) Wolfbeis, O. S., Ed. *Fiber Optic Chemical Sensors and Biosensors*; Press, Boca Raton, Fl., 1991.

(8) Wolfbeis, O. S. "Fiber optic chemical sensors and biosensors", *Analytical Chemistry* **2000**, *72*, 81R-89R.

(9) Wolfbeis, O. S. "Fiber-optic chemical sensors and biosensors", *Analytical Chemistry* **2006**, *78*, 3859-3873.

(10) Wolfbels, O. S. "Fiber-optic chemical sensors and biosensors", *Analytical Chemistry* **2008**, *80*, 4269-4283.

(11) Orellana, G.; Moreno-Bondi, M. C. *Frontiers in Chemical Sensors: Novel Principles and Techniques*; Springer:: New York, 2005.

(12) Baldini, F.; Chester, A. N.; Homola, J.; Martellucci, S. *Optical Chemical Sensors*; Springer: New York, 2006.

(13) Narayanaswamy, R.; Wolfbeis, O. S., Eds. *Optical Sensors − Industrial, Environmental and Diagnostic Applications*; Springer, 2004.

(14) Dermot, D. *Principles of chemical and biological sensors*; Wiley-Interscience Dublin, Ireland 1998.

(15) Mizaikoff, B. In *SPIE conference on Infrared Opitcal Fibers and Their Applications*: Boston, Massachusetts, 1999; Vol. 3849.

(16) Mizaikoff, B. "Infrared optical sensors for water quality monitoring", *Water Science & Technology* **1999**, *47*, 35-42.

(17) Mizaikoff, B.; Jakusch, M.; Kraft, M. "Infrared fiber-optic sensors - Versatile tool for water monitoring - Optical chemical sensors gain importance in environmental monitoring, process analysis/control; Now complement separation techniques and spectroscopy", *Sea Technol.* **1999**, *40*, 25-+.

(18) Grice, K.; Alexander, R.; Kagi, R. I. "Diamondoid hydrocarbon ratios as indicators of biodegradation in Australian crude oils", *Org. Geochem.* **2000**, *31*, 67-73.
(19) Sassen, R.; Post, P. "Enrichment of diamondoids and C-13 in condensate from Hudson canyon, US Atlantic", *Organic Geochemistry* **2008**, *39*, 147-151.
(20) Vazquez, D.; Mansoori, G. A. "Identification and measurement of petroleum precipitates", *Journal of Petroleum Science and Engineering* **2000**, *26*, 49-55.
(21) Lapham, L.; Chanton, J.; Martens, C.; Sleeper, K.; Woosley, R. "Microbial activity in surficial sediments overlying acoustic wipeout zones at a Gulf of Mexico cold seep", *Geochemistry Geophysics Geosystems* **2008**, *9*, 17.
(22) Roberts, H. H.; Aharon, P. "Hydrocarbon-derived carbonate buildups of the Northern Gulf of Mexico continental slope: a review of submersible investigations", *Geo-Marine Letters* **1994**, *14*, 135-148.
(23) Kirchner, M. T.; Boese, R.; Billups, W. E.; Norman, L. R. "Gas hydrate single-crystal structure analyses", *Journal of the American Chemical Society* **2004**, *126*, 9407-9412.
(24) Kvenvolden, K. A. "Gas hydrates - geological perspective and global change", *Reviews of Geophysics* **1993**, *31*, 173-187.
(25) Hammerschmidt, E. G. "Formation of gas hydrates in natural gas transmission lines", *Industrial and Engineering Chemistry* **1934**, *26*, 851-855.
(26) Zhong, Y.; Rogers, R. E. "Surfactant effects on gas hydrate formation", *Chemical Engineering Science* **2000**, *55*, 4175-4187.
(27) Sloan, E. D. *Clathrate Hydrates of Natural Gases*; Marcel Dekker, Inc.: New York, 1998.
(28) Lerche, I.; Bagirov, E. "Guide to gas hydrate stability in various geological settings", *Mar. Pet. Geol.* **1998**, *15*, 427-437.
(29) Duncanson, M., Tulsa, OK 2005; Noria Corporation.
(30) Araujo, A. M.; Santos, L. M.; Fortuny, M.; Melo, R.; Coutinho, R. C. C.; Santos, A. F. "Evaluation of water content and average droplet size in water-in-crude oil emulsions by means of near-infrared spectroscopy", *Energy & Fuels* **2008**, *22*, 3450-3458.
(31) Begak, O. Y.; Syroezhko, A. M. "Monitoring of the sources of environmental pollution with crude oil", *Russian Journal of Applied Chemistry* **2001**, *74*, 636-639.

CHAPTER 2

Background

This thesis is focused on the design and application of mid-infrared (MIR) sensor platforms for the analysis of hydrocarbon containing systems in extreme environments. Therefore, this chapter describes background information on optical chemical sensors and their application at such conditions. Furthermore, fundamentals of infrared (IR) spectroscopy are covered with emphasis on attenuated total reflection (IR-ATR) spectroscopic techniques.

2.1 Optical chemical sensors

2.1.1 *Chemical sensors*

During the past three decades, research and development in the area of chemical sensors has exponentially expanded in terms of financial investment, number of papers published, and number of active researchers worldwide [1-3]. Hence, the research field of chemical sensors is considered among the fastest growing areas in modern analytical chemistry [2, 4-7]. The increasing interest in chemical sensors is driven by the need for in-situ and on-line applications in the field of environmental monitoring, industrial process analysis and control, biological/biochemical analysis, and high throughput screening in the medical/pharmaceutical fields [1].

A chemical sensor differentiates from a physical transducer by providing information on the chemical composition of its environment [1]. Therefore, chemical sensors may be defined as devices that responds to a chemical or physical quantity, and consequently produce a signal output as a measure of that quantity [6]. A thorough review of chemical sensors and the main characteristics of an "ideal" sensor has been presented in detail by Diamond [1].

2.1.2 *Optical sensors*

The field of chemical sensing can be divided into four main areas: thermal, mass, electrochemical, and optical transducers. Optical chemical sensors are based on the interaction between chemical species and light waves, which changes either the intensity, amplitude, polarization, phase, or wavelength of the incident radiation [8]. Because the field of telecommunications has been rapidly progressing, technologies such as fiber optics waveguides and laser diodes have become affordable, thus contributing to the rapid evolution of optical sensing devices [3, 9]. Specifically, the application of optical fibers for signal transportation and signal transduction has enabled the conversion of bench-top optical instrumentation into portable optical sensors capable of in-situ analysis in the field [3, 10-13 9, 14].

Optical sensing offers several advantages compared to other transduction techniques[15-18]. Because the signal is optical, it is less susceptible to magnetic fields, surface potentials, or electrical interferences [1]. Additionally, optical fibers allow the

transmission of optical signals over very long distances enabling remote sensing, therefore rendering these systems suitable for use in extreme environments [8]. Detailed information on applications of optical sensors can be found in several reviews [3, 12-15, 19].

Optical sensors based on optical fibers may be further divided into two categories: extrinsic or intrinsic sensors [1]. In an extrinsic sensor, the waveguide (most commonly an optical fiber) is used simply to transmit light to and from the sensing location [20]. Extrinsic sensors are already widely used in biomedicine [21], environmental monitoring [22], and process control and safety [23]. These sensors have several attractive features including simplicity, chemical robustness, thermal tolerance, inherent safety, electrical passivity, and compatibility with telemetry [1]. Additionally, extrinsic sensors may be miniaturized, thus making them compatible with *in vivo* applications [20]. On the contrary, in an intrinsic sensor, the waveguide itself plays an active role in the transduction process. The analyte directly interacts with the radiation transported in the waveguide and transforms chemical information into a detectable optical/analytical signal [8]. Intrinsic sensors present a number of attractive features in addition to those found in most extrinsic sensors. Intrinsic sensors may be used for studies of interfacial processes and of thin films taking advantage of the evanescent field for optically discriminating chemical species via interactions with this leaky mode [20]. These sensors present flexibility in the choice of their sensing mode, and in their analytical features by manipulation of material parameters such as the waveguide material and structure [3]. For instance, the interaction of an evanescent wave can be influenced by the design of the waveguide, its geometry, cladding, and reagents in close proximity to the waveguide [3, 20].

2.1.3 *General applications of optical sensors*

A range of recently developed optical chemical sensors and their applications have been described in detail in many reviews [2-7, 10-15, 20, 24, 25]. This section highlights only a few of the most recent findings contrasting the technologies applied in this thesis.

2.1.3.1 Fluorescence sensors

Sensors based on the principle of fluorescence are used for determining a broad range of analytes in liquid, solid, and gaseous samples, if the analytes exhibit intrinsic fluorescence or may quench or enhance fluorescence associated with selected reagents or markers/labels [2, 3, 13, 20]. Recently, Park et al. described the development of fiber optic sensors for the detection of inter- and intracellular dissolved oxygen [26]. Preejith et al. developed a tapered fluorescent fiber optic evanescent wave based sensor for serum protein [27]. Planar waveguide chemical sensors based on detection of fluorescence have been developed for a broad range of analytes including oxygen [28-31], solution with different pH [29], carbon dioxide [32], and a variety of biological species [33-35]. A recent overview of direct fluorescence sensing for biomedical applications has been summarized by McDonaugh et al.[3]

2.1.3.2 Ultraviolet-Visible (UV-Vis) sensors

Sensing based on UV absorption has mainly been used in environmental analysis to monitor pollutants such as heavy metals, hydrocarbons, and volatile organic compounds (VOC) in air and water [3, 12, 13]. For example, Tau and Sarma reported a sensor to detect Cr(VI) in water based on a flexible fused silica capillary and intrinsic evanescent-wave UV absorption of Cr ions in a water sample in the capillary [36]. A UV-differential optical absorption spectroscopy (UV-DOAS) based sensor was utilized to

measure the concentrations of ozone and NO_2 in the atmosphere; in addition, the contribution of NO_2 in limiting ozone formation was evaluated [37]. UV-DOAS was also utilized to monitor VOCs and aromatic hydrocarbons in ambient air in the vicinity of a refinery [38]. A similar approach was used to identify VOCs that were primarily resulting from vehicle emissions in a field study in Mexico [39].

2.1.3.3 Raman sensors

Raman spectroscopy is a useful technique for sensing of gaseous and liquid analytes. In particular, it is advantageous over IR spectroscopy for aqueous media sensing, since there is little interference from the vibrational spectrum of water [3]. Thus, Raman spectroscopy is a useful technique for application in biomedical diagnostics where aqueous environments are ubiquitous. Owen et al. have summarized the progress in Raman spectroscopy and its application in toxicological testing and tissue engineering [40]. This review demonstrated that Raman spectroscopy may be used as a non-invasive tool to study living cells. Principal components analysis of Raman spectra has been applied to distinguish between different cancer cells [41]. Kneipp et al. have used a Raman imaging system based on fiber optic probes to image breast tissue [42].

The disadvantages of conventional Raman spectroscopy, such as low scattering cross-sections, may be overcome by using surface enhanced Raman spectroscopy (SERS) techniques [43]. Additionally, with better understanding of the details of the plasmonic interaction and advances in materials fabrication, SERS is being increasingly applied in applicatuon areas including biomedicine and environmental analysis [44-47].

2.1.3.4 Infrared sensors

Applications of NIR fiber optic sensors for environmental monitoring have been extensively covered in the literature [25, 48-53]. The main advantage of NIR-based fiberoptic sensor systems is the availability of virtually any length of optical fiber required for remote sensing with material-associated attenuation losses close to the theoretical levels [25]. Major drawbacks of NIR sensors include limited selectivity and sensitivity due to relatively unspecific absorption features of organic molecules in this frequency range resulting from overtone vibrations. On the other hand, the mid-infrared spectral regime is in principle ideally suited for optical sensing applications [8].

Fundamental rotational and vibrational transitions in the MIR region (4000–400 cm^{-1}) provide strong and molecular-specific absorption bands, thus rendering mid-infrared optical sensing both sensitive and selective [54-57]. Furthermore, the inherent selectivity provided by the fingerprint region (1200–400 cm^{-1}) of the MIR spectrum renders this technique even more attractive for optical sensing[52, 58]. Additionally, the development and commercial availability of appropriate IR transparent materials contributed to the rapid evolution of MIR sensing schemes in recent years [9].

The basic principle of molecular level detection for the majority of published MIR sensors utilizes the well-recognized technique of attenuated total reflection (ATR) spectroscopy, and the resulting evanescent field, which may be derived from the general principle of internal reflection spectroscopy first explained by Harrick [8, 59, 60]. Utilizing optical fibers or elongated ATR-elements offers several advantages over conventional reflection or transmission based systems [8]. Firstly, since signal transportation is separated from signal generation, an inherently robust sensing method is provided.

Secondly, the optical path length may be increased with the number of internal reflections and the length of the active sensing region. Thirdly, measurements in aqueous matrices (i.e., strong IR absorbers) , particularly if an appropriate chemical recognition layer with a thickness larger than the penetration depth of the evanescent field is provided [8, 61].

In general, two classes of recognition layers (enrichment membranes) have been utilized for liquid phase IR-ATR sensors: polymer membranes [62-65] and sol-gel materials [66-69]. The enrichment layer/membrane is designed to extract analytes of interest from the aqueous medium, thus enhancing the analyte signal, which is generated by molecule-specific absorption of light via interaction with the evanescent field [70, 71]. Utilization of coated IR-ATR waveguides enables detection limits at low µg/L (ppb) levels for a wide variety of organic compounds with low susceptibility to temperature, turbidity, salinity, and humic acids, which are commonly encountered during direct analysis of e.g., natural samples from aqueous environments [72-77]. Hence, direct liquid phase detection of hydrocarbons and pesticides in water has been intensively investigated using MIR optic chemical sensor systems during the last two decades [9, 62, 64, 72-90].

As of today, only a few studies have reported on gas analysis based on surface modified IR fiber optics, because these methods were shown to be not very sensitive [91, 92]. Yet, the development of hollow waveguides (HWG) has provided a vital element to the field of MIR gas sensing enabling e.g., gas phase VOC analysis in a compact format [93-96].

Comprehensive reviews and articles on the various applications of optical sensors and polymers used for optical sensors are found in the relevant literature [3, 9, 12, 13, 17, 22, 69, 97-99]. As of now, novel developments in the field of mid-infrared sensing are largely focused on technological improvements of the optical components required for

establishing MIR sensor systems [3, 9, 25, 100]. Significant progress in the miniaturization of light sources (e.g., quantum cascade lasers) and optics (e.g., chip-integrated waveguides) is evident [101]. Thus, in combination with advanced chemical recognition schemes [102], a new generation of molecule specific optical sensors can be envisioned [25].

2.1.4 *Optical sensors in extreme environment: submersible MIR sensor systems*

In the past decade, a relatively novel field of chemical sensing applications involving monitoring subsea and coastal water environments has emerged in environmental and marine-aquatic chemistry communities [103]. These developments are a result of the continuous increase in environmental pollution of fresh/seawater reserves caused by expanding industrialization and concomitant domestic waste [75, 104]. In addition, substantial interest has emerged in studying target analytes in their native environments, if they are not stable when removed from the pressure and temperature regime they are initially present in, such as e.g., high temperature hydrothermal vent fluids and gas hydrates [105].

There have been extensive efforts to design chemical sensors and analyzers capable of operating at in situ subsea environmental conditions [103]. The majority of these efforts have been recently reviewed in two dedicated book volumes discussing chemical sensor systems for aquatic sciences [106, 107]. These volumes include chapters describing a variety of continuous flow analyzers, electrochemical sensors, and optical sensors for in situ measurements of dissolved chemical species. However, most of the above-mentioned work is focused on the research necessary to develop prototype sensor

systems, and only comparatively few chemical sensors are readily available that are sufficiently robust for routine and widespread use in deep sea environments [103].

Recently, Raman spectrometers, infrared spectrometers, and mass spectrometric devices have been introduced for a variety of subsea sensing applications. Several studies utilizing Raman spectrometers exploring hydrothermal gas vents and hydrate systems were carried out, mostly focusing on characterizing mineral components, gas hydrate structures and compositions, dissolved gases, and gas bubbles [108-113]. Additionally, detection and monitoring of dissolved gases and a wide range of VOCs were conducted using submersible mass spectrometers [114-123].

From the general description on the applicability of MIR sensors above, it is evident that they are highly suited for environmental and industrial monitoring in extreme environments, yet providing the demanded molecular selectivity and sensitivity. The recent availability of MIR transparent robust optical waveguides permitted analytical access to remote and potentially hazardous locations [3, 9, 13, 25, 124-126]. However, to date there has been only one submersible FT-IR spectrometer system demonstrated, which was designed and developed by our research group in the past decade. The feasibility of this approach has been demonstrated by multi-component analysis of aliphatic and aromatic hydrocarbons in seawater, which may be applied to a water depth of approx. 1,000 m [74, 87, 127]. The described system implemented core components from a commercial Bruker Vector 22 FT-IR spectrometer. An unclad silver halide fiber with a diameter of 700 µm and length of 38 cm in U-shaped geometry coated with an ethylene-co-propylene enrichment layer was used as the sensing fiber for quantitative evaluation of VOCs. The assembled instrument was enclosed in a sealed aluminum pressure vessel.

Overall, the complete system dimensions were approx. 1 m in length, 0.32 m in diameter, and approx. 95 kg of dry weight. Furthermore, the thesis of Dobbs has presented design considerations and initial efforts towards the development of the second generation of submersible MIR spectrometers and chemical sensing platforms for subsea exploration at significantly reduced dimensions [128].

2.2 Fundamentals of infrared spectroscopy

Infrared (IR) spectroscopy is based on the interaction of infrared radiation with matter. The IR spectrum of a compound provides important information on its chemical nature and molecular structure. Most commonly, the spectrum is obtained by measuring the absorption of IR radiation, although infrared emission and reflection are also commonly applied techniques. While infrared spectroscopy is most commonly applied for the analysis of organic materials, inorganic structures also provide highly specific vibrational spectra, as also shown in this thesis.

The infrared region of the electromagnetic spectrum is generally considered in the wavelength range from approx. 800 nm to 1000 μm; the corresponding wave number range is from 12,900 to 10 cm^{-1} (**Figure 2.1**). The entire electromagnetic spectrum ranges from cosmic rays and X-rays to visible light and extending into microwaves; independent of the wavelength, radiation may be considered as a wave or particle traveling at the speed of light (**Figure 2.1**) [129]. Each regime is characterized by a different wavelength and frequency. Frequency, *v*, is the number of oscillations of an electromagnetic wave per second [57]. It is measured in Hz, where 1 Hz = 1 cycle/sec. The wavelength, λ, is defined as the length of one complete wave cycle. By convention,

infrared wavelengths are typically reported in wavenumbers, ω, (cm^{-1}) [57]. The relationship between these parameters is as follows:

$$\lambda = \frac{c}{\nu}, \qquad \text{Equation 2.1}$$

where c is the speed of light in vacuum (3×10^{10} cm/sec). Furthermore,

$$\omega = \frac{1}{\lambda} \qquad \text{Equation 2.2}$$

Radiant energies in the IR region are of the order of magnitude relevant for vibrational and rotational transitions. Hence, IR spectroscopy is frequently referred to as a vibrational spectroscopic technique. The IR region is usually further subdivided into three regimes (**Figure 2.1**). The near-infrared (NIR) region extends from 770 nm to 2.5 µm (12,900 to 4000 cm^{-1}), the mid-infrared (MIR) region from 2.5 to 50 µm (4000 to 200 cm^{-1}), and the far-infrared region from 50 to 1000 µm (200 to 10 cm^{-1}) [129].

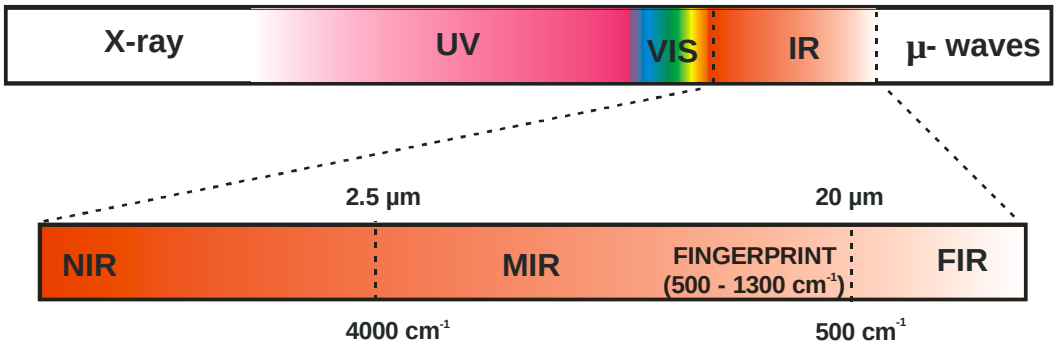

Figure 2.1: Electromagnetic spectrum with emphasis on the Mid-infrared (MIR) region (4000 -500 cm^{-1}).

The fundamental principle of IR absorption spectroscopy is based on the fact that radiation absorbed by a sample results in a decrease of initial light intensity (**Figure 2.2**).

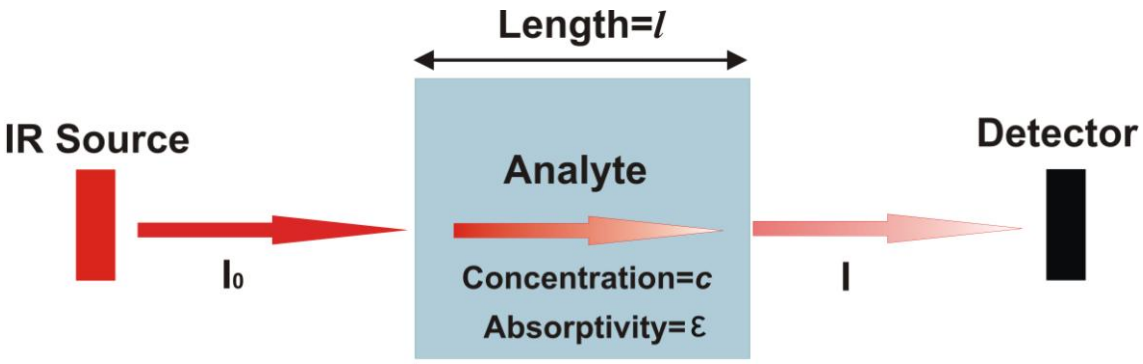

Figure 2.2: Principles of absorption spectroscopy.

The light intensity (incident radiation), I, is the energy per second per unit area of the light beam. Transmittance, *T*, is defined as the fraction of initial that passes through the sample:

$$T = \frac{I}{I_0} \qquad \text{Equation 2.3}$$

Therefore, *T* has the range of 0–1. Expressed as percentage (100*T*), transmission is usually given using a scale of 0 to 100%. In spectroscopy, absorbance (*A*) is a more frequently utilized expression for quantitative applications, and may be calculated by rearranging Equation 2.3:

$$A = -\log(T) = \log\left(\frac{I_0}{I}\right)$$ Equation 2.4

Furthermore, the absorbance is directly proportional to the concentration, *c*, of the light-absorbing species in the sample. This relationship is expressed by the Lambert-Beer law and provides the fundamentals for quantitative absorption spectroscopy:

$$A = \varepsilon c l \,,$$ Equation 2.5

where ε is the molar absorptivity, *c* is the concentration, and *l* is the optical path length (i.e., absorption path length) of the radiation propagating through the sample (**Figure 2.2**). *A* is a dimensionless parameter, *c* is usually given in units of moles per liter (M), *l* is commonly expressed in centimeters, and ε has the units $M^{-1}cm^{-1}$ [130]. The molar absorptivity is and individual (molecular) characteristic of any substance.

As IR spectroscopy is frequently used for quantitative determinations, the Lambert-Beer law reveals the linear dependence of the absorbance (*A*) on the concentration (*c*). However, at high analyte concentrations, the relationship may become non-linear, largely due to deviations in ε arising from electrostatic interactions between molecules in close proximity [130].

2.3 Principles of infrared-attenuated total reflection spectroscopy

Infrared-attenuated total reflection (IR-ATR) spectroscopy, an infrared reflection technique, was first described in the early 1960s by Fahrenfort and Harrick [59, 70]. ATR spectroscopy is based on the concept of total internal reflection (TIR). In TIR, radiation

is propagated through an optically dense waveguide with a refractive index (n_1) surrounded by an optically rarer medium (n_2); with $n_1 > n_2$ (**Figure 2.3**). Radiation propagating towards the interface between the waveguide and the surrounding medium at incident angles greater than the critical angle (θ_c) will be totally internally reflected (**Figure 2.3**).

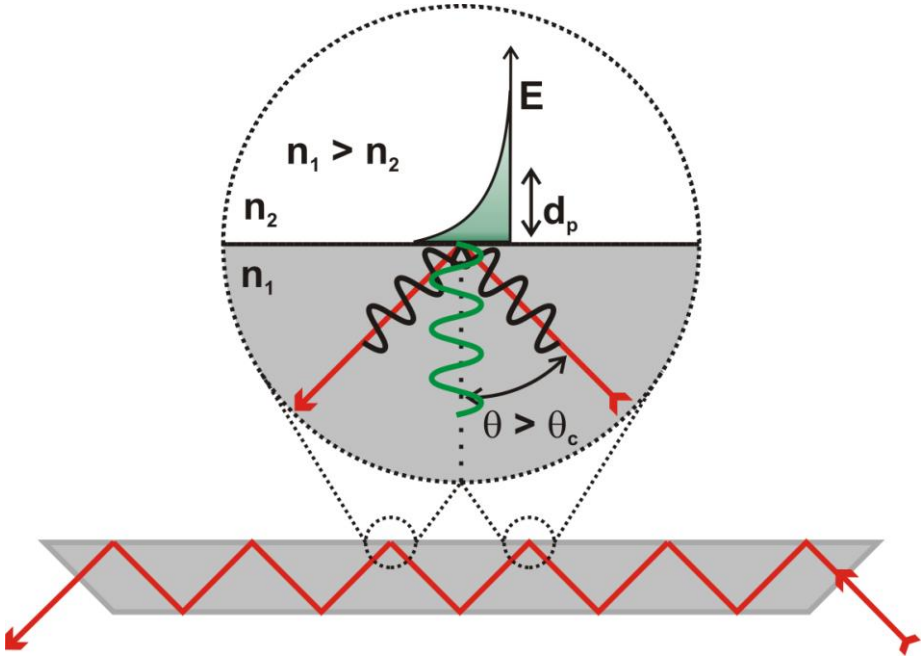

Figure 2.3: Principles of attenuated total reflection spectroscopy.

The critical angle is defined by the refractive indices of the waveguide and the surrounding medium:

$$\theta_c = \sin^{-1} \frac{n_2}{n_1}$$ Equation 2.6

At each internal reflection point, a standing wave is formed commonly referred to as the evanescent field, which penetrates into the optically rare medium normal to the reflection interface resulting from the superposition of electrical fields for incoming and reflected waves [59]. **Figure 2.3** presents a schematic representation of the evanescent field resulting from total internal reflection of light propagated through a waveguide (here, a trapezoidal internal reflection element).

The intensity of the evanescent field, *E*, exponentially decays with the distance from the optical interface following:

$$E = E_0 e^{\left(\frac{-z}{d_p}\right)}, \qquad \text{Equation 2.7}$$

where E_0 is the evanescent field intensity at the surface ($z = 0$); z is the distance from the surface; and d_p is the penetration depth where E_0 has decreased to a value of $1/e$ [59]. The penetration depth is dependent on the refractive indices of the waveguide and the surrounding medium, n_1 and n_2; the incident angle of the propagated radiation θ; and the wavelength of radiation, λ:

$$d_p = \frac{\lambda}{2\pi\sqrt{n_1^2 \sin^2\theta - n_2^2}} \qquad \text{Equation 2.8}$$

One of the major advantages of IR-ATR spectroscopy is the fact that absorption spectra are readily obtainable on a wide variety of sample types with minimum sample preparation [57, 129, 130]. The ATR method is frequently used to acquire spectra of challenging (i.e., opaque) samples such as e.g., polymer films, rubbers, food, fabrics, powders, and turbid liquid media [59]. It is important to note that, in practice, the effective interaction between the evanescent field and sample extends beyond d_p. The maximum

distance from the optical interface from which analytical information on a sample can be obtained is defined as the effective sample thickness (d_e). In ATR spectroscopy, the relationship between the attenuation of reflected light (R) at N reflection points and the sample absorption properties is established via d_e [59, 60]:

$$\ln R(\lambda) = -\varepsilon c \mathrm{N} d_e, \qquad \text{Equation 2.9}$$

where ln$R$ is comparable to ln$T$ for transmission-absorption spectroscopy, and Nd_e is the absorption pathlength comparable to l. Therefore, the sample absorbance in IR-ATR spectra may be expressed in a modified form of the Lambert-Beer law:

$$A(\lambda) \cong \varepsilon c \mathrm{N} d_e \qquad \text{Equation 2.10}$$

2.3.1 *Waveguide materials*

A variety of IR transparent ATR crystal materials and optical fibers are available to fulfill the conditions of total internal reflection for IR-ATR spectroscopic measurements [131-133]. **Table 2.1** provides a listing of most commonly used IR-ATR waveguides, however, represent only a fraction of available IR transparent materials [9, 131-133].

From a geometrical point of view, variations in thickness and length of the applied waveguides determine the number of internal reflections [134]. Additionally, the refractive indices control the penetration depth, and the optical properties of the waveguide material define the attenuation losses of guided IR radiation [131-133].

Table 2.1: Waveguide materials suitable for MIR sensing applications.

Material	Transmission range (cm^{-1})	Refractive index	Comments
Fibers			
Silver halides (AgX)	2500-500	2.1 @ 10.6 μm	insoluble in water incompatible with strong acids and bases
Chalcogenides (AsSeTe glasses)	10,000-900	2.9 @ 10.6 μm	insoluble in water incompatible with strong acids and bases
Sapphire (Al_2O_3)	50,000-2500	1.62 @ 5 μm	insoluble in water incompatible with strong acids and bases
ATR crystal			
Zinc selenide (ZnSe)	17,000-720	2.41 @ 9.5 μm	incompatible with acids and strong alkalis insoluble in water and organic solvents
Germanium (Ge)	5,500-600	4.00 @ 9.72 μm	insoluble in water insoluble in most bases and acids
Silicon (Si)	4000-1500	1.62 @ 5 μm	insoluble in water insoluble in most bases and acids
Thallium bromoiodide (KRS-5)	20,000-250	2.37 @ 10 μm	slightly soluble in water soluble in bases insoluble in most acids

2.3.2 *Measurement approaches*

2.3.2.1 Uncoated waveguides

As mentioned in section 2.3, the interaction of the evanescent field with the surrounding medium provides analytical information on IR absorbing species within the penetration depth. Because the path of excitation radiation is separated from the actual measurement, minimal disturbances may be anticipated. Therefore, attenuated total reflection has become a well-established and widely used technique in analytical chemistry, and is particularly important in the MIR due to the rather large penetration depth.

In this thesis, MIR transparent silver halide (AgX, where X is Br and Cl) optical fibers and trapezoidal ZnSe crystal are used; these elongated ATR elements with an increased number of internal reflections provide enhanced sensitivity for the in situ measurements. The utilization of uncoated waveguides (**Figure 2.4a**) for analytical sensing is well suited to evaluate major components of liquid phase samples via the direct exposure of a sample matrix to the evanescent field (studies in Chapter 3, 4, and 5). Depending on the absorption characteristics of the targeted analyte and matrix interferences, the sensitivity may range from parts per million to low mass percentages [135]. Measurements utilizing uncoated waveguides require no sample preparation, and enable almost real-time measurements providing IR spectra in the matter of seconds. However, if lower detection limits and enhanced sensitivity are needed, the performance of these waveguides needs to be improved by chemical enhancements based on enrichment membranes such as e.g., polymers [62].

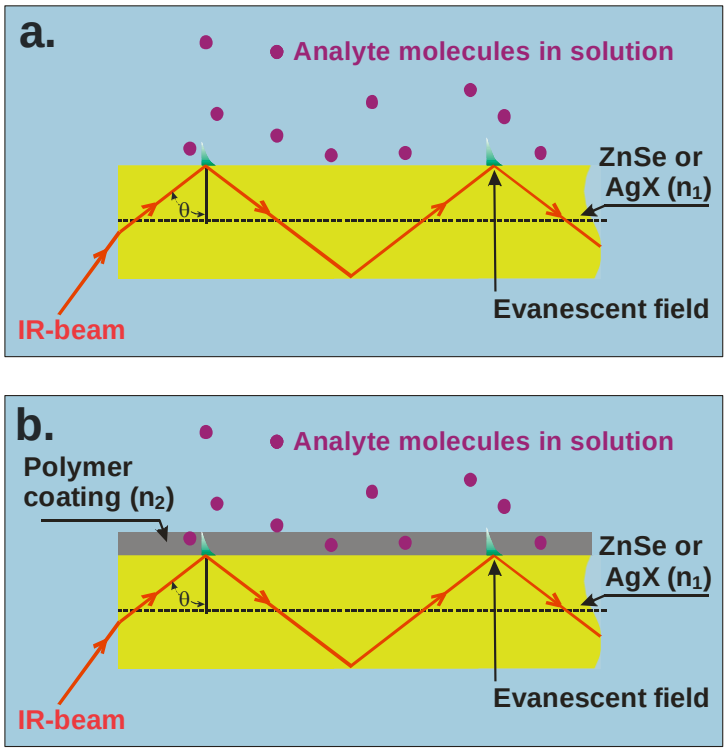

Figure 2.4: IR-ATR sensing strategy utilizing (a.) uncoated and (b.) polymer modified optical waveguide.

2.3.2.2 Coated waveguides

Polymeric enrichment layers are frequently applied if matrix components (e.g., water) strongly interfere with analyte absorption features. The enrichment membrane facilitates the suppression of background bulk matrix interferences, as the film thickness is generally exceeding the penetration depth of the evanescent field (d_p). In the case of water, the surface of optical waveguides is usually coated with hydrophobic polymers to minimize the amount of water in the sensing area, as shown in **Figure 2.4b** [62, 69, 89, 136, 137]. Additionally, polymer films may also serve for enhancing the optical signal during the detection of small compounds [62, 69, 137]. If the analyte has a higher affinity for the

polymer layer/membrane than the bulk matrix solution, the analyte will preferentially partition into the polymer (**Figure 2.4b**). Thus, the analyte content within the membrane is significantly increased; when probed by the evanescent field much lower detection limits are achieved due to this enrichment effect usually providing at least one order of magnitude improvement in sensitivity [62, 89]. This technique has successfully been demonstrated for enriching organic molecules from water into a polymer layer using mid-infrared ATR techniques [62, 68, 89]. However, selecting an appropriate enrichment membrane may be challenging, as the polymer membrane should exhibit high thermal, chemical, and physical stability, while providing high analyte affinity with rapid and reversible diffusion characteristics.

2.3 REFERENCES:

(1) Dermot, D. *Principles of chemical and biological sensors*; Wiley-Interscience Dublin, Ireland 1998.

(2) Janata, J.; Josowicz, M.; Vanysek, P.; DeVaney, D. M. "Chemical sensors" *Analytical Chemistry* **1998**, *70*, 179R-208R.

(3) McDonagh, C.; Burke, C. S.; MacCraith, B. D. "Optical chemical sensors" *Chem. Rev.* **2008**, *108*, 400-422.

(4) Janata, J. "Chemical sensors" *Analytical Chemistry* **1990**, *62*, R33-R44.

(5) Janata, J. "Chemical sensors" *Analytical Chemistry* **1992**, *64*, R196-R219.

(6) Janata, J.; Bezegh, A. "Chemical sensors" *Analytical Chemistry* **1988**, *60*, R62-R74.

(7) Janata, J.; Josowicz, M.; Devaney, D. M. "Chemical sensors" *Analytical Chemistry* **1994**, *66*, R207-R228.

(8) Mizaikoff, B. In *Habilitaionsshrift*; Vienna University of Technology: Vienna, Austria, 2000; Vol. 1.

(9) Mizaikoff, B. "Mid-IR Fiber-optic Sensors" *Analytical Chemistry* **2003**, *75*, 258A-267A.

(10) Wolfbeis, O. S. "Fiber-optic chemical sensors and biosensors" *Analytical Chemistry* **2002**, *74*, 2663-2677.

(11) Wolfbeis, O. S. "Fiber-optic chemical sensors and biosensors" *Analytical Chemistry* **2004**, *76*, 3269-3283.

(12) Wolfbeis, O. S. "Fiber-optic chemical sensors and biosensors" *Analytical Chemistry* **2006**, *78*, 3859-3873.

(13) Wolfbels, O. S. "Fiber-optic chemical sensors and biosensors" *Analytical Chemistry* **2008**, *80*, 4269-4283.

(14) Wolfbeis, O. S. "Fiber optic chemical sensors and biosensors" *Analytical Chemistry* **2000**, *72*, 81R-89R.

(15) Wolfbeis, O. S., Ed. *Fiber Optic Chemical Sensors and Biosensors*; Press, Boca Raton, Fl., 1991.

(16) Orellana, G.; Moreno-Bondi, M. C. *Frontiers in Chemical Sensors: Novel Principles and Techniques*; Springer:: New York, 2005.

(17) Baldini, F.; Chester, A. N.; Homola, J.; Martellucci, S. *Optical Chemical Sensors*; Springer: New York, 2006.

(18) Narayanaswamy, R.; Wolfbeis, O. S., Eds. *Optical Sensors − Industrial, Environmental and Diagnostic Applications*; Springer, 2004.

(19) Holst, G.; Mizaikoff, B. In *Handbook of Optical Fibre Sensing Technology*, 2002, pp 729-755.

(20) Potyrailo, R. A.; Hobbs, S. E.; Hieftje, G. M. "Optical waveguide sensors in analytical chemistry: today's instrumentation, applications and trends for future development" *Fresenius J. Anal. Chem.* **1998**, *362*, 349-373.

(21) Mignani, A. G.; Baldini, F. "Fibre-optic sensors in health care" *Phys. Med. Biol.* **1997**, *42*, 967-979.

(22) Rogers, K. R.; Poziomek, E. J. "Fiber optic sensors for environmental monitoring" *Chemosphere* **1996**, *33*, 1151-1174.

(23) Dao, N. Q.; Jouan, M. "THE RAMAN LASER FIBER OPTICS (RLFO) METHOD AND ITS APPLICATIONS" *Sens. Actuator B-Chem.* **1993**, *11*, 147-160.
(24) Janata, J. "Environmental chemical sensors - New challenge and opportunity" *Critical Reviews in Analytical Chemistry* **1998**, *28*, 27-34.
(25) Mizaikoff, B. "Infrared optical sensors for water quality monitoring" *Water Science and Technology* **2003**, *47*, 35-42.
(26) Park, E. J.; Reid, K. R.; Tang, W.; Kennedy, R. T.; Kopelman, R. "Ratiometric fiber optic sensors for the detection of inter- and intra-cellular dissolved oxygen" *J. Mater. Chem.* **2005**, *15*, 2913-2919.
(27) Preejith, P. V.; Lim, C. S.; Chia, T. F. "Serum protein measurement using a tapered fluorescent fibre-optic evanescent wave-based biosensor" *Meas. Sci. Technol.* **2006**, *17*, 3255-3260.
(28) McDonagh, C.; Kolle, C.; McEvoy, A. K.; Dowling, D. L.; Cafolla, A. A.; Cullen, S. J.; MacCraith, B. D. "Phase fluorometric dissolved oxygen sensor" *Sens. Actuator B-Chem.* **2001**, *74*, 124-130.
(29) Malins, C.; Niggemann, M.; MacCraith, B. D. "Multi-analyte optical chemical sensor employing a plastic substrate" *Meas. Sci. Technol.* **2000**, *11*, 1105-1110.
(30) Burke, C. S.; McGaughey, O.; Sabattie, J. M.; Barry, H.; McEvoy, A. K.; McDonagh, C.; MacCraith, B. D. "Development of an integrated optic oxygen sensor using a novel, generic platform" *Analyst* **2005**, *130*, 41-45.
(31) Chang-Yen, D. A.; Gale, B. K. "An integrated optical oxygen sensor fabricated using rapid-prototyping techniques" *Lab Chip* **2003**, *3*, 297-301.
(32) Burke, C. S.; Markey, A.; Nooney, R. I.; Byme, P.; McDonagh, C. "Development of an optical sensor probe for the detection of dissolved carbon dioxide" *Sens. Actuator B-Chem.* **2006**, *119*, 288-294.
(33) Duveneck, G. L.; Abel, A. P.; Bopp, M. A.; Kresbach, G. M.; Ehrat, M. "Planar waveguides for ultra-high sensitivity of the analysis of nucleic acids" *Anal. Chim. Acta* **2002**, *469*, 49-61.
(34) Huang, S. H.; Tseng, F. G. "Development of a monolithic total internal reflection-based biochip utilizing a microprism array for fluorescence sensing" *J. Micromech. Microeng.* **2005**, *15*, 2235-2242.
(35) Rowe-Taitt, C. A.; Golden, J. P.; Feldstein, M. J.; Cras, J. J.; Hoffman, K. E.; Ligler, F. S. "Array biosensor for detection of biohazards" *Biosens. Bioelectron.* **2000**, *14*, 785-794.
(36) Tao, S. Q.; Sarma, T. V. S. "Evanescent-wave optical CrVI sensor with a flexible fused-silica capillary as a transducer" *Opt. Lett.* **2006**, *31*, 1423-1425.
(37) Wu, B. Z.; Chang, C. C.; Sree, U.; Chiu, K.; Lo, J. G. "Measurement of non-methane hydrocarbons in Taipei city and their impact on ozone formation in relation to air quality" *Anal. Chim. Acta* **2006**, *576*, 91-99.
(38) Lin, T. Y.; Sree, U.; Tseng, S. H.; Chiu, K. H.; Wu, C. H.; Lo, J. G. "Volatile organic compound concentrations in ambient air of Kaohsiung petroleum refinery in Taiwan" *Atmos. Environ.* **2004**, *38*, 4111-4122.
(39) Velasco, E.; Lamb, B.; Westberg, H.; Allwine, E.; Sosa, G.; Arriaga-Colina, J. L.; Jobson, B. T.; Alexander, M. L.; Prazeller, P.; Knighton, W. B.; Rogers, T. M.; Grutter, M.; Herndon, S. C.; Kolb, C. E.; Zavala, M.; de Foy, B.; Volkamer, R.;

Molina, L. T.; Molina, M. J. "Distribution, magnitudes, reactivities, ratios and diurnal patterns of volatile organic compounds in the Valley of Mexico during the MCMA 2002 & 2003 field campaigns" *Atmos. Chem. Phys.* **2007**, *7*, 329-353.

(40) Owen, C. A.; Notingher, I.; Hill, R.; Stevens, M.; Hench, L. L. "Progress in Raman spectroscopy in the fields of tissue engineering, diagnostics and toxicological testing" *J. Mater. Sci.-Mater. Med.* **2006**, *17*, 1019-1023.

(41) Shafer-Peltier, K. E.; Haka, A. S.; Motz, J. T.; Fitzmaurice, M.; Dasari, R. R.; Field, S. "Model-based biological Raman spectral imaging" *J. Cell Biochem.* **2002**, *39*, 125.

(42) Kneipp, J.; Schut, T. B.; Kliffen, M.; Menke-Pluijmers, M.; Puppels, G. "Characterization of breast duct epithelia: a Raman spectroscopic study" *Vib. Spectrosc.* **2003**, *32*, 67-74.

(43) Stuart, D. A.; Biggs, K. B.; Van Duyne, R. P. "Surface-enhanced Raman spectroscopy of half-mustard agent" *Analyst* **2006**, *131*, 568-572.

(44) Zhang, X. Y.; Shah, N. C.; Van Duyne, R. P. "Sensitive and selective chem/biosensing based on surface-enhanced Raman spectroscopy (SERS)" *Vib. Spectrosc.* **2006**, *42*, 2-8.

(45) Vodinh, T. "SERS chemical sensors and biosensors - new tools for environmental and biological analysis" *Sens. Actuator B-Chem.* **1995**, *29*, 183-189.

(46) Vo-Dinh, T.; Yan, F.; Wabuyele, M. B. In *Surface-Enhanced Raman Scattering: Physics and Applications*; Springer-Verlag Berlin: Berlin, 2006; Vol. 103, pp 409-426.

(47) Yonzon, C. R.; Stuart, D. A.; Zhang, X. Y.; McFarland, A. D.; Haynes, C. L.; Van Duyne, R. P. "Towards advanced chemical and biological nanosensors - An overview" *Talanta* **2005**, *67*, 438-448.

(48) Buerck, J.; Roth, S.; Kraemer, K.; Scholz, M.; Klaas, N. "Application of a fiber-optic NIR-EFA sensor system for in situ monitoring of aromatic hydrocarbons in contaminated groundwater" *Journal of Hazardous Materials* **2001**, *83*, 11-28.

(49) Sensfelder, E.; Burck, J.; Ache, H. J. "Determination of hydrocarbons in water by evanescent wave absorption spectroscopy in the near-infrared region" *Fresenius J. Anal. Chem.* **1996**, *354*, 848-851.

(50) Burck, J.; Mensch, M.; Kramer, K. "Field experiments with a portable fiber-optic sensor system for monitoring hydrocarbons in water" *Field Anal. Chem. Technol.* **1998**, *2*, 205-219.

(51) Burck, J.; Conzen, J. P.; Beckhaus, B.; Ache, H. J. "Fiberoptic evanescent-wave sensor for in-situ determination of nonpolar organic-compounds in water" *Sens. Actuator B-Chem.* **1994**, *18*, 291-295.

(52) Mizaikoff, B.; Jakusch, M.; Kraft, M. "Infrared fiber-optic sensors - Versatile tool for water monitoring - Optical chemical sensors gain importance in environmental monitoring, process analysis/control; Now complement separation techniques and spectroscopy" *Sea Technol.* **1999**, *40*, 25-+.

(53) Blair, D. S.; Burgess, L. W.; Brodsky, A. M. "Evanescent fiber optic chemical sensor for monitoring volatile organic compounds in water" *Analytical Chemistry* **1997**, *69*, 2238-2246.

(54) Harris, D. C.; Bertolucci, M. D. *Symmetry and Spectroscopy: An Introduction to Vibrational and Electronic Spectroscopy*; Dover Publication, Inc.: New York, 1978.
(55) Pavia, D. L.; Lampman, G. M.; Kriz, G. S. *Introduction to Spectroscopy: A Guide for Students of Organic Chemistry*, Second ed.; Saunders College Publishing: Fort Worth, 1996.
(56) Skoog, D. A.; Holler, F. J.; Nieman, T. A. *Principles of Instrumental Analsyis*, Fifth ed.; Brooks Cole, 1997.
(57) Harris, D. C. *Quantitative Chemical Analysis*, Sixth ed.; W. H. Freeman and Company: New York, 2003.
(58) Mizaikoff, B. "Infrared optical sensors for water quality monitoring" *Water Science & Technology* **1999**, *47*, 35-42.
(59) Harrick, N. J. *Internal Reflection Spectroscopy*; John Wiley & Sons: New York, 1967.
(60) Harrick, N. J.; Carlson, A. I. "Internal Reflection Spectroscopy: Validity of Effective Thickness Equations" *Applied Optics* **1971**, *10*, 19-23.
(61) Jakuch, M.; Mizaikoff, B. 2001; Society of Photo-Optical Instrumentation Engineers; 93-98.
(62) Heinrich, P.; Wyzgol, R.; Schrader, B.; Hatzilazaru, A.; Luebbers, D. W. "Determination of Organic Compounds by IR/ATR Spectroscopy with Polymer-coated Internal Reflection Elements" *Applied Spectroscopy* **1990**, *44*, 1641-1646.
(63) Goebel, R.; Krska, R.; Kellner, R.; Seitz, R. W.; Tomellini, S. A. "Investigation of different polymers as coating materials for IR/ATR spectroscopic trace analysis for chlorinated hydrocarbons in water" *Appl. Spectrosc.* **1994**, *48*, 678-683.
(64) Mizaikoff, B.; Goebel, R.; Krska, R.; Taga, K.; Kellner, R.; Tacke, M.; Katzir, A. "Infrared fiber-optical chemical sensors with reactive surface coatings" *Sens. Actuators, B* **1995**, *B29*, 58-63.
(65) Jakusch, M.; Janotta, M.; Mizaikoff, B.; Mosbach, K.; Haupt, K. "Molecularly imprinted polymers and infrared evanescent wave spectroscopy. A chemical sensors approach" *Analytical Chemistry* **1999**, *71*, 4786-4791.
(66) MacCraith, B. D. "Optical chemical sensors based on sol-gel-derived films" *Crit. Rev. Opt. Sci. Tech.* **1997**, *CR68*, 64-89.
(67) Han, L.; Niemczyk, T. M.; Lu, Y.; Lopez, G. P. "Chemical sensors based on surface-modified sol-gel-coated infrared waveguides" *Appl. Spectrosc.* **1998**, *52*, 119-122.
(68) Janotta, M.; Karlowatz, M.; Vogt, F.; Mizaikoff, B. "Sol-gel based mid-infrared evanescent wave sensors for detection of organophosphate pesticides in aqueous solution" *Anal. Chim. Acta* **2003**, *496*, 339-348.
(69) Janotta, M.; Katzir, A.; Mizaikoff, B. "Sol-gel-coated mid-infrared fiber-optic sensors" *Appl. Spectrosc.* **2003**, *57*, 823-828.
(70) Fahrenfort, J. "Attenuated Total Reflection. A New Principle for the Production of Useful Infrared Reflection Spectra of Organic Compounds" *Spectrochimica Acta* **1961**, *17*, 698-709.
(71) Harrick, N. J. *Internal Reflection Spectroscopy*; Harrick: Ossining, N.Y., 1979.

(72) Goebel, R.; Krska, R.; Neal, S.; Kellner, R. "Performance studies of an IR fiber optic sensor for chlorinated hydrocarbons in water" *Fresenius. J. Anal. Chem.* **1994**, *350*, 514-519.
(73) Walsh, J. E.; MacCraith, B. D.; Meaney, M.; Vos, J. G.; Regan, F.; Lancia, A.; Artjushenko, S. "Sensing of chlorinated hydrocarbons and pesticides in water using polymer coated mid-infrared optical fibers" *Analyst (Cambridge, U. K.)* **1996**, *121*, 789-792.
(74) Kraft, M.; Mizaikoff, B. "A Mid-infrared Sensor for Monitoring of Chlorinated Hydrocarbons in the Marine Environment" *International Journal of Environmental Analytical Chemistry* **2000**, *78*, 367-383.
(75) Kraft, M.; Jakusch, M.; Karlowatz, M.; Katzir, A.; Mizaikoff, B. "New frontiers for mid-infrared sensors: Towards deep sea monitoring with a submarine FT-IR sensor system" *Appl. Spectrosc.* **2003**, *57*, 591-599.
(76) Beyer, T.; Hahn, P.; Hartwig, S.; Konz, W.; Scharring, S.; Katzir, A.; Steiner, H.; Jakusch, M.; Kraft, M.; Mizaikoff, B. "Mini spectrometer with silver halide sensor fiber for in situ detection of chlorinated hydrocarbons" *Sens. Actuators, B* **2003**, *B90*, 319-323.
(77) Dobbs, G. T.; Balu, B.; Young, C.; Kranz, C.; Hess, D. W.; Mizaikoff, B. "Mid-infrared chemical sensors utilizing plasma-deposited fluorocarbon membranes" *Analytical Chemistry* **2007**, *79*, 9566-9571.
(78) Pejcic, B.; Myers, M.; Ross, A. "Mid-Infrared Sensing of Organic Pollutants in Aqueous Environments" *Sensors* **2009**, *9*, 6232-6253.
(79) Acha, V.; Meurens, M.; Naveau, H.; Agathos, S. N. "ATR-FTIR sensor development for continuous on-line monitoring of chlorinated aliphatic hydrocarbons in a fixed-bed bioreactor" *Biotechnol. Bioeng.* **2000**, *68*, 473-487.
(80) Flavin, K.; Mullowney, J.; Murphy, B.; Owens, E.; Kirwan, P.; Murphy, K.; Hughes, H.; McLoughlin, P. "The development of novel organically modified sol-gel media for use with ATR/FTIR sensing" *Analyst* **2007**, *132*, 224-229.
(81) Howley, R.; MacCraith, B. D.; O'Dwyer, K.; Masterson, H.; Kirwan, P.; McLoughlin, P. "Determination of hydrocarbons using sapphire fibers coated with poly(dimethylsiloxane)" *Applied Spectroscopy* **2003**, *57*, 400-406.
(82) Krska, R.; Taga, K.; Kellner, R. "New IR fiber-optic chemical sensor for in situ measurements of chlorinated hydrocarbons in water" *Appl. Spectrosc.* **1993**, *47*, 1484-1487.
(83) Jakusch, M.; Mizaikoff, B.; Kellner, R.; Katzir, A. "Towards a remote IR fiber-optic sensor system for the determination of chlorinated hydrocarbons in water" *Sens. Actuators, B* **1997**, *B38*, 83-87.
(84) Mizaikoff, B. "Mid-infrared evanescent wave sensors - a novel approach for subsea monitoring" *Meas. Sci. Technol.* **1999**, *10*, 1185-1194.
(85) Holst, G.; Mizaikoff, B. "Fiber optic sensors for environmental applications" *Handbook of Optical Fibre Sensing Technology* **2002**, 729-755.
(86) Mizaikoff, B. "Infrared optical sensors for water quality monitoring" *Water Sci. Technol.* **2003**, *47*, 35-42.
(87) Steiner, H.; Jakusch, M.; Kraft, M.; Karlowatz, M.; Baumann, T.; Niessner, R.; Konz, W.; Brandenburg, A.; Michel, K.; Boussard-Pledel, C.; Bureau, B.; Lucas,

J.; Reichlin, Y.; Katzir, A.; Fleischmann, N.; Staubmann, K.; Allabashi, R.; Bayona, J. M.; Mizaikoff, B. "In situ sensing of volatile organic compounds in groundwater: First field tests of a mid-infrared fiber-optic sensing system" *Applied Spectroscopy* **2003**, *57*, 607-613.

(88) Steiner, H.; Staubmann, K.; Allabashi, R.; Fleischmann, N.; Katzir, A.; Reichlin, Y.; Mizaikoff, B. "Online sensing of volatile organic compounds in groundwater using mid-infrared fiber optic evanescent wave spectroscopy: a pilot scale test" *Water Sci. Technol.* **2003**, *47*, 121-126.

(89) Karlowatz, M.; Kraft, M.; Mizaikoff, B. "Simultaneous quantitative determination of benzene, toluene, and xylenes in water using mid-infrared evanescent field spectroscopy" *Anal. Chem.* **2004**, *76*, 2643-2648.

(90) Regan, F.; Meaney, M.; Vos, J. G.; MacCraith, B. D.; Walsh, J. E. "Determination of pesticides in water using ATR-FTIR spectroscopy on PVC/chloroparaffin coatings" *Anal. Chim. Acta* **1996**, *334*, 85-92.

(91) Taga, K.; Mizaikoff, B.; Kellner, R. "Fiber optic evanescent field sensors for gaseous species using mir transparent fibers" *Fresenius J. Anal. Chem.* **1994**, *348*, 556-559.

(92) Mizaikoff, B.; Taga, K.; Kellner, R. "Infrared fiber optic gas sensor for chlorofluorohydrocarbons" *Vib. Spectrosc.* **1995**, *8*, 103-108.

(93) Kim, S. S.; Menegazzo, N.; Young, C.; Chan, J.; Carter, C.; Mizaikoff, B. "Mid-Infrared Trace Gas Analysis with Single-Pass Fourier Transform Infrared Hollow Waveguide Gas Sensors" *Applied Spectroscopy* **2009**, *63*, 331-337.

(94) Kim, S. S.; Young, C.; Vidakovic, B.; Gabram-Mendola, S. G. A.; Bayer, C. W.; Mizaikoff, B. "Potential and Challenges for Mid-Infrared Sensors in Breath Diagnostics" *Ieee Sensors Journal* **2010**, *10*, 145-158.

(95) Wilk, A.; Kim, S. S.; Mizaikoff, B. "An approach to the spectral simulation of infrared hollow waveguide gas sensors" *Analytical and Bioanalytical Chemistry* **2009**, *395*, 1661-1671.

(96) Young, C.; Kim, S. S.; Luzinova, Y.; Weida, M.; Arnone, D.; Takeuchi, E.; Day, T.; Mizaikoff, B. "External cavity widely tunable quantum cascade laser based hollow waveguide gas sensors for multianalyte detection" *Sens. Actuator B-Chem.* **2009**, *140*, 24-28.

(97) Gobel, R.; Krska, R.; Kellner, R.; Kastner, J.; Lambrecht, A.; Tacke, M.; Katzir, A. "Enhancing the sensitivity of chemical sensors for chlorinated hydrocarbons in water by the use of tapered silver-halide fibers and tunable diode-lasers" *Applied Spectroscopy* **1995**, *49*, 1174-1177.

(98) Gobel, R.; Krska, R.; Kellner, R.; Seitz, R. W.; Tomellini, S. A. "Investigation of different polymers as coating materials for ir atr spectroscopic trace analysis of chlorinated hydrocarbons in water" *Applied Spectroscopy* **1994**, *48*, 678-683.

(99) Gobel, R.; Seitz, R. W.; Tomellini, S. A.; Krska, R.; Kellner, R. "Infrared attenuated total-reflection spectroscopic investigations of the diffusion behavior of chlorinated hydrocarbons into polymer membranes" *Vib. Spectrosc.* **1995**, *8*, 141-149.

(100) Hvozdara, L.; Pennington, N.; Kraft, A.; Karlowatz, M.; Mizaikoff, B. "Quantum cascade lasers for mid-infrared spectroscopy" *Vib. Spectrosc.* **2002**, *30*, 53-58.

(101) Kim, S. S.; Young, C.; Mizaikoff, B. "Miniaturized mid-infrared sensor technologies" *Analytical and Bioanalytical Chemistry* **2008**, *390*, 231-237.
(102) Sellergren, B., Ed. *Molecularly Imprinted Polymers*; Elsevier, 2000
(103) Johnson, K. S.; Needoba, J. A.; Riser, S. C.; Showers, W. J. "Chemical sensor networks for the aquatic environment" *Chem. Rev.* **2007**, *107*, 623-640.
(104) Mizaikoff, B. "Mid-infrared evanescent wave sensors - a novel approach for subsea monitoring" *Meas. Sci. Technol.* **1999**, *10*, 1185-1194.
(105) Hester, K. C.; Dunk, R. M.; Walz, P. M.; Peltzer, E. T.; Sloan, E. D.; Brewer, P. G. "Direct measurements of multi-component hydrates on the sealoor: Pathways to growth" *Fluid Phase Equilib.* **2007**, *261*, 396-406.
(106) Buffle, J.; Horvai, G. In *IUPAC Series on Analytical andPhysical Chemistry of Environmental Systems*; Wiley: Chichester, England, 2000; Vol. 6.
(107) Varney, M. *Chemical sensors in oceanography*; Gordon andBreach: Amsterdam, The Netherlands, 2000.
(108) Battaglia, T. M.; Dunn, E. E.; Lilley, M. D.; Holloway, J.; Dable, B. K.; Marquardt, B. J.; Booksh, K. S. "Development of an In Situ Fiber Optic Raman System to Monitor Hydrothermal Vents" *Analyst (Cambridge, United Kingdom)* **2004**, *129*, 602-606.
(109) Brewer, P. G.; Malby, G.; Pasteris, J. D.; White, S. N.; Peltzer, E. T.; Wopenka, B.; Freeman, J.; Brown, M. O. "Development of a Laser Raman Spectrometer for Deep-ocean Science" *Deep-Sea Research, Part I: Oceanographic Research Papers* **2004**, *51*, 739-753.
(110) Hester, K. C.; Dunk, R. M.; White, S. N.; Brewer, P. G.; Peltzer, E. T.; Sloan, E. D. "Gas Hydrate Measurements at Hydrate Ridge using Raman Spectroscopy" *Geochimica et Cosmochimica Acta* **2007**, *71*, 2947-2959.
(111) Hester, K. C.; White, S. N.; Peltzer, E. T.; Brewer, P. G.; Sloan, E. D. "Raman Spectroscopic Measurements of Synthetic Gas Hydrates in the Ocean" *Marine Chemistry* **2006**, *98*, 304-314.
(112) Pasteris, J. D.; Wopenka, B.; Freeman, J. J.; Brewer, P. G.; White, S. N.; Peltzer, E. T.; Malby, G. E. "Raman Spectroscopy in the Deep Ocean: Successes and Challenges" *Applied Spectroscopy* **2004**, *58*, 195A-208A.
(113) White, S. N.; Dunk, R. M.; Peltzer, E. T.; Freeman, J. J.; Brewer, P. G. "In Situ Raman Analyses of Deep-sea Hydrothermal and Cold Seep Systems (Gorda Ridge and Hydrate Ridge)" *Geochemistry, Geophysics, Geosystems* **2006**, *7*, No pp given.
(114) Camilli, R.; Hemond, H. F. "NEREUS/Kemonaut, A Mobile Autonomous Underwater Mass Spectrometer" *TrAC, Trends in Analytical Chemistry* **2004**, *23*, 307-313.
(115) Fries, D. P.; Short, R. T.; Langebrake, L. L.; Patten, J. T.; Kerr, M. L.; Kibelka, G.; Burwell, D. C.; Jalbert, J. C. "In-water Field Analytical Technology: Underwater Mass Spectrometry, Mobile Robots, and Remote Intelligence for Wide and Local Area Chemical Profiling" *Field Analytical Chemistry and Technology* **2001**, *5*, 121-130.
(116) Hemond, H.; Camilli, R. "NEREUS: Engineering Concept for an Underwater Mass Spectrometer" *TrAC, Trends in Analytical Chemistry* **2002**, *21*, 526-533.

(117) Janfelt, C.; Lauritsen, F. R.; Toler, S. K.; Bell, R. J.; Short, R. T. "Method for Quantification of Chemicals in a Pollution Plume Using a Moving Membrane-based Sensor Exemplified by Mass Spectrometry" *Analytical Chemistry (Washington, DC, United States)* **2007**, *79*, 5336-5342.
(118) Ketola, R. A.; Kotiaho, T.; Cisper, M. E.; Allen, T. M. "Environmental Applications of Membrane Introduction Mass Spectrometry" *Journal of Mass Spectrometry* **2002**, *37*, 457-476.
(119) Kibelka, G. P. G.; Timothy Short, R.; Toler, S. K.; Edkins, J. E.; Byrne, R. H. "Field-deployed Underwater Mass Spectrometers for Investigations of Transient Chemical Systems" *Talanta* **2004**, *64*, 961-969.
(120) Short, R. T.; Fries, D. P.; Kerr, M. L.; Lembke, C. E.; Toler, S. K.; Wenner, P. G.; Byrne, R. H. "Underwater Mass Spectrometers for In Situ Chemical Analysis of the Hydrosphere" *Journal of the American Society for Mass Spectrometry* **2001**, *12*, 676-682.
(121) Short, R. T.; Fries, D. P.; Toler, S. K.; Lembke, C. E.; Byrne, R. H. "Development of an Underwater Mass-spectrometry System for In Situ Chemical Analysis" *Measurement Science and Technology* **1999**, *10*, 1195-1201.
(122) Short, R. T.; Toler, S. K.; Kibelka, G. P. G.; Rueda Roa, D. T.; Bell, R. J.; Byrne, R. H. "Detection and Quantification of Chemical Plumes using a Portable Underwater Membrane Introduction Mass Spectrometer" *TrAC, Trends in Analytical Chemistry* **2006**, *25*, 637-646.
(123) Wenner, P. G.; Bell, R. J.; Van Amerom, F. H. W.; Toler, S. K.; Edkins, J. E.; Hall, M. L.; Koehn, K.; Short, R. T.; Byrne, R. H. "Environmental Chemical Mapping using an Underwater Mass Spectrometer" *TrAC, Trends in Analytical Chemistry* **2004**, *23*, 288-295.
(124) Gotz, R.; Mizaikoff, B.; Kellner, R. "Application of sapphire fibres to IR fibre-optic evanescent field gas sensors" *Mikrochimica Acta* **1997**, 833-835.
(125) Gotz, R.; Mizaikoff, B.; Kellner, R. "Application of sapphire fibers to an IR fiber-optic sensor for the investigation of polymers at elevated temperature" *Applied Spectroscopy* **1998**, *52*, 1248-1252.
(126) Mizaikoff, B. In *SPIE conference on Infrared Opitcal Fibers and Their Applications*: Boston, Massachusetts, 1999; Vol. 3849.
(127) Kraft, M.; Jakusch, M.; Mizaikoff, B. "A Miniaturised Fourier-Transform Infrared Spectrometer for Seawater Monitoring" *IEEE* **1998**, 1701-1703.
(128) Dobbs, G. T., Georgia Institute of Technology, Atlanta, 2007.
(129) Ingle, J. D.; Crouch, S. R. *Spectrochemical Analysis*; Prince-Hall Inc.: Upper Saddle River, NJ, 1988.
(130) Kellner, R.; Mermet, J. M.; Otto, M.; Vlcarcel, M.; Widmer, H. M. *Analytical chemistry*, second ed.; Wiley-VCH Verlag GmbH & Co. KGaA, 2004.
(131) "Harrick Scientific Products, Inc." *http://www.harrickscI.com/,* **March 2010**.
(132) "MacroOptica Ltd" *http://www.macrooptica.com/,* **March 2010**.
(133) "PIKE Technologies" *http://www.piketech.com/,* **March 2010**.
(134) Dobbs, G. T.; Mizaikoff, B. "Shining new light on old principles: Localization of evanescent field interactions at infrared-attenuated total reflection sensing interfaces" *Applied Spectroscopy* **2006**, *60*, 573-583.

(135) Michel, K.; Bureau, B.; Boussard-Pledel, C.; Jouan, T.; Adam, J. L.; Staubmann, K.; Baumann, T. "Monitoring of Pollutant in Wastewater by Infrared Spectroscopy using Chalcogenide Glass Optical Fibers" *Sensors and Actuators, B: Chemical* **2004**, *B101*, 252-259.
(136) Murphy, B.; McLoughlin, P. "Determination of Chlorinated Hydrocarbon Species in Aqueous Solution using Teflon Coated ATR Waveguide/FTIR Spectroscopy" *International Journal of Environmental Analytical Chemistry* **2003**, *83*, 653-662.
(137) Dobbs, G. T.; Balu, B.; Young, C.; Kranz, C.; Hess, D. W.; Mizaikoff, B. "Mid-infrared chemical sensors utilizing plasma-deposited fluorocarbon membranes", *Analytical Chemistry* **2007**, *79*, 9566-9571

CHAPTER 3

Quantification of Diamondoid Compound, Adamantane, in Organic Media via Infrared Attenuated Total Reflection Spectroscopy

This chapter establishes the quantitative determination of the diamondoid compound adamantane in organic media via infrared attenuated total reflection (IR-ATR) spectroscopy at unmodified waveguide surfaces. Limits of detection (LOD) and quantification (LOQ) of adamantane in dichloromethane, hexane, and carbon tetrachloride were determined. Quantitative IR-ATR measurements additionally facilitated the determination of adamantane solubility limit in dichloromethane, hexane, and in carbon tetrachloride. The developed analytical strategy further enabled the successful detection and quantification of adamantane in crude oil matrices.

3.1 MOTIVATION

The need for understanding the nature of diamondoids present in crude oil, and their role during production and processing of petroleum is well recognized around the world [1, 2]. Diamondoids occur naturally in virtually all crude oils, intermediate petroleum distillates, and finished petroleum products [3]. These compounds—including their alkylated homologues—have frequently been considered hazardous materials in the petroleum industry, as they are inclined to deposit during production and transportation of natural gas, gas condensates, and light crude oils [4]. At high concentrations, diamondoid compounds may segregate from reservoir fluids due to drastic changes in pressure and temperature during production [1]. Consequently, it is important to rapidly

assess whether or not diamondoids occur in a reservoir fluid at concentrations with the potential to adversely affect production operations.

As of today, the "gold standard" for quantifying diamondoids in petroleum products is the well-established analytical method of gas chromatography combined with mass spectrometry (GC-MS) [5-8]. Detection limits of 60–140 ppb of diamondoids in petroleum product are possible with GC-MS [5]. However, GC-MS has some practical drawbacks for on-site analysis including the large size of the instrument, complicated sample preparation, and length of time required to perform the analysis. Thus, there is the need for a more cost-effective, rapid, and minituarizable technique for on-site and potentially in-situ analysis of diamondoids.

Unlike GC-MS, IR-ATR spectroscopy provides the distinct advantage of substantial measurement flexibility, enabling to readily adapt IR-ATR to a wide variety of measurement problems. It also provides the distinct opportunity for miniaturization, rendering this analytical tool suitable for quantitative evaluation of single- and multi-constituent sample systems. With IR-ATR spectroscopy, quantitative results may be obtained within several seconds to minutes without any sample preparation, rendering this technique particularly suitable for in-situ or rapid on-ship analysis.

As of today, infrared attenuated total reflection (IR-ATR) spectroscopic analysis has yet to be reported as a flexible and possibly miniaturizable analytical tool for rapid quantification of adamantane in organic matrices relevant to the petroleum industry, even though IR-ATR appears ideally suited for this application [9-14]. Thus, in this chapter, the applicability of this technique for characterization and detection of diamondoids is studied.

3.2 BACKGROUND

3.2.1 Diamondoids

3.2.1.1 *Structure*

Diamondoids are a class of saturated hydrocarbons that consist of a diamond-like carbon cage, where all carbon atoms are sp^3 hybridized, and dangling bonds at the edges of the cage system are terminated with hydrogen atoms [15]. The lower diamondoids have chemical formulas of $C_{4n+6}H_{4n+12}$, where *n* equals the number of diamond-cage subunits. The smallest member of the diamondoid family, adamantane ($C_{10}H_{16}$), is composed of a single diamond unit cell, followed by its homologues diamantane, triamantane, tetramantane, pentamantane, hexamantane, and heptamentane, etc. (**Figure 3.1**).

3.2.1.2 *Discovery*

Adamantane was the first diamondoid discovered and isolated from a sample of Czechoslovakian petroleum in 1933 [16]. Adamantane, higher diamondoids, and their various substituted equivalents are widely found in crude oils, intermediate petroleum distillates, and finished petroleum products [2]. Lin and Wilk observed a suite of petroleum polymantanes, including tetramantane, pentamantane, and hexamantane in a gas condensate produced from a very deep petroleum reservoir located in the United States Gulf Coast [17]. Dahl et al. reported the successful separation of a wide variety of the higher diamondoids containing 4 (tetramentane) to 11 (undecamantane) diamond-crystal cages from petroleum[18].

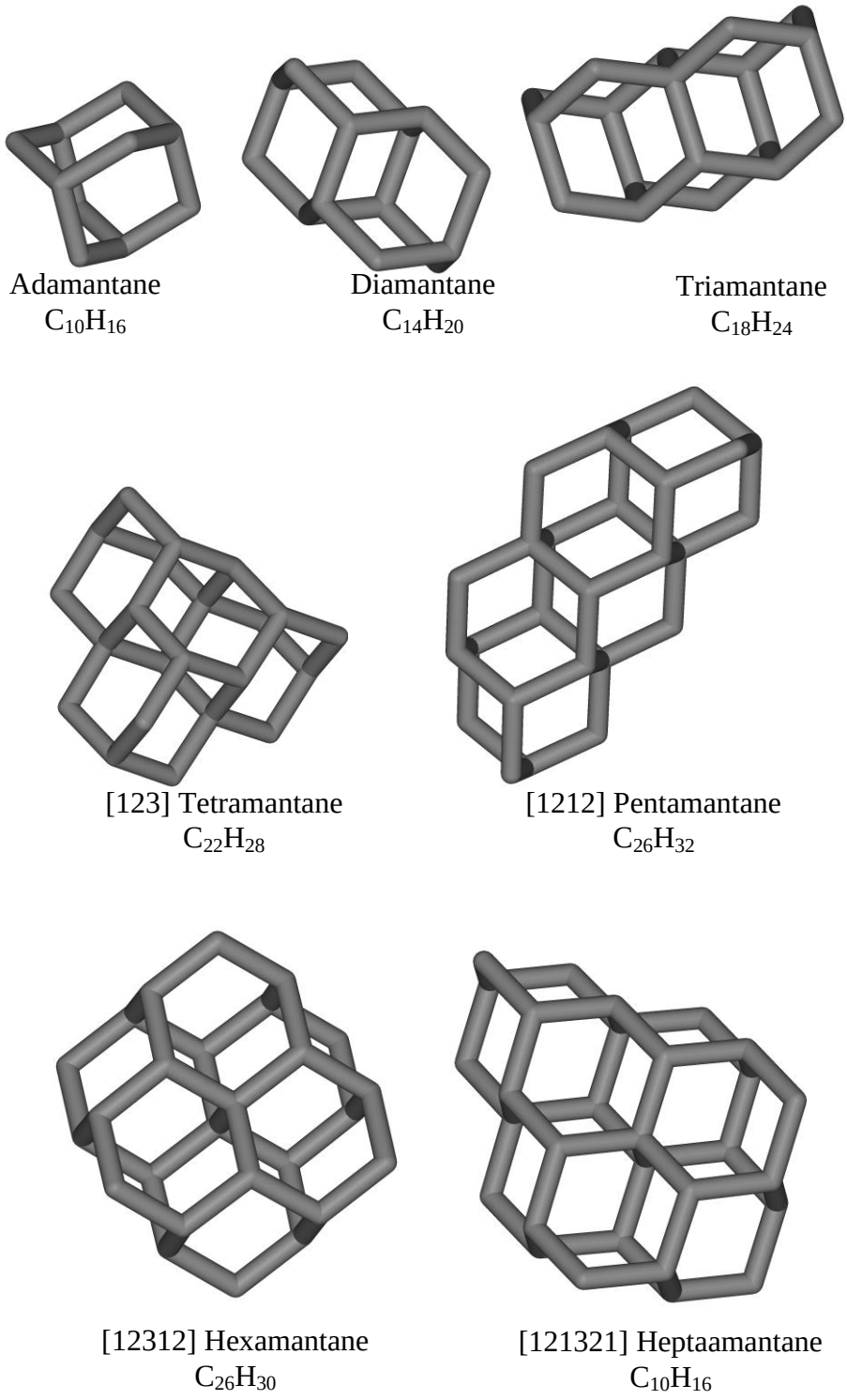

Figure 3.1: Diamondoid structures (hydrogen atoms have been omitted for clarity; all structures are fully saturated).

3.2.1.3 *Synthesis*

Diamondoids have been obtained via synthetic methods as well. Presently, the most efficient syntheses of all of the lower diamondoids, from adamantane to triamantane, involve the carbocation-mediated superacid equilibration reaction discovered by P. von R. Schleyer [19]. Schleyer's 1957 synthesis [20] transformed adamantane from an exotic species into one of the staples of organic chemistry [21]. However, when applying this method to the higher diamondoids, i.e., tetramantane and higher, it is limited by strict kinetic (mechanistic) constraints, and all attempts to synthesize the higher diamondoids have been proven ineffective to date [22]. Recently, there has been one case of tetramantanes prepared by complex yet low-yielding alternative synthetic pathways devised by McKervey's research group [22, 23].

3.2.1.4 *Significance*

Adamantane and its derivatives reveal remarkable rigidity, strength, and thermodynamic stability, as well as interesting electronic properties [15, 24, 25]. Hence, adamantane (and other diamondoids) have gained interest in research and engineering because of their numerous applications in chemistry [26, 27], polymer science[28, 29], pharmaceutical science [30-33], forensics [6, 7, 34, 35], geology [2, 8, 17, 36-39], and nanotechnology [40].

Compounds containing adamantyl radicals are useful catalysts for many chemical reactions, such as the refining of halogen atoms and preparation of heterogeneous bimetallic catalysts [26, 27]. The rigid, spherical structure of adamantane reduces inter chain interaction in polymers and assists the synthesis of polymers, such as MAE-PPV [28, 29].

Adamantane-containing molecules have also been found to have antiviral activity [30-33]. They have been used in the treatment of influenza[33], HIV-1[32], leukemia and deafness [31], and many other diseases [30].

Since adamantane and higher diamondoids are found in most petroleum products, they are utilized in so-called forensic environmental investigations. Fingerprinting adamantane and higher diamondoids provides a diagnostic pattern for correlation and differentiation of spilled oils [6, 7, 34, 35]. Additionally, because of variation in the thermal stability of methyl-substituted diamondoids, geologists have applied certain isomer ratios as parameters for the elucidation of the thermal maturity, migration history, source rock type, and the age of condensates from the wells worldwide [2, 36, 41, 42]. Additionally, from an astrophysical viewpoint there has been substantial interest of this class of molecules since nanometersized "diamond-like" molecules have been found in meteorites [24, 43, 44]. Recent interest in higher diamondoids has been renewed by molecular simulation studies, suggesting possible applications in nanotechnology [45-47] and use as seed crystals in CVD diamond production [48].

3.2.1.5 *Natural formation*

Despite their unique properties, application relevance, and natural occurrence, the formation process of diamondoid compounds within the geosphere remains largely unexplained [39, 41, 49]. Researchers have proposed that diamondoids may be created via carbocation-mediated rearrangements arising when newly generated petroleum reacts with superacid sites at naturally occurring clay minerals such as montmorillonite [2, 38, 39]. However, higher-order diamondoid homologues are considered to be formed from lower

homologues [2] in a polymerization-like process at extreme temperature and pressure conditions [3].

3.2.2 Vibrational spectroscopy and diamondoids

3.2.2.1 *Experimental research*

From a spectroscopic point of view, adamantane has been subject to numerous structural studies [50]. In 1959, Mair et al. presented transmission IR spectra comparing synthetic adamantane to natural adamantane isolated from petroleum; however, no explanation of absorption signatures or experimental procedures was provided [51]. Six years later, Snyder and Schachtschneider recorded infrared spectra of adamantane at -189 ºC and compared the position of experimental vibrational modes to theoretically calculated ones [52]. In the early 1970s, Broxton et al. recorded the first infrared spectra of adamantane and fifteen other representative series of 1-substituted adamantanes in the region of 4000 to 600 cm^{-1} [53]. In the same year, infrared and laser Raman spectra of adamantane-h_{16} and d_{16} in solution and plastic crystalline phases at room temperature were obtained [54]. In 1975, heat of vaporization and frequency shifts of the infrared-active internal modes of adamantane as a function of temperature change (225 to 298 K) were reported by Lee and Slusky [55]. In addition, Raman analysis of the vibrational spectra of crystalline adamantane both as a function of temperature and at room temperature as a function of hydrostatic pressure were reported [56].

In the next two decades, the first far-infrared absorption spectrum of adamantane [57] and a first mentioning of near-infrared spectroscopy used to record the overtone spectra of adamantane in various phases and temperatures occurred [58]. Further utilizing infrared

spectroscopy, Corn et al. have studied the phase transition considering CH stretching and bending vibrations of randomly H-substituted isotopically diluted $C_{10}D_{15}H$ at atmospheric pressure as a function of temperature (7 to 300 K) [59]. The pressure dependence of the CH stretching bands was determined at low temperature (7 K) and room temperature (298 K) [60]. In 1992, Rassat et al. showed surface effects and forbidden transitions in the reflection-infrared (RIR) spectrum of adamantane[61]. Because of the difference in local symmetry to which molecules at the surface and in the bulk of a crystal are subjected, the selection rules which differentiate between infrared (IR) and Raman spectroscopy were modified.

3.2.2.2 *Theoretical studies*

In addition to the experimental studies, a variety of theoretical methods have been applied to predict the vibrational spectra for diamondoid molecules. A vibrational assignment of adamantane and some of its isotopomers have been recorded and assigned using valence empirical force field shifts [50]. Szazs and Kovacs interpreted experimental vibrational spectra of adamantane compounds using the scaled quantum mechanical (SQM) method [62]. Molecular polarizability and changes in the polarizability associated with the stretch of CC and CH bonds have been calculated for adamantane as well [63]. The Raman and IR spectra of adamantane and a selection of its ionic and dehydrogenated radical species were computed using density functional theory (DFT)[21]. That same year, an infrared spectroscopic study on deposited diamondoid nanoparticles (5–350 nm in size) confirmed previous DFT computations of individual molecular diamondoid

structures [64]. The Raman spectrum of crystalline cyclohexamantane was interpreted with DFT calculations by Richardson et al.[65].

3.2.2.3 *Recent developments*

As a result of recent breakthroughs in the isolation of higher diamondoids from petroleum products [18], a new wave of experimental studies of diamondoids originated in order to better detect, identify, and characterize these species. A highly detailed Raman spectra assignment of the normal modes of vibration of both adamantane and deuterated adamantane has been published by Jenson [66]. Raman spectra of diamondoids with dimensions from adamantane to heptamantane have also recently been published [67]. More recently, Oomens et al. reported the first infrared spectra for individual higher diamondoid molecules with a direct comparison between theoretical and experimental data.[15]

As presented above, the literature coverage of diamondoids, and particularly adamantane, is extensive including a variety of experimental and theoretical studies on IR active vibrational mode assignments of diamondoids. **Table 3.1** presents general modes of diamondoids, which were reviewed by Oomens et al [15]. Additionally, **Table 3.2** highlights selected studies where vibrational modes of adamantane in particular were present.

Table 3.1: General vibrational signature assignments for diamondoids.

General assignment pertinent to all diamondoid molecules	
Spectral Ranges (cm^{-1})	General description
2900	CH stretch
1450	CH_2 scissor
1000–1400	CH_2 rock, wag, twist
< 1000	Skeletal deformation

Table 3.2: Fundamental mode assignments of adamantane.

Fundamental Modes of Adamantane							
Wavenumbers (cm^{-1})	Assignment	Wavenumbers (cm^{-1})	Assignment	Wavenumbers (cm^{-1})	Assignment	Wavenumbers (cm^{-1})	Assignment
Nicholas (1940) KBr disk		Broxton (1971) solution		Bristic (1995) solid		Jensen (2004) liquid	
2933	ν CH_2	2929 vs	asym CH_2 stretch	2940 s	ν_{20} CH_2 stretch	2950	CH stretch
2907	ν CH	2908 vs	CH stretch	2910	ν_{21} CH stretch	2944	CH stretch
2857	ν CH_2	2850	sym SH_2 stretch	2850 s	ν_{22} CH_2 stretch	2913	CH stretch
1453	CH_2 scissor	2670 w		2670 w	$\nu_{24} + \nu_{25}$	1450	CH_2 scissors
1357	CH_2 wag	2658 w	1354 + 1307	2660 w		1353	CH_2 wag
1155	CH deformation	2640 vw		2640 w	$\nu_{22} - \nu_{25} + \nu_{26}$	1312	CH wag
1101	skeletal	2568 vw		2560 w	$\nu_{23} + \nu_{26}$	1105	CH_2 rock
966	skeletal	1453 s	CH_2 scissor	1455 m	ν_{23} scissor	972	CC stretch
799	CH_2 rock	1354 m	CH deformation	1359 m	ν_{24} wag	800	CC stretch
		1307 vw	skeletal	1310 w	ν_{25} CH bend	638	CCC bend
		1099 m		1105 w	ν_{26} rock	444	CCC wag
		967 w		970 w	ν_{27} rock		
		795 vw (sh)		950 w	ν_{11} CC stretch		
		784 w	CH_2 rock	800 w	ν_{28} CC stretch		
		762 vw		718 vw			
				640 vw	ν_{28} CCC deformation		

*v - very, w –weak, m-medium, s- strong, sh-shoulder.

3.3 INTRODUCTION

In this chapter, IR-ATR spectroscopy has been applied for the quantification of adamantane in organic matrices including dichloromethane (DCM), hexane, carbon tetrachloride, and for the direct evaluation of adamantane in crude oil standard. In addition, the feasibility of this analytical technique for analyzing real-world crude oil samples was demonstrated. For commercial applications it is crucial that large quantities of diamondoids of different degrees of purity be available at a reasonable cost. Solubility data are essential in the design of separation processes to recover diamondoids from petroleum [68]; thus, the value of IR-ATR spectroscopy was further demonstrated with the determination of adamantane solubility limits in organic solvents and crude oil standards.

3.4 MATERIALS AND METHODS

3.4.1 Instrumentation

IR-ATR spectra were recorded from 4000 to 400 cm^{-1} using a Bruker Equinox 55 Fourier transform (FT-IR) spectrometer (Bruker Optics Inc., Billerica, MA). The spectrometer was equipped with a liquid nitrogen cooled mercury-cadmium-telluride (MCT) detector (Infrared Associates, Stuart, FL) and an in-compartment horizontal ATR unit (Gateway, Specac Inc., Woodstock, GA) with a trough top plate and 6-reflection trapezoidal ZnSe (n_D=2.43 at λ = 5 μm) ATR crystal (MacroOptica, Moscow, Russia).

3.4.2 Reagents

Adamantane samples were prepared by dissolving high-purity (99.0%) adamantane (Aldrich Chemical Company, Milwaukee, WI) in dichloromethane (DCM),

hexane, carbon tetrachloride (Certified ACS grade, Fisher Scientific, Fair Lawn, NJ), crude oil standard (ASTM D5307 Crude Oil Internal Standard; 25% by weight of Heptadecane, Hexadecane, Pentadecane, and Tetradecane, Aldrich Chemical Company, Milwaukee, WI), and in natural crude oil (ExxonMobil Research and Engineering Company, Annadale, N J) at room temperature followed by rapid mixing for 10 min. The mass of adamantane was determined using a GR-200 analytical mass balance (A&D Company, engineering Milpitas, CA). The volume of organic solvents and crude oil standards were measured using a 100-1000 μL Eppendorf pipet (calibrated pipette with error <0.3% RSD by volume, Eppendorf North America Inc., New York, NY).

3.4.3 Experimental procedures

Prior to IR-ATR analysis, each sample was prepared by adding a precisely measured quantity of adamantane to 2 mL of solvent. Each sample mixture was then rigorously stirred for ~10 min prior to deposition of a 1 mL aliquot of the sample onto the ZnSe crystal waveguide surface, which was then covered with a glass plate to minimize solvent evaporation and facilitate extended measurement times. Following sample deposition, five consecutive measurements were recorded at intervals of 90 s. Each sample preparation and measurement procedure was repeated in triplicate for each individual adamantane standard. All IR-ATR spectra represent the average of 100 sample scans at a spectral resolution of 1 cm^{-1} while the instrument was purged with dry air. A neat ZnSe crystal surface was used to acquire a reference spectrum for each measurement.

3.4.4 Spectral data analysis

Using the software package OPUS (Bruker Optics Inc., Billerica, MA), infrared absorption features of adamantane were evaluated by peak area analysis. Figure 2 highlights the spectral regions utilized for data analysis in representative IR-ATR spectra of adamantane dissolved in various solvents. Peak areas from each spectral region collected during replicated measurements were averaged and used for further calculations. Consequently, from here on, the three averaged peak areas for a given spectral region and respective sample mixture is indicated as Avg. PA.

To establish quantitative calibration functions for each combination of adamantane and solvent, a first order linear fit was applied. To test the applicability of the established calibrations for unknown samples, a set of blind samples was prepared and analyzed for each matrix (blind samples were prepared following the same procedures as the calibration samples). The limit of detection (LOD) and limit of quantification (LOQ) of adamantane in each organic solvent and crude oil standard were extracted from the calibration plot (LOD definition: 3σ concentration determination from the regression fit using the criterion of three times the noise of a blank sample. LOQ: 6σ concentration determination from the regression fit using the criterion of six times the noise of a blank sample). The solubility limit of adamantane in organic solvents and in crude oil standards was calculated by determining the point of intersect between the first order calibration line and a second first order regression line fit through measurement points collected above saturation concentrations.

3.5 RESULTS AND DISCUSSION

3.5.1 IR spectra of adamantane in organic solvents

The present chapter is focused on developing a novel method for directly quantifying dissolved adamantane in several organic matrices via IR-ATR spectroscopy, and then applying this strategy to determine adamantane concentrations in a multi-component crude oil reference standard. The first IR spectrum of adamantane was reported by Mair et al. [51]; since then, a variety of publications have reproduced and expanded upon the initial findings, i.e., that adamantane exhibits characteristic vibrational absorption features resulting from CH stretches near 2900 cm^{-1}, CH_2 scissoring at ~1450 cm^{-1}, CH_2 rocks, wags, and twists in the range 1400–1000 cm^{-1}, and skeletal deformations below 1000 cm^{-1} [66] (**Table 3.1, Figure 3.2**).

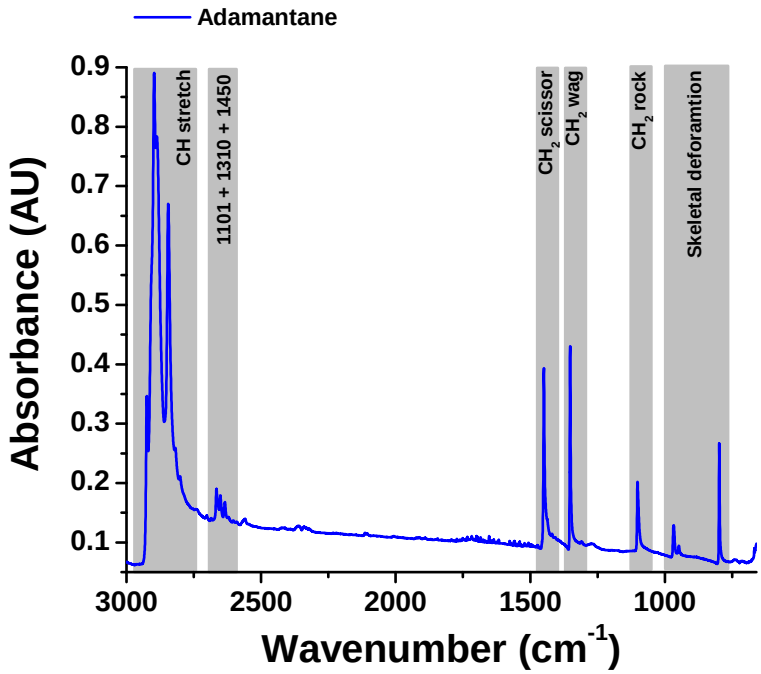

Figure 3.2: IR-ATR spectra of adamantane with major vibrational modes assigned.

The absorption feature predominantly utilized for adamantane quantification in this study is centered at ~1099 cm^{-1}, which corresponds to the CH rocking (ν_{16}) or CH_2 wagging (ν_{26}) feature (**Figure 3.2**) [66]. Visual inspection of the spectra provided in **Figure 3.3** illustrate that there are no significant spectral interferences from solvents, which renders the peak at 1099 cm^{-1} suitable for quantification studies of adamantane in the respective organic solvents with potential application using other similar solvents.

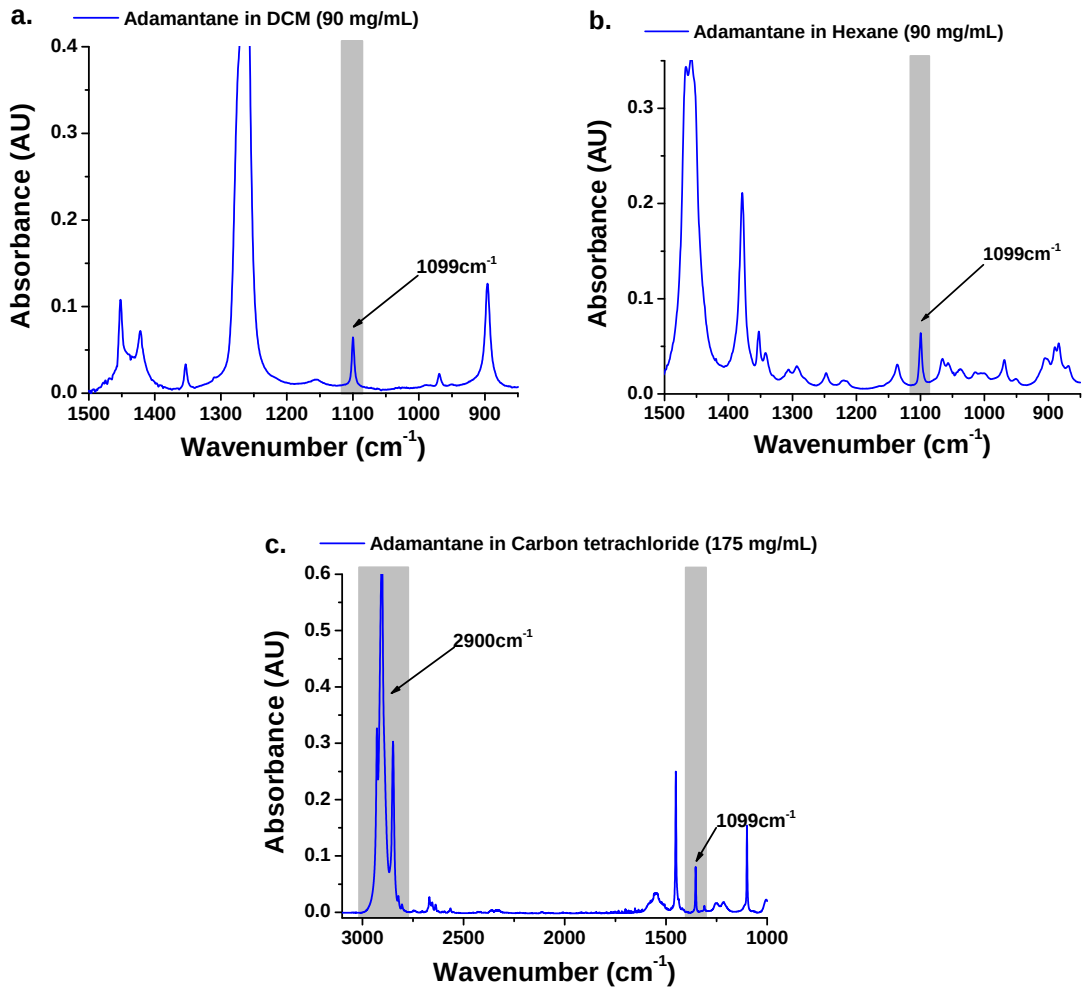

Figure 3.3: IR-ATR spectral region of adamantane in (a.) DCM, (b.) hexane, and (c.) carbon tetrachloride.

It was determined from spectral analysis that the precise peak position of the adamantane CH rocking (ν_{16}) or CH_2 wagging (ν_{26}) feature in dichloromethane, hexane, and carbon tetrachloride was 1099.8 ± 0.1 cm^{-1}. For quantitative analysis of adamantane in carbon tetrachloride, CH stretch features (2954.5–2828.5 cm^{-1}) were also analyzed, as carbon tetrachloride has no background absorptions in that spectral region.

3.5.2 Quantitative evaluation of adamantane

Figure 3.4 displays the increase of IR absorption intensities for both the 1099 cm^{-1} feature of adamantane in DCM and for CH stretches of adamantane in carbon tetrachloride in response to increasing concentrations of adamantane in the respective solvent.

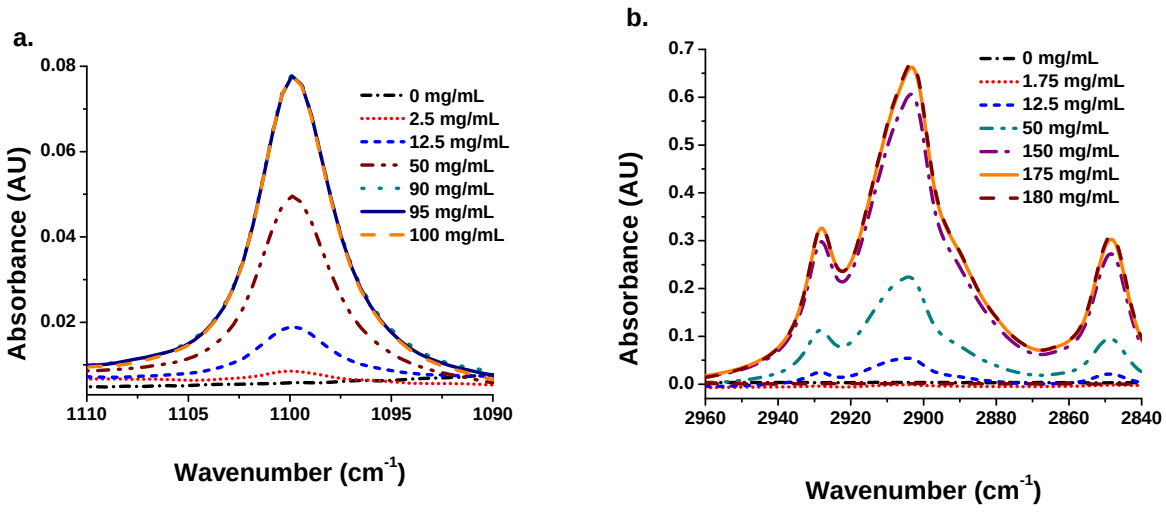

Figure 3.4: A series of IR-ATR spectra focused on the adamantane absorption feature used for quantitative evaluation of adamantane in (a.) DCM and (b.) carbon tetrachloride.

As a result of the limited solubility of adamantane in these organic solvents, spectral absorption intensities level off once the solubility limit of adamantane has been reached. IR-ATR data revealed only a slight variance in absorption intensity upon saturation, which is attributed to light scattering from settling of undissolved particulates on the waveguide surface. Hence, the solubility limit of adamantane in these solvents can be determined from evaluating these spectral signatures, as indicated in **Figure 3.5**. The peak area of each characteristic absorption feature was integrated (Avg. PA) for establishing a first order linear calibration function to correlate absorbance vs. concentration of adamantane in solution from the lowest detectable concentration up to the solubility limit (**Figure 3.5**).

Table 3.3 summarizes the linear fit parameters for adamantane in DCM, hexane, and carbon tetrachloride, and confirms that a suitable first order linear correlation function is obtained for the quantification of adamantane in these solvents. The linear fit equation follows: $y = m*x + b$ with a goodness of the fit (R^2) equaling 0.996, 0.999, and 0.998 for adamantane in DCM, hexane, carbon tetrachloride, respectively. Furthermore, a first order linear fit was also established for quantifying adamantane using the CH stretch in carbon tetrachloride with $R^2 = 0.999$. LOD and LOQ of adamantane in all studied solvents and for the given instrument configuration were calculated: dichloromethane, 0.16 mg/mL (121 ppm), 0.62 mg/mL (468 ppm); hexane, 0.25 mg/mL (379 ppm), 0.97 mg/mL (1472 ppm); and carbon tetrachloride, 0.4 mg/mL (251 ppm), 0.8 mg/mL (502 ppm), respectively, as summarized in **Table 3.4**.

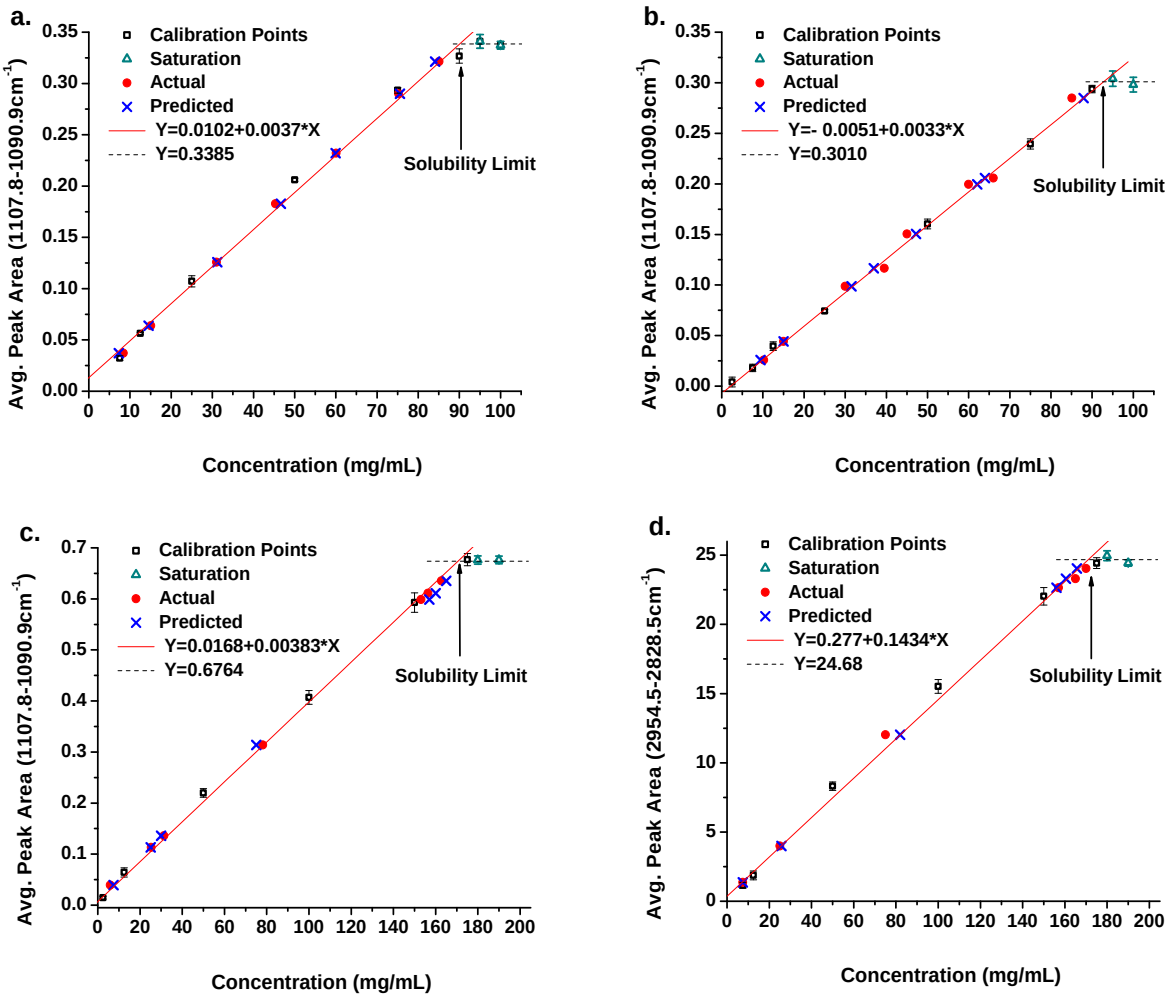

Figure 3.5: First order linear calibration plot with blind sample concentrations (actual), predicted concentrations, and the solubility limit of adamantane in (a.) DCM, (b.) hexane, (c.) carbon tetrachloride, and (d.) CH stretch region in carbon tetrachloride. (The error bars displayed are twice the standard deviation.)

Table 3.3: Calibration points used for constructing first order linear calibration plot.

DCM		**Hexane**		**Carbon tetrachloride (CH stretch)**			**Crude oil standard**	
Conc. (mg/mL)	Avg. PA (1107.8-1090.9 cm^{-1})	Conc. (mg/mL)	Avg. PA (1107.8-1090.9 cm^{-1})	Conc. (mg/mL)	Avg. PA (1107.8-1090.9 cm^{-1})	Avg. PA (2954.5-2828.5 cm^{-1})	Conc. (mg/mL)	Avg. PA (1107.8-1090.9 cm^{-1})
2.50	0.014	2.50	0.004	2.73	0.014	0.260	2.47	-0.013
7.62	0.032	7.62	0.018	12.65	0.064	1.866	7.22	0.006
12.52	0.056	12.60	0.039	50.13	0.219	8.310	12.6	0.027
25.28	0.107	25.23	0.074	100.13	0.406	15.519	25	0.081
50.22	0.201	50.08	0.160	150.03	0.592	22.032	49.6	0.182
75.17	0.293	75.12	0.239	175.18	0.676	24.430	67.9	0.255
90.42	0.327	90.13	0.293					

Table 3.4: Limits of detection (LOD) and limits of quantification (LOQ) for adamantane in organic solvents and crude oil standard.

	DCM		**Hexane**		**Carbon tetrachloride (CH stretch)**				**Crude oil standard**	
	LOD	LOQ	LOD	LOQ	LOD	LOQ	LOD	LOQ	LOD	LOQ
Mass (mg/mL)	0.16	0.62	0.25	0.97	0.50	1.49	0.4	0.8	0.12	0.78
PPM	121	468	379	1472	314	935	251	502	154	1018
% by mass	0.01	0.05	0.04	0.15	0.03	0.09	0.03	0.05	0.02	0.1

To test the applicability of the established calibrations for unknown samples, a set of blind samples was prepared and analyzed for each matrix. **Figure 3.5** displays the actual concentration of the blind samples vs. the predicted concentrations using the established calibration function. The average absolute mass error for these solutions amounted to 1.66 mg/mL (with a lowest error of 0 mg/mL and a highest error of 6.9 mg/mL), thereby yielding an average relative error of 4% (range: 0–13.3%), and an average absolute mass error of 0.18% (range: 0–0.46 %). The absolute mass error for predicting adamantane concentrations was calculated by subtracting the predicted from the actual concentration; the relative error was calculated by dividing the absolute mass error by the actual concentration multiplied by one hundred. Finally, the absolute mass error was determined by dividing the absolute mass error by the density of the solvent and multiplying by one hundred. Detailed performance data for these experiments is summarized in **Table 3.5**. In addition, the solubility limit of adamantane in these solvents was derived by determining the point of intersect between the first order calibration function and the line through the saturation concentrations, as shown in **Figure 3.5.** The resulting solubility limit for adamantane in dichloromethane is 88.7 mg/mL (6.7% by weight); in hexane, 89.7 mg/mL (13.6%); and in carbon tetrachloride, 172.2 mg/mL (10.8%).

Table 3.5: Comparison between blind samples (actual concentrations) and predicted concentrations of adamantane.

Actual conc. (mg/mL)	Predicted conc. (mg/mL)	Absolute mass error (mg/mL)	Relative error %	Absolute mass error %
DCM				
8.4	7.3	1.1	13.3	0.08
15.05	14.5	0.5	3.8	0.04
31	31.2	0.2	0.7	0.02
45.35	46.7	1.3	2.8	0.10
60.1	60.0	0.1	0.2	0.01
75.25	75.6	0.3	0.5	0.03
85.1	84.1	1.0	1.2	0.07
Hexane				
10.2	9.4	0.8	7.7	0.12
15.1	15.0	0.1	0.5	0.01
30.4	31.6	1.2	3.8	0.18
39.5	36.9	2.6	6.5	0.39
45.35	47.2	1.8	4.1	0.28
60.1	62.1	2.0	3.3	0.3
66	64.0	2.0	3.1	0.31
85.1	87.9	2.8	3.3	0.43
Carbon tetrachloride				
5.9	7.5	1.6	20.8	0.10
25.3	25.15	0.2	0.7	0.01
31.3	30.2	1.1	3.7	0.07
78.1	75.1	3.0	4.0	0.19
153.1	157.5	4.4	2.8	0.28
156.4	160	3.6	2.3	0.23
162.7	165	2.3	1.4	0.14
(CH stretch) Carbon tetrachloride				
7.5	7.5	0.0	0.6	0
25.8	25.3	0.5	2.2	0.03
82.0	75.1	6.9	9.1	0.43
156.0	157.5	1.5	0.9	0.09
160.5	165	4.5	2.7	0.28
165.7	170.4	4.7	2.8	0.29
Crude oil standard				
5.75	5.19	0.56	9.8	0.07
8.05	8.35	0.30	3.7	0.04
13.85	14.00	0.15	1.1	0.02
16.5	17.06	0.56	3.4	0.07
24.0	23.99	0.01	0.0	0.00
60.03	57.23	2.8	4.7	0.36

3.5.3 Evaluation of adamantane in crude oil matrices

Adamantane concentrations in petroleum products occur over an extremely wide range, from parts per billion (ppb) (1 ppb = 1 μg/kg) to thousands of parts per million (ppm) (1 ppm = 1 mg/kg); however, lower concentrations are more typical [2, 5]. Generally high concentrations of diamondoids are common where there has been evidence of thermal cracking in crude oil [36, 69]. Sassen et al. [36] recently reported on a series of condensate samples from the Kimmeridgian and Albian reservoirs containing a high relative abundance of diamondoid compounds at 4742 ppm (adamantane, 4038 ppm) and 4774 ppm (adamantane, 4266 ppm), respectively. Experimental characterization of diamondoid properties in geologic systems and their geographic distribution can help better elucidate the thermal maturity, migration history, source rock type, and age of condensates from the wells worldwide [36]. Overall, diamondoid properties may be useful criteria for characterization of highly mature condensates at a global level in absence of typical diagnostic information from common biomarkers [36].

To this end, in the final set of experiments mixtures of crude oil standard and adamantane were prepared and analyzed in a manner similar to the aforementioned experiments for assessing the real-world applicability of the developed IR sensing strategies. The absorbance peak at 1099.5 cm^{-1} was used for the quantification of adamantane in crude oil standards, as indicated in **Figure 3.6**. A first order linear correlation function was obtained for the quantification of adamantane in crude oil with R^2 = 0.999 (**Figure 3.6**; refer to **Table 3.3** for the parameters of the linear fit). The applicability of the established calibration was again tested with a set of blind samples.

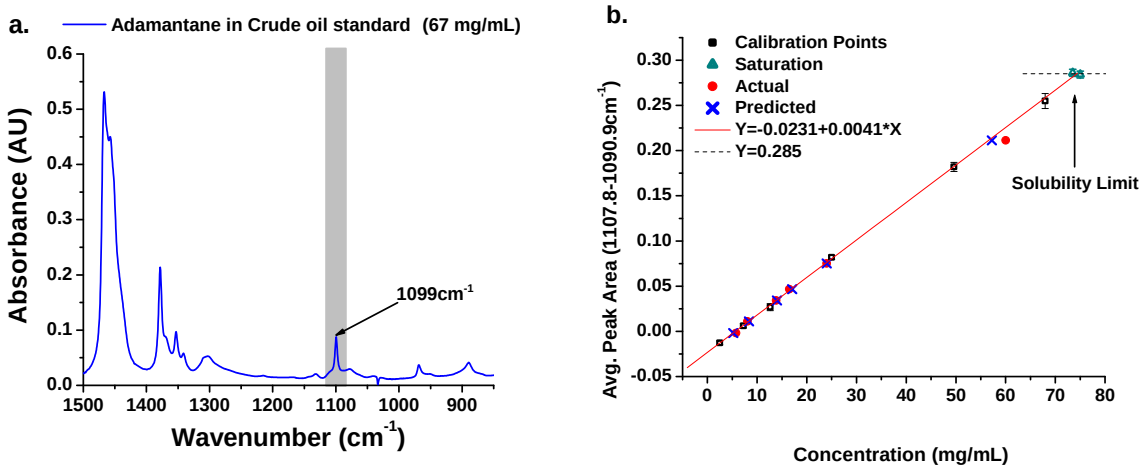

Figure 3.6: (a.) IR-ATR spectral region of adamantane in crude oil standards. (b.) First order linear calibration plot with blind sample concentrations (actual), predicted concentrations, and the solubility limit of adamantane in crude oil. (The error bars displayed are twice the standard deviation.)

Figure 3.6 shows the actual concentration of the blind samples vs. the predicted concentrations using the established calibration function. For the analysis of adamantane in crude oil standards, the average absolute mass error was determined at 0.73 mg/mL with an average relative error of 3.8% and an absolute mass error of 0.09% **(Table 3.3)**. Notably, the difference between the actual concentrations and the predicted concentrations appears to increase, as adamantane approaches the solubility limit. This observation is attributed to an increase in optical losses by scattering resulting from the deposition of undissolved particulates at the waveguide surface at higher concentrations. The solubility limit for adamantane in crude oil was determined at 74.7 mg/mL (9.6% by weight); the LOD of adamantane in crude oil standard was calculated at 0.12 mg/mL (154 ppm) and the LOQ at 0.78 mg/mL (1018 ppm).

Finally, the applicability of the developed quantification method for analyzing real-world crude oil samples was demonstrated in a series of IR-ATR measurements for natural crude oil samples containing adamantane **(Figure 3.7)**. **Figure 3.7a** demonstrates that the peak located at 1099 cm^{-1} enables us to detect adamantane unambiguously in crude oil samples. **Figure 3.7b** illustrates that the absorption intensity of the adamantane feature at 1099 cm^{-1} increases with the concentration of adamantane in crude oil, thereby verifying the ability to quantify adamantane in real-world samples.

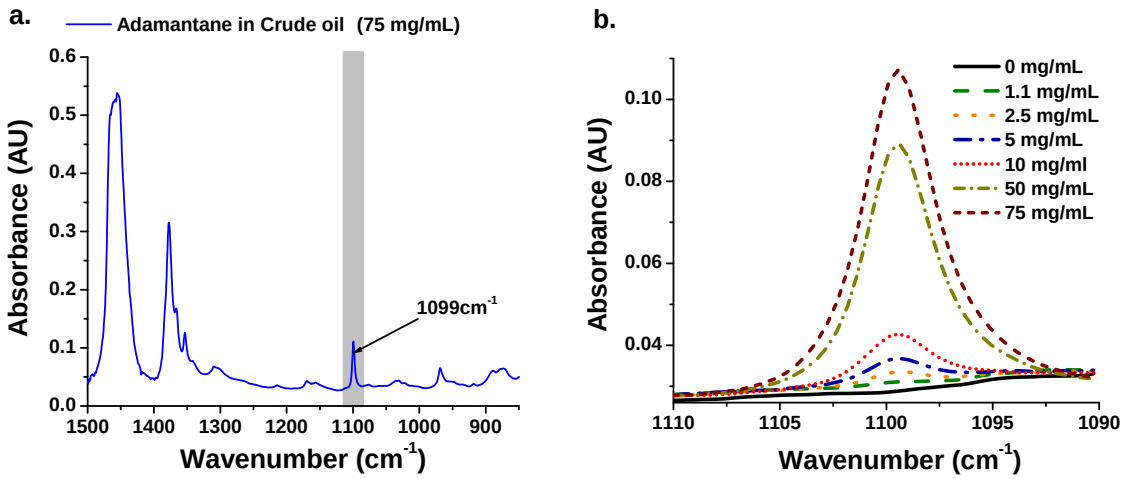

Figure 3.7: (a.) IR-ATR spectrum of adamantane in natural crude oil. (b.) Series of IR-ATR spectra highlighting the increase of the adamantane absorption feature in crude oil with increasing concentration.

3.6 CONCLUSIONS

This chapter has focused on the quantification of adamantane in organic solvents including DCM, hexane, and carbon tetrachloride using IR-ATR spectroscopy; furthermore, this method was applied to the quantification of adamantane in crude oil standard. In addition, the feasibility of applying this analytical technique to real-world crude oil samples was demonstrated. Currently established LOQ and LOD values for adamandane in crude oil standards using IR-ATR spectroscopy are somewhat higher than those obtained by well-established analytical methods such as gas chromatography combined with mass spectrometry (GC-MS) [6-8].

However, unlike GC-MS, IR-ATR spectroscopy provides a sensitive and flexible instrumental scheme for environmental and industrial molecular monitoring particularly useful for application in liquid phase environments [10]. Quantitative results may be obtained via IR-ATR spectroscopy within several seconds to minutes without any sample preparation, thus rendering this technique particularly suitable for in-situ or rapid on-ship analysis. While IR-ATR methods developed to date may have only been appropriate for high-maturity crude oil fluids as a complimentary supplement to GC-MS at higher concentrations, further advancements in tunable laser technology (e.g., quantum cascade lasers) and thin-film IR waveguides promise an improvement of detection limits by more than one order of magnitude [6-8].

In summary, IR sensing technologies promise in-situ quantification capabilities for adamantane and higher diamondoids in crude oils readily amenable to real-world scenarios, provided there is little or no spectral interference from the sample matrix. Thus far, these initial efforts provide a promising outlook for low-level detection and

monitoring of diamondoid constituents in naturally occurring crudes and petroleum samples. As high concentrations of diamondoid compounds may segregate from reservoir fluids, and therefore may adversely affect transport processes, it is essential to identify and monitor relevant concentration changes, and to quantitatively determine critical concentrations of adamantane in petroleum products. The present study demonstrates that IR evanescent field sensing techniques may facilitate rapid in-situ analysis amenable to field deployment even in extreme environments.

3.7 OUTLOOK

3.7.1 Improving detection and quantification limits

In order to enhance sensitivity and lower detection capabilities of IR-ATR technique toward diamondoids in organic media/crude oil, application of diffusion-based extraction membranes may be utilized [11, 70, 71]. The waveguide-sensing platform, here a ZnSe crystal, could be coated with a polymer-like film, which would enrich/capture diamondoids from organic media/crude oil in the evanescent wave region of the crystal. The application of polymer-like films has been shown in literature [72] and in the present thesis (see Chapters 6 & 7) to decrease the detection limits by at least one order of magnitude.

Polymer or polymer-like films are commonly deposited onto the waveguide surface for enhancing the detectivity for small compounds [11, 70, 71]. However, diamondoid compounds are quite bulky and relatively large molecules, thus the selection of the enrichment layer can be challenging. However, Molecular Diamond Technologies (a subsidary of Chevron, USA) has reported the extraction of diamondoids by reverse phase

HPLC, and thus, it is a reasonable proposition that using similar "extraction materials" [73] for coating IR waveguides may improve the sensitivity of the IR-ATR method.

However, a drawback of this strategy is that any membrane material has to exhibit high thermal, chemical, and physical stability, while providing high analyte affinity with rapid, reversible diffusion characteristics for serving as part of an in-situ sensor in extreme environments. Additionally, with the application of a polymer-like layer, the response time of the measurement is increase compared to bare waveguides. Hence, thorough investigations on potential enrichment materials are required for optimization of the sensing behavior.

3.7.2 Spectroscopic studies on diamondoids in real world samples

For future experiments it would be very interesting to conduct IR characterization and quantification studies for higher order diamondoids and their derivatives. Additionally, IR-ATR analysis of real world crude oils containing diamondoids would be of importance to prove that this technique may be used as in-situ sensor in extreme environments.

Sassen has recently published a contribution examining isotopic ratios of diamondoids in natural samples[36], and has also provided one of these samples for IR-ATR analysis in the course of this thesis. According to Sassen, the sample contains approximately 97% adamantane, 3% diamantane, and small percentages (<0.5%) of their derivatives (ethyl, methyl). (Note: these characteristics were provided after IR-ATR experiments were completed and peaks were assigned.) This natural diamondoids sample originate from hot gas field in the East Texas Basin, with each single crystal having dimensions of ~2–3 mm across (**Figure 3.8**).

The IR-ATR spectra were recorded using the experimental procedure described in **Section 3.4.** The goal of this experiment was to demonstrate that the IR-ATR technique may be utilized for studying natural samples containing mixtures of diamondoids. **Figure 3.9** presents IR spectra comparing a commercially purchased adamantane sample to the natural sample. Analyzing **Figure 3.9** it is evident that majority of the sample is adamantane; however, minor peaks of diamantane can be detected at 1466 cm^{-1} (CH_2 scissor), 1377 cm^{-1}, 1284 cm^{-1}, 1044 cm^{-1}, 1049 cm^{-1} (CH_2 rock/wag/twist), 982 cm^{-1}, and 882 cm^{-1} (skeletal deformations) [15, 44]; possibly, also their methyl and ethyl derivatives are detected at 2955 cm^{-1} (CH stretch) [15, 53], which was confirmed by GC-MS measurements conducted by Sassen.

To the best of our knowledge, these experiments present the first application of IR-ATR analysis to real word diamondoid samples. Here, the IR-ATR technique was clearly capable of differentiating between adamantane and diamantane absorption profiles (**Figure 3.9**). The next step would be to apply IR-ATR for analysis of natural samples consisting of variety of diamondoids and their derivatives.

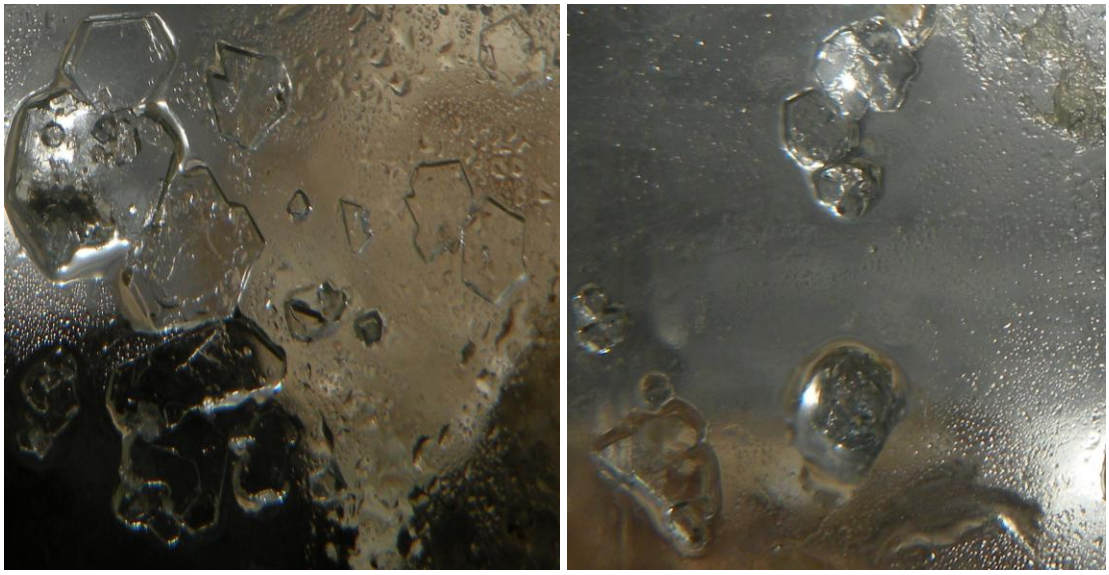

Figure 3.8: Optical microscopy images of the natural diamondoid sample (each single crystal is approx. 2-3 mm in diameter).

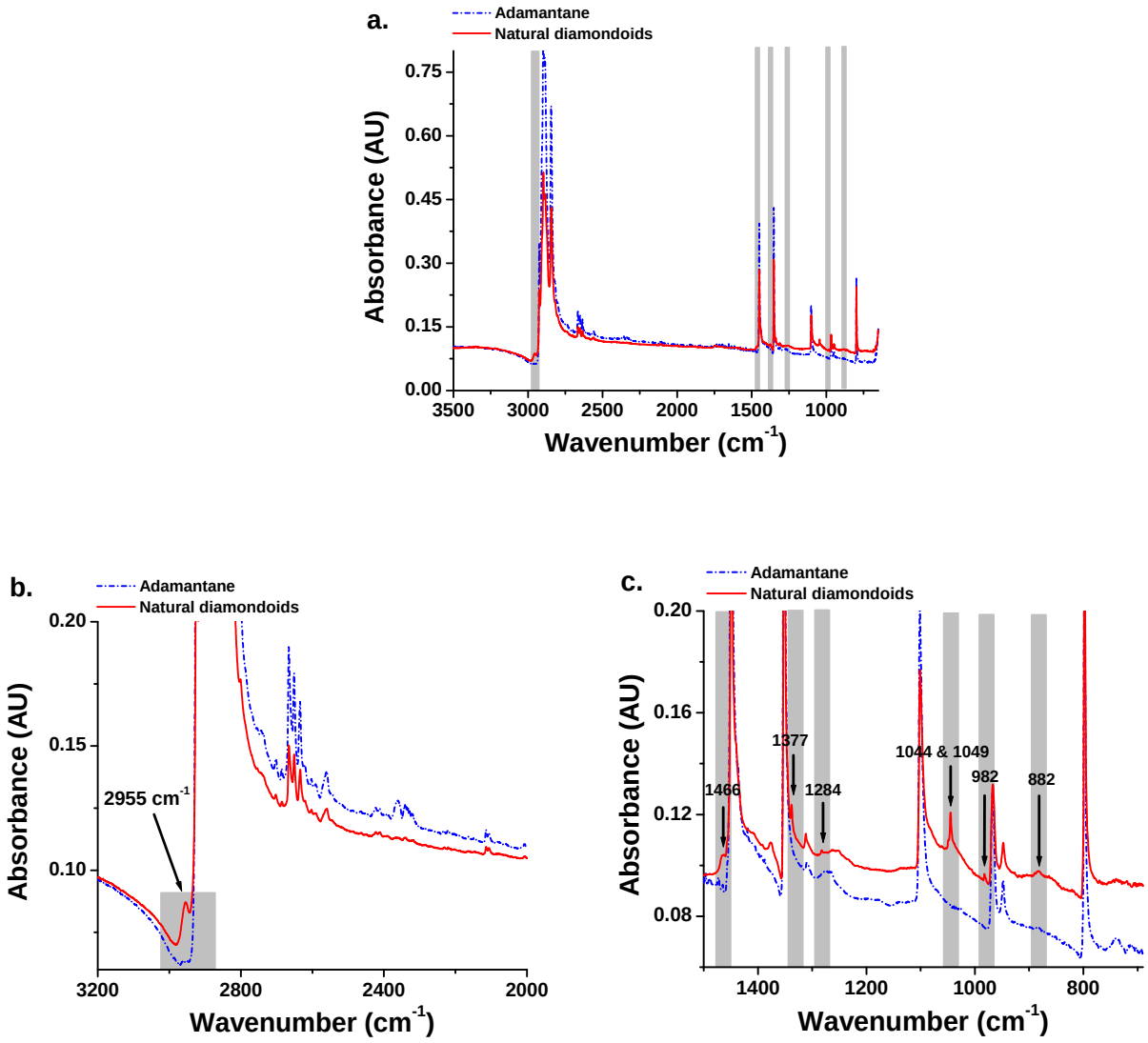

Figure 3.9: IR spectra of adamantane and natural diamondoids – highlighted gray areas represent regions where spectral differences are seen, (a.) full spectra, (b.) enlarged region (3200-2000 cm^{-1}), (c.) enlarged region (1500-700 cm^{-1}).

3.8 REFERENCES:

(1) Mansoori, G. A. "Modeling of asphaltene and other heavy organic depositions", *Journal of Petroleum Science and Engineering* **1997**, *17*, 101-111.

(2) Dahl, J. E.; Moldowan, J. M.; Peters, K. E.; Claypool, G. E.; Rooney, M. A.; Michael, G. E.; Mello, M. R.; Kohnen, M. L. "Diamondoid hydrocarbons as indicators of natural oil cracking", *Nature* **1999**, *399*, 54-57.

(3) Grice, K.; Alexander, R.; Kagi, R. I. "Diamondoid hydrocarbon ratios as indicators of biodegradation in Australian crude oils", *Organic Geochemistry* **2000**, *31*, 67-73.

(4) Vazquez, D.; Mansoori, G. A. "Identification and measurement of petroleum precipitates", *Journal of Petroleum Science and Engineering* **2000**, *26*, 49-55.

(5) Yang, C.; Wang, Z. D.; Hollebone, B. P.; Peng, X.; Fingas, M.; Landriault, M. "GC/MS quantitation of diamondoid compounds in crude oils and petroleum products", *Environmental Forensics* **2006**, *7*, 377-390.

(6) Stout, S. A.; Douglas, G. S. "Diamondoid hydrocarbons - Application in the chemical fingerprinting of natural gas condensate and gasoline", *Environmental Forensics* **2004**, *5*, 225-235.

(7) Wang, Z. D.; Yang, C.; Hollebone, B.; Fingas, M. "Forensic fingerprinting of diamondoids for correlation and differentiation of spilled oil and petroleum products", *Environ. Sci. Technol.* **2006**, *40*, 5636-5646.

(8) Wei, Z.; Moldowan, J. M.; Zhang, S. C.; Hill, R.; Jarvie, D. M.; Wang, H. T.; Song, F. Q.; Fago, F. "Diamondoid hydrocarbons as a molecular proxy for thermal maturity and oil cracking: Geochemical models from hydrous pyrolysis", *Org. Geochem.* **2007**, *38*, 227-249.

(9) Mizaikoff, B.; Karlowatz, M.; Kraft, M. "Mid-infrared sensors for marine monitoring", *Proc. SPIE* **2001**, *4204*, 263-273.

(10) Mizaikoff, B. "Infrared optical sensors for water quality monitoring", *Water Sci. Technol.* **2003**, *47*, 35-42.

(11) Karlowatz, M.; Kraft, M.; Mizaikoff, B. "Simultaneous quantitative determination of benzene, toluene, and xylenes in water using mid-infrared evanescent field spectroscopy", *Anal. Chem.* **2004**, *76*, 2643-2648.

(12) Goebel, R.; Seitz, R. W.; Tomellini, S. A.; Krska, R.; Kellner, R. "Infrared attenuated total reflection spectroscopic investigations of the diffusion behavior of chlorinated hydrocarbons into polymer membranes", *Vib. Spectrosc.* **1995**, *8*, 141-149.

(13) Kraft, M.; Mizaikoff, B. "A mid-infrared sensor for monitoring of chlorinated hydrocarbons in the marine environment", *International Journal of Environmental Analytical Chemistry* **2000**, *78*, 367-383.

(14) Mizaikoff, B. "Mid-IR fiber-optic sensors", *Anal. Chem.* **2003**, *75*, 258A-267A.

(15) Oomens, J.; Polfer, N.; Pirali, O.; Ueno, Y.; Maboudian, R.; May, P. W.; Filik, J.; Dahl, J. E.; Liu, S. G.; Carlson, R. M. K. "Infrared spectroscopic investigation of higher diamondoids", *Journal of Molecular Spectroscopy* **2006**, *238*, 158-167.

(16) Petrov, A. A., Ed. *Petroleum Hydrocarbons*; Springer-Verlag: Berlin, Germany, 1987.

(17) Lin, R.; Wilk, Z. A. "Natural occurrence of tetramantane ($C_{22}H_{28}$) pentamantane ($C_{26}H_{32}$) and hexamantane ($C_{30}H_{36}$) in a deep petroleum reservoir", *Fuel* **1995**, *74*, 1512-1521.

(18) Dahl, J. E.; Liu, S. G.; Carlson, R. M. K. "Isolation and structure of higher diamondoids, nanometer-sized diamond molecules", *Science* **2003**, *299*, 96-99.

(19) Schleyer, P. v. R., Ed. *Cage Hydrocarbons*; Wiley: New York, 1990.

(20) Schleyer, P. V. "A simple preparation of adamantane", *J. Am. Chem. Soc.* **1957**, *79*, 3292-3292.

(21) Yan, G.; Brinkmann, N. R.; Schaefer, H. F. "Energetics and structures of adamantane and the 1-and 2-adamantyl radicals, cations, and anions", *Journal of Physical Chemistry A* **2003**, *107*, 9479-9485.

(22) McKervey, M. A. "Synthetic approaches to large diamondoid hydrocarbons", *Tetrahedron* **1980**, *36*, 971-992.

(23) Dahl, J. E. P.; Moldowan, J. M.; Peakman, T. M.; Clardy, J. C.; Lobkovsky, E.; Olmstead, M. M.; May, P. W.; Davis, T. J.; Steeds, J. W.; Peters, K. E.; Pepper, A.; Ekuan, A.; Carlson, R. M. K. "Isolation and structural proof of the large diamond molecule, cyclohexamantane (C26H30)", *Angew. Chem.-Int. Edit.* **2003**, *42*, 2040-2044.

(24) Anders, E.; Zinner, E. "Interstellar grains in primitive meteorites - diamond, silicon-carbide, and graphite", *Meteoritics* **1993**, *28*, 490-514.

(25) Korolkov, D. V.; Sizova, O. V. "Electronic structure of adamantane", *International Journal of Quantum Chemistry* **2002**, *88*, 606-613.

(26) Beller, M.; Seayad, J.; Tillack, A.; Jiao, H. "Catalytic Markovnikov and anti-Markovnikov functionalization of alkenes and alkynes: Recent developments and trends", *Angew. Chem.-Int. Edit.* **2004**, *43*, 3368-3398.

(27) Taoufik, M.; Santini, C. C.; Basset, J. M. "New optically active organogermane compounds containing the adamantyl radical for heterogeneous bimetallic catalysis. Part II", *Journal of Organometallic Chemistry* **1999**, *580*, 128-136.

(28) Jeong, H. Y.; Lee, Y. K.; Talaie, A.; Kim, K. M.; Kwon, Y. D.; Jang, Y. R.; Yoo, K. H.; Choo, D. J.; Jang, J. "Synthesis and characterization of the first adamantane-based poly(p-phenylenevinylene) derivative: an intelligent plastic for smart electronic displays", *Thin Solid Films* **2002**, *417*, 171-174.

(29) Jensen, J. J.; Grimsley, M.; Mathias, L. J. "Adamantyl-substituted phenolic polymers", *Journal of Polymer Science Part a-Polymer Chemistry* **1996**, *34*, 397-402.

(30) Spasov, A. A.; Khamidova, T. V.; Bugaeva, L. I.; Morozov, I. S.; J., P. C. *Pharm. Chem. J. (translation of Khim.-Farm. Zh.)* **2000**, *34*.
(31) Ruppersberg, J. P.; Fakler, B. P. *PCT Int. Appl* **2002**, *31*.
(32) Boukrinskaia, A. G.; Serbin, A. V.; Bogdan, O. P.; Stotskaya, L. L.; Alymova, I. V.; Klimochkin, Y. N. *PCT Int. Appl* **1995**, *32*.
(33) Stotskaya, L. L.; K. Munshi; K. N. Kozeletskaya; A. A. Sominina; O. I. Kiselev; K. V. Zaitseva; Y. V. Natochin; Serbin, A. V. *Khim-Farm. Zh* **1995**, *29*.
(34) Wang, Z. D.; Stout, S. A.; Fingas, M. "Forensic fingerprinting of biomarkers for oil spill characterization and source identification", *Environmental Forensics* **2006**, *7*, 105-146.
(35) Alimi, H.; Ertel, T.; Schug, B. "Fingerprinting of hydrocarbon fuel contaminants: Literature review", *Environmental Forensics* **2003**, *4*, 25-38.
(36) Sassen, R.; Post, P. "Enrichment of diamondoids and C-13 in condensate from Hudson canyon, US Atlantic", *Org. Geochem.* **2008**, *39*, 147-151.
(37) Sassen, R. "Geochemical and carbon isotopic studies of crude-oil destruction, bitumen precipitation, and sulfate reduction in the deep Smackover formation", *Org. Geochem.* **1988**, *12*, 351-&.
(38) Wei, Z.; Moldowan, J. M.; Jarvie, D. M.; Hill, R. "The fate of diamondoids in coals and sedimentary rocks", *Geology* **2006**, *34*, 1013-1016.
(39) Wei, Z.; Moldowan, J. M.; Fago, F.; Dahl, J. E.; Cai, C.; Peters, K. E. "Origins of thiadiamondoids and diamondoidthiols in petroleum", *Energy & Fuels* **2007**, *21*, 3431-3436.
(40) Ramezani, H.; Mansoori, G. A. In *Molecular Building Blocks for Nanotechnology: From Diamondoids to Nanoscale Materials and Applications*, 2007; Vol. 109, pp 44-71.
(41) Chen, J. H.; Fu, J. M.; Sheng, G. Y.; Liu, D. H.; Zhang, J. J. "Diamondoid hydrocarbon ratios: Novel maturity indices for highly mature crude oils", *Org. Geochem.* **1996**, *25*, 179-190.
(42) Li, J. G.; Philp, P.; Cui, M. Z. "Methyl diamantane index (MDI) as a maturity parameter for Lower Palaeozoic carbonate rocks at high maturity and overmaturity", *Org. Geochem.* **2000**, *31*, 267-272.
(43) Ott, U. "Interstellar grains in meteorites", *Nature* **1993**, *364*, 25-33.
(44) Pirali, O.; Vervloet, M.; Dahl, J. E.; Carlson, R. M. K.; Tielens, A.; Oomens, J. "Infrared spectroscopy of diamondoid molecules: New insights into the presence of nanodiamonds in the interstellar medium", *Astrophysical Journal* **2007**, *661*, 919-925.
(45) Brenner, D. W.; Shenderova, O. A.; Areshkin, D. A.; Schall, J. D.; Frankland, S. J. V. "Atomic modeling of carbon-based nanostructures as a tool for developing new materials and technologies", *CMES-Comp. Model. Eng. Sci.* **2002**, *3*, 643-673.

(46) Cagin, T.; Che, J. W.; Gardos, M. N.; Fijany, A.; Goddard, W. A. "Simulation and experiments on friction and wear of diamond: a material for MEMS and NEMS application", *Nanotechnology* **1999**, *10*, 278-284.

(47) Drexler, K. E., Ed. *Nanosystems: Molecular Machinery, Manufacturing, and Computation*; Wiley: New York, 1992.

(48) Lifshitz, Y.; Kohler, T.; Frauenheim, T.; Guzmann, I.; Hoffman, A.; Zhang, R. Q.; Zhou, X. T.; Lee, S. T. "The mechanism of diamond nucleation from energetic species", *Science* **2002**, *297*, 1531-1533.

(49) Wei, Z.; Moldowan, J. M.; Dahl, J.; Goldstein, T. P.; Jarvie, D. M. "The catalytic effects of minerals on the formation of diamondoids from kerogen macromolecules", *Org. Geochem.* **2006**, *37*, 1421-1436.

(50) Bistricic, L.; Baranovic, G.; Mlinaricmajerski, K. "A vibrational assignment of adamantane and some of its isotopomers - empirical versus scaled semiepirical force-field", *Spectrochimica Acta Part a-Molecular and Biomolecular Spectroscopy* **1995**, *51*, 1643-1664.

(51) Mair, B. J.; Shamaiengar, M.; Krouskop, N. C.; Rossini, F. D. "Isolation of adamantane from petroleum", *Anal. Chem.* **1959**, *31*, 2082-2083.

(52) Snyder, R. G.; Schachts.Jh "A valence force field for saturated hydrocarbons", *Spectrochimica Acta* **1965**, *21*, 169-&.

(53) Broxton, T. J.; Deady, L. W.; Kendall, M.; Topsom, R. D. "Infrared spectra of adamantanes", *Appl. Spectrosc.* **1971**, *25*, 600-&.

(54) Bailey, R. T. "Spectroscopic and thermodynamic studies of molecular crystals .1. Internal vibrations of adamantane in plastic phase", *Spectrochimica Acta Part a-Molecular Spectroscopy* **1971**, *A 27*, 1447-&.

(55) Lee, W. Y.; Slutsky, L. J. "Heat of vaporization, infrared-spectrum, and lattice energy of adamantane", *Journal of Physical Chemistry* **1975**, *79*, 2602-2604.

(56) Burns, G.; Dacol, F. H.; Welber, B. "lattice vibrational study of the phase-transition in the plastic crystal adamantane (C10H16)", *Solid State Communications* **1979**, *32*, 151-155.

(57) Bertie, J. E.; Francis, B. F.; Jacobs, S. M. "The far-infrared spectrum of the tetragonal phase adamantane ii at 4.6-degrees-K", *J. Chem. Phys.* **1981**, *74*, 6522-6523.

(58) Howard, D. L.; Henry, B. R. "Temperature and phase effects on the overtone spectra of several adamantanes", *Journal of Physical Chemistry A* **1998**, *102*, 561-570.

(59) Corn, R. M.; Shannon, V. L.; Snyder, R. G.; Strauss, H. L. "Orientational dynamics and disorder of solid adamantane as studied by infrared-spectroscopy", *J. Chem. Phys.* **1984**, *81*, 5231-5238.

(60) Salmon, D.; Shannon, V. L.; Strauss, H. L. "The C-H infrared stretching bands of ordered and disordered phases of adamantane", *J. Chem. Phys.* **1989**, *90*, 773-782.

(61) Rassat, A.; Fabre, C.; Messaoudi, A.; Setton, R.; Ceolin, R.; Bernier, P.; Zahab, A. "Surface effects and forbidden transitions in the reflection-infrared (rir) spectrum of footballene and of adamantane", *Comptes Rendus De L Academie Des Sciences Serie Ii* **1992**, *315*, 1653-1659.

(62) Szasz, G.; Kovacs, A. "Investigation of the density-functional theory-derived scaled quantum mechanical method for cage-like systems: the vibrational analysis of adamantane", *Mol. Phys.* **1999**, *96*, 161-167.

(63) Gough, K. M.; Dwyer, J. R.; Dawes, R. "Ab initio analysis of C-H and C-C stretching intensities in Raman spectra of hydrocarbons", *Can. J. Chem.-Rev. Can. Chim.* **2000**, *78*, 1035-1043.

(64) Chen, Y. R.; Chang, H. C.; Cheng, C. L.; Wang, C. C.; Jiang, J. C. "Size dependence of CH stretching features on diamond nanocrystal surfaces: Infrared spectroscopy and density functional theory calculations", *Journal of Chemical Physics* **2003**, *119*, 10626-10632.

(65) Richardson, S. L.; Baruah, T.; Mehl, M. J.; Pederson, M. R. "Theoretical confirmation of the experimental Raman spectra of the lower-order diamondoid molecule: cyclohexamantane (C26H30)", *Chemical Physics Letters* **2005**, *403*, 83-88.

(66) Jensen, J. O. "Vibrational frequencies and structural determination of adamantane", *Spectrochimica Acta Part a-Molecular and Biomolecular Spectroscopy* **2004**, *60*, 1895-1905.

(67) Filik, J.; Harvey, J. N.; Allan, N. L.; May, P. W.; Dahl, J. E. P.; Liu, S. G.; Carlson, R. M. K. "Raman spectroscopy of diamondoids", *Spectrochimica Acta Part a-Molecular and Biomolecular Spectroscopy* **2006**, *64*, 681-692.

(68) Chan, Y. C.; Choy, K.; Liu, S. G.; Sciamanna, S. F.; Dahl, J. E.; Carlson, R. M. K. "Solubility of diamantane, trimantane, tetramantane, and their derivatives in organic solvents", *Journal of Chemical and Engineering Data* **2008**, *53*, 1767-1771.

(69) Sassen, R., Post, P., Jung, W., DeFreitas, D.A., McDade, E.C. In *Petroleum Systems of Divergent Continental Margin Basins, 25th Annual Meeting Gulf Coast Section Society of Economic Paleontologists and Mineralogists Foundation Bob F. Perkins Research Conference,pp. 832-861.*, 2005.

(70) Heinrich, P.; Wyzgol, R.; Schrader, B.; Hatzilazaru, A.; Luebbers, D. W. "Determination of organic compounds by IR/ATR spectroscopy with polymer-coated internal reflection elements", *Appl. Spectrosc.* **1990**, *44*, 1641-1646.

(71) Janotta, M.; Karlowatz, M.; Vogt, F.; Mizaikoff, B. "Sol-gel based mid-infrared evanescent wave sensors for detection of organophosphate pesticides in aqueous solution", *Analytica Chimica Acta* **2003**, *496*, 339-348.

(72) Dobbs, G. T.; Balu, B.; Young, C.; Kranz, C.; Hess, D. W.; Mizaikoff, B. "Mid-infrared chemical sensors utilizing plasma-deposited fluorocarbon membranes", *Analytical Chemistry* **2007**, *79*, 9566-9571.

(73) http://www.chm.bris.ac.uk/pt/diamond/, Universtiy of Bristol, CVD Diamond Film Group, **May 2010**

CHAPTER 4

Toward in-situ Detection of Cold Seep Derived Authigenic Carbonates via Infrared Attenuated Total Reflection Spectroscopy

In the present chapter, infrared attenuated total reflection (IR-ATR) spectroscopy investigations on gravity core marine sediment samples collected around hydrocarbon seeps revealed that carbonates formed from different sources of HCO_3^- may be identified by different infrared (IR) spectroscopic absorption profiles of the ν_3 asymmetric carbonate stretching vibration. These profiles have been utilized to establish an analytical model for diagnosing the diversity of processes associated with the precipitation of carbonate minerals. An IR indicator parameter was derived that is suitable for the identification of microbially mediated authigenic carbonate precipitations around cold seep ecosystems. The obtained results demonstrate that IR-ATR spectroscopy may be applied as a rapid and cost-effective identification method for locations with active or previously active seepage areas.

4.1 MOTIVATION

Cold seeps are essential reservoirs of carbon; at appropriate temperature and pressure conditions, carbon from this resource is incorporated into gas hydrates, which are recognized among the most relevant carbon sinks. Microbial processes around cold seeps may sequester this carbon as authigenic carbonates. The carbon isotopic composition of these carbonates may vary greatly indicating an almost equally wide range of potential geochemical processes involved in carbonate precipitation [1]. Hence, analyzing carbon isotopic ratios of seep-related minerals

provides access to an important geological archive, as these deposits represent one of the few permanent records of an otherwise ephemeral phenomenon [1-3].

The magnitude of hydrocarbon greenhouse gasses trapped within hydrate and carbonate formations indicates the biogeochemical significance of cold seep ecosystems within the global carbon cycle [4, 5]. Therefore, detailed studies are essential to improve our understanding of the role of cold seeps.

Current standard procedures for locating cold seeps at the oceanic seafloor involve detecting anomalous features on the seafloor using acoustic technologies or detecting oil slicks at the water surface via satellites [6-9]. Once these seeps are remotely located, submersible vehicles are then deployed to locate their seafloor source [10-12] by visualizing outcropping hydrate, carbonate mounds, bubble streams, and chemosynthetic communities. Samples are then taken for the detailed characterization of the geochemical, molecular, and microbial processes occurring at the site [13, 14]. Hence, it would be ideal to provide a rapid, shipboard, or in-situ research tool, which facilitates a qualitative and at least semi-quantitative method to identify and characterize active or previously active seepage areas. Such a method would work in concert with in-situ or on-ship/submersible detection and analysis during a field survey to fully characterize a seep site.

To this end, this chapter proposes that IR-ATR spectroscopy[15-18] utilizing an internal total reflection waveguide may potentially serve as an optical sensing platform for identifying carbonates, which are characteristic of the past or current presence of hydrocarbon seepage.

4.2 BACKGROUND

4.2.1 Cold seeps

Cold seeps were discovered in 1984 by Charles Paull in the Gulf of Mexico at a depth of 3,200 meters (10,499 ft) [19, 20]; these are perhaps the most intensively studied cold seeps in the world (**Figure 4.1a**). However, also new sites continue to be detected even in this well-explored region [21-23].

Cold seeps, also referred to as methane or hydrocarbon seeps, are associated with passive and active continental margins within a variety of geological contexts including hypersaline fluid seepage, petroleum or natural gas escape, methane hydrates, and areas of tectonism, erosion, and slides [4, 24]. Cold seeps represent discrete sites where fluids are in chemical disequilibrium with seawater, and typically rich in methane and other hydrocarbons that seep from deeper sediment depths to the sediment–water interface [25].

These seeps provide an abundant source of energy for the establishment of complex chemosynthetic communities (i.e., clams, mussels, and tube worms), and for sediment microbial populations [20, 26-28] (**Figure 4.1b**). At cold seeps, enhanced microbial activity and fluid flow facilitate the development of unique seafloor features such as gas hydrates, mud volcanoes, and authigenic carbonate mounds [25, 29]. The combination of methane saturated seeping fluids with low temperatures and high pressures promotes gas hydrate formation [30] (**Figure 4.1c**). Carbonate mounds are produced from dissolved inorganic carbon, the byproduct of organic matter oxidation [4, 11, 31] (**Figure 4.1d**). If the fluid flow is rapid enough, mud volcanoes may emanate from the seafloor and express themselves into the water column [32]. Due to hydrates, carbonates, and mud volcanoes unique geophysical signatures are established, which

render such seafloor features useful for identifying cold seeps from a surface ship or satellites [14, 33, 34].

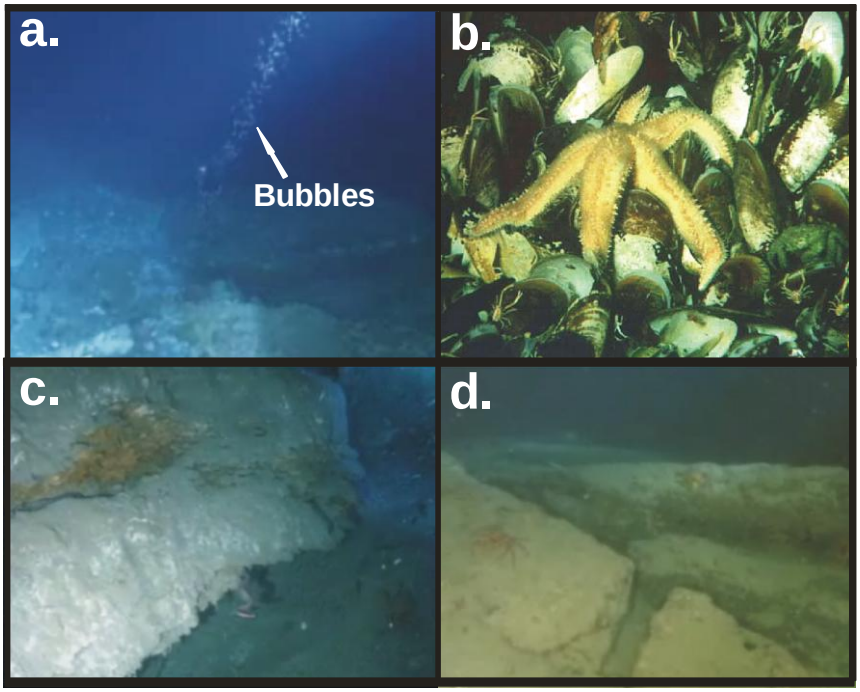

Figure 4.1: (a.) Hydrocarbon gas bubbles emerging from the seafloor, (b.) chemosynthetic organisms around cold seep ecosystems (mollusk shell accumulations), (c.) a massive, sediment draped gas hydrate outcrop, (d.) large authigenic carbonate ledges and mounds. (Images courtesy of Roger Sassen)

4.2.2 Carbonates

Carbonates are naturally occurring minerals containing the carbonate ion (CO_3^{2-}). The most common anhydrous carbonate minerals can be found in the Dana Classification -14 of carbonate minerals [35-37]. Carbonate mineral precipitation occurs, if there is a local saturation of alkali earth metal ions (i.e., Ca^{2+}, Mg^{2+}, etc.) in combination with–bicarbonate (HCO_3-):

$$HCO_3^- + OH^- + (Ca^{2+}, Mg^{2+}) \rightarrow (Ca, Mg)CO_3 + H_2O \qquad \text{Equation 4.1}$$

At cold seeps, bicarbonate is frequently produced as a byproduct of microbially driven anaerobic oxidation of methane (AOM) [13, 34, 38-40]:

$$CH_4 + SO_4^- \rightarrow HCO_3^- + HS^- + H_2O \qquad \text{Equation 4.2}$$

In this work, three anhydrous carbonate minerals were predominately studied: calcite, dolomite, and Mg-calcite.

4.2.2.1 *Calcite*

Calcite gets its name from "*chalix*", which is the Greek word for lime. Calcite is the most stable polymorph of calcium carbonate ($CaCO_3$). Calcite crystals are trigonal-rhombohedral [41]. Calcite is a very common and widespread mineral with highly variable forms and colors comprising approx. 4% (by weight) of the Earth's crust, and is formed in many different geological environments [42].

Calcite is a common constituent of sedimentary rocks, and limestone in particular. Additionally, calcite is frequently the primary constituent of the shells of marine organisms such as e.g., plankton including coccoliths and planktic foraminifera, red algae, sponges, brachiopoda, echinoderms, etc. [11, 43]. Today, calcite is used in cements and mortars, and for the production of lime; limestone is used in the steel industry, glass industry, ornamental stone, chemical and optical fields, and as mineral specimens [35, 42, 44].

4.2.2.2 *Dolomite*

Dolomite $CaMg(CO_3)_2$ was named in 1971 after the French mineralogist Deodat de Dolomieu. The mineral dolomite crystallizes in the trigonal-rhombohedral system [45]. Ideal dolomite has a crystal lattice consisting of alternating layers of Ca and Mg separated by layers of CO.

Dolomite is a sedimentary rock-forming mineral that can be found in massive beds of several hundred feet thickness. Dolomite can form in lakes, on or beneath the shallow seafloor, in zones of brine reflux, and in early to late burial settings [45]. About 80% of the oil and gas reservoirs in North American carbonate rocks are in dolomites, and up to 50% of the world's carbonate reservoirs are dolomites [45].

Dolomite is an unusual carbonate mineral. It is common in ancient platform carbonates, yet it is rare in recent sediments and, without bacterial mediation, is nearly impossible to precipitate in the laboratory at earth surface temperatures. Disputes have arisen as to how these dolomite beds were formed with many theories existing in the literature [11, 45-49]. Dolomite can form as a primary precipitate, a diagenetic replacement (dolomitization), or as a hydrothermal/metamorphic phase—all that it requires is permeability, a mechanism that facilitates fluid flow, and a sufficient supply of magnesium [45]. Dolomitization is the diagenetic conversion of calcium carbonate into dolomite within Mg-rich environments [43, 47]. Dolomite is often used as an ornamental stone, as a concrete aggregate, and as a source of magnesium oxide. It is also used in horticulture to lower the acidity of soil [35, 42, 44].

4.2.2.3 *Magnesian calcite (Mg-calcite)*

Mg-calcite $(Ca,Mg)CO_3$ is a common marine carbonate often encountered in cold seep ecosystems, but it is not classified in the Dana scheme [1, 11, 43]. Mg-calcite is

a magnesium rich variety of calcite, and important not to be confused with magnesium calcite (Dolomite $CaMg(CO_3)_2$).

Magnesian calcites are an important mineral component of modern and ancient carbonate sediments [50]. These phases are found primarily in the skeletons of marine invertebrates and as cements [51]. In order for Mg-calcite to form, Mg^{2+} is incorporated into calcite crystals following surface adsorption, which results in significant perturbation of crystal growth. The most thermodynamically stable forms of magnesian calcite were predicted to contain between 2 and 7 mole% $MgCO_3$ [52]. Within cold seep ecosystems, the formation of Mg-calcite is intimately connected with microbial activity [4, 11, 53-55].

4.2.3 Infrared spectroscopy and carbonates

The feasibility of IR spectroscopic techniques for classifying and differentiating anhydrous carbonate minerals was recognized over 60 years ago [56-60]. One of the earliest detailed reports on the IR spectra of carbonate minerals was by Hunt et al. in 1950. They were first to acknowledge the ability to discriminate among carbonate species based on unique carbonate signatures occurring in the 752-714 cm^{-1} range [58]. In the following two years, Miller and Wilkins constructed an extensive collection of infrared spectra of pure inorganic salts (159 compounds) [60]. Additionally, the characteristic fundamental absorption frequencies of carbonate ions were established [58, 61, 62].

Alder and Kerr have shown that there are four fundamental absorption bands in the spectra of carbonates, the frequencies of which correspond to particular deformational modes of the CO_3^{2-} ion, which collectively provide discriminatory signatures with respect to the crystal system and molecular composition [61, 63, 64].

Four fundamental absorption modes are IR active for carbonate minerals:

- ν_1 symmetric C-O stretch, typically observed between 1085 and 1050 cm^{-1}, is unique to each aragonite group species [61, 62, 64];
- ν_2 out-of-plane absorption feature occurs in the range of 860 – 820 cm^{-1} and is relatively weak [62];
- ν_3 asymmetric carbonate stretch region (1550 – 1350 cm^2) is the strongest carbonate absorption feature [62];
- ν_4 planar bending vibration is seen in the 750 – 695 cm^{-1} region [62, 64].

Furthermore, a variety of IR spectroscopic methodologies, sample preparation procedures, and data evaluation strategies have been developed, which assist in IR spectroscopy to gain recognition as a powerful analytical tool for carbonate research [56-58, 61-64].

Since these pioneering studies utilizing transmission-absorption IR spectroscopy for identifying the most common anhydrous carbonate minerals, a variety of IR-ATR applications for evaluating carbonate minerals have been reported in literature [62, 65-71]. Despite extensively reported applications for IR spectroscopy in carbonate mineralogy, few studies have demonstrated the ability of IR methods to analyze carbonate minerals in marine sediments [66, 69, 70].

Chester and Elderfield described an infrared (transmission-absorption spectroscopy) method for determining the total carbonate amount in various marine sediments utilizing the ν_3 carbonate absorption band [66]. In a separate paper they have extensively discussed the utility of carbonate spectral features for identifying common anhydrous carbonate minerals [62]. Additionally, two quantitative applications on the use of infrared spectroscopy were established: determination of calcite-dolomite ratios in carbonate rocks, and calcite-aragonite ratios in shell material [62].

In 1992, Herbet et al., presented a study utilizing transmission-absorption spectra and similar evaluation methods in contrast to those of Chester and Elderfield to quantify the major components of deep-sea sediments, such as, clays, quartz, and carbonates [69]. A method for quantifying total carbonate mass percentages in marine solid samples (sediments, corals) utilized the ν_3 peak area by FT-IR coupled to the total attenuated reflectance (ATR) technique is described by Mecozzi et al. [70].

4.3 INTRODUCTION

In the present chapter, IR-ATR spectroscopy is successfully used for characterizing the diversity, distribution, and origin of carbonate minerals in marine sediment samples surrounding the cold seeps at Mississippi Canyon 118 (MC118) in the Gulf of Mexico (**Figure 4.2**). Specifically, the IR spectroscopic analysis of sediment has focused on the qualitative and semi-quantitative evaluation of IR signatures utilizing two vibrational modes of the carbonate ion (CO_3^-): the ν_4 planar bending vibration and the ν_3 asymmetric carbonate stretch region (shaded regions in **Figure 4.3**). It is proven that these vibrational modes are highly informative for the identification and characterization of carbonate minerals related to cold seep areas [61, 62, 64].

Furthermore, an analytical model has been developed for rapidly diagnosing the diversity of the processes associated with the precipitation of carbonate minerals. In particular, an IR indicator parameter has been established that is capable of immediate identification of cold seep derived and microbially mediated authigenic carbonates.

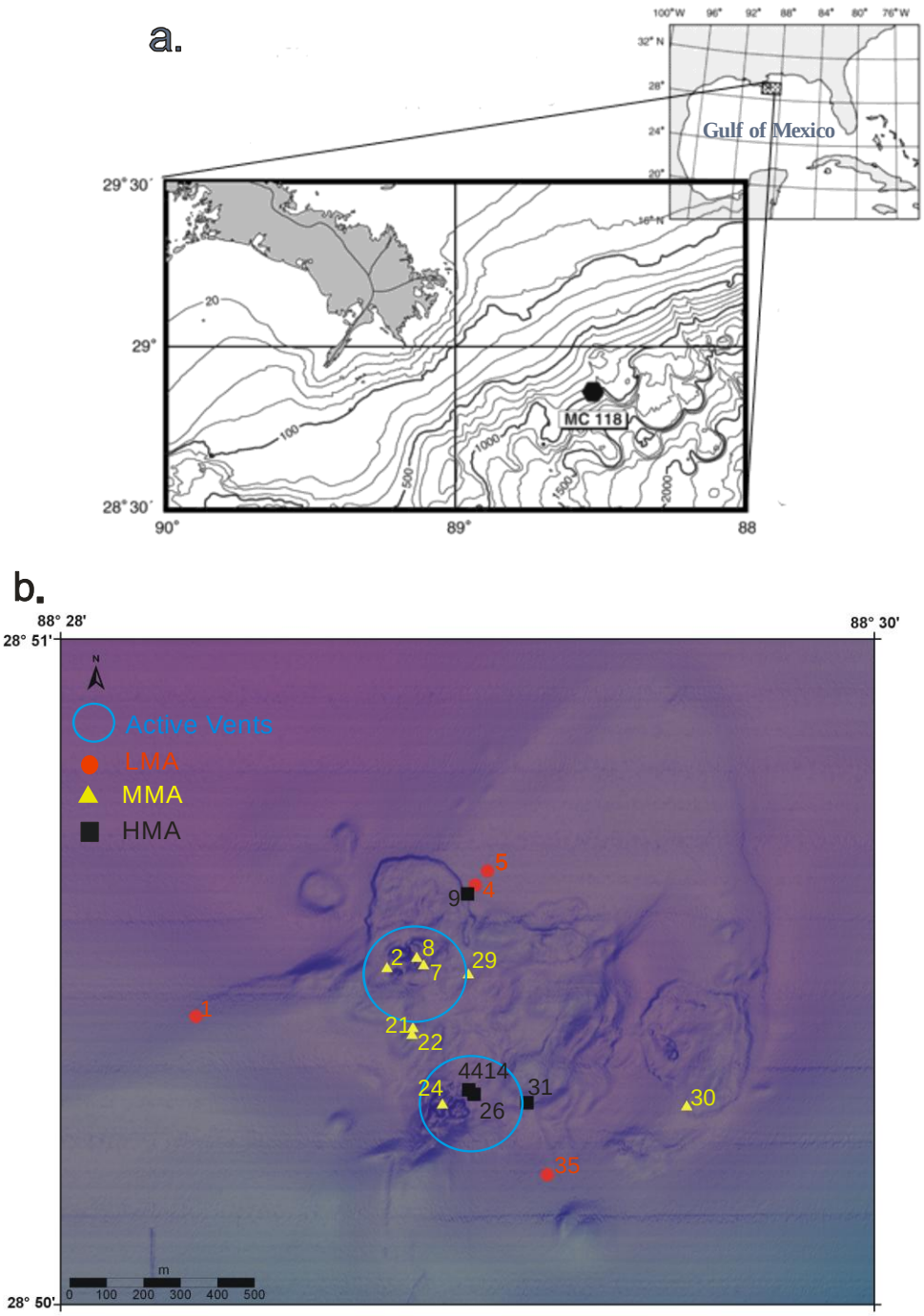

Figure 4.2: (a.) Seafloor map of the Gulf of Mexico and close-up of Mississippi Canyon 118 (MC 118). (b.) MC118 map: red, yellow and black core numbers exhibit microbial activity as low (LMA), moderate (MMA), and high (HMA), respectively. Active vents are shown by blue circle. (Courtesy of Dr. Leonardo Macelloni, Mississippi Mineral Research Institute.)

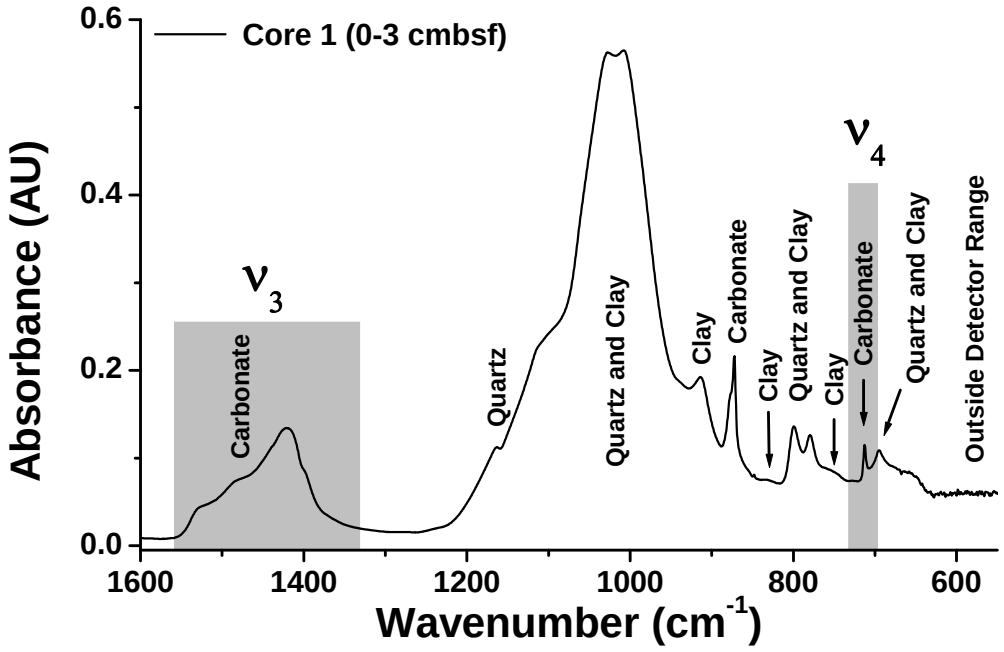

Figure 4.3: Representative IR-ATR spectrum of dried Core 1 (0-3 cmbsf) sediments collected from MC118.

4.4 METHODS AND MATERIALS

4.4.1 Gravity core collection

In May and October of 2005, gravity cores (Figure 4) were collected at MC118 site off the Research Vessel (R/V) Pelican (operated by Louisiana Universities Marine Consortium) [25]. Core positions were targeted using previously collected chirp sonar sub-bottom profile data [72]. The gravity core collection details have been published by Lapham et al.[25]

During the May cruise, core numbers 1–10 were collected and locations determined by the on-board GPS (global positioning system). For the October cruise, cores 21–39 were collected and locations determined by the presence of an ultra short baseline transponder (USBL; LinkQuest Inc., California) connected to the core barrel

wire [25]. Core depths ranged between 22 and 460 cm below the seafloor (cmbsf). A summary of the gravity core locations examined in this chapter can be found in **Table A-1.1**. Gravity cores were collected using the apparatus shown in **Figure 4.4**.

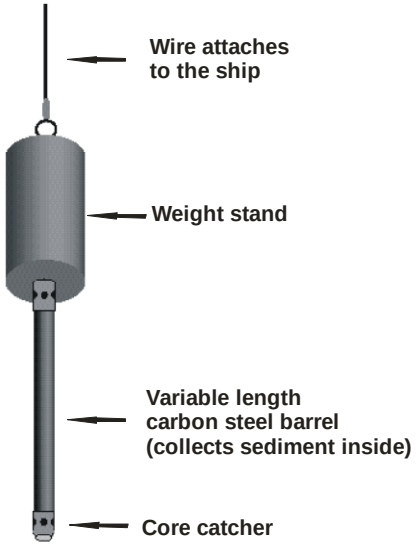

Figure 4.4: Illustration of gravity core collector (adapted from http://walrus.wr.usgs.gov/pv/pvgravcore.html).

4.4.2 IR-ATR measurement procedures

IR-ATR spectra of carbonate minerals were recorded in the spectral range 4000–400 cm^{-1} using a Bruker Equinox 55 FT-IR spectrometer (Bruker Optics Inc., Billerica, MA) equipped with a liquid nitrogen (LN_2) cooled mercury-cadmium-telluride (MCT) detector (Infrared Associates, Stuart, FL), and a Specac Gateway in-compartment horizontal ATR unit (Specac Inc., Woodstock, GA). Each sample was directly deposited onto a trapezoidal ZnSe (n_D = 2.43 at λ = 5 μm) ATR waveguide (MacroOptica, Moscow, Russia) with six effective reflection regions (72×10×6 mm; 45°).

Sediment samples obtained from our collaborators at Florida State University (FSU) were prepared by drying at 60^{O}C for 12 hours. Each sediment sample was hand ground into a fine powder with a ceramic mortar and pestle. Acetone (Certified ACS grade, Fisher Scientific, Fair Lawn, NJ) was then added (approx. 2 mL per 300 mg of sample) to form a suspension for reproducible application onto the waveguide surface.

Prior to the sample deposition, the sample chamber was purged with dry air for 5 min to minimize atmospheric CO_2 and water vapor interference followed by the collection of a reference spectrum using the neat ZnSe crystal. After collection of the reference spectrum, approx. 1 mL of the sample suspension was pipetted onto the waveguide surface. All IR-ATR spectra were recorded at 90 s intervals throughout the drying process until a stable spectral signature was obtained. IR-ATR reference and sample spectra were generated by averaging 100 scans at a spectral resolution of 1 cm^{-1}.

4.4.3 GC-IRMS measurement procedure

The stable carbon isotopic compositions of bulk carbonates ($\delta\ ^{13}C\ -CO_3$) within selected sediment samples were determined using gas chromatography coupled with isotope-ratio mass spectrometry (GC-IRMS). Approximately ~300 mg of sediment was placed into a 20 mL glass serum vial and sealed with a butyl rubber stopper and aluminium cap. The vial was then flushed with nitrogen for 4 min and 2 mL of 70% phosphoric acid (Certified ACS grade, Fisher Scientific, Fair Lawn, NJ) was added to fully convert the carbonates to CO_2 gas for several hours. Five microliters of the evolved CO_2/N_2 gas mixture were then directly injected into a continuous flow Hewlett-Packard 5890 GC equipped with a 6m Poroplot Q column at

35°C and a Finnigan Mat Delta S isotope ratio mass spectrometer at Florida State University. Isotope ratios were reported using the standard ‘‘del’’ notation, $\delta^{13}C$ (‰) = $(R_{(sample)}/R_{(PDB\ standard)} - 1)*1000$, where R is the ratio of the heavy to light isotope (^{13}C:^{12}C) and PDB (Pee Dee Belemnite) is the same ratio of a standard. Randomly selected samples were measured in duplicates; the absolute analytical error was <0.8‰ with an average error <0.3‰ based on 16 samples. For the purposes of this paper, the sediment samples which have negative $\delta\ ^{13}C$ values will be referred as ^{13}C-depleated (cold seep derived authigenic carbonates), and samples which have positive $\delta\ ^{13}C$ values will be referred as ^{13}C-enriched (biogenic carbonates).

4.4.4 Quantification procedure for dolomite/calcite using IR-ATR spectroscopy

In this chapter, a method developed by Dobbs [73] for the semi-quantitative evaluation of the relative mass percentages of calcite and dolomite within the carbonate composition of marine sediment samples has been applied for evaluating the ν_4 peak area obtained from IR-ATR spectra.

Five standards of calcite-dolomite were analyzed **(Figure 4.5a**). A peak integration method using the OPUS software package (Bruker Optics Inc., Billerica, MA) was developed to evaluate the ν_4 spectral absorptions of calcite (716.3 – 705.2 cm^{-1}) and dolomite (733.9 – 721.9 cm^{-1}) [73]. This integration method was utilized for evaluating all calcite-dolomite compositions in the present chapter. Peak areas (PA) from each spectral region were averaged and used for construction of the first order linear correlation function, y=0.565+97.639*x (**Figure 4.5b**) In this chapter, this correlation function was used to extract the relative mass percentages of calcite and dolomite with respect to the total carbonate content. The x-axis of the calibration plot was obtained from the ratio of the dolomite absorption intensity divided by the sum of intensities for calcite and dolomite (D/(C+D)), where C = calcite and D = dolomite.

Dual y-axes represent the inverse relationship in composition, enabling simultaneous calculation of the respective mass percentage contributions for calcite and dolomite.

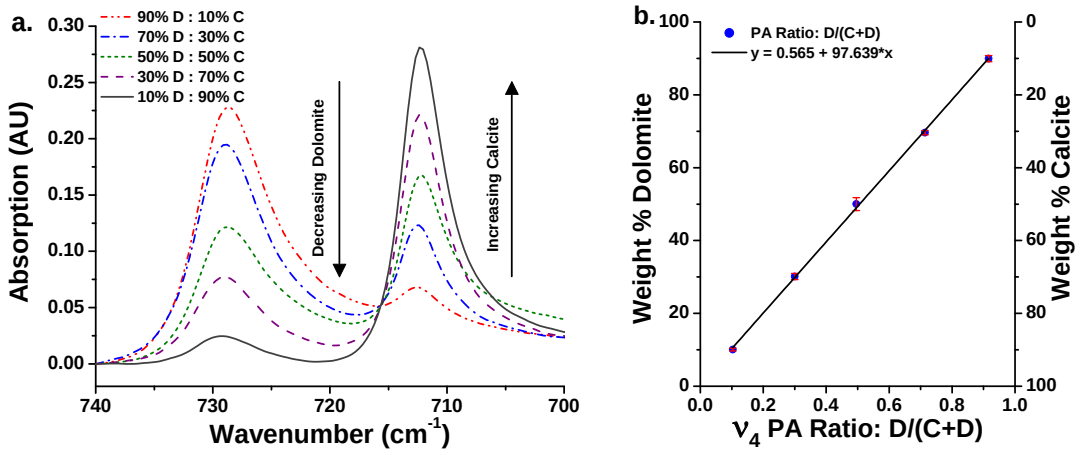

Figure 4.5: (a.): IR-ATR spectra highlighting the ν_4 carbonate region for calibration standards used to establish the first order correlation fit for quantification of calcite and dolomite. (b.) First order calibration function for determining the mass % of calcite and dolomite contributions to the total carbonate content using Prop. PA ratios for ν_4. (Figure adapted from the thesis of G. Dobbs)

4.4.5 Spectral deconvolution

To calculate values for indicators *A*, *B*, and *F*, a spectral deconvolution of the carbonate peak in the ν_3 and the ν_4 region was performed. A commercial peak fitting module (PFM) (Microcal Origin 7.5 software package; OriginLab Corporation, Northampton, USA) was used for deconvolution of single and multiple peak data for IR-ATR peaks resulting from ν_4 planar bending vibrations (750–695 cm^{-1}), and ν_3 asymmetric carbonate stretching vibrations (1550–1350 cm^{-1}). The deconvolution procedure involved data import from the OPUS program, specification of a spectral

sub-range (for the ν_3 region: 1600-1300 cm^{-1}; for the ν_4 region: 720-710 cm^{-1} for samples with calcite, and 740-710 cm^{-1} for samples with dolomite and calcite), and selecting a Lorenzian distribution peak approximation, including the number of peaks, manual location of the peak positions, and initial half-width estimates. All settings were kept constant for every ν_3 region and every ν_4, region deconvolution. Only the sub-range for the ν_3 region peak analysis was varied ±5 cm^{-1} for optimization purposes. The parameters obtained by fitting were the location, width, areas of the peaks, and goodness of the fit, which were used for further calculations.

4.5 RESULTS AND DISCUSSION

4.5.1 Object of investigation: MC118

Numerous hydrocarbon seeps have been found in the Gulf of Mexico, where hydrocarbons usually originate from deeply seeded petroleum reservoirs [2, 11, 13, 34]. A typical seep site is MC118 (**Figure 4.2**) [25]. MC118 (location: 28.852295 N; -88.491950 W) is a well-characterized location, and a potential candidate for establishing a long-term seafloor observatory consisting of a variety of sensors and sensor networks for monitoring and better understanding the dynamics of cold seep ecosystems [5, 74-76].

The site is an exemplary natural laboratory that exhibits the diverse and complex biogeochemical characteristics of cold seep ecosystems [25, 34]. Two active hydrocarbon vents are located at MC118: NW and SW (blue circles in **Figure 4.2b**). These vent areas are of substantial interest, as massive gas hydrate and carbonate formations have been observed surrounding the fluid seeps [25]. Carbonate minerals are ubiquitous throughout the MC118 site, and are characterized by high diversity and complexity with respect to origin, composition, diagenesis, and distribution of the

involved constituents [43,11]. In the remainder of the present chapter, two types of carbonate precipitations are of particular interest: authigenic and biogenic formations.

Seepage comprising methane, hydrocarbons (i.e., petroleum), and other organic matter may be oxidized by sediment microbial communities, thereby establishing chemical gradients essential to authigenic ("formed-in-place") carbonate formation [2, 11, 12]. The local saturation of alkaline earth metal ions (i.e., Ca^{2+}, Mg^{2+}, etc.) in combination with a byproduct of microbial activity, i.e., bicarbonate (HCO_3^-), allows for the precipitation of authigenic carbonates [1, 4]. These authigenic carbonates comprise a diverse carbon isotopic composition, identified as the $\delta^{13}C$ depending on the carbon source ($\delta^{13}C$ of organic matter = -20‰, $\delta^{13}C$ of non-methane hydrocarbon = -27‰, and $\delta^{13}C$ of methane = -56.5‰) (**Figure 4.6**) [4,11].

Biogenic carbonates at MC118 are transported into the geological system from an external source. These carbonates are primarily calcite products of planktonic foraminifera and coccolithophore algae [34, 43, 77, 78]. Biogenic carbonates are produced in the vesicles of the algae (Golgi body), and then extruded to cover the cell surface [79]. The primary carbon source of biogenic carbonates is bicarbonate from carbon dioxide dissolved in sea water, and is characterized by a $\delta^{13}C$ isotopic composition of + 0‰ (**Figure 4.6**) [4, 80]. Due to mixing of seep related authigenic carbonates and biogenic carbonates, the bulk sediment samples around MC118 site reveal highly diverse $\delta^{13}C$ compositions ranging from +0 to -55‰ [4].

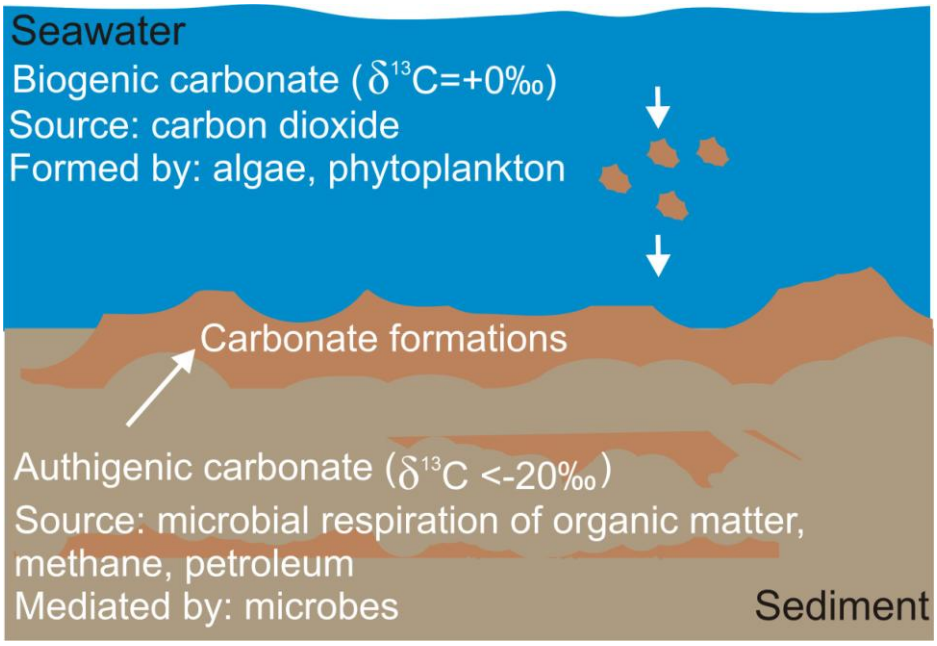

Figure 4.6: Possible pathways of authigenic and biogenic carbonate formations in marine sediments.

In May and October of 2005, gravity cores were collected at MC118 off the Research Vessel (R/V) Pelican[25] and IR-ATR analysis of 16 selected gravity cores was conducted as a function of depth (i.e., a total of 110 sediment samples) with core depths ranging between 22 and 460 cm below the surface (cmbsf) (**Figure 4.2b**). For verification of the obtained IR data, the bulk carbon isotopic compositions of selected sediment samples were determined using gas chromatography coupled with mass spectrometry (GC-MS), and $\delta\ ^{13}C$ values were calculated for comparison with IR-ATR findings, as shown in **Table 4.1**. To comprehensively present the collected IR-ATR spectroscopic data with respect to the natural settings of the MC118 site, the examined sediment samples collected from the gravity cores were arranged into three groups, and assigned relative labels of low (LMA), moderate (MMA), and high

(HMA) microbial activity (**Figure 4.2b, Table 4.1**). The utility of this group identification was introduced by Lapham et al. and is adopted herein[25].

Table 4.1: List of sediments samples collected from the MC118 site. Summary of carbon isotope data of marine sediment, calcite and dolomite compositions with respect to the total carbonate content (calcite = 100 – dolomite), and visual spectral profiles in sediment samples of selected sediment depth. (*samples where Mg-calcite concentration is too high for quantifications of calcite and dolomite). See next page

	Core #	Depth (cmbsf)	Spectral profile	Dolomite (%)	$\delta^{13}C$ (‰)
LMA	1	0-18	I	1-2	+0.68
		90-213	II	24-46	+0.99
	4	5-31	I	1-6	+0.89
		53-114	II	21-49	+0.65
		153-156	I	0	+1.33
	5	0-43	I	3-6	+1.17
		70-113	II	20-33	+0.32
		150-193	I	5-12	+0.99
	35	0-53	I	4-10	+0.15
		75-134	II	26-62	+0.28
MMA	8	0-3	I	1	+0.31
		15-18	IV	12	-9.31
		30-123	III	35-49	-9.21
	7	0-23	I	1-3	+0.99
		60-203	III	44-61	-9.36
	2	0-175	III	14-49	-3.55
	29	0-3	I	2	+0.96
		20-23	IV	0	-4.67
		40-103	III	37-40	-6.00
	21	0-53	I	1-5	+1.32
		88-115	III	*	-18.8
	22	0-24	I	0-2	+0.73
		50-63	III	*	-18.45
	24	0-15	III	*	-7.96
	30	15-123	III	7-56	-0.86
HMA	9	0-9	IV	0	-9.69
		40-120	III	*	-9.34
		233-431	II	45-64	+0.79
	26	0-3	I	2	+0.82
		15-47	III	37-69	-7.31
	4414	0-24	III	*	-9.90
	31	0-3	IV	0	-4.54
		17-123	III	16-59	-33.28

4.5.2 IR-ATR analysis of MC118 gravity core sediments

The qualitative and semi-quantitative evaluation of IR spectra obtained from sediment samples recovered from MC118 was based on two characteristic vibrational modes of the carbonate ion: the ν_4 planar bending vibration (750–695 cm^{-1}), and the ν_3 asymmetric carbonate stretching region (1550–1350 cm^{-1}), as shown in **Figure 4.3**.

4.5.2.1 ν_3 *asymmetric carbonate stretch*

The ν_3 carbonate vibrational mode is the strongest carbonate absorption feature active in all hexagonal and rhombohedral carbonates, and is comprised of multiple vibrational contributions [62]. This absorption region is not typically used for species classification due to its broad spectral characteristics, and because similar frequencies of peak maxima are prevalent for several carbonate minerals [66]. To date, this peak has primarily been utilized for quantifying the total carbonate mass in sediments and rocks [62, 70]; however, the present study determined that a significant diversity was observed within the ν_3 carbonate profiles of the IR spectra collected for MC118 sediments **(Figure 4.7a-d).** From visual evaluation of all IR sediment spectra collected here, four distinct ν_3 carbonate spectral profiles were identified and denominated as: I, II, III, and IV **(Figure 4.7a-d).** These unique changes in the ν_3 carbonate IR signature of sediment samples were further utilized for deriving an analytical model, which may be utilized for the immediate detection of hydrocarbon seep related authigenic carbonates.

However, signatures in the ν_3 region may not directly discriminate between different carbonate species. Consequently, combining this information with

signatures obtained in the ν_4 region for all sediment samples verified that the different spectral profiles of ν_3 are not just a result of different carbonate mineral species.

4.5.2.2 *ν_4 planar bending vibration*

The ν_4 carbonate vibrational mode is the most utilized absorption feature for identifying carbonate minerals [62]. In the present study, the ν_4 signature is utilized to differentiate between calcite, dolomite, and Mg-calcite within the sediments samples. **Figure 4.7e-h** shows four typical ν_4 spectral profiles representative for these sediments. Strong carbonate absorption bands are observed in the IR-ATR spectra collected from the sediment samples of MC118 (**Table A-1.2**). Among all MC118 sediments evaluated in this study, calcite (713 cm^{-1}) and dolomite (729 cm^{-1}) [62, 65] were the most frequently observed carbonate minerals, with calcite being the only species detected in all collected samples. Some sediment samples were characterized by the IR absorption of Mg-calcite (ν_4 singlet at approx. 718 cm^{-1}),[65, 68] which appears as a shouldering feature covering the spectral region between calcite and dolomite, and which varies from relatively low **(Figure 4.7g)** to relatively high **(Figure 4.7h)** concentrations.

To develop a better understanding of the spatial distribution of major carbonate species in sediments collected from MC118, a semi-quantitative evaluation of the relative mass percentages of calcite and dolomite within the carbonate composition was performed (**Section 4.4.4).** This evaluation is based on the method pioneered by Chester and Elderfield, which was later expanded by other researchers [62, 68, 73, 81]. The relative mass percentage (%) values for calcite and dolomite to the overall carbonate composition were calculated using a first order linear calibration equation (**Figure 4.5b**), and ranged within 36-100% and 0–64%, respectively (**Table**

4.1, Table A-1.2). As the location of the Mg-calcite absorption peak between calcite and dolomite may affect this estimation, relative percentages for dolomite and calcite in the sediment samples containing Mg-calcite were not calculated.

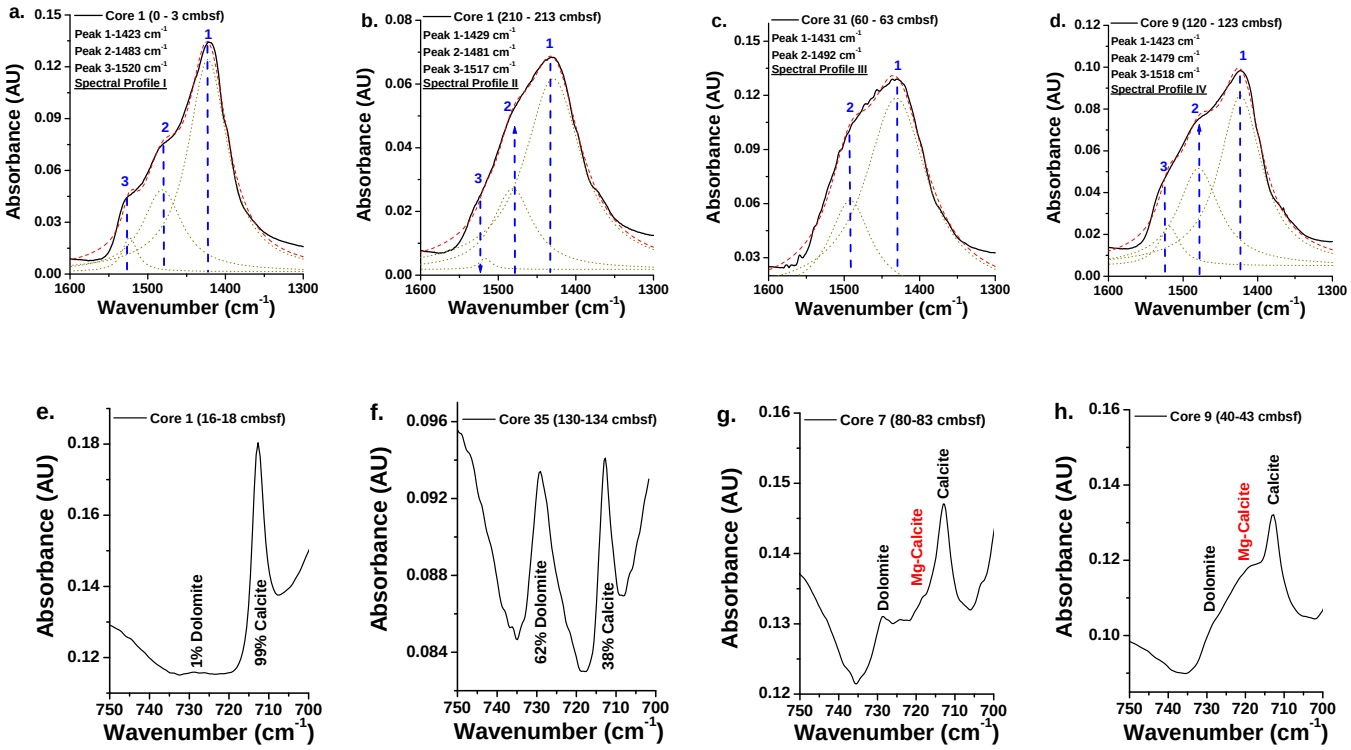

Figure 4.7: Observed ν_3 carbonate absorption features from IR-ATR spectra of (a.) core 1 (0-3 cmbsf), (b.) core 1 (210-213 cmbsf), (c.) core 31 (60-63 cmbsf), and (d.) core 9 (120-123 cmbsf). (Dotted green line represents deconvoluted peaks, dashed red line represents the fit of deconvoluted peaks to ν_3 carbonate absorption feature, deconvolution procedure can be found in section). Selected views of ν_4 carbonate absorption features for IR-ATR spectra obtained from (e.) core 1 (16-18 cmbsf), (f.) core 35 (130-134 cmbsf), (g.) core 7 (80-83 cmbsf), (h.) core 9 (40-43 cmbsf).

4.5.3 IR signatures of marine sediment samples

To study the relationship between different ν_3 spectral profiles and the natural settings at MC118, the collected IR-ATR spectroscopic data was grouped according to the microbial activity level (**Figure 4.2b, Table 4.1**). Four LMA cores were analyzed with IR-ATR, revealing that the ν_3 carbonate C-O stretch of the top sediment layers displayed spectral profile I—a feature of biogenic calcite [82], with a narrow peak at 1413 cm^{-1} and minor shoulders at approx. 1480 and 1520 cm^{-1} (**Figure 4.7a**). From examining the ν_4 planar bending vibration for these sediment samples, small amounts of dolomite (<5%) were detected (**Table 4.1**).

As deeper sediment samples of these LMA cores were analyzed, it was apparent that the ν_3 carbonate C-O stretch no longer resembled spectral profile I; instead, broadened spectral characteristics were evident, as characterized by spectral profile II (**Figure 4.7b**). As sediment samples from theses cores were also characterized by positive $\delta\ ^{13}C$ values, no contribution from microbially mediated carbonates may safely be assumed [4, 11]. Additionally, examining the ν_4 planar bending vibration revealed that the concentration of dolomite significantly increased with depth to >20%. Yet again, in the deepest regions of these cores, the analyzed sediment samples showed IR signatures resembling spectral profile I, while, coincidentally, the dolomite concentration again decreased to a few percent (**Table 4.1**). These observations confirm the conclusion that the ν_3 IR feature broadens with an increase in dolomite concentration, as characterized by spectral profile II, and that spectral profile I exemplifies samples consisting mostly of biogenic calcite.

The IR-ATR analysis of MMA core sediment samples in the ν_4 spectral region suggests that dolomite is present in the majority of these core samples (**Table 4.1**). In these cores, the appearance of dolomite is accompanied by the presence of ^{13}C-

depleted authigenic carbonates, and the obtained IR spectra in the ν_3 region resemble spectral profile III (**Figure 4.7c**). Accordingly, it is concluded that spectral profile III represents samples with both dolomite concentrations >20%, and the appearance of ^{13}C-depleted authigenic carbonate precipitates.

Cores of HMA exhibit ν_3 spectroscopic features resembling all four spectral profiles (Table 2). The first few cmbsf of sediment in these cores (except core 26—biogenic calcite, spectral profile I) reveal small (<5%) dolomite concentrations, show negative $\delta\ ^{13}C$ values, and exhibit broad ν_3 spectroscopic features, resembling spectral profile IV (**Figure 4.7d**). Deeper HMA sediment samples with increasing dolomite concentration (>20%) and still negative $\delta\ ^{13}C$ values of carbonates exhibit a resemblance to spectral profile III. In some of the deepest sediments without detectable ^{13}C-depleted carbonates, but relatively high dolomite contributions, spectral profile II is observed (**Table 4.1**). A complete collection of IR spectra and mineral characterizations is given in **Figure A-1.1**.

Summarizing the results obtained for LMA, MMA, and HMA sediment samples, it is evident that each spectral profile is representative of different natural settings:

- Spectral profile I is distinctive of sediment samples consisting of biogenic calcite characterized by positive $\delta\ ^{13}C$ values;
- Spectral profile II is observed for sediments with high dolomite concentrations (>20%), and biogenic calcite characterized by positive $\delta\ ^{13}C$ values;
- Spectral profile III describes sediments with authigenic carbonates (calcite and dolomite) with negative $\delta\ ^{13}C$ values;

- Spectral profile IV represents samples with authigenic calcite, and is characterized by negative $\delta\,^{13}C$ values.

The evaluated IR data of the collected sediment samples clearly indicate that ^{13}C-depleted authigenic carbonates reveal specific broadening of the ν_3 carbonate C-O stretch (spectral profile III and IV), and are characteristic of MMA and HMA cores, which are located in close proximity to cold seeps. Therefore, it is evident that using IR-ATR spectroscopy enables direct detection of ^{13}C-depleted authigenic carbonates, and thus facilitates locating cold seep sites. However, the appearance of dolomite mineral in sediments causes spectral broadening (spectral profile II), which is similar to that of ^{13}C-depleted authigenic carbonates. Thus, visually differentiating profiles III and IV from profile II is difficult; consequently, a more sophisticated and robust evaluation procedure based on changes in IR carbonate signatures has been developed.

4.5.4 Establishing an IR based indicator for ^{13}C-depleted authigenic carbonates

To establish a reliable IR-based analytical model for detecting ^{13}C-depleted authigenic carbonates, a numerical indicator sensitive only to ^{13}C-depleted authigenic carbonates, and not to the additional presence of dolomite, is required.

4.5.4.1 *Categories*

Initially, six categories of marine sediments were identified (with three sediment core samples per category), as summarized in **Table 4.2**. An analyzed sediment sample was then assigned to a category based on the carbonate make-up and $\delta\,^{13}C$ value. Within these six categories, only gravity cores containing dolomite and calcite carbonates were used.

Category 1 consists of the sediment samples characterized by positive $\delta\ ^{13}C$ values, comprising biogenic calcite and minimal dolomite contribution (<5%). Analyzing this category provides IR absorption features of sediment samples with a majority of biogenic calcite. Categories 2 and 3 comprise sediment samples with positive $\delta\ ^{13}C$ values, consisting of biogenic calcite and dolomite concentrations ranging from >5 to 62%. These two categories demonstrate IR spectral changes due to an increase in concentration of dolomite in marine sediments. Category 4 represents sediment samples with negative $\delta\ ^{13}C$ calcite and minimal dolomite contribution (<5%). Analyzing this category provides IR absorption features of sediment samples with a majority of authigenic calcite. In categories 5 and 6, all samples showing ^{13}C-depleted calcite and dolomite concentrations ranging from >5 to 61% are summarized. In these two categories, changes in the ν_3 region are associated with two factors: ^{13}C-depleted calcite, and the presence of dolomite within the sediment samples.

Table 4.2: Six categories established depending on their carbonate make up δ ^{13}C along with six indicators. (D = dolomite, δ^{13}C(+) = ^{13}C enriched samples, δ^{13}C(-) = ^{13}C depleted sediment samples, ± represents standard deviation, AU-arbitrary units).

		Indicators						
Category	**Description**	***A*** (AU)	***B*** (AU)	***C*** (cm^{-1})	***D*** (cm^{-1})	***E*** (cm^{-1})	***F*** (AU)	**Average *F***
1	D<5%, δ^{13}C(+)	2.72 ± 0.64	20.08 ± 2.30	1422	1481	1523	57.80 ± 4.58	
2	5%<D<49%, δ^{13}C(+)	4.01± 1.8	21.46 ± 6.89	1427	1483	1521	45.87 ± 5.38	55.6 ± 8.7
3	D>49%, δ^{13}C(+)	8.51 ± 2.09	N/A	1433	1486	N/A	63.20 ± 4.47	
4	D<5%, δ^{13}C(-)	1.87 ± 0.25	10.50 ± 1.35	1423	1479	1517	108.44 ± 10.23	
5	5%<D<49%, δ^{13}C(-)	3.73 ± 1.35	N/A	1430	1487	N/A	101.57 ± 6.77	103.9 ± 9.3
6	D >48%, δ^{13}C(-)	5.15 ± 0.79	N/A	1435	1488	N/A	100.43 ± 12.48	

4.5.4.2 *Indicators*

Six different indicators (*A*-*F*) were developed to unambiguously identify the changes in the ν_3 region, as the contribution of authigenic carbonates to the overall carbonate make-up increases (**Table 4.2**). The first indicator (*A*) is calculated by dividing the area under peak 1 by the sum of peak areas 2 and 3 **(Figure 4.7 a-d**) for all samples within the six categories. The second indicator (*B*) represents the ratio of the areas under peaks 1 and 3. Indicators *C*-*E* are the frequency positions of peaks 1, 2, and 3, respectively. Indicator *F* is calculated as the ratio of the sum of areas under three peaks (1, 2, and 3) of the ν_3 C-O stretch, and the sum of areas in the ν_4 region (calcite and/or dolomite). All reported values for the six indicators are averages with the standard deviations given in **Table 4.2**.

The value of indicator *A* increases as the dolomite concentration in the sediment samples increases; however, as the contribution of ^{13}C-depleted carbonates increases, no significant change is detected (**Table 4.2**). Therefore, indicator *A* is not useful for detecting ^{13}C-depleted carbonates as it is sensitive only to changes associated with the addition of dolomite; alternatively, this knowledge may also be derived from spectroscopic features in the ν_4 region.

Examining the values of indicator *B*, it is evident that, as the concentration of dolomite increases, the deconvolution of the third peak becomes impossible; thus, these values are not presented for categories 3, 5, and 6 (**Table 4.2**). Even though the value of *B* decreases by approx. 50% with the addition of ^{13}C-depleted carbonates (Category 4), no firm conclusion is obtained due to the disappearance of the third peak.

Indicator *C* indicates that the position of the first peak is subject to a blue shift by approx. 10 cm^{-1} as the dolomite concentration in the samples increases. However,

no changes were observed with addition of ^{13}C-depleted carbonates. Hence, this indicator is of minor utility, as it only reveals changes associated with the addition of dolomite. Analyzing indicators *D* and *E*, no significant changes, except the disappearance of the third peak as dolomite concentration increases, are detected (**Table 4.2**). The data presented in **Table 4.2** clearly indicate that five (*A*-*E*) indicators are apparently not conclusive, as they are extremely sensitive to the appearance of dolomite, making following the spectroscopic changes due only to the appearance of ^{13}C-depleted carbonates difficult.

However, indicator *F* was found to clearly point towards the presence of ^{13}C-depleted carbonates in sediment samples (**Table 4.2**). The *F* value of 55.6 ± 8.7 (average ± standard deviation) for categories 1, 2, and 3 (^{13}C-rich sediments) rises to 103.9 ± 9.3, while it almost doubles in magnitude for categories 4, 5, and 6 (^{13}C-depleted sediments), enabling a clear differentiation between the two cases. In addition, it is important to note that the values of indicator *F* for categories 1, 2 and 3 (with the only known difference being the dolomite concentration) show minimal variation, which supports the conclusion that the dolomite content does not strongly affect the value of this indicator. The same behavior is evident in comparing indicator *F* values for categories 4, 5 and 6.

In conclusion, after comprehensive analysis of IR carbonate spectral changes in the ν_3 spectral region, indicator *F* was determined to be highly suitable for detecting the presence of ^{13}C-depleted authigenic carbonates without interference from dolomite minerals within marine sediment samples.

4.5.5 Utilizing indicator *F* for gravity core sediment sample analysis

To test the applicability of indicator *F*, 13 additional gravity cores at different depth levels were analyzed and evaluated (**Figure 4.8**). **Figure 4.8a** shows sediment

samples characterized by positive $\delta^{13}C$ values having an average indicator *F* value of 53.5 ± 11.4, and sediment samples with negative $\delta^{13}C$ values having average *F* values of 104.3 ± 15.8. The clustering profile of indicator *F* values in **Figure 4.8a** clearly corroborates the potential of classifying sediment samples by the contribution of ^{13}C-depleted authigenic carbonate.

Furthermore, using indicator *F* facilitates the detection of changes in the contribution of ^{13}C-depleted authigenic carbonate as a function of core depth (**Figure 4.8b**). For example, cores 9 (223-331 cmbsf), 29 (0-3), 26 (0-3), 7 (10-13), and 8 (0-3) show no detectable contribution of ^{13}C-depleted authigenic carbonate based on IR-ATR results (*F* values at approx. 61.2 ± 4.6); however, at other core depths (9 (5-6, 120-123 cmbsf), 29 (20-100), 26 (15-40), 7 (200-203), and 8 (15-123)) the *F* values rises to 99.9 ± 10.7, thus indicating the presence of ^{13}C-depleted authigenic carbonate in these sediment layers, which is confirmed by the $\delta^{13}C$ values given in **Table 4.2**. Consequently, this information may be used for locating areas of past seepage activity. Furthermore, analyzing the areas of presently active seepage as a function of core depth may provide information as to when this seepage was formed.

Within selected samples, the limitation of information based exclusively on IR-ATR spectroscopy is evident. For example, when analyzing sediment samples from core 30 (**Figure 4.8b**), with *F* values of 62, 69, and 77, corresponding to $\delta^{13}C$ values of -0.8, -1.4, and -2.5, respectively, the *F* values of 62 and 69 are close to (upper bound) *F* values characteristic of positive $\delta^{13}C$ sediment samples. In such borderline cases, the detection of ^{13}C-depleted authigenic carbonates using only IR-ATR data may remain challenging. However, it is important to note that the general trends derived from the developed analytical model still hold true even in samples

such as core 30, as the contribution of ^{13}C-depleted authigenic carbonate increases, resulting in increasing *F* values.

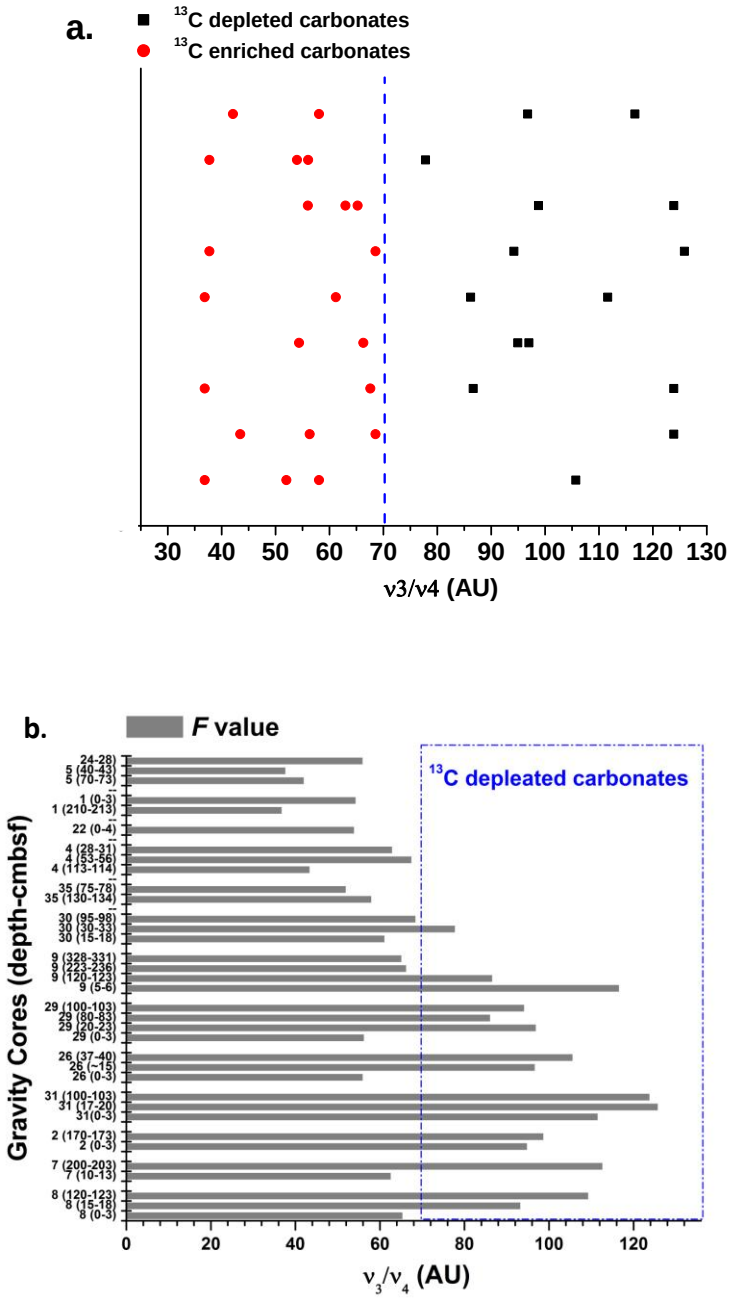

Figure 4.8: (a.) Indicator *F* values for sediment samples (b.) Indicator *F* values as a function of depth of the sediment samples. (AU-arbitrary units)

4.6 CONCLUSIONS

In this study, IR-ATR spectroscopy was utilized for the first time for evaluating and characterizing the distribution, variations, and origin of carbonate minerals within sediment formations surrounding a hydrocarbon seep site—MC 118 in the Gulf of Mexico. A semi-quantitative analysis of calcite-dolomite compositions relative to the overall carbonate content in sediment samples was established, which presents a first approximation of the characteristic variability of dolomite compositions within marine sediment at MC118 site.

Furthermore, IR-ATR spectroscopic studies of gravity core sediment samples revealed distinct absorption profiles of the ν_3 asymmetric carbonate stretch spectral region, which enabled the derivation of an analytical model based on IR data for directly detecting and classifying ^{13}C-depleted authigenic carbonates associated with cold seep ecosystems. Thus, IR-ATR spectroscopy provides a direct on-ship and, in future, in-situ analytical tool for characterizing hydrocarbon seep sites, thereby facilitating advances in rapid spatiotemporal characterization of cold seep ecosystems.

4.7 OUTLOOK

From this chapter, it is evident that IR-ATR spectroscopy represents a technique capable of evaluating carbonate minerals in marine sediments on ship and potentially in-situ. A variety of information can clearly be obtained simply through qualitative and semi-quantitative applications of this technique; however, additional research is required to improve the accuracy of IR-ATR analysis.

First, it is important to note that the spectral changes of the ν_3 asymmetric carbonate absorption feature are derived from changes in the morphological and

crystal structure of carbonates, which is controlled by physiochemical changes (e.g., chemical and biological changes in pore water chemistry) during carbonate precipitation [83]. In this work, spectral changes due physiochemical changes of sediment carbonates resulting from diagenetic change (dolomitization, as shown by the appearance of dolomite) were taken into the account when constructing the analytical model; however, there is a possibility that other physiochemical changes of sediment carbonates resulting from geophysical or geochemical processes (i.e., sediment uplift, lithification, etc.) could result in similar spectroscopic observations, and be limiting factors for this technique [82]. Thus, to improve the sensitivity of this technique, a larger and more diverse sample size should be analyzed in the future; in addition, this should aid with construction of an analytical model that takes into account interference from other carbonates, e.g., Mg-calcite.

During this study, 110 samples from the MC118 site in the Gulf of Mexico were analyzed; to fully understand the capabilities and limitations of this technique, a diversity of samples needs to be studied, not only from different sites in the Gulf of Mexico, but from different global locations. Also, more thorough characterization of major sediment components from various geographic regions and marine settings coupled with advanced data evaluation routines (i.e., the application of multivariate calibration and classification routines) is necessary to realize the full potential of IR spectroscopic strategies for quantifying carbonate minerals in marine sediments. Overall, the simplicity and potential of the method presented in this chapter is expected to motivate broader application of this technique for on-ship screening of oceanic sediments.

4.8 REFERENCES:

(1) Naehr, T. H.; Eichhubl, P.; Orphan, V. J.; Hovland, M.; Paull, C. K.; Ussler, W.; Lorenson, T. D.; Greene, H. G. "Authigenic Carbonate Formation at Hydrocarbon Seeps in Continental Margin Sediments: A Comparative Study" *Deep-Sea Research, Part II: Topical Studies in Oceanography* **2007**, *54*, 1268-1291.

(2) Naehr, T. H.; Stakes, D. S.; Moore, W. S. "Mass wasting, ephemeral fluid flow, and barite deposition on the California continental margin" *Geology* **2000**, *28*, 315-318.

(3) Hein, J. R.; Normark, W. R.; McIntyre, B. R.; Lorenson, T. D.; Powell, C. L. "Methanogenic calcite, C-13-depleted bivalve shells, and gas hydrate from a mud volcano offshore southern California" *Geology* **2006**, *34*, 109-112.

(4) Formolo, M. J.; Lyons, T. W.; Zhang, C.; Kelley, C.; Sassen, R.; Horita, J.; Cole, D. R. "Quantifying Carbon Sources in the Formation of Authigenic Carbonates at Gas Hydrate Sites in the Gulf of Mexico" *Chemical Geology* **2004**, *205*, 253-264.

(5) Sassen, R.; Roberts, H. H.; Jung, W.; Lutken, C. B.; DeFreitas, D. A.; Sweet, S. T.; Guinasso Jr., N. L. "The Mississippi Canyon 118 Gas Hydrate Site: A Complex Natural System" *Proceedings of the Offshore Technology Conference* **2006**, *Paper Number: 18132*.

(6) Fingas, M. F.; Brown, C. E. "Review of oil spill remote sensing" *Spill Science & Technology Bulletin* **1997**, *4*, 199-208.

(7) Gens, R. "Oceanographic applications of SAR remote sensing" *Giscience & Remote Sensing* **2008**, *45*, 275-305.

(8) Sager, W. W.; Lee, C. S.; Macdonald, I. R.; Schroeder, W. W. "High-frequency near-bottom acoustic reflection signatures of hydrocarbon seeps on the Northern Gulf of Mexico continental slope" *Geo-Marine Letters* **1999**, *18*, 267-276.

(9) Sager, W. W.; MacDonald, I. R.; Hou, R. S. "Side-scan sonar imaging of hydrocarbon seeps on the Louisiana continental slope" *AAPG Bull.* **2004**, *88*, 725-746.

(10) MacDonald, I. R.; Guinasso, N. L., Jr.; Sassen, R.; Brooks, J. M.; Lee, L.; Scott, K. T. "Gas Hydrate that Breaches the Sea Floor on the Continental Slope of the Gulf of Mexico" *Geology* **1994**, *22*, 699-702.

(11) Roberts, H. H.; Aharon, P. "Hydrocarbon-Derived Carbonate Buildups of the Northern Gulf of Mexico Continental slope: A Review of Submersible Investigations" *Geo-Marine Letters* **1994**, *14*, 135-148.

(12) Roberts, H. H.; Carney, R. S. "Evidence of Episodic Fluid, Gas, and Sediment Venting on the Northern Gulf of Mexico Continental Slope" *Economic Geology and the Bulletin of the Society of Economic Geologists* **1997**, *92*, 863-879.

(13) Sassen, R.; Joye, S.; Sweet, S. T.; DeFreitas, D. A.; Milkov, A. V.; MacDonald, I. R. "Thermogenic Gas Hydrates and Hydrocarbon Gases in Complex Chemosynthetic Communities, Gulf of Mexico Continental Slope" *Organic Geochemistry* **1999**, *30*, 485-497.

(14) Lapham, L. L.; Chanton, J. P.; Martens, C. S.; Higley, P. D.; Jannasch, H. W.; Woolsey, J. R. "Measuring temporal variability in pore-fluid chemistry to

assess gas hydrate stability: Development of a continuous pore-fluid array" *Environmental Science & Technology* **2008**, *42*, 7368-7373.

(15) Mizaikoff, B. "Mid-infrared evanescent wave sensors - a novel approach for subsea monitoring" *Measurement Science & Technology* **1999**, *10*, 1185-1194.

(16) Kraft, M.; Karlowatz, M.; Mizaikoff, B.; Stuck, R.; Steden, M.; Ulex, M.; Amann, H. "Sensor head development for mid-infrared fibre-optic underwater sensors" *Measurement Science & Technology* **2002**, *13*, 1294-1303.

(17) Kraft, M.; Jakusch, M.; Karlowatz, M.; Katzir, A.; Mizaikoff, B. "New frontiers for mid-infrared sensors: Towards deep sea monitoring with a submarine FT-IR sensor system" *Applied Spectroscopy* **2003**, *57*, 591-599.

(18) Mizaikoff, B. "Mid-IR fiber-optic sensors" *Analytical Chemistry* **2003**, *75*, 258A-267A.

(19) Paull, C. K.; Hecker, B.; Commeau, R.; Freemanlynde, R. P.; Neumann, C.; Corso, W. P.; Golubic, S.; Hook, J. E.; Sikes, E.; Curray, J. "Biological communities at the florida escarpment resemble hydrothermal vent taxa" *Science* **1984**, *226*, 965-967.

(20) Kennicutt, M. C.; Brooks, J. M.; Bidigare; Wade, T. L.; McDonald, T. J. "Vent-type taxa in a hydrocarbon seep region on the louisiana slope" *Nature* **1985**, *317*, 351-353.

(21) Milkov, A. V.; Sassen, R. "Preliminary assessment of resources and economic potential of individual gas hydrate accumulations in the Gulf of Mexico continental slope" *Marine and Petroleum Geology* **2003**, *20*, 111-128.

(22) MacDonald, I. R.; Bohrmann, G.; Escobar, E.; Abegg, F.; Blanchon, P.; Blinova, V.; Bruckmann, W.; Drews, M.; Eisenhauer, A.; Han, X.; Heeschen, K.; Meier, F.; Mortera, C.; Naehr, T.; Orcutt, B.; Bernard, B.; Brooks, J.; de Farago, M. "Asphalt volcanism and chemosynthetic life in the Campeche Knolls, Gulf of Mexico" *Science* **2004**, *304*, 999-1002.

(23) MacDonald, I. R.; Sager, W. W.; Peccini, M. B. "Gas Hydrate and Chemosynthetic Biota in Mounded Bathymetry at Mid-Slope Hydrocarbon Seeps: Northern Gulf of Mexico" *Marine Geology* **2003**, *198*, 133-158.

(24) Sibuet, M.; Olu, K. "Biogeography, biodiversity and fluid dependence of deep-sea cold-seep communities at active and passive margins" *Deep-Sea Research Part Ii-Topical Studies in Oceanography* **1998**, *45*, 517-+.

(25) Lapham, L. L.; Sleeper K.; Woosley R. J. "Microbial activity in surficial sediments overlying acoustic wipeout zones at a Gulf of Mexico cold seep" *Geochemistry Geophysics Geosystems* **2008**, *9*, 17.

(26) Fisher, C. R.; Urcuyo, I. A.; Simpkins, M. A.; Nix, E. "Life in the slow lane: Growth and longevity of cold-seep vestimentiferans" *Marine Ecology-Pubblicazioni Della Stazione Zoologica Di Napoli I* **1997**, *18*, 83-94.

(27) Macdonald, I. R.; Boland, G. S.; Baker, J. S.; Brooks, J. M.; Kennicutt, M. C.; Bidigare, R. R. "Gulf of Mexico hydrocarbon seep communities .2. Spatial-distribution of seep organisms and hydrocarbons at Bush Hill" *Marine Biology* **1989**, *101*, 235-247.

(28) Nikolaus, R.; Ammerman, J. W.; MacDonald, I. R. "Distinct pigmentation and trophic modes in Beggiatoa from hydrocarbon seeps in the Gulf of Mexico" *Aquatic Microbial Ecology* **2003**, *32*, 85-93.

(29) Roberts, H. H.; Carney, R. S. "Evidence of episodic fluid, gas, and sediment venting on the northern Gulf of Mexico continental slope" *Economic Geology and the Bulletin of the Society of Economic Geologists* **1997**, *92*, 863-879.

(30) Sloan, E. D. *Clathrate Hydrates of Natural Gases*, 2nd ed.; Marcel Dekker, Inc.: New York, 1998.
(31) Bohrmann, G.; Greinert, J.; Suess, E.; Torres, M. "Authigenic carbonates from the Cascadia subduction zone and their relation to gas hydrate stability" *Geology* **1998**, *26*, 647-650.
(32) MacDonald, I. R.; Buthman, D. B.; Sager, W. W.; Peccini, M. B.; Guinasso, N. L. "Pulsed oil discharge from a mud volcano" *Geology* **2000**, *28*, 907-910.
(33) Macdonald, I. R.; Guinasso, N. L.; Ackleson, S. G.; Amos, J. F.; Duckworth, R.; Sassen, R.; Brooks, J. M. "Natural oil-slicks in the gulf-of-mexico visible from space" *Journal of Geophysical Research-Oceans* **1993**, *98*, 16351-16364.
(34) Sassen, R.; Roberts, H. H.; Carney, R.; Milkov, A. V.; DeFreitas, D. A.; Lanoil, B.; Zhang, C. L. "Free hydrocarbon gas, gas hydrate, and authigenic minerals in chemosynthetic communities of the northern Gulf of Mexico continental slope: relation to microbial processes" *Chemical Geology* **2004**, *205*, 195-217.
(35) http://webmineral.com/dana/dana.php?class=14, **Dana Carbonate Classification, May 2010**.
(36) Gaines, R. V.; Skinner, H. K.; Foord, E. E.; Mason, B.; Rosenzwieg, A. *Dana's New Mineralogy: The System of Mineralogy of James Dwight Dana and Edward Salisbury Dana*, 8th ed. ed.; Wiley: New York, 1997.
(37) Barthelmy, D. "Mineralogy Database" *http://www.webmineral.com/dana/V-14.shtml***, June 2010**.
(38) Aharon, P.; Fu, B. "Microbial Sulfate Reduction Rates and Sulfur and Oxygen Isotope Fractionations at Oil and Gas seeps in Deepwater Gulf of Mexico" *Geochimica et Cosmochimica Acta* **2000**, *64*, 233-246.
(39) Joye, S. B.; Boetius, A.; Orcutt, B. N.; Montoya, J. P.; Schulz, H. N.; Erickson, M. J.; Lugo, S. K. "The Anaerobic Oxidation of Methane and Sulfate Reduction in Sediments from Gulf of Mexico Cold Seeps" *Chemical Geology* **2004**, *205*, 219-238.
(40) Peckmann, J.; Thiel, V. "Carbon Cycling at Ancient Methane-Seeps" *Chemical Geology* **2004**, *205*, 443-467.
(41) Klein, C., Hurlbut, C., Jr. *Manual of Mineralogy*, 20th ed.; Wiley, 1985.
(42) http://www.galleries.com/minerals/carbonat/class.htm, Mineral Gallery, **May 2010.**
(43) Milliman, J. D. *Marine Carbonates*; Springer: New York, 1974.
(44) http://www.mindat.org/, The mineral and locality database, **May 2010**.
(45) Warren, J. "Dolomite: occurrence, evolution and economically important associations" *Earth-Science Reviews* **2000**, *52*, 1-81.
(46) Machel, H. G. "Concepts and Models of Dolomitization: A Critical Reappraisal" *Geological Society Special Publication* **2004**, *235*, 7-63.
(47) Machel, H. G.; Mountjoy, E. W. "Chemistry and environments of dolomitization - a reappraisal" *Earth-Science Reviews* **1986**, *23*, 175-222.
(48) Machel, H. G.; Mountjoy, E. W. "Chemistry and environments of dolomitization - a reappraisal (reply)" *Earth-Science Reviews* **1987**, *24*, 213-215.
(49) Machel, H. G.; Lonnee, J. "Hydrothermal dolomite - a product of poor definition and imagination" *Sedimentary Geology* **2002**, *152*, 163-171.
(50) Land, L. S. "Diagenesis of skeletal carbonates" *Journal of Sedimentary Petrology* **1967**, *37*, 914-&.

(51) Chave, K. E. "Aspects of the biogeochemistry of magnesium .1. Calcareous marine organisms" *Journal of Geology* **1954**, *62*, 266-283.
(52) Berner, R. A. "Role of Magnesium in the Crystal Growth of Calcite and Aragonite from Sea Water" *Geochimica et Cosmochimica Acta* **1975**, *39*, 489-504.
(53) Botz, R.; Faber, E.; Whiticar, M. J.; Brooks, J. M. "Authigenic Carbonates in Sediments from the Gulf of Mexico" *Earth and Planetary Science Letters* **1988**, *88*, 263-272.
(54) Hutchinson, D. R.; Ruppel, C. D.; Roberts, H. S.; Carney, R. S.; Smith, M. A. In *Gulf of Mexico - Its Origin (History, Archaeology, and Geology)*; Holmes, C. W., Ed.; Texas A&M University Press: College Station, In Press; Vol. 1.
(55) Sassen, R.; Roberts, H. H.; Carney, R.; Milkov, A. V.; DeFreitas, D. A.; Lanoil, B.; Zhang, C. "Free Hydrocarbon Gas, Gas hydrate, and Authigenic Minerals in Chemosynthetic Communities of the Northern Gulf of Mexico Continental Slope: Relation to Microbial Processes" *Chemical Geology* **2004**, *205*, 195-217.
(56) Adler, H. H.; Bray, E. E.; Stevens, N. P.; Hunt, J. M.; Keller, W. D.; Pickett, E. E.; Kerr, P. F. In *Reference Clay Minerals; American Petroleum Institute Research Project 49. Preliminary Report No. 8*; Columbia University: New York, 1951, pp 7-146.
(57) Hunt, J. M.; Turner, D. S. "Determination of Mineral Constituents of Rocks by Infrared Spectroscopy" *Analytical Chemistry* **1953**, *25*, 1169-1174.
(58) Hunt, J. M.; Wisherd, M. P.; Bonham, L. C. "Infrared Absorption Spectra of Minerals and other Inorganic Compounds" *Analytical Chemistry* **1950**, *22*, 1478-1497.
(59) Louisfert, J.; Pobeguin, T. "Differentiation of Calcium Carbonates by Means of Infrared Absorption Spectra" *Compt. rend.* **1952**, *235*, 287-289.
(60) Miller, F. A.; Wilkins, C. H. "Infrared Spectra and Characteristic Frequencies of Inorganic Ions" *Analytical Chemistry* **1952**, *24*, 1253-1294.
(61) Adler, H. H.; Kerr, P. F. "Infrared Spectra, Symmetry, and Structure Relations of Some Carbonate Minerals" *American Mineralogist* **1963**, *48*, 839-853.
(62) Chester, R.; Elderfield, H. "The Application of Infra-red Absorption Spectroscopy to Carbonate Mineralogy" *Sedimentology* **1967**, *9*, 5-21.
(63) Adler, H. H.; Kerr, P. F. "Infrared study of aragonite and calcite" *American Mineralogist* **1962**, *47*, 700-&.
(64) Adler, H. H.; Kerr, P. F. "Infrared Absorption Frequency Trends for Anhydrous Normal Carbonates" *American Mineralogist* **1963**, *48*, 124-137.
(65) Bottcher, M. E.; Gehlken, P.-L.; Steele, D. F. "Characterization of Inorganic and Biogenic Magnesian Calcites by Fourier Transform Infrared Spectroscopy" *Solid State Ionics* **1997**, *101-103*, 1379-1385.
(66) Chester, R.; Elderfield, H. "The Infra-red Determination of Total Carbonate in Marine Carbonate Sediments" *Chemical Geology* **1966**, *1*, 277-290.
(67) Dauphin, Y. "Infrared Spectra and Elemental Composition in Recent Carbonate Skeletons: Relationships between the n2 Band Wavenumber and Sr and Mg Concentrations" *Applied Spectroscopy* **1997**, *51*, 253-258.
(68) Dauphin, Y. "Infrared Spectra and Elemental Composition in Recent Biogenic Calcites: Relationships Between the n4 Band Wavelength and Sr and Mg Concentrations" *Applied Spectroscopy* **1999**, *53*, 184-190.

(69) Herbert, T. D.; Tom, B. A.; Burnett, C. "Precise Major Component Determinations in Deep-Sea Sediments using Fourier Transform Infrared Spectroscopy" *Geochimica et Cosmochimica Acta* **1992**, *56*, 1759-1763.
(70) Mecozzi, M.; Pietrantonio, E.; Amici, M.; Romanelli, G. "Determination of Carbonate in Marine Solid Samples by FTIR-ATR Spectroscopy" *Analyst (Cambridge, United Kingdom)* **2001**, *126*, 144-146.
(71) Tatzber, M.; Stemmer, M.; Spiegel, H.; Katzlberger, C.; Haberhauer, G.; Gerzabek, M. H. "An Alternative Method to Measure Carbonate in Soils by FT-IR Spectroscopy" *Environmental Chemistry Letters* **2007**, *5*, 9-12.
(72) Sleeper, K., A. Lowrie, A. Bosman, L. Macelloni, and C. T. Swann "Bathymetric mapping and high resolution seismic profiling by AUV in MC 118 (Gulf of Mexico)." *Paper #OTC 18133 PP, paper presented at Offshore Technology Conference, Houston, TX*. **2006**.
(73) Dobbs, G. T., Georgia Institute of Technology, Atlanta, 2007.
(74) Woolsey, J. R., P. Higley, L. L. Lapham, J. P. Chanton, C. Lutken, K. Sleeper, R. Culp, S. Sharpe, and D. Ross technology., G. o. M. H. R. C. U. o. M. C. f. M. R. a. e., Ed., 2005, pp 11 pp.
(75) Lutken, C. B.; Brunner, C. A.; Lapham, L.; Chanton, J.; Rogers, R.; Sassen, R.; Dearman, J.; Lynch, L.; Kuykendall, J.; Lowrie, A. "Analyses of Core Samples from Mississippic Canyon 118" *Proceedings of the Offshore Technology Conference* **2006**, *Paper Number: 18208*.
(76) McGee, T. M.; Woolsey, J. R. "A remote station to monitor gas hydrate outcrops in the Gulf of Mexico" *Annals of the New York Academy of Sciences* **2000**, *912*, 527-532.
(77) Balsam, W. L.; Beeson, J. P. "Sea-Floor Sediment Distribution in the Gulf of Mexico" *Deep-Sea Research, Part I: Oceanographic Research Papers* **2003**, *50*, 1421-1444.
(78) Pierce, R. W.; Hart, G. F. *Phytoplankton of the Gulf of Mexico: Taxonomy of Calcareous Nannoplankton*; LSU Press: Baton Rouge, 1979.
(79) Stanley, S. M.; Ries, J. B.; Hardie, L. A. "Seawater chemistry, coccolithophore population growth, and the origin of Cretaceous chalk" *Geology* **2005**, *33*, 593-596.
(80) Aharon, P.; Graber, E. R.; Roberts, H. H. "Detection of hydrocarbon venting on the Gulf of Mexico sea-floor from determinations of delta-C-13 and DIC of the water column overlying seeps" *Aapg Bulletin-American Association of Petroleum Geologists* **1991**, *75*, 1514-1514.
(81) Vagenas, N. V.; Gatsouli, A.; Kontoyannis, C. G. "Quantitative Analysis of Synthetic Calcium Carbonate Polymorphs using FT-IR Spectroscopy" *Talanta* **2003**, *59*, 831-836.
(82) Dobbs G. T., Luzinova Y., Mizaikoff B., Vancouver, British Columbia, CANADA 2008.
(83) Falini, G.; Albeck, S.; Weiner, S.; Addadi, L. "Control of aragonite or calcite polymorphism by mollusk shell macromolecules" *Science* **1996**, *271*, 67-69.

CHAPTER 5

Infrared Spectroscopic Monitoring of Surface Effects during Gas Hydrate Formation in the Presence of Sodium Dodecyl Sulfate

The main objective of this chapter is to expand the understanding on the role of surfactants during gas hydrate formation at surfaces. Mid-infrared (MIR) evanescent field absorption spectroscopy, utilizing silver halide fiberoptic waveguides routed through a pressurized cell, was applied for studying these processes. This experimental method allowed detailed spectroscopic observations of detergent-related surface processes during sodium dodecyl sulfate (SDS) mediated gas hydrate formation. The processes involving the key molecular players—water, SDS, and propane gas—were spectroscopically monitored in close vicinity of the fiber surface, thus providing evidence for the role of SDS as a promoter of gas hydrate growth. Based on unique insights into the individual contributions of the involved molecules, a mechanism for the SDS-induced decrease of hydrate nucleation time, and the correlated promotion of hydrate formation is proposed.

5.1 MOTIVATION

Since the discovery of gas hydrates in the deep sea, and in regions with permafrost areas, significant interest has emerged related to their potential as natural gas resources [1-3]. On a molecular level, gas hydrates draw attention due to their ability to serve as high capacity gas storage medium [1, 4]. However, industrial applications involving hydrate storage processes have been limited by two major problems affecting

the potential of scaling to economically feasible levels: (1) the unfavorable kinetics of gas hydrate formation; and, (2) the low percentage of water molecules effectively converted into hydrates [1, 2].

Several studies clearly indicated that SDS is an effective promoter for reducing the induction time of hydrate nucleation and/or increasing the rate of hydrate growth after nucleation [1, 5-7]. The role of the surfactant can be related to the surface and interfacial activity of surfactant molecules, which promote gas solubilization in water and positively affect the nucleation ability at the interface [3, 8, 9]. While common understanding of surfactant effects during the hydrate formation in unstirred gas/liquid systems has progressed remarkably during the past decades, only limited direct experimental evidence is available to fully describe the role of surfactant molecules during hydrate nucleation and growth [1, 6, 10-26]. To this end, this chapter describes propane hydrate formation in the presence of SDS studied via surface sensitive MIR evanescent field absorption spectroscopy.

5.2 BACKGROUND

5.2.1 Gas hydrates

5.2.1.1 *History and significance*

Gas hydrates, also called gas clathrates, are naturally occurring solids comprised of water molecules forming a rigid lattice of cages containing a small guest molecule (e.g., CH_4, C_2H_4, C_2H_6, C_3H_8, and CO_2) [27]. Although the term clathrate is more appropriate, because it implies a non-stoichiometric gas and water composition, the term hydrate is more commonly used [28].

The initial discovery of gas hydrate structures is credited to Sir Humphrey Davy, when he demonstrated that a solid could be formed when an aqueous solution of chlorine was cooled below 9.0°C [29]. In 1823, Faraday confirmed the existence of this solid compound and suggested that its composition was approximately one part chlorine and 10 parts water [30]. Interest in clathrate hydrates over the next 120 years focused on identifying hydrate guests and corresponding compositions. In 1934, the potential of gas hydrates to block oil and gas flow lines originated research on inhibiting their growth [31]. Although hydrates are a hindrance to maintaining flow in oil and gas pipelines, various beneficial applications of clathrate hydrates have also been also explored ranging from water desalination [32] to gas storage and transportation of methane [33] and hydrogen [34, 35]. A significant novel development occurred in the 1960s when it was realized that clathrate hydrates of natural gas exist in vast quantities in the earth's crust [36-38]. Natural gas hydrates have been discovered worldwide: in arctic permafrost ~100 meters below the ice and in continental slope sediments where water depths exceed 300 meters [4] (**Figure 5.1**). Current estimates show that hydrates could contain from 10^{15} to more than 10^{17} m^3 of methane at standard temperature and pressure (STP) [39, 40]. Naturally occurring gas hydrates are of significance for three primary reasons: (1) as potential alternative energy sources; (2) as geohazards; and (3) as to their role within the global climate [27, 41-47].

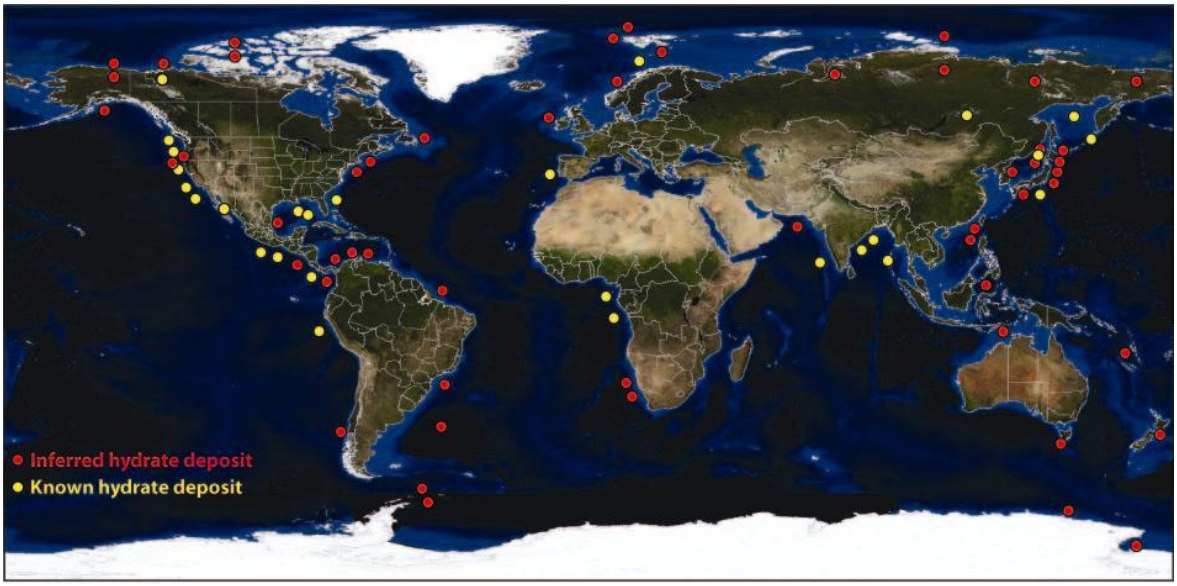

Figure 5.1: Worldwide distribution of gas hydrate deposits. Red circles are inferred, yellow circles are recovered. (Hester et al., 2009)

5.2.1.1.1 Energy

The need for energy drives much of the current natural hydrate research, and hydrate exploration programs are in progress worldwide [48, 49]. Estimates on the amount of methane stored in gas hydrates are highly speculative and widely spread [27]. Current estimates of the amount of methane carbon in gas hydrates are roughly at $10x10^{18}$ [50] and $11.4x10^{18}$ g [51]. If these estimates of reservoir sizes are correct, then the amount of methane carbon in gas hydrates is twice the carbon present in all known fossil fuel deposits (coal, oil, and natural gas) [27]. Considerable research efforts are focused on developing economically viable technologies for the extraction of gas hydrates as an alternative energy resource [41, 42, 45]. Currently, there are three principal methods of

recovering hydrates: thermal stimulation, depressurization, and inhibitor injection [27]. Western Siberia was the first permafrost region to recover methane from hydrates; however, the operations were costly and did not show sufficient progress [52]. Alaska's North Slope oil fields were found to contain hydrates, and the first attempt by the United States to tap into these hydrates was reported in April 2003 [53]. Advances have been made in recovering gas hydrates; however, a global scale on the recovery of methane from these structures is likely years if not decades away [27, 41, 42, 45].

5.2.1.1.2 Hazard

Besides being an unconventional potential source of methane, gas hydrate deposits are also significant as possible geologic hazards [27, 54]. If the temperature is increased at a fixed pressure, or the pressure decreased at a fixed temperature, or both, the hydrate deposits may become instable and dissociate. This makes hydrates a potential explosive hazard for exploration rigs, production platforms, and pipelines, especially at deep water conditions [54]. The hazards from dissociated hydrates have been evaluated in detail by Lerche and Bagirov [55].

5.2.1.1.3 Climate

The possible connections between the Earth climate and hydrates have long been of interest to geoscientists, and the debate is far from resolved today [27, 43, 44, 46, 56]. Since methane is both sequestered and released from gas hydrates depending on the pressure-temperature regime, the potential exists that methane from gas hydrates may reach the atmosphere [27]. A large release of methane from this source could have a significant effect on the global climate, past, present, and future. However, the extent of this influence has not yet been quantitatively determined even for the present climatic cycle

[27, 51], and a variety of contradictory opinions exist on this issue. For example, Nisbet suggests that the dissociation of clathrates contributed to the rapid increase in atmospheric methane at the end of the last glaciation, which accelerated the retreat of the continental ice sheets [57]. On the contrary, Paull et al. points out that clathrates are responsible for limiting the extent of glaciation [58].

5.2.1.2 *Structure*

The crystal structure of gas hydrates was largely elucidated via X-ray diffraction studies in the early 1950s [59]. Clathrate hydrate are represented in many different crystal structures [60], however, currently there are only three structures known to occur in natural environments: structure-I (sI), structure-II (sII), and structure-H (sH). sI and sII each have two cavity dimensions (small and large), whereas sH has three dimensions (small, medium, large) [61]. sI predominates in the Earth's natural environments [28].

The relationship between the guest molecule, the cage sizes, and their ratios in the lattice largely determines which structure will form, especially for simple (i.e., single guest) hydrate systems [62]. **Figure 5.2 and Table 5.1** contain the general structural characteristics for the cage units respective to each hydrate classification, as summarized by Sloan [41]. sI is a body-centered cubic crystal system that contains large $5^{12}6^2$ and small 5^{12} cages in a ratio of 3:1. These cavities may be filled with smaller gas molecules (diameter 0.4-0.55 nm) [28] such as methane, ethane, carbon dioxide, and hydrogen sulfide [56].

Hydrate sII has a diamond cubic crystal system that contains the larger $5^{12}6^4$ cages, as well as 5^{12} cages in a ratio of 1:2 [56]. Molecules exceeding the dimensions to fit in the $5^{12}6^2$ cage (diameter 0.6-0.7 nm) [28] such as propane and isobutene are examples of

sII guests. The stoichiometry for sII hydrate is approximately 24 gas : 136 H_2O. sH has a hexagonal crystal system and contains three cage types: large $5^{12}6^8$, medium $4^3 5^6 6^3$, and small 5^{12} cages in a ratio of 1:2:3 [61]. Two guests are required to form sH, where one guest stabilizes the small and medium cages, such as methane, and a larger guest (0.8-0.9 nm) stabilizes the $5^{12}6^8$ cages, such as methylcyclohexane [61].

In all three structures, there is typically only one guest molecule within each cage; however, at unusual conditions such as very high pressure multiple-cage occupancy has been observed with unusually small guests including hydrogen or noble gases. These cases are reviewed in detail by Sloan [28].

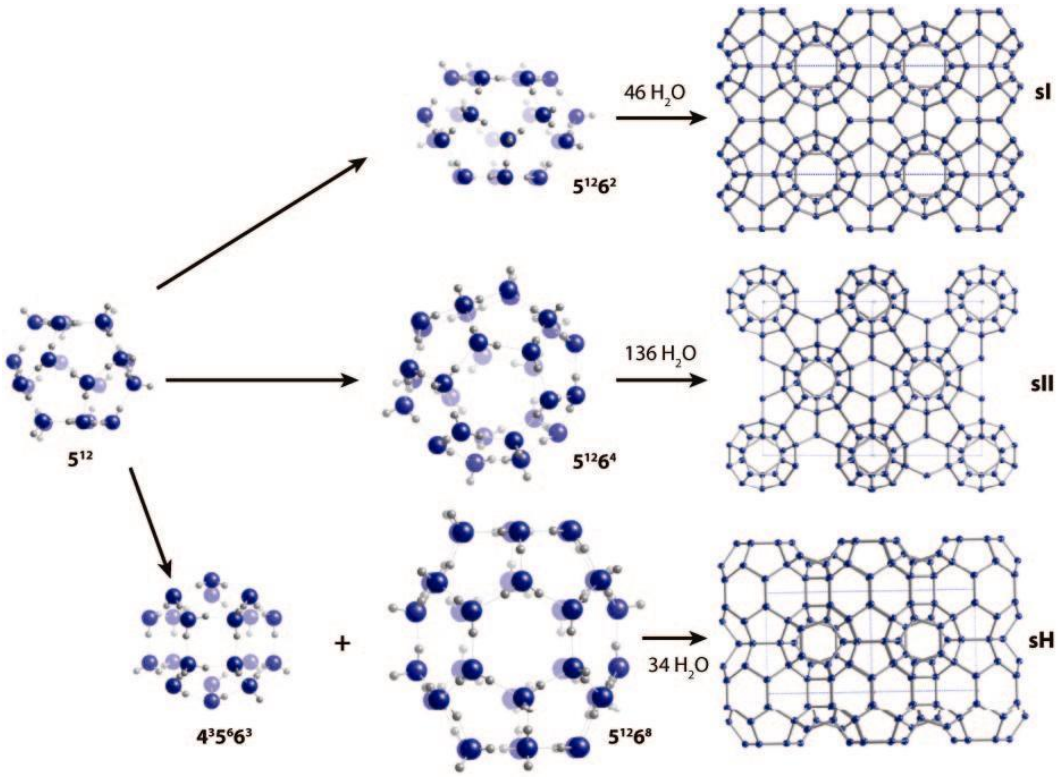

Figure 5.2: Three hydrate structures found in nature and the cage building blocks for each structure. (Hester et al., 2009)

*A widely adopted nomenclature for cage structures follows the description; n_i^{mi}, where n_i is the number of sides for face type "i" and m_i is the number of faces with n_i sides.

Table 5.1: Cage characteristics for the three known clathrate hydrate structures.

Hydrate crystal structure	**sI**		**sII**		**sH**		
Cavity	Small	Large	Small	Large	Small	Medium	Large
Description*	5^{12}	$5^{12}6^2$	5^{12}	$5^{12}6^4$	5^{12}	$4^35^66^3$	$5^{12}6^8$
Number of cavities per unit cell	2	6	16	8	3	2	1
Average cavity radius (Å)	3.95	4.33	3.91	4.73	3.91	4.06	5.71
Number of water per unit cell	46		136		34		

*A widely adopted nomenclature for cage structures follows the description; n_i^{mi}, where n_i is the number of sides for face type "i" and m_i is the number of faces with n_i sides.

5.2.1.3 *Formation*

Gas hydrates form, if small (< 0.9 nm) guest molecules contact water at ambient temperature (< 300 K) and moderate pressure (> 0.6 MPa) [28]. On a molecular scale, single small guest molecules are encapsulated by hydrogen-bonded water cavities in these non-stoichiometric hydrates [28]. Guest-molecule repulsions open different sizes of water cages, which combine to form the three well-defined unit crystals shown in **Figure 5.2**.

In the past few years, simple gas hydrates of methane, ethane, and propane have been studied in detail in our laboratory by Dobbs et al. [63, 64]. The phase equilibria of the pure gases in contact with water have been mapped out, both experimentally and computationally, by Sloan [41]. This chapter of the dissertation concentrates on propane gas hydrates grown from surfactant solutions prepared with sodium dodecyl sulfate (SDS) and deionized (DI) water. **Figure 5.3** presents a literature summary of data points

for the pressure vs. temperature phase diagram for the propane + water system with V – Vapor, L_W –Liquid water, L_{hc} –Liquid hydrocarbon, and sII-propane hydrate [65].

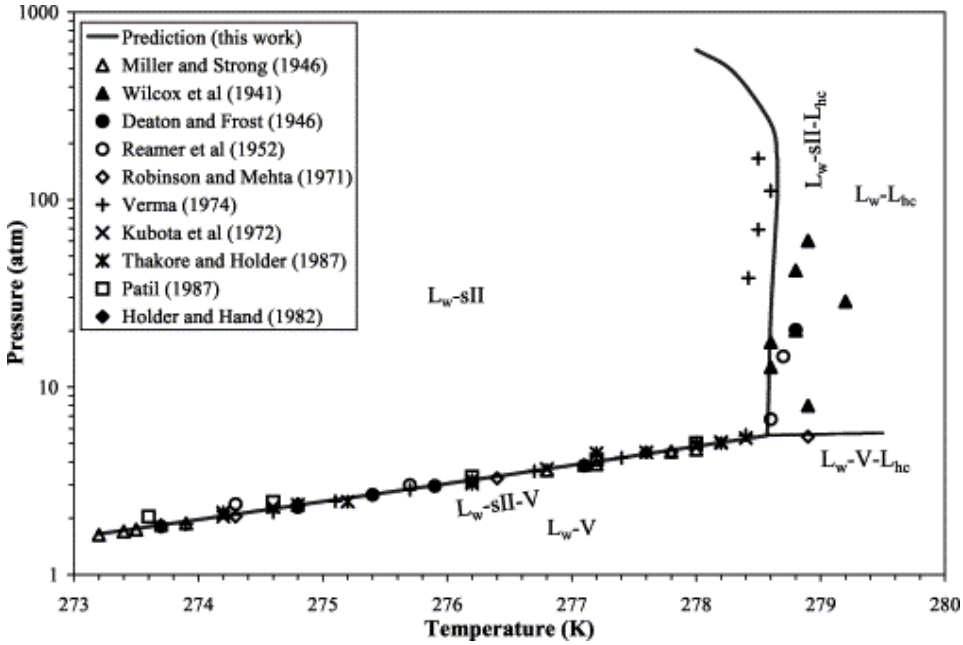

Figure 5.3: Pressure vs. temperature diagram for propane + water system. (Ballard et al., 2001)

Throughout this work, propane gas hydrates were usually grown at temperatures ranging between 0 and 4°C, as shown in **Figure 5.4.** Pressure limits were established prior to experiments to prevent liquefaction of propane gas. Temperatures were maintained below 4°C to ensure favorable hydrate growth conditions during the experiments.

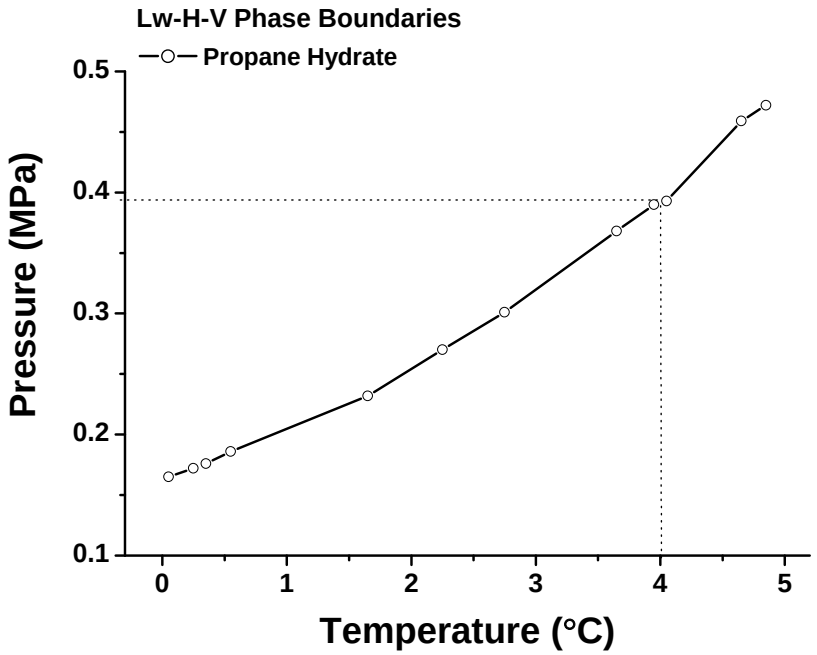

Figure 5.4: Published values for liquid water (Lw)-liquid water (H)-hydrate (V)-vapor phase boundaries respective to the simple hydrates of propane grown from deionized water. (Sloan, 1998)

5.2.2 Infrared spectroscopy of gas hydrates

Bertie and co-workers made a significant contribution to infrared (IR) studies of gas hydrates [66-69] suggesting that the strength of the hydrogen bonds in the gas hydrates is very similar to that of ice [66, 69]. Following the pioneering studies of Bertie et al., various studies were conducted utilizing IR spectroscopy in transmission-absorption configurations for the investigation of clathrate films grown from vapor deposition, and on the epitaxial growth at highly reflective surfaces in vacuum chambers [41, 67, 69-74]. Beyond this work, IR has not yet been a widely adopted technique for hydrate studies,

which likely results from the strong IR absorption of liquid water encountered during conventional transmission-absorption measurements [41, 67, 69-74].

Recently, methods based on attenuated total reflection (ATR) IR spectroscopy have been developed to analyze gas hydrates [63, 75-79]. These studies demonstrated the potential of IR-ATR spectroscopy as a straightforward and valuable analytical tool for investigating clathrate hydrates in-situ at appropriate temperatures and pressures [63, 75-79]. In the study by Oyama et al., the capability of the ATR technique to spectroscopically study gas hydrates was demonstrated for the first time [78]. IR-ATR was used to compare the spectral profiles of CO_2(gas) and CO_2(aqueous) with that of CO_2(hydrate) for simple sI CO_2 hydrates grown from an aqueous solution [78]. In 2004, Zhang and Ewing reported a detailed analysis of IR-ATR spectra for sI SO_2 clathrate [79].

Using IR spectroscopy, Prasad et al. studied the formation of CO_2 clathrates, both sI and sII structures, in naturally occurring minerals, thereby additionally demonstrating the metastable nature of sII CO2 hydrate [80]. In 2008, Dartois and Deboffle analyzed methane hydrate crystal by IR spectroscopy, and specifically focused at the ν_3 asymmetric CH-stretching mode of the entrapped methane molecule in water cages, thereby providing an infrared spectroscopic identification for astrophysically relevant methane clathrate hydrates [75]. In the following year, a brief note was published on the dissociation behavior of methane gas hydrates in sediments, as investigated by ATR-IR spectroscopy [76].

The latest findings were reported by Kumar et al., where the cage occupancies of CO_2, CO_2/H_2 and $CO_2/H_2/C_3H_8$ hydrates were determined on the basis of the peak area ratios of the CO_2 asymmetric stretch vibrations in the small and large cages obtained

from the FTIR spectra, and the hydrate phase composition obtained from gas chromatography [77]. Additionally, as previously mentioned our research group has shown MIR evanescent field spectroscopic investigations on the nucleation, growth, and dissociation of simple gas hydrates, as shown by Dobbs et al. [63, 64]

5.2.3 Gas hydrates growth in the presence of surfactant

Numerous studies have been performed to determine how the addition of surfactant to liquid water affects the hydrate nucleation and formation [1, 6, 10-26]. Several of these studies have indicated that certain surfactants promote hydrate nucleation, and thus, accelerate hydrate growth [1, 5, 16, 20]. Among the surfactants investigated, sodium dodecyl sulfate (SDS) **(Figure 5.5)** was found to be among the most effective molecules for reducing the induction time for hydrate nucleation and/or increasing the rate of hydrate growth after nucleation [1, 4-6].

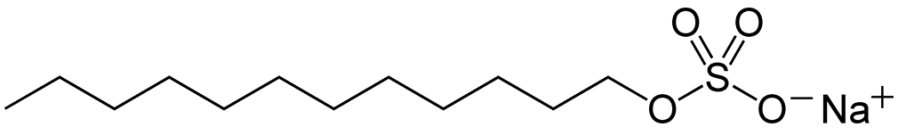

Figure 5.5: Molecular structure of sodium dodecyl sulfate.

Melnikov and co-workers were the first to observe propane hydrate formation in a chamber partially charged with water containing SDS [16, 17]. In the presence of SDS, hydrate crystals were no longer formed as a dense film at the horizontal gas/liquid interface, but migrated toward the vertical walls of the pressure vessel. Upward growing

porous layers were evident with the pores containing a liquid solution introduced by capillary forces, thereby maintaining the gas/water contact within the confines of the hydrate layers. Therefore, it was proposed that the nucleation and growth of hydrate originates at the water/solid interface via a mechanism driven by capillary effects. This hypothesis of a capillarity-driven hydrate-formation mechanism was later supported by Watanbe et al., Gayet et al., and Otukani et al.[13, 24, 26]

Zhong and Rogers also reported a significant decrease in hydrate nucleation times upon addition of SDS, and suggested the utility of surfactants in facilitating the high-rate production of natural gas hydrates, which may be stored or transported as fuel gas stocks [1]. It was experimentally shown that, at a concentration of 242 ppm SDS, a significant change in hydrate induction time occurs, which was defined as the critical micelle concentration (CMC). If the surfactant exceeds a concentration of 242 ppm in solution, hydrates develop extremely fast in a quiescent system [1]. It is noteworthy that following these experiments the authors have proposed that the CMC at the hydrate forming conditions occurs significantly below the accepted CMC for SDS at STP (approximately 2300-2700 ppm) [81, 82]. Based on these results, surfactant micelle formation mechanisms were proposed where the micelles are hypothesized to play a major role in the hydrate nucleation and formation [1, 83]. SDS micelles containing gas molecules may adsorb at the surface and displace already structured water clusters [84], which in turn promotes and accelerates hydrate formation [41].

Independent experiments by Sun et al. and Han et al. appear to support the proposed hypothesis of surfactant micelle formation mechanisms [14, 85]. Indeed, Sun et al. have measured the surface tension of SDS solutions in contact with methane at methane

hydrate forming conditions, and have determined the CMC for SDS to be 500 ppm [85]. Han et al. have proposed that the CMC for SDS is reached at a concentration of 300 ppm by observing the maximum gas content increase and the leveling off during gas hydrate formation [14].

However, the surfactant micelle formation mechanism has been disputed by Di Profio et al., Watanabe et al., and Zhang et al. [6, 10, 11, 13, 15, 26] Specifically, based on electrical conductivity measurements it was reported that there was no indication of micelle formation for the relevant SDS concentrations at hydrate formation conditions [11]. Watanabe et al. suggested that SDS forms a hydrated solid in lieu of micelles for concentrations exceeding the CMC under hydrate formation conditions, since the temperature during hydrate formation is below the Krafft point at which the solubility of the surfactant is equal to the CMC [10, 24-26]. This conclusion was supported by Zhang et al., who demonstrated that at methane hydrate formation conditions the Krafft point of SDS does not shift from the Krafft point at atmospheric pressure [15]. In a separate paper, the authors have investigated the relationship between tetrahydrofuran (THF) hydrate induction and SDS adsorption at the hydrate/liquid interface. The adsorption behavior was studied with ξ-potential measurements and pyrene fluorescence measurements, thus providing evidence that the reduced induction time may result from the adsorption of DS^- (dodecyl sulfate) at the hydrate/liquid interface [86, 87].

It is necessary to highlight that the concentration profiles of SDS and hydrate-forming gas during hydrate nucleation, growth, and dissociation in the vicinity of surfaces (as described in this chapter) have not been reported to date. Yet, elucidating these surface effects may provide a significant step forward e.g., for hydrate-based

industrial applications, as a detailed understanding of these processes enables deliberately optimizing hydrate formation conditions, particle packing, and gas storage capacity at larger scales.

5.3 INTRODUCTION

The present chapter provides direct spectroscopic evidence on the role of SDS during gas hydrate formation at surfaces utilizing in-situ MIR evanescent field absorption techniques via a silver halide fiberoptic waveguide routed through a custom designed pressure cell [63]. Pioneering experimental evidence is provided that detergents—here, SDS—facilitate the transport of gas molecules to the solid/liquid interface where gas hydrate nucleates. As a result, a mechanism is proposed describing the role of SDS in decreasing hydrate nucleation times, and in promoting hydrate formation, based on direct spectroscopic evidence on the importance of interactions among surface-induced structured water assemblies, propane gas molecules, and SDS.

5.4 MATERIALS AND METHODS

5.4.1 Reagents

Aqueous solutions of 380 ± 2 ppm (mg/L) of SDS (Sigma-Aldrich, Reagent Grade, St. Louis, MO) prepared with deionized (DI) water (R=18.2 MΩ·cm at 25°C) without additives to further facilitate hydrate growth. Propane gas (Instrument Grade, >99.5%) purchased from Air Gas (Decatur, GA) was used for clathrate formation.

5.4.2 Gas hydrate pressure vessel

In this study, a 304 stainless steel (SS) vessel developed by our research team with a sample volume of approximately 500 mL was used to facilitate hydrate formation conditions and IR spectroscopic access [63, 64, 88], as shown in **Figure 5.6**. Primary cooling of the sample volume was achieved by continuously flowing a thermo-regulated solution (50/50 water/ethylene glycol) through a 304 SS tube tightly wrapped in a 1" cooling coil at a flow rate of approximately 85 mL/min. The internal cooling coil provided nine continuous loops with 1.5" of effective coil length inside the pressure vessel. A custom high-pressure optical viewport (0.75" effective viewing diameter) provided access for visual inspection of the sample during hydrate formation and measurements. An imaging system, consisting of an Intel PC Camera (Model CS110, Intel Corporation, Santa Clara, CA) with a universal serial bus (USB) interface enabled image capture and viewing during hydrate growth inside the vessel chamber, and was correlated with the IR spectra acquisition [89].

The internal temperature of the pressure vessel was monitored using a Model THX-400-NPT-72 1/4" MNPT pipe-plug thermistor probe with a 2252 ohm resistance at 25°C (Omega Engineering Inc., Stamford, CT). Pressure monitoring of the sample volume was facilitated by a Sensor System Solutions, Inc. (3S, Inc., Irvine, CA) Model 5100 amplified media isolated silicon pressure transducer (Part No. 5100-B2-1000-A-P1) suitable for operation at harsh conditions up to pressures of 1000 psi (6.9 MPa).

For spectroscopic access probing a cross-section of the hydrate formation chamber, a fiber coupling system with custom-made PTFE ferrules and Swagelok components (Swagelok, Solon, OH) was developed, suitable for sealing and routing a

300 mm long core-only silver halide (AgX, X = $Cl_{0.3-0.4}Br_{0.7-0.6}$) fiber with a diameter of 700 µm through the liquid phase contained within the pressure vessel. The optical setup for in-situ spectroscopic monitoring of gas hydrate formation and dissociation was coupled to a Bruker IFS/66 Fourier transform infrared (FT-IR) spectrometer (Bruker Optics Inc., Billerica, MA). Radiation modulated by the interferometer was guided outside of the spectrometer and focused onto a polished in-coupling facet of a 700 µm diameter core-only AgX fiberoptic waveguide via an off-axis parabolic mirror with a 2-in. focal length. IR radiation was propagated via total internal reflection along the AgX fiber, and routed through the hydrate chamber, thus creating an evanescent field along the fiber surface due to the refractive index contrast with the surrounding medium (approximately 2.1 for the AgX fiber and 1.36 for the aqueous sample matrix). The emanating divergent cone of IR radiation was collimated at the distal end of the fiber with another 2-in. focal length off-axis parabolic mirror, and then focused onto a Stirling-cooled mercury-cadmium-telluride (MCT) detector (Model K508, Infrared Associates, Stuart, FL) using another 2-in. focal length off-axis paraboloid. The detected signal was processed via an impedance-matched MCT-1000 preamplifier (Infrared Associates, Stuart, FL), and connected to an external input channel of the FT-IR spectrometer. A polycarbonate box was constructed around the entire hydrate setup to enable purging the optical path with compressed dry air to stabilize the atmospheric humidity and CO_2 within the open path of the IR radiation.

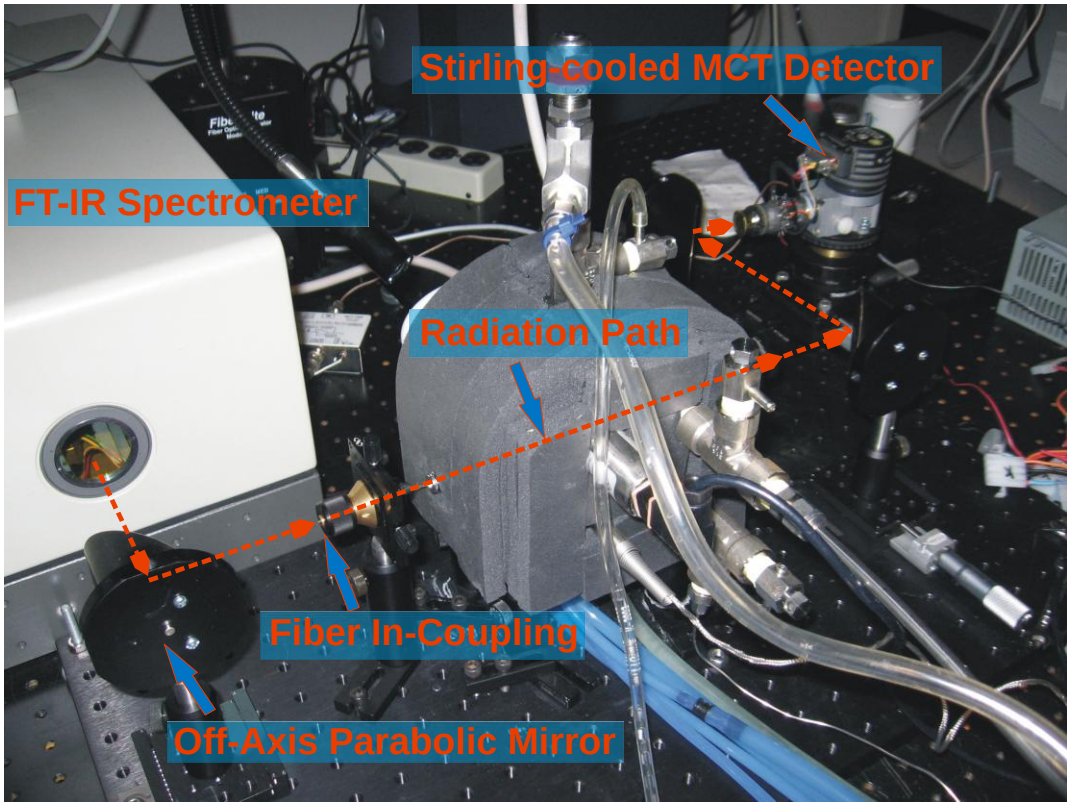

Figure 5.6: Optical image describing the setup utilized for MIR fiberoptic spectroscopic studies monitoring propane gas hydrate growth and dissociation. The silver halide fiber probes a cross-section of the pressure vessel via evanescent field absorption spectroscopy. The dashed line indicates the radiation path**.**

5.4.3 Gas hydrate formation and IR spectra acquisition

Prior to any experiment, the pressure chamber was purged with plentiful amounts of propane gas. Then, the polycarbonate box around the hydrate setup was purged with compressed dry air until stable atmospheric conditions (humidity and CO_2) were achieved, as determined via continuously recorded IR spectra. After stabilization, a

reference spectrum was collected (averaging 250 spectra at a spectral resolution of 0.5 cm^{-1}). Next, continuous spectroscopic measurements (averaging 250 spectra with resolution of 0.5 $cm^{-1)}$ were started, and the pressure vessel was filled with approximately 315 mL of aqueous solution containing 380 ppm of SDS, submerging the internal cooling coil, as well as the AgX fiber routed through the liquid sample. The chamber was then pressurized with propane gas followed by initiation of the cooling process. Pressure and temperature data were continuously logged throughout the entire measurement series, and correlated with the recorded IR spectra. Hydrate dissociation was typically initiated by reducing the chamber pressure below the liquid/solid hydrate phase boundary determined by the system temperature and the respective hydrocarbon gas.

5.4.5 Water ice formation procedure

Water ice formation experiments were performed using the same experimental procedure described for propane gas hydrate with two exceptions: (i) ice formation was initiated by lowering the temperature in absence of guest propane gas, and (ii) ice dissociation was initiated by raising the vessel temperature rather than changing the vessel pressure

5.4.6 Evanescent field penetration depth

The depth at which the evanescent field probes into the adjacent sample is dependent on the optical parameters summarized in Equation 1 [90]. The focus of the present study was to closely monitor molecular events in the spectral region of 3000-

2800 cm^{-1}. The penetration depth of the evanescent field (d_p) for this spectral region was calculated at 278-298 nm using

$$d_p = \frac{\lambda}{2\pi\sqrt{n_1^2 \sin^2\theta - n_2^2}}, \qquad \text{Equation 5.1}$$

where θ is the incident angle of radiation normal to the reflection interface (45 deg), n_1 is the refractive index of the silver halide fiber (2.1), n_2 is the refractive index of the sample solution (1.36) surrounding the silver halide fiber, and λ is the wavelength of the radiation propagated through the waveguide (3000-2800 cm^{-1}). Hence, in this study, the term "vicinity of the fiber surface" describes an analytical volume extending approximately 300 nm from the waveguide surface into the adjacent liquid or solid sample medium.

5.4.7 Non-spectroscopic evaluation of gas hydrates growth

During the present studies, alternative tools complementary to IR spectroscopy were applied for determining hydrate nucleation times, growth, and dissociation for additional verification. Conventional indicators for the nucleation of gas hydrates grown from aqueous solution include visual observation, and pressure and temperature changes [63, 64]. The nucleation of gas hydrate in a closed non-isobaric system is generally accompanied by a rapid decrease in system pressure from the incorporation of dissolved gas into the hydrate structures [41]. Also, an increase or irregular fluctuation of the solution temperature is usually observed resulting from the latent heat of hydrate formation during the phase transition of liquid water to ice [41]. Pressure and temperature recordings

obtained during the formation of propane hydrate with SDS indicating abrupt changes in the data streams of temperature and pressure, which are characteristic of hydrate nucleation and growth, are shown in **Figure 5.7**.

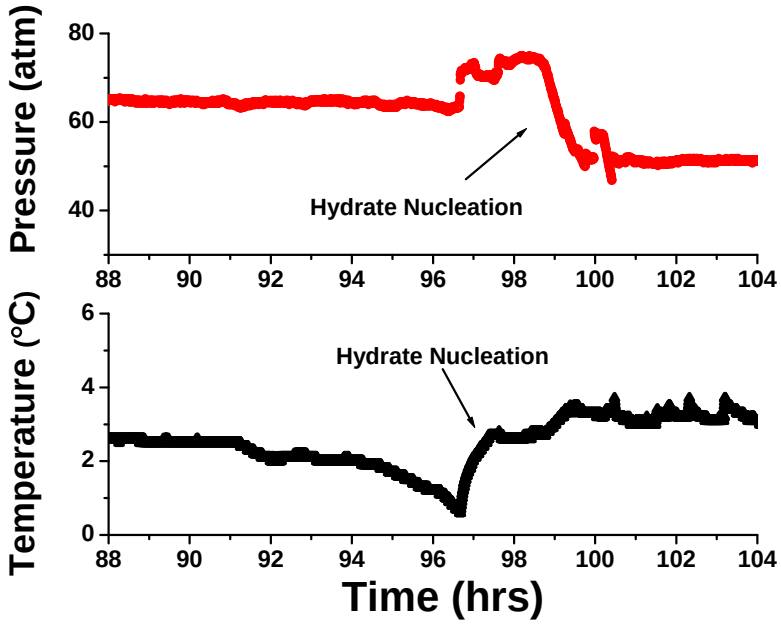

Figure 5.7: Pressure and temperature traces recorded during propane hydrate formation with SDS indicating a rapid drop in pressure and increase in temperature at hydrate nucleation. The pressure increase at ~96-97 hrs reflects the intermittent introduction of propane into the sample chamber. Temperature spikes are resulting from localized hydrate growth in close proximity to the submersed temperature probe as opposed to bulk solution temperature changes.

In addition, an optical viewport provided access for visual inspection of the processes occurring inside the sample chamber during hydrate measurements. An imaging system consisting of a PC-operated video camera enabled image capture and continuous viewing inside the hydrate growth chamber. **Figure 5.8** shows selected images captured during pre-nucleation, nucleation, growth, and dissociation of propane hydrate. Hence, correlation between spectroscopic data, changes in pressure and temperature, and visual observations provide sufficient evidence of hydrate nucleation, growth, and dissociation, thereby establishing a laboratory-based observatory system essential for studies of gas hydrate formation.

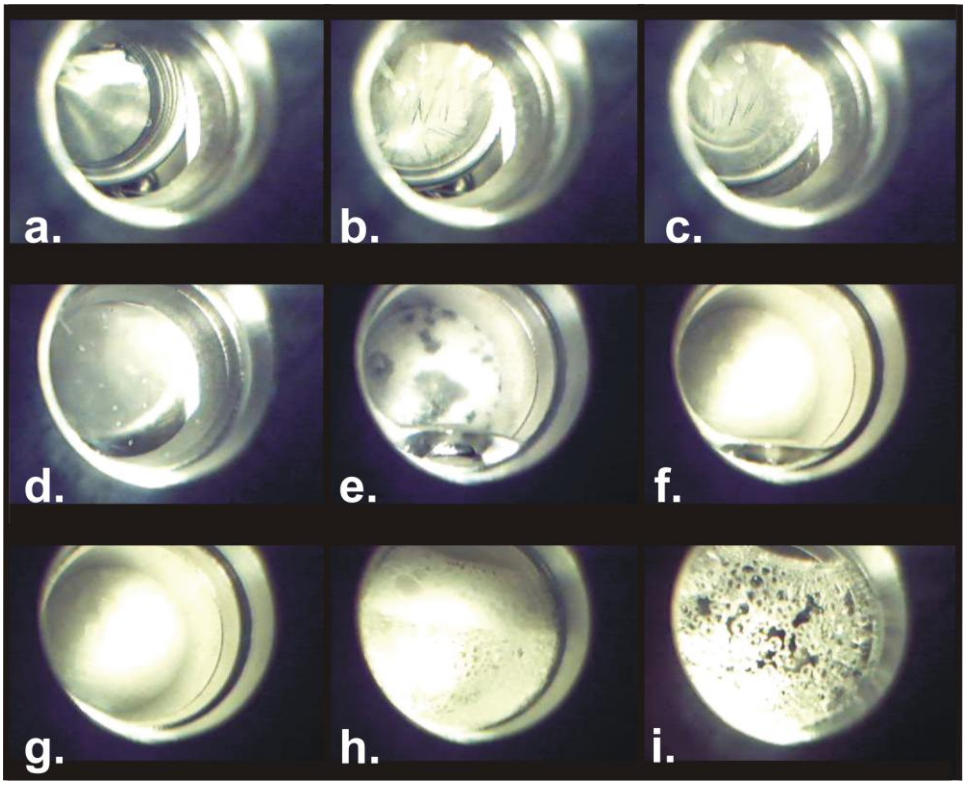

Figure 5.8: Image series depicting the sample chamber contents throughout propane hydrate growth with SDS. An optical image of liquid water (a.) is followed by hydrate nucleation (b.) and growth (c. – f). The final image series shows solid hydrate (g.), and pressure induced dissociation with the formation of surfactant foam (h.) until returning to the initial conditions with gas bubbles attached to the sapphire window of the viewport (i.).

5.4.8 IR spectra acquisition without a pressure vessel

Neat SDS and propane gas spectra were recorded using a Bruker Equinox 55 Fourier transform infrared spectrometer (Bruker Optics Inc., Billerica, MA). The spectrometer was equipped with a liquid nitrogen cooled mercury-cadmium-telluride (MCT) detector (Infrared Associates, Stuart, FL), and an in-compartment horizontal attenuated total reflection (ATR) unit (Gateway, Specac Inc., Woodstock, GA) equipped with a trough top plate and a trapezoidal ZnSe ATR crystal (n_D = 2.43 at λ = 5 µm, MacroOptica, Moscow, Russia) providing six internal reflections.

Aliquots of 1 mL solution containing 3.2 g/L of SDS in DI were deposited at the ZnSe crystal surface, and IR spectra were continuously recorded until the water phase evaporated. Propane gas spectra was obtained by placing a portion of the propane gas hydrate sample retrieved from the pressure vessel within the internal sample compartment of the FT-IR spectrometer for open-path IR transmission-absorption spectroscopic evaluation of the outgassing constituents during dissociation. All IR spectra represent the average of 100 spectra recorded at a spectral resolution of 2 cm^{-1} while the instrument—with exception of the sample compartment—was purged with dry air.

5.4.8 Data evaluation

The obtained IR spectra were analyzed by evaluating the height of a characteristic peak maximum, or via the peak area (PA) integration of selected absorption features using the Bruker OPUS software package (Bruker Optics Inc., Billerica, MA). Peak

height evaluation was performed at symmetric absorption features, using a Lorentzian local least squares minimization curve fitting function.

5.5 RESULTS AND DISCUSSION

5.5.1 IR monitoring of gas hydrate formation

In the present study, gas hydrates were formed from DI water containing 380 ppm of SDS in a customized pressure cell, enabling spectroscopic monitoring, as shown in **Figure 5.6**. The SDS concentration was selected based upon studies by Zhong and Rogers [91], which demonstrated that ethane hydrate induction times significantly decreased at concentrations exceeding 242 ppm. During these experiments, it was observed that SDS indeed accelerated nucleation during hydrate formation and that, after nucleation, the hydrate grew at comparable rates at the walls of the pressure vessel, at the surface of the cooling coil, and at the surface of the silver halide (AgX) waveguide. Therefore, it is assumed that interactions of constituents at and with the silver halide fiber surface—and possibly photo reduced silver Ag^0 in part present at this interface—lead to comparable effects observed for the stainless steel surfaces exposed during these experiments, i.e., the walls of the pressure vessel and the cooling coil.

There are three major molecular components involved in the hydrate forming system studied here: water, propane, and SDS. Using fiberoptic IR evanescent field absorption spectroscopy, processes involving the presence and transformation of these molecular constituents in close vicinity to the fiber surface were monitored. Given the optical conditions in this study, an exponentially decaying evanescent field comprising an

analytical volume extending approximately 300 nm from the waveguide surface into the adjacent liquid or solid sample medium generates the analytical signal.

5.5.1.1 *Monitoring of water*

The process of water transitioning from the liquid phase to the solid (gas hydrate) state is observable by significant changes of four primary IR absorption features of water (**Figure 5.9**):

(i) the intense and broad absorption feature (3750–2750 cm^{-1}) related to the O-H stretch (ν_{OH}) shifts to the red by approx. 120 cm^{-1} [92] ;

(ii) the lowest intensity absorption feature (2375–1875 cm^{-1}) comprising the 3rd libration overtone ($3\nu_L$) shifts to the blue [92-99];

(iii) the frustrated rotation feature (< 1000 cm^{-1}) also known as the libration mode (ν_L) shifts to the blue [92-99];

(iv) the strongly absorbing H-O-H bending mode (ν_2) (1750–1500 cm^{-1}) decreases in intensity [92].

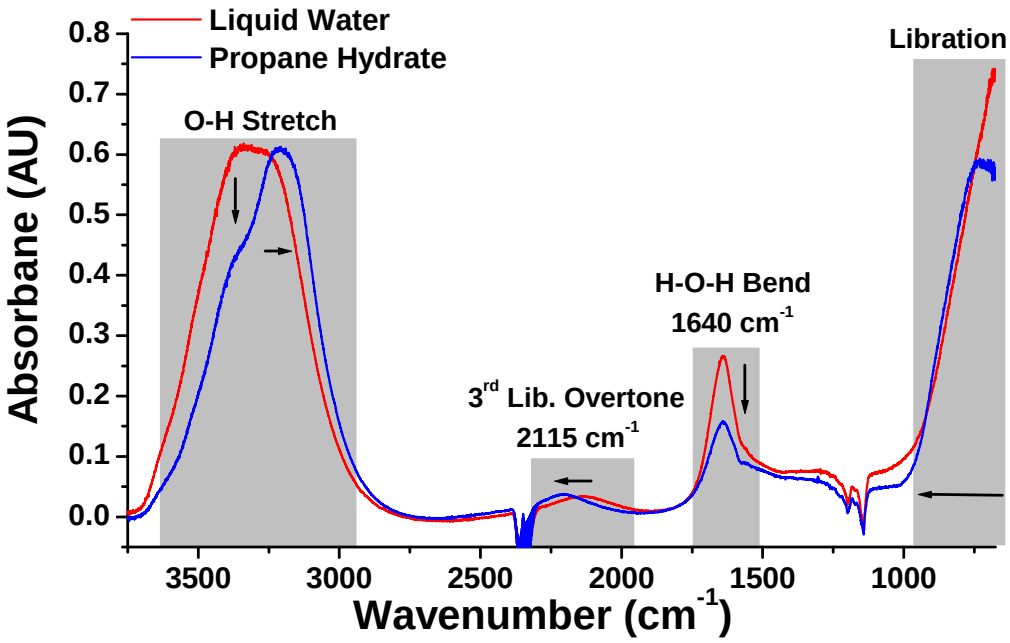

Figure 5.9: Fiberoptic IR-ATR spectra for liquid water and propane hydrate with labeled absorption features for water and indication of the spectral changes during the formation of gas hydrate.

In this chapter, IR data collected throughout hydrate nucleation, growth, and dissociation was evaluated by combining the intensity-independent evaluation of $3\nu_L$ with the inversely related amplitude responses associated with the respective ν_2 feature [63]. A detailed description of monitoring IR features as water converts to gas hydrate has previously been described in detail by Dobbs [63, 64].

5.5.1.2 *Monitoring of propane and SDS*

During the propane gas hydrate formation experiment in the presence of SDS, IR spectra were continuously collected, thereby monitoring hydrate nucleation, growth, and

dissociation. Upon hydrate nucleation, the recorded IR spectra revealed the appearance and rapid increase in intensity of five absorbance peaks in the spectral regime of 3000-2800 cm^{-1} corresponding to the CH stretching region (2964, 2938, 2918, 2875, and 2850 cm^{-1}), as illustrated in **Figure 5.10**. Since the only molecules containing CH groups within the studied system are SDS and propane gas, the observed absorbance peaks must be associated with concentration changes of SDS and/or propane gas within the exponentially decaying evanescent field propagating along the surface of silver halide fiber serving as the ATR waveguide**.** Thus, two control experiments were conducted to determine which absorptions peaks are associated with propane gas, and which associate with SDS molecules.

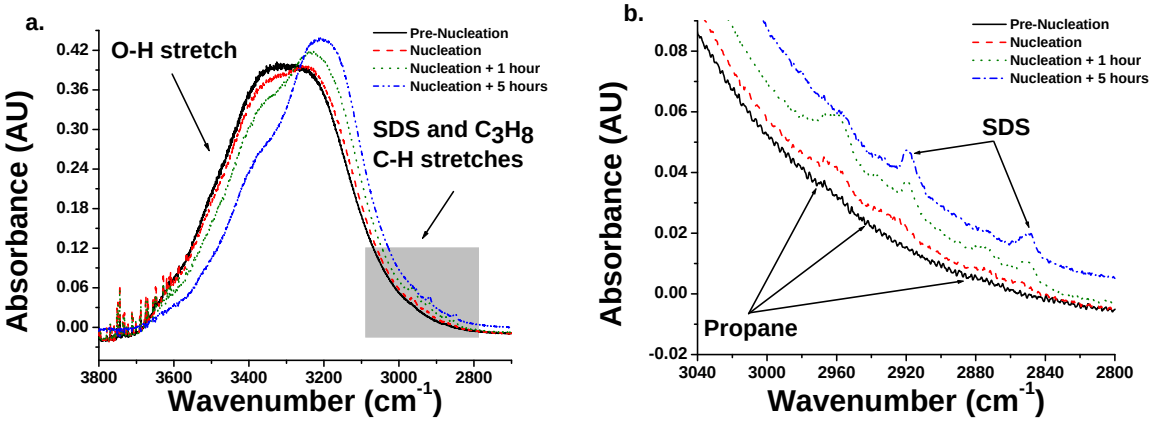

Figure 5.10: (a.) MIR evanescent field spectra displaying spectral changes of water during propane hydrate formation revealing the appearance of SDS and propane absorption features upon hydrate nucleation, (b.) enlarged C-H stretch region.

5.5.1.2.1 Control experiment #1 - offline IR spectra acquisition

To determine which absorptions peaks are associated with propane gas upon completion of a propane gas hydrate experiment, a small portion of solid hydrate was removed from the pressure chamber and spectroscopically analyzed. As the solid gas hydrate sample was melting/outgassing, IR spectra were continuously collected, and unambiguously identified as propane gas. In addition, the IR spectra of 3.2 g/L SDS in DI water were recorded to verify the position of the characteristic absorbance peaks of SDS. The collected propane gas and SDS spectra are overlaid in **Figure 5.11a** confirming that the absorbance feature at 2964 cm^{-1} (νCH-band) corresponds to propane gas, while SDS gives rise to the absorbance signatures at 2850 and 2918 cm^{-1} (symmetric (ν_sCH), and asymmetric (ν_{as}CH) $-CH_2$ stretching and deformation bands, respectively). However, due to a significant overlap of SDS and propane gas absorption features in the spectral region of 2960-2860 cm^{-1}, no firm association of the peaks at 2938 and 2875 cm^{-1} may be established.

5.2.1.2.2 Control experiment #2 - ice formation

Further validation of propane gas and SDS peak positions may be derived from IR comparison studies of propane hydrate and pure water ice formation—both in the presence of SDS, as shown in **Figure 5.11b**. During the spectroscopic studies of pure water ice formation, no propane gas is present within the system; therefore, if any absorbance peaks are observed within the CH spectral region, they have to be associated with SDS. Water ice formation studies were conducted using the same experimental protocol as for gas hydrate studies (see water ice formation procedure in "materials and methods" section). The IR spectra continuously collected during water ice nucleation

and formation revealed a rapid increase of absorbance intensity for two peaks (2850 and 2918 cm^{-1}) upon ice nucleation, thereby confirming that these peaks are associated with SDS molecules. The other three peaks (2938, 2964, and 2875 cm^{-1}) are absent in these spectra. As the latter signatures are only present during propane gas hydrate experiments, they are associated with an increase in the concentration of propane gas along the surface of the silver halide fiber. Two control experiments confirmed that the absorbance features at 2938, 2964, and 2875 cm^{-1} (νCH-band) [100, 101] correspond to propane gas, while SDS gives rise to the absorbance signatures at 2850 and 2918 cm^{-1} (symmetric (ν_sCH), and asymmetric (ν_{as}CH) $-CH_2$ stretching and deformation bands, respectively)[101, 102, 103]. With the CH stretching features unambiguously assigned to SDS and propane, it was possible to closely monitor the behavior of SDS and propane gas in the vicinity of the waveguide surface during the progression of the gas hydrate growth.

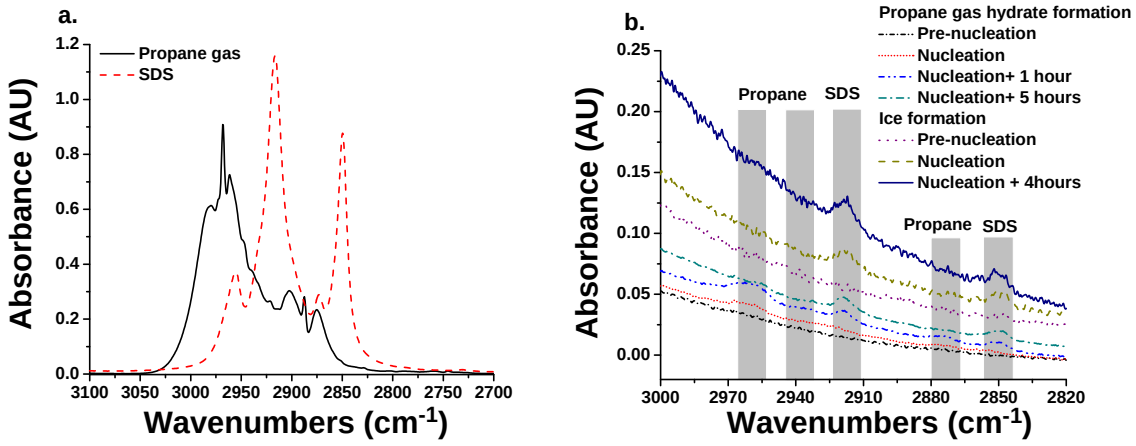

Figure 5.11: (a.) IR-ATR spectra of propane gas and SDS, (b.) MIR evanescent field spectra displaying spectral changes of water during propane hydrate and water ice formation revealing the appearance of SDS and propane absorption features upon hydrate nucleation, and the appearance of only SDS signatures upon water ice nucleation.

5.5.2 Propane hydrate formation in the presence of SDS

After an entire propane gas hydrate experiment lasting approximately 13 days, IR spectra collected throughout the study were evaluated by maximum peak height analysis for the 3rd libration overtone ($3\nu_L$) at 2210 cm^{-1}, and by peak area (PA) integration analysis for the H-O-H bending mode (ν_2) at 1640 cm^{-1}. Furthermore, peak area integration analysis of the symmetric ν_sCH band at 2850 cm^{-1} associated with SDS, and of the νCH-band at 2964 cm^{-1} associated with propane gas were performed to unambiguously monitor any increase or decrease in concentration of these species during hydrate formation, growth, and dissociation at the waveguide surface.

5.5.2.1 *H-O-H bending mode (ν_2)*

PA integration (in the spectral range of 1791-1573.2 cm^{-1}) was applied for evaluating the phase-related (liquid vs. solid) amplitude changes of ν_2 throughout gas hydrate formation and dissociation, as shown in **Figure 5.12a**. An initial increase in PA at 19 hrs is observed, which results from the system pressurization. Furthermore, occasional spikes in PA were later determined to be contributions from fluctuations in ambient humidity, relative to the humidity present during collection of the initial reference spectrum, given the duration of the conducted experiments. Hydrate nucleation (which was simultaneously confirmed by non-spectroscopic parameters, including *in-situ* recorded temperature and pressure traces, as well as visual inspection (**Figures 5.7 and 5.8**)) is evident by a sharp decrease in PA at approximately 97 hrs after starting the data collection. Following hydrate nucleation, a gradual decrease in PA is observed until approximately 110 hrs, which indicates that hydrate formation in proximity to the fiber

surface is completed. At 241 hrs, dissociation of the formed gas hydrate was induced by a pressure change, and monitored by an increase in PA (ν_2 intensity increases) with progression of the dissociation process. The decrease in PA at around 250 hrs resulted from a segment of solid gas hydrate impacting at the fiber surface, which was determined by analyzing the images captured simultaneously via the pressure cell viewport. Hydrate dissociation was completed after approx. 262 hrs without any spectroscopically or visually detectable solid gas hydrate remaining in the pressure chamber.

5.5.2.2 *3rd libration overtone ($3\nu_L$)*

Evaluation of the $3\nu_L$ overtone feature at approx. 2210 cm^{-1} was performed by monitoring the shift of the peak maximum position throughout the hydrate formation and dissociation process. The temperature dependence of the $3\nu_L$ peak maximum is readily observed during the first 75 hrs of the study, while the temperature was decreased to reach hydrate formation conditions**.** A strong blue shift of approximately 100 cm^{-1} associated with water transitioning from the initial liquid phase to the solid state (propane gas hydrate) was observed following the peak maximum of $3\nu_L$ in the period from 97 to 110 hrs. Reversibility of this shift in peak position was observed following the pressure-induced dissociation of gas hydrate starting at 241 hrs until completion of the hydrate dissociation at 262 hrs.

5.5.2.3 *C-H stretch of SDS and propane*

For studying the role of SDS and propane during gas hydrate formation, the SDS peak at 2850 cm^{-1}, and the propane gas peak at 2964 cm^{-1} were evaluated by peak area

integration of the spectral regions 2861.5-2846.5 cm^{-1} and 2973.9-2947.5 cm^{-1}, respectively, as shown in **Figure 5.12a**. A substantial increase in PA of the SDS and propane gas peaks was observed 97 hrs after starting the data collection, which corresponds to the nucleation of gas hydrate following the data evaluation of the ν_2 and $3\nu_L$ peaks associated with water. Lasting for approximately 5 hrs, the PA of the propane peak was gradually decreasing, which indicates that the concentration of propane gas in the proximity of the waveguide surface has continuously been reduced to an undetectable level. In contrast, the PA of the SDS peak—and thus, the concentration of SDS within the evanescent field emanating from the waveguide surface—remained constant throughout gas hydrate growth. Upon initiation of the gas hydrate dissociation, the PA of the SDS peak decreased to an undetectable level once the gas hydrate dissociation was completed. Again, the brief increase in PA of SDS and propane gas at approximately 250 hrs is attributed to the segment of solid gas hydrate impacting the fiber.

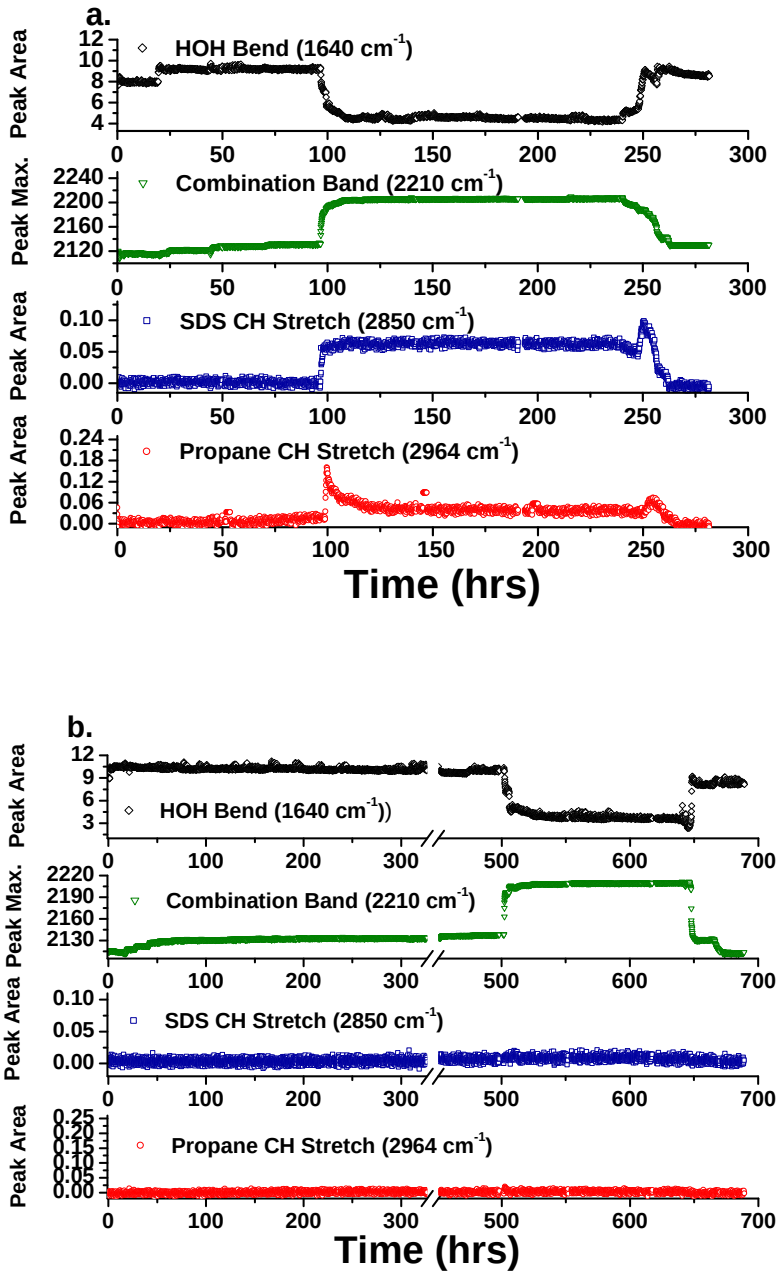

Figure 5.12: Analysis of fiberoptic evanescent field spectra evaluating the H-O-H and combination bands characteristic for water during propane hydrate growth from DI water (a) with SDS, and (b) in absence of SDS. (The data gap in (b) is resulting from an instrument down-time.)

5.5.3 Propane hydrate formation in the absence of SDS

Over periods of approximately 30 days, propane hydrate formation studies in the absence of SDS were performed using the same experimental protocol as for the propane gas hydrate studies involving SDS; the IR spectra collected during propane hydrate nucleation, growth, and dissociation were analyzed using the same data evaluation protocols. During these control experiments, significant differences in the IR spectra were observed, compared to gas hydrate formation experiments involving SDS, as shown in **Figure 5.12b**. The collected IR spectra did not provide any evidence for absorbance peaks in the spectral region 3000-2800 cm^{-1} where propane gas signatures should occur. Evaluation of the $3\nu_L$ overtone vibration along with the ν_2 feature revealed that hydrate nucleation occurred approximately 500 hrs after starting the data collection, as evident in **Figure 12b**. During these experiments, the pressure-induced hydrate dissociation was initiated at 650 hrs. To confirm the visual observation, the spectral region characteristic for the CH features was evaluated by peak integration analysis. As evident in **Figure 5.12b**, no PA increase for the CH region was observable during gas hydrate formation in the absence of SDS. As discussed in detail below, these findings substantiate the potential role of SDS as a propane gas carrier during the formation of gas hydrates.

5.5.4 Unraveling the role of SDS during gas hydrate formation and growth

Based on the experimental data obtained during these studies the role of SDS surfactant during gas hydrate formation is derived, as schematically shown in **Figure 5.13**. It is important to note that utilizing the spectroscopic data produced in these studies

we were not able to definitely differentiate between SDS molecular assemblies, micelles, or small SDS particulates of hydrated solids [26], as the intensity of absorption signatures was relatively weak and the peaks were quite diffuse. However, based on literature data it is likely that the peak positions at 2850 cm^{-1} and 2917 cm^{-1} indicate the formation of hydrated solids at the later stages of the process [103, 104] .

The obtained spectroscopic data (**Figures 5.10 and 5.12a**) clearly indicate that the major role of SDS is the delivery of hydrocarbon gas molecules to the surface (solid/water interface) where the gas hydrate nucleation occurs. This delivery mechanism originates from hydrophobic interactions between SDS and propane, as confirmed by studies demonstrating an increase of hydrocarbon solubility in water upon the addition of SDS [3, 8]. Furthermore, the surface tension at the water/gas interface decreases, which allows more hydrocarbon gas to migrate to the bulk [85]. One may suggest that the diffusion of propane gas from the water-gas interface to the water-solid interface can be controlling the time of gas hydrate nucleation; however the experiment without SDS (**Section 5.5.3**) should provide comparable rates of propane diffusion to the water-solid interface. Thus, this scenario may safely be dismissed.

From a thermodynamic point of view, the addition of SDS to water may render the system entropically more favorable for gas hydrate nucleation at the solid surfaces. If non-polar and relatively small solute molecules - here propane gas - are added to a water matrix, water molecules structure around these constituents without reducing their hydrogen-bonding sites—a process known as hydrophobic solvation [105]. The organization process of water molecules, which are hydrophobically forced to reorient around non-polar solutes while maintaining an extensive H-bonded network, is

entropically a highly unfavorable process [105]. With the addition of SDS molecules to the system, non-polar gas molecules, such as propane, associate with the surfactant molecules via strong hydrophobic interactions, thereby forming surfactant-gas associates. The formation of such associated structures reduces the driving force for the water structuring process, and thus renders the system entropically more favorable.[105]

Since SDS-propane gas associates are less solubilized by water molecules due to the significant increases in size [105], the induced desolubilization facilitates their delivery to and deposition at the liquid/solid interface, i.e., the chamber walls, the cooling coil, and the surface of the fiberoptic waveguide [9]. In addition to the migration of SDS-gas assemblies to the surface, the negatively charged polar moiety of SDS is characterized by a high affinity toward metal, metal oxide, and silver halide surfaces, which are slightly positively charged at the experimental pH of 5.5 [9, 106-108]. This affinity further promotes the interfacial deposition of SDS-gas assemblies.

At (metal) surfaces, water is strongly suspected to form a structured layer [84, 109, 110]. Therefore, upon deposition of SDS-gas assemblies at the surfaces of the hydrate chamber and of the optical fiber (here, silver halide), structured water molecules are displaced, while gas molecules are released in close vicinity due to the reduced surface tension as SDS interacts with the surface. Consequently, enhanced concentrations of solubilized gas molecules and of structured water molecule assemblies providing pre-organized fragments of crystalline water structures, are locally present, thereby facilitating the formation of solid gas hydrate particles, i.e., clathrate structures at or near the surface [41].

The spectroscopic data recorded in this study confirms the nucleation of gas hydrate at the waveguide surface, and the presence of surfactant, along with propane, within the evanescent field **(Figure 5.10**). In the first 30-60 min following nucleation, the absorbance intensity of the propane and the SDS IR signatures slowly increased due to SDS-propane assemblies migrating toward the waveguide surface where clathrate particle growth is observed (**Figure 5**.**12a**).

Approximately 5 hrs after the initial nucleation, propane absorbance signatures significantly decrease, while SDS IR absorption remains constant throughout the hydrate growth (**Figure 5.10**)**.** The decrease in propane concentration along the silver halide fiber surface results from the gas encapsulation within the clathrate cages; this reduces the detectable amount of propane within the evanescent field emanating from the waveguide surface. In contrast, the SDS concentration remains largely constant throughout the hydrate growth, since SDS molecules adsorb to the surface of the silver halide fiber and onto gas hydrate particles [86] and remain present within the interstitial water of gas hydrates. Given its molecular dimensions, SDS may not be incorporated into the water cages [4]. As pressure-induced hydrate dissociation occurs, the characteristic SDS absorbance signatures decrease beyond the detection limit of IR evanescent field absorption spectroscopy (**Figure 5.12a**) as the surfactant is reconstituted into the bulk solution [9].

In support of the proposed hypothesis, the control experiments revealed that, in the absence of SDS and despite the formation of gas hydrate, no propane gas signatures are recorded within the evanescent field during IR studies (**Figure 5.12b**). This further confirms the role of SDS in facilitating the transport of gas molecules to the surface for

enhanced interaction with structured water molecule assemblies during detergent-mediated hydrate nucleation.

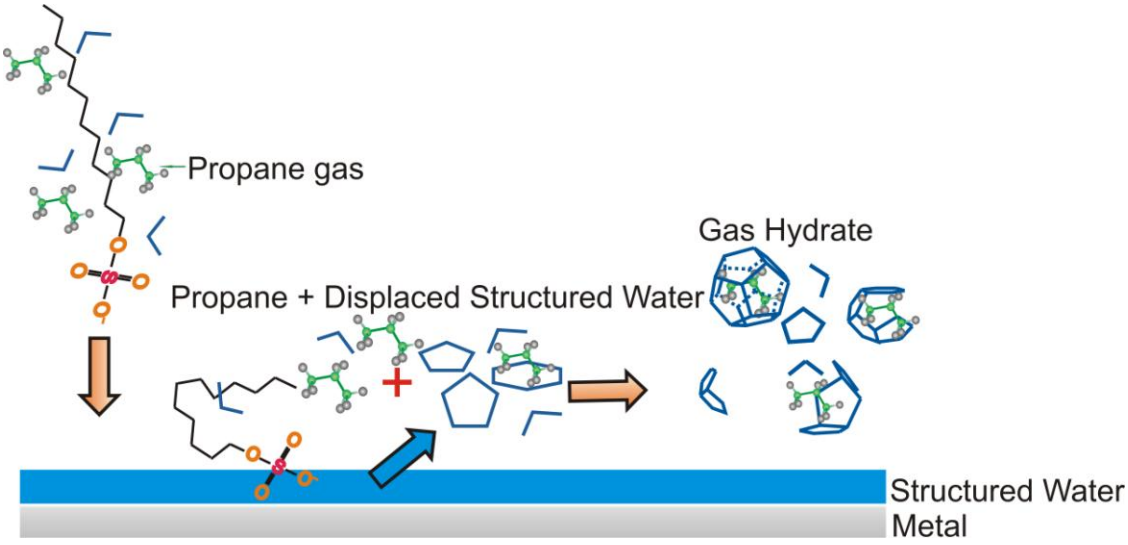

Figure 5.13: Schematic illustration of the mechanism of gas hydrate nucleation in the presence of SDS. A structured layer of water molecules is present at the metal (oxide) surface and displaced by SDS-gas assemblies migrating toward the liquid/solid interface. Reduction of the surface tension results in the release of gas molecules in the vicinity of the surface readily available for gas hydrate formation with displaced prearranged water fragments for enhanced gas hydrate formation.

5.6 CONCLUSIONS

This chapter describes an effective and original IR technique for monitoring gas hydrate formation in the presence of SDS surfactant at a molecular level. The intensity-independent evaluation of the 3rd libration overtone, coupled with the inversely related amplitude responses of the H-O-H absorption band, provides a straightforward evaluation

technique for monitoring gas hydrate nucleation, growth, and dissociation, and for elucidating the involved molecular mechanisms.

Supporting evidence for the role of SDS as a nucleation promotor was established throughout the present study, providing unique insights on the role of surfactants in gas hydrate formation. The obtained experimental data allowed the derivation of a mechanism as to how SDS decreases the induction time for hydrate nucleation and promotes hydrate formation. In general, fiberoptic mid-infrared evanescent field spectroscopy reveals a significant potential for in-depth studies on a wide variety of surfactants to elucidate the molecular mechanisms involved in promoting gas hydrate nucleation and growth.

5.7 OUTLOOK

5.7.1 Differentiation between micelles, admicelles, and individual SDS molecules

In this chapter, in-situ studies using MIR evanescent field absorption spectroscopy were utilized for observation of detergent-related surface processes during SDS mediated gas hydrate formation. As with most linear optical methods used for interface studies, MIR fiber-optic spectroscopy technique relies on absorption within the evanescent field; hence, surface sensitivity here translates into addressing a regime on the order of the wavelength of the light, i.e., several hundreds of nanometers or even micrometers [111].

Thus, the data produced in the studies herein do not enable definite differentiation between SDS molecular assemblies, micelles, admicelles, individual SDS molecules, or small SDS particulates and hydrated solids.

Thus, it is suggested using vibrational sum frequency spectroscopy (VSFS), a highly surface-sensitive analytical technique, as a complimentary technique to MIR evanescent field spectroscopy to differentiate between different conformations of SDS molecules during gas hydrate nucleation. VSFS has been already successfully been used to differentiate between SDS monolayers and SDS micelles, and may be the appropriate technique for confirming the proposed molecular models of hydrate growth discussed in the present studies [112, 113, 114].

5.8 REFERNCES:

(1) Zhong, Y.; Rogers, R. E. "Surfactant effects on gas hydrate formation" *Chemical Engineering Science* **2000**, *55*, 4175-4187.

(2) Lee, S.; Zhang, J. S.; Mehta, R.; Woo, T. K.; Lee, J. W. "Methane hydrate equilibrium and formation kinetics in the presence of an anionic surfactant" *Journal of Physical Chemistry C* **2007**, *111*, 4734-4739.

(3) Peng, B. Z.; Chen, G. J.; Luo, H.; Sun, C. Y. "Solubility measurement of methane in aqueous solution of sodium dodecyl sulfate at ambient temperature and near hydrate conditions" *Journal of Colloid and Interface Science* **2006**, *304*, 558-561.

(4) Sloan, E. D. *Clathrate Hydrates of Natural Gases*; Marcel Dekker, Inc.: New York, 1998.

(5) Ganji, H.; Manteghian, M.; Zadeh, K. S.; Omidkhah, M. R.; Mofrad, H. R. "Effect of different surfactants on methane hydrate formation rate, stability and storage capacity" *Fuel* **2007**, *86*, 434-441.

(6) Di Profio, P.; Arca, S.; Germani, R.; Savelli, G. 2007; Asme-Amer Soc Mechanical Eng; 49-55.

(7) Link, D. D.; Ladner, E. P.; Elsen, H. A.; Taylor, C. E. "Formation and dissociation studies for optimizing the uptake of methane by methane hydrates" *Fluid Phase Equilibria* **2003**, *211*, 1-10.

(8) Roy, S.; Mehra, A.; Bhowmick, D. "Prediction of solubility of nonpolar gases in micellar solutions of ionic surfactants" *Journal of Colloid and Interface Science* **1997**, *196*, 53-61.

(9) Eastoe, J.; Rankin, A.; Wat, R.; Bain, C. D. "Surfactant adsorption dynamics" *International Reviews in Physical Chemistry* **2001**, *20*, 357-386.

(10) Watanabe, K.; Niwa, S.; Mori, Y. H. "Surface tensions of aqueous solutions of sodium alkyl sulfates in contact with methane under hydrate-forming conditions" *Journal of Chemical and Engineering Data* **2005**, *50*, 1672-1676.

(11) Di Profio, P.; Arca, S.; Germani, R.; Savelli, G. "Surfactant promoting effects on clathrate hydrate formation: Are micelles really involved?" *Chem. Eng. Sci.* **2005**, *60*, 4141-4145.

(12) Sun, Z. G.; Wang, R. Z.; Ma, R. S.; Guo, K. H.; Fan, S. S. "Natural gas storage in hydrates with the presence of promoters" *Energy Conversion and Management* **2003**, *44*, 2733-2742.

(13) Gayet, P.; Dicharry, C.; Marion, G.; Graciaa, A.; Lachaise, J.; Nesterov, A. "Experimental determination of methane hydrate dissociation curve up to 55 MPa by using a small amount of surfactant as hydrate promoter" *Chem. Eng. Sci.* **2005**, *60*, 5751-5758.

(14) Han, X., Wang, S., Chen, X., Liu, F. , Yokohama, Japan 2002; 1036-1039.

(15) Zhang, J. S.; Lee, S.; Lee, J. W. "Does SDS micellize under methane hydrate-forming conditions below the normal Krafft point?" *Journal of Colloid and Interface Science* **2007**, *315*, 313-318.

(16) Kutergin, O. B.; Melnikov, V. P.; Nesterov, A. N. "Influence of surfactants on the mechanism and kinetics of the formation of gas hydrates" *Doklady Akademii Nauk* **1992**, *323*, 549-553.

(17) Mel'nikov, V. P., Nesterov, A.N., and Feklistov V.V. "Formation of gas hydrates in the presence of additives consisting of surface-active substances, " *Khimiia v Interesakh Ustoichivogo Razvitiia* **1998** *6*, 97-102.
(18) Karaaslan, U.; Uluneye, E.; Parlaktuna, M. "Effect of an anionic surfactant on different type of hydrate structures" *Journal of Petroleum Science and Engineering* **2002**, *35*, 49-57.
(19) Karaaslan, U.; Parlaktuna, M. "Promotion effect of polymers and surfactants on hydrate formation rate" *Energy Fuels* **2002**, *16*, 1413-1416.
(20) Karaaslan, U.; Parlaktuna, M. "Surfactants as hydrate promoters?" *Energy Fuels* **2000**, *14*, 1103-1107.
(21) Okutani, K.; Kuwabara, Y.; Mori, Y. H. "Surfactant effects on hydrate formation in an unstirred gas/liquid system: Amendments to the previous study using HFC-32 and sodium dodecyl sulfate" *Chem. Eng. Sci.* **2007**, *62*, 3858-3860.
(22) Sun, Z. G.; Wang, R. Z.; Ma, R. S.; Guo, K. H.; Fan, S. S. "Effect of surfactants and liquid hydrocarbons on gas hydrate formation rate and storage capacity" *International Journal of Energy Research* **2003**, *27*, 747-756.
(23) Sun, Z. G.; Ma, R. S.; Wang, R. Z.; Guo, K. H.; Fa, S. S. "Experimental studying of additives effects on gas storage in hydrates" *Energy Fuels* **2003**, *17*, 1180-1185.
(24) Okutani, K.; Kuwabara, Y.; Mori, Y. H. "Surfactant effects on hydrate formation in an unstirred gas/liquid system: An experimental study using methane and sodium alkyl sulfates" *Chem. Eng. Sci.* **2008**, *63*, 183-194.
(25) Rogers, R. E.; Zhang, G.; Dearman, J. S.; Woods, C. E. "Investigations into surfactant/gas-hydrate relationship" *Journal of Petroleum Science and Engineering* **2007**, *56*, 82-88.
(26) Watanabe, K.; Imai, S.; Mori, Y. H. "Surfactant effects on hydrate formation in an unstirred gas/liquid system: An experimental study using HFC-32 and sodium dodecyl sulfate" *Chem. Eng. Sci.* **2005**, *60*, 4846-4857.
(27) Kvenvolden, K. A. "Gas hydrates - geological perspective and global change" *Reviews of Geophysics* **1993**, *31*, 173-187.
(28) Sloan, E. D. "Fundamental principles and applications of natural gas hydrates" *Nature* **2003**, *426*, 353-359.
(29) Davy, H. In *The Bakerian Lecture.* : London, **1811**; Vol. **101**, pp **1-35.**
(30) Faraday, M.: ***L.ondon*, 1823**; Vol. **113**, pp **160-165.**
(31) Hammerschmidt, E. G. "Formation of gas hydrates in natural gas transmission lines" *Industrial and Engineering Chemistry* **1934**, *26*, 851-855.
(32) Max, M. D., Johnson, A.H., Dillon, W.P. , Ed. *Economic Geology of Natural Gas Hydrate.*; Springer: Dordrecht, The Netherlands, 2006.
(33) Gudmundsson, J. S.; Andersson, V.; Levik, O. I.; Mork, M. In *Gas Hydrates: Challenges for the Future*; Holder, G. D., Bishnoi, P. R., Eds.; New York Acad Sciences: New York, 2000; Vol. 912, pp 403-410.
(34) Mao, W. L.; Mao, H. K.; Goncharov, A. F.; Struzhkin, V. V.; Guo, Q. Z.; Hu, J. Z.; Shu, J. F.; Hemley, R. J.; Somayazulu, M.; Zhao, Y. S. "Hydrogen clusters in clathrate hydrate" *Science* **2002**, *297*, 2247-2249.

(35) Florusse, L. J.; Peters, C. J.; Schoonman, J.; Hester, K. C.; Koh, C. A.; Dec, S. F.; Marsh, K. N.; Sloan, E. D. "Stable low-pressure hydrogen clusters stored in a binary clathrate hydrate" *Science* **2004**, *306*, 469-471.
(36) Makogon, Y. F. "Hydrate formation in the gas-bearing beds under permafrost conditions." *Gazovaia Promyshlennost* **1965**, *5*, 14-15.
(37) Katz, D. L. "Depths to Which Frozen **Gas** Fields (Gas Hydrates) MayBe Expected." *J. Pet. Technol.* **1971**, **419-423**.
(38) Chersky, **Y.** "Detection of a Pool of Natural Gas in a Solid (Hydrate **Gas)**State." *Dokl. Acad. Sci. USSR-Earth Sci. Sect.* **1972**, **197-200**.
(39) Klauda, J. B.; Sandler, S. I. "Global distribution of methane hydrate in ocean sediment" *Energy Fuels* **2005**, *19*, 459-470.
(40) Milkov, A. V.; Dickens, G. R.; Claypool, G. E.; Lee, Y. J.; Borowski, W. S.; Torres, M. E.; Xu, W. Y.; Tomaru, H.; Trehu, A. M.; Schultheiss, P. "Co-existence of gas hydrate, free gas, and brine within the regional gas hydrate stability zone at Hydrate Ridge (Oregon margin): evidence from prolonged degassing of a pressurized core" *Earth Planet. Sci. Lett.* **2004**, *222*, 829-843.
(41) Sloan Jr., E. D. *Clathrate Hydrates of Natural Gases*, 2nd ed.; Marcel Dekker, Inc.: New York, 1998.
(42) Kvenvolden, K. A. "Potential Effects of Gas Hydrate on Human Welfare" *Proceedings of the National Academy of Sciences of the United States of America* **1999**, *96*, 3420-3426.
(43) Milkov, A. V.; Sassen, R.; Novikova, I.; Mikhailov, E. "Gas Hydrates at Minimum Stability Water Depths in the Gulf of Mexico: Significance to Geohazard Assessment" *Gulf Coast Association of Geological Societies Transactions* **2000**, *50*, 217-224.
(44) Kvenvolden, K. A. "Methane Hydrate in the Global Organic Carbon Cycle" *Terra Nova* **2002**, *14*, 302-306.
(45) Milkov, A. V.; Sassen, R. "Economic Geology of Offshore Natural Gas Hydrate Accumulations and Provinces" *Mar. Pet. Geol.* **2002**, *19*, 1-11.
(46) Kvenvolden, K. A.; Rogers, B. W. "Gaia's Breath-Global Methane Exhalations" *Mar. Pet. Geol.* **2005**, *22*, 579-590.
(47) Milkov, A. V. "Molecular and Stable Isotope Compositions of Natural Gas Hydrates: A Revised Global Dataset and Basic Interpretations in the Context of Geological Settings" *Organic Geochemistry* **2005**, *36*, 681-702.
(48) Holder, G. D.; Kamath, V. A.; Godbole, S. P. "The potential of natural-gas hydrates as an energy resource" *Annual Review of Energy* **1984**, *9*, 427-445.
(49) Pooladi-Darvish, M. "Gas production from hydrate reservoirs and its modeling" *Journal of Petroleum Technology* **2004**, *56*, 65-71.
(50) Kvenvolden, K. A. "Methane hydrate - a major reservoir of carbon in the shallow geosphere" *Chem. Geol.* **1988**, *71*, 41-51.
(51) Macdonald, G. J. "Role of methane clathrates in past and future climates" *Clim. Change* **1990**, *16*, 247-281.
(52) Makogon, Y. F. "Hydrates of Natural Gas" *Pennwell, Tulsa, Okla.* **1981**, 237.
(53) NETL; Laboratory), N. E. T., 2003.
(54) Lerche, I.; Bagirov, E. "Guide to gas hydrate stability in various geological settings" *Mar. Pet. Geol.* **1998**, *15*, 427-437.

(55) Larche, I., Bagirov, E. In *Izvestiya Nauk Azerbaijana. Seriya Nauk o Zemie*, 1993/1994; Vol. 1-6, pp 116-124.
(56) Buffett, B. A. "Clathrate hydrates" *Annual Review of Earth and Planetary Sciences* **2000**, *28*, 477-507.
(57) Nisbet, E. G. "The end of the ice-age" *Can. J. Earth Sci.* **1990**, *27*, 148-157.
(58) Paull, C. K.; Ussler, W.; Dillon, W. P. "Is the extent of glaciation limited by marine gas-hydrates" *Geophys. Res. Lett.* **1991**, *18*, 432-434.
(59) Vanderwaals, J. H.; Platteeuw, J. C. "Clathrate solutions" *Adv. Chem. Phys.* **1959**, *2*, 1-57.
(60) Belosludov, V. R.; Lavrentiev, M. Y.; Dyadin, Y. A. "Theory of clathrates" *J. Incl. Phenom. Mol. Recogn. Chem.* **1991**, *10*, 399-422.
(61) Ripmeester, J. A.; Tse, J. S.; Ratcliffe, C. I.; Powell, B. M. "A new clathrate hydrate structure" *Nature* **1987**, *325*, 135-136.
(62) Ripmeester, J. A. In *Gas Hydrates: Challenges for the Future*; Holder, G. D., Bishnoi, P. R., Eds.; New York Acad Sciences: New York, 2000; Vol. 912, pp 1-16.
(63) Dobbs G. T., Luzinova. Y., Mizaikoff B., Vancouver, British Columbia, CANADA 2008.
(64) Dobbs, G. T., Georgia Institute of Technology, Atlanta, 2007.
(65) Ballard, A. L.; Sloan, E. D. "Hydrate phase diagrams for methane plus ethane plus propane mixtures" *Chem. Eng. Sci.* **2001**, *56*, 6883-6895.
(66) Bertie, J. E.; Bates, F. E.; Hendricksen, D. K. "Far infrared-spectra and x-ray powder diffraction patterns of structure i hydrates of cyclopropane and ethylene-oxide at 100 degreesk" *Can. J. Chem.-Rev. Can. Chim.* **1975**, *53*, 71-75.
(67) Bertie, J. E.; Devlin, J. P. "Infrared Spectroscopic Proof of the Formation of the Structure I Hydrate of Oxirane from Annealed Low-temperature Condensate" *Journal of Chemical Physics* **1983**, *78*, 6340-6341.
(68) Bertie, J. E.; Jacobs, S. M. "Far ir absorption and rotational vibrations of guest molecules in structure 1 clathrate hydrates between 4.3 and 100k" *Can. J. Chem.-Rev. Can. Chim.* **1977**, *55*, 1777-1785.
(69) Bertie, J. E.; Jacobs, S. M. "Infrared Spectra from 300 to 10 cm-1 of Structure II Clathrate Hydrates at 4.3 K" *Journal of Chemical Physics* **1978**, *69*, 4105-4113.
(70) Fleyfel, F.; Devlin, J. P. "FT-IR Spectra of 90 K Films of Simple, Mixed, and Double Clathrate Hydrates of Trimethylene Oxide, Methyl Chloride, Carbon Dioxide, Tetrahydrofuran, and Ethylene Oxide Containing Decoupled Water-d2" *Journal of Physical Chemistry* **1988**, *92*, 631-635.
(71) Fleyfel, F.; Devlin, J. P. "Carbon Dioxide Clathrate Hydrate Epitaxial Growth: Spectroscopic Evidence for Formation of the Simple Type-II Carbon Dioxide Hydrate" *Journal of Physical Chemistry* **1991**, *95*, 3811-3815.
(72) Fleyfel, F.; Richardson, H. H.; Devlin, J. P. "Comparative Sulfur Dioxide Infrared Spectra: Type I and II Clathrate Hydrate Films, Large Gas-phase Clusters, and Anhydrous Crystalline Films" *Journal of Physical Chemistry* **1990**, *94*, 7032-7037.
(73) Devlin, J. P.; Buch, V. "Surface of Ice as Viewed from Combined Spectroscopic and Computer Modeling Studies" *Journal of Physical Chemistry* **1995**, *99*, 16534-16548.

(74) Williams, K. D.; Devlin, J. P. "Formation and Spectra of Clathrate Hydrates of Methanol and Methanol-ether Mixtures" *Journal of Molecular Structure* **1997**, *416*, 277-286.
(75) Dartois, E.; Deboffle, D. "Methane clathrate hydrate FTIR spectrum Implications for its cometary and planetary detection" *Astron. Astrophys.* **2008**, *490*, L19-L22.
(76) Jin, Y.; Oyama, H.; Nagao, J. "Infrared Spectroscopy of Gas Hydrate Dissociation Behavior During Depressurization" *Jpn. J. Appl. Phys.* **2009**, *48*, 2.
(77) Kumar, R.; Lang, S.; Englezos, P.; Ripmeester, J. "Application of the ATR-IR Spectroscopic Technique to the Characterization of Hydrates Formed by CO2, CO2/H-2 and CO2/H-2/C3H8" *Journal of Physical Chemistry A* **2009**, *113*, 6308-6313.
(78) Oyama, H.; Ebinuma, T.; Shimada, W.; Takeya, S.; Nagao, J.; Uchida, T.; Narita, H. "An Experimental Study of Gas-hydrate Formation by Measuring Viscosity and Infrared Spectra" *Canadian Journal of Physics* **2003**, *81*, 485-492.
(79) Zhang, Z. F.; Ewing, G. E. "Infrared studies of the SO2 clathrate hydrate" *Journal of Physical Chemistry A* **2004**, *108*, 1681-1686.
(80) Prasad, P. S. R.; Prasad, K. S.; Thakur, N. K. "FTIR signatures of type-II clathrates of carbon dioxide in natural quartz veins" *Current Science* **2006**, *90*, 1544-1547.
(81) Flockhart, B. "Effect of temperature on critical micelle concentration of some paraffin-chain salts" *Journal of Colloid Science* **1961**, *16*, 484-&.
(82) Rana, D.; Neale, G. H.; Hornof, V. "Surface tension of mixed surfactant systems: lignosulfonate and sodium dodecyl sulfate" *Colloid and Polymer Science* **2002**, *280*, 775-778.
(83) Zhang, G. C.; Rogers, R. E.; French, W. T.; Lao, W. J. "Investigation of microbial influences on seafloor gas-hydrate formations" *Marine Chemistry* **2007**, *103*, 359-369.
(84) Drost-Hansen, W. "Thermal anomalies in aqueous systems: Manifestations of interfacial phenomena?" *Chemical Physics Letters* **1968**, *2*, 647-652.
(85) Sun, C. Y.; Hen, G. J.; Yang, L. Y. "Interfacial tension of methane plus water with surfactant near the hydrate formation conditions" *Journal of Chemical and Engineering Data* **2004**, *49*, 1023-1025.
(86) Zhang, J. S.; Lo, C.; Somasundaran, P.; Lu, S.; Couzis, A.; Lee, J. W. "Adsorption of sodium dodecyl sulfate at THF hydrate/liquid interface" *Journal of Physical Chemistry C* **2008**, *112*, 12381-12385.
(87) Zhang, J. S.; Lee, S.; Lee, J. W. "Kinetics of methane hydrate formation from SDS solution" *Industrial & Engineering Chemistry Research* **2007**, *46*, 6353-6359.
(88) Pennington, N. Masters Thesis, Georgia Institute of Technology, Atlanta, 2003.
(89) Fesevur, F. "Dorgem" *http://dorgem.sourceforge.net/*, **June 2010**.
(90) Harrick, N. J. *Internal Reflection Spectroscopy*; John Wiley & Sons: New York, 1967.
(91) Rogers, R. E.; Zhong, Y. In *Gas Hydrates: Challenges for the Future*, 2000; Vol. 912, pp 843-850.

(92) Brubach, J. B.; Mermet, A.; Filabozzi, A.; Gerschel, A.; Roy, P. "Signatures of the Hydrogen Bonding in the Infrared Bands of Water" *Journal of Chemical Physics* **2005**, *122*, 184509/184501-184509/184507.
(93) Millo, A.; Raichlin, Y.; Katzir, A. "Mid-infrared Fiber-optic Attenuated Total Reflection Spectroscopy of the Solid-Liquid Phase Transition of Water" *Applied Spectroscopy* **2005**, *59*, 460-466.
(94) Libnau, F. O.; Kvalheim, O. M.; Christy, A. A.; Toft, J. "Spectra of Water in the Near- and Mid-infrared Region" *Vibrational Spectroscopy* **1994**, *7*, 243-254.
(95) Fox, J. J.; Martin, A. E. "Investigations of Infrared Spectra (2.5-7.5 m). Absorption of Water" *Proc. Roy. Soc. (London)* **1940**, *A174*, 234-262.
(96) Ockman, N. "The Infrared and Raman Spectra of Ice" *Advance in Phys.* **1958**, *7*, 199-220.
(97) Giguere, P. A.; Harvey, K. B. "The Infrared Absorption of Water and Heavy Water in Condensed States" *Canadian Journal of Chemistry* **1956**, *34*, 798-808.
(98) Bertie, J. E.; Whalley, E. "Infrared Spectra of Ices Ih and Ic in the Range 4000 to 350 cm-1" *Journal of Chemical Physics* **1964**, *40*, 1637-1645.
(99) Ockman, N.; Sutherland, G. B. B. M. "Infrared and Raman Spectra of Single Crystals of Ice" *Proceeding of the Royal Society of London. Series A, Mathematical and Physical Sciences* **1958**, *247*, 434-440.
(100) Gayles, J. N.; King, W. T. "Infrared spectrum of propane" *Spectrochimica Acta* **1965**, *21*, 543-&.
(101) Hasan, M. A.; Zaki, M. I.; Pasupulety, L. "IR investigation of the oxidation of propane and likely C-3 and C-2 products over group IVB metal oxide catalysts" *Journal of Physical Chemistry B* **2002**, *106*, 12747-12756.
(102) Padalkar, K. V.; Gaikar, V. G.; Aswal, V. K. "Characterization of mixed micelles of sodium cumene sulfonate with sodium dodecyl sulfate and cetyl trimethylammonium bromide by SANS, FTIR spectroscopy and NMR spectroscopy" *Journal of Molecular Liquids* **2009**, *144*, 40-49.
(103) Sperline, R. P. "Infrared spectroscopic study of the crystalline phases of sodium dodecyl sulfate" *Langmuir* **1997**, *13*, 3715-3726.
(104) Sperline, R. P.; Song, Y.; Freiser, H. "Temperature dependent structure of adsorbed sodium dodecyl sulfate at the Al_2O_3/water interface" *Langmuir* **1997**, *13*, 3727-3732.
(105) Israelachvili, J. N. *Intermolecular and Surface Forces*, 2nd ed.; Academic Press: London, 1991.
(106) Upadhyaya, A.; Acosta, E. J.; Scamehorn, J. F.; Sabatini, D. A. "Adsorption of anionic-cationic surfactant mixtures on metal oxide surfaces" *Journal of Surfactants and Detergents* **2007**, *10*, 269-277.
(107) Luvalle, J. E.; Jackson, J. M. "The zeta potential of silver bromide in the presence of various substances of photographic interest" *J. Phys. Chem.* **1957**, *61*, 1216-1222.
(108) Lee, E. M.; Koopal, L. K. "Adsorption of cationic and anionic surfactants on metal oxide surfaces: Surface charge adjustment and competition effects" *Journal of Colloid and Interface Science* **1996**, *177*, 478-489.

(109) Ostroverkhov, V.; Waychunas, G. A.; Shen, Y. R. "New information on water interfacial structure revealed by phase-sensitive surface spectroscopy" *Physical Review Letters* **2005**, *94*.
(110) Zheng, J. M.; Chin, W. C.; Khijniak, E.; Pollack, G. H. "Surfaces and interfacial water: Evidence that hydrophilic surfaces have long-range impact" *Adv. Colloid Interface Sci.* **2006**, *127*, 19-27.
(111) Buck, M.; Himmelhaus, M. "Vibrational spectroscopy of interfaces by infrared-visible sum frequency generation" *Journal of Vacuum Science & Technology a-Vacuum Surfaces and Films* **2001**, *19*, 2717-2736.
(112) Richmond, G. L. "Structure and bonding of molecules at aqueous surfaces" *Annual Review of Physical Chemistry* **2001**, *52*, 357-389.
(113) Becraft, K. A.; Moore, F. G.; Richmond, G. L. "In-situ spectroscopic investigations of surfactant adsorption and water structure at the CaF2/aqueous solution interface" *Physical Chemistry Chemical Physics* **2004**, *6*, 1880-1889.
(114) Richmond, G. L. "Molecular bonding and interactions at aqueous surfaces as probed by vibrational sum frequency spectroscopy" *Chemical Reviews* **2002**, *102*, 2693-2724.

CHAPTER 6

Mid-infrared Fiberoptic Sensors for the Detection of Trace Amounts of Water in Hydrocarbon Matrices

This chapter focuses on quantifying trace amounts of water in hexane (as a model for oil and petroleum) using mid-infrared (MIR) evanescent field absorption spectroscopy. A silver halide fiberoptic waveguide was utilized to interrogate in-situ water-in-hexane emulsions. Unmodified and surface-modified fibers (the latter modified with either non- or crosslinked polyacrylic layers) were utilized for the measurements. The limits of detection (LOD) and limits of quantification (LOQ) of water in hexane utilizing tin-crosslinked polyacrylic acid modified fibers were 76 and 170 ppm, respectively. The IR absorption signature of water in hexane can be observed for concentrations as low as 10 ppm. The obtained results indicate that the proposed sensing technique enables the in-situ detection and monitoring of water in industrial oils and petroleum products.

6.1 MOTIVATION

Water content measurement technologies are important for evaluating the quality of petroleum products and industrial oils [1, 2]. Small amounts of emulsified water in petroleum products may facilitate corrosion of refinery equipment [3, 4]. Most industrial machinery requires lubrication by oil to operate efficiently and reliably; oil is also used as

a hydraulic fluid in heavy equipment. Both lubrication and hydraulic oils degrade at a much faster rate, if contaminated with water. For example, the amount of water in turbine oil is critical to the performance and longevity of the equipment [5-7]. Thus, the quantification of water in various petroleum products and industrial oils is crucial. The ability to measure water contamination of oil on-site, as soon as possible after drawing a sample or even in-situ is a substantial benefit in obtaining accurate results on potential water levels. Off-site analysis for traces of water in oil may be compromised due to the potential variability in the water concentration introduced by storage, transportation, or shipment of a sample [7]. There is a variety of commercially available instruments for the detection of water content in oil, however, they frequently lack in sensitivity and reproducibility when measuring low ppm (parts per million) levels of water in oil. Thus, there is need for an in-situ, cost-effective, and rapidly responding sensor to detect water in industrial oils and petroleum products at low ppm levels.

Currently, the primary standard for measuring water in oil remains to be the Karl Fischer coulometric titration (KF) [1, 8, 9]. Detection limits of 10–50 ppm water in oil are desirable for early warning to prevent equipment failure. Detection limits as low as 10 ppm are possible using KF titration. However, KF has some practical drawbacks for on-site analysis, including complicated sample preparation, the use of hazardous and expensive chemical reagents, and the length of time required to perform the analysis [9].

A few published articles describe spectroscopic techniques for tracing water in oil [1, 6, 9-12]. Photoacoustic spectroscopy (PAS) is capable of the non-destructive analysis of trace levels of water in oil-based products with LOD of 45-515 ppm [6]. Araujo et al. proposed a setup utilizing an in-situ NIR (near-infrared) probe capable of in-situ

measurements detecting amounts of water in crude oil in the range of 0.53-6.3% (5300-63000 ppm) [4]. Zhao et al. have developed an experimental setup for low water content measurements in crude oil based on NIR spectral absorption based on a fiber-optic sensor [12]. The lowest measured concentration of oil in water reported in this work was 0.1% (approximately 1000 ppm). NIR and mid-infrared (MIR) spectroscopy were used to determine water in lubricating oils for marine engines in the range from 0.1 to 3.7%. (1000-37000 ppm) [10]. Additionally, accurate determinations of water were shown using bench-top Fourier transform infrared (FTIR) spectroscopy. However, the lowest currently achievable detection limits for water in oil are on the order of 100–500 ppm depending on the type of oil [13].

In principle, IR spectroscopy offers a reliable option for providing rapid detection of water in oil-derived products with no or minimal sample preparation [14]. Specifically, sensors utilizing evanescent field absorption spectroscopy provide the capability of evaluating both viscous and highly absorbing samples (i.e., oil and water) [15-17]. To this end, this chapter presents the design and application of MIR evanescent field fiber-optic absorption spectroscopy for the detection of water in a hydrocarbon matrix (hexane). Such MIR evanescent field fiber-optic sensors eliminate many of the concerns associated with measuring water via KF. This spectroscopic method may be far less time consuming than KF measurements, and does not require any hazardous reagents.

6.2 INTRODUCTION

Water is a common contaminant in a variety of industrial oils and petroleum products. Thus, quantification of water in these products is crucial. This chapter

demonstrates an original MIR evanescent field fiber-optic setup for the detection of water in water/hexane emulsions. To increase the sensitivity and improve limits of detection, a waveguide-based sensing platform (silver halide fiber) was coated with a layer of hydrophilic polymer (tin-crosslinked polyacrylic acid, PAA-Sn), which attracts water into the sensing region comprised by the evanescent field. Polymer or polymer-like films have frequently been deposited onto the waveguide surface for enhancing analyte detection of a variety of compounds [18-21]. In this work, water detection in hexane (used as a model for oil/petroleum derived matrices) enabled limits of detection (LOD) and limits of quantification (LOQ) at 76 and 170 ppm, respectively. Moreover, the water IR absorption signature was still observed at 10 ppm. To the best of our knowledge, this is the smallest amount of water detected to date using IR based evanescent field sensing techniques.

6.3 EXPERIMENTAL SECTION

6.3.1 Reagents and solutions

Hexane (Certified ACS grade) was purchased from Fisher Scientific (Fair Lawn, NJ) and used as a model system for oil/petroleum derived substances. Natural crude oil was supplied by ExxonMobil Research and Engineering Company (Annadale, N J). Deionized (DI) water (R=18.2 MΩ·cm at 25°C) was used as the target analyte. The volume of water was measured using a 0.1-10, 1-100, and 50-1000 μL Eppendorf pipettes (calibrated pipette with error <0.3% RSD by volume, Eppendorf North America Inc., New York, NY). PAA (number average molecular weight of 100,000 g/mol) was purchased from Aldrich as a 35% aqueous solution. The polymer was precipitated in a

10-fold excess (volume) of acetone (Fisher Scientific) and dried. To prepare the PAA-Sn coating, 0.2 g of the polymer was first dissolved in 10 ml of ethanol. Then 0.1 g of $SnCl_4$ x $5H_2O$ was added to the polymer solution and stirred (~ 5 min) until complete dissolution. The coating was deposited within 20 min after the solution preparation.

6.3.2 PAA layer deposition

Core-only silver halide fibers (AgX, X = $Cl_{0.3-0.4}Br_{0.7-0.6}$) were purchased from JT Ingram Technologies Inc., and were coated with a PAA/PAA-Sn layer by a dip-coating method (using DC Mono 160 dip-coater from NIMA Technologies Ltd.). This technique involved dipping the fiber clamped at one end into a polymer solution (ethanol from Fisher Scientific). Prior to deposition, the fiber was rinsed with methylethylketone (Fisher Scientific) to remove possible contaminations. The coated fiber (protected from light) was allowed to dry at ambient air followed by annealing at 70^oC for two hours in an oven. The same experiment was conducted at a silicon wafer (Semiconductor Processing Co.) to determine the thickness and swellability of the deposited layers via ellipsometry. The morphology of the fiber - unmodified and covered with the polymer films - was imaged with atomic force microscopy (AFM).

6.3.3 Instrumentation and characterization

The stirring cell experimental setup was designed around a Bruker Equinox 55 Fourier transform (FTIR) spectrometer (Bruker Optics Inc., Billerica, MA). Ellipsometry was performed with a COMPEL automatic ellipsometer (InOmTech, Inc.) at an angle of incidence of 70^0. The refractive index for PAA was assumed to be n =1.5. AFM studies

were performed using a Dimension 3100 (Digital Instruments, Inc.) microscope in tapping mode to study the surface morphology of the modified substrates at ambient air using silicon tips with spring constants of 50 N/m. Imaging was performed at scan rates in the range of 1-2 Hz. Static contact angle measurements were performed using a contact angle goniometer (Kruss, Model DSA10). The contact angle was calculated using the tangent method. Contact angle measurements were performed with a static time of 60 seconds before the angle measurement. For contact angle measurements at the fiber surface, the fiber was flattened using cold pressing. The contact angles were determined with an accuracy of $\pm$ 4 degrees.

6.3.4 Stirring cell

A blender with volume of approximately 1000 mL was adapted to enable preparation of a water-in-hexane emulsion and detection of water in the hexane matrix. The mixing speed was controlled with a potentiometer connected to the blender cell. For spectroscopic access probing a cross-section of the stirring cell, a fiber coupling system with custom-made PTFE ferrules and Swagelok components (Swagelok, Solon, OH) was developed that was suitable for sealing and routing a 45 cm long bare core silver halide (AgX) fiber with a diameter of 700 μm through the liquid phase contained within the stirring cell. (The ends of the optical fiber were manually polished; see **Appendix Section A-2.1**) The optical setup for in-situ spectroscopic monitoring of the oil in water matrix was developed around a FT-IR Bruker Equinox 55. Radiation modulated by the interferometer was guided outside of the spectrometer and focused onto a polished in-coupling facet of the fiberoptic waveguide via an off-axis parabolic mirror with a 2-in.

focal length. IR radiation was propagating via total internal reflection along the AgX fiber routed through the stirring cell, thus creating an evanescent field along the fiber surface due to the refractive index contrast with the surrounding medium (approximately 2.1 for the AgX fiber and 1.36 for the aqueous sample matrix). The emanating divergent cone of IR radiation was collimated at the distal end of the fiber with another 2-in. focal length off-axis parabolic mirror, and then focused onto a liquid nitrogen-cooled mercury-cadmium-telluride (MCT) detector (Model K508, Infrared Associates, Stuart, FL) using another 2-in. focal length off-axis paraboloid. The detected signal was processed via an impedance-matched MCT-1000 preamplifier (Infrared Associates, Stuart, FL), and connected to an external input channel of the FT-IR spectrometer (**Figure 6.1).**

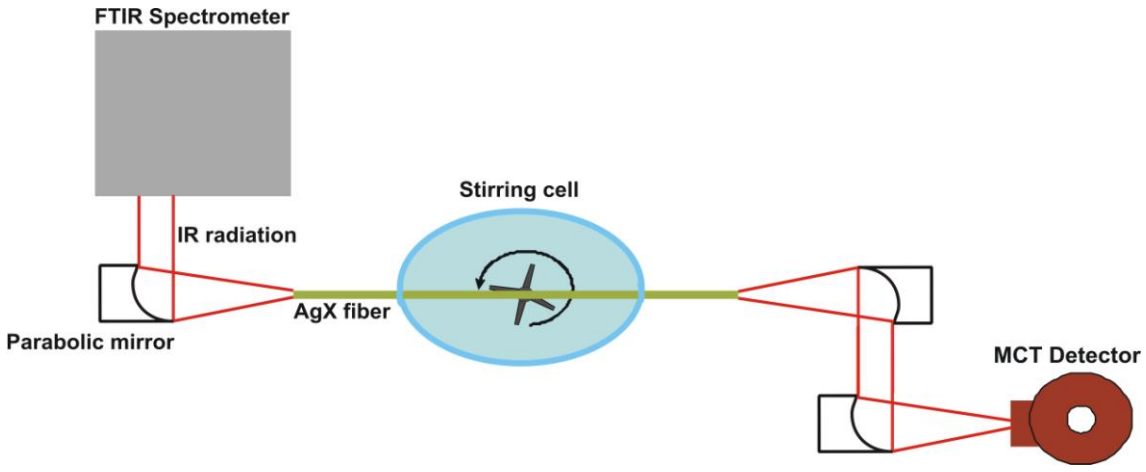

Figure 6.1: Experimental set up.

6.3.5 Rotations in the stirring cell

To measure the number of rotations per minute (RPM) of the stirring cell, a small magnet was attached to the mixer rotor with aid of super glue and an electromagnetic coil was placed in the proximity of the rotor. When the magnet passes the coil, a current pulse is generated in the coil. To estimate the pulse frequency (which corresponds to the rotor RPM), the signal from the coil was digitized with aid of a computer sound card. The pulse frequency was estimated by Fourier transformation of the current pulses in Labview. **Figure 6.2** presents the RPM as a function of the potentiometer settings. In this work, setting 24 was used producing approximately 3000 RPM.

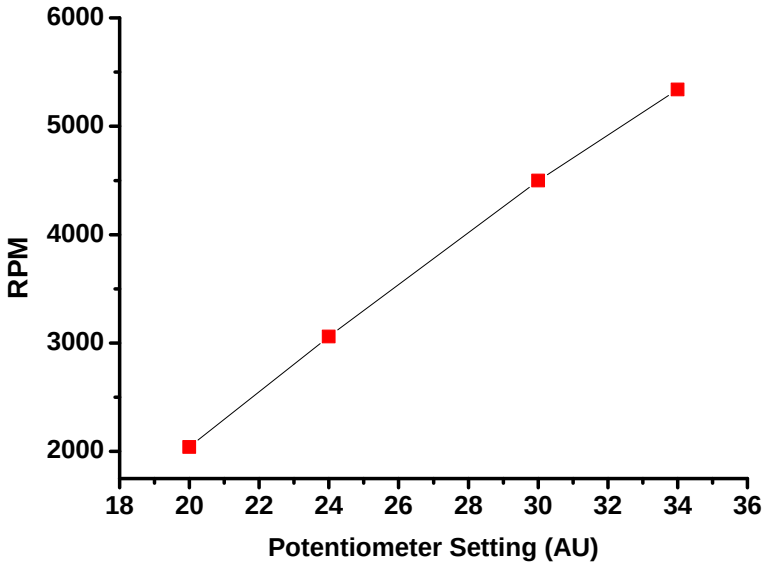

Figure 6.2: Rotations per minute (RPM) in the stirring cell as a function of potentiometer settings. Measurements were conducted with assistance of Dr. Zdyrko at Clemson University.

6.3.6 Spectral data analysis

During the experiments in this chapter, for each sample concentration six spectra were acquired (averaging 250 scans each) in 120 s intervals at 2 cm^{-1} spectral resolution; thus, measuring each concentration for 12 minutes. Using the OPUS software (Bruker Optics Inc., Billerica, MA), the infrared absorption features of water were evaluated by peak area analysis. Peak areas underneath the O-H absorption stretch at 3750–3000 cm^{-1} were integrated. Peak areas from each spectral region collected during replicate measurements were averaged, and used for further calculations. In the remainder of this chapter, the three averaged peak areas for a given spectral region and respective sample mixture are referred to as PA.

To establish quantitative calibration functions for analyzing water in hexane, the PAs were plotted versus the percentage of water in hexane. The LOD and LOQ of water in hexane were extracted from the calibration plot (LOD: 3σ concentration determination from the regression fit using the criterion of three times the noise of a blank sample. LOQ: 6σ concentration determination from the regression fit using the criterion of six times the noise of a blank sample).

6.4 RESULTS AND DISCUSSION

This research is focused on quantifying trace amounts of water in a hydrocarbon matrix (hexane) using MIR fiber-optic evanescent field absorption spectroscopy. To model real world conditions where water is usually emulsified in an oil-like matrix, an optical fiber was immersed in a hexane-water mixture placed in a blender (**Figure 6.1**). Continuous turbulent stirring of the mixture (at 3000 RPM) caused formation of a water-

in-hexane emulsion. This emulsion created without any surfactant addition is representative of a macro-emulsion with droplets ranging in size from several microns to tens of microns [22, 23].

From the initial trials, it was evident that the experimental setup allows monitoring of the components within this turbid mixture (**Figure 6.3**). Water has a very intense and broad absorption feature observed from 3750–2750 cm^{-1}, which corresponds to the O-H stretch, as well as a strongly absorbing H-O-H bending mode that occurs at 1750–500 cm^{-1}. The lowest intensity absorption from approx. 2375–1875 cm^{-1} is the 3rd libration overtone. The libration mode - also called frustrated rotation - exhibits an intense absorption feature at < 1000 cm^{-1} [24]. In this study, the most intense O-H absorbance water peak was used for detection of water in hexane, as shown in **Figure 6.3a**. Crude oil, from which industrial oil and petroleum products are derived, exhibits strong signatures at 2940–2880 cm^{-1}, which represent C-H stretch and C-H bending vibrations in the range of 1500–1350 cm^{-1} [25]. It is evident that hexane, which is a hydrophobic substance such as crude oil, has an IR spectrum very similar to oil, and may thus be used as a surrogate during the present initial experiments (**Figure 6.3b)**.

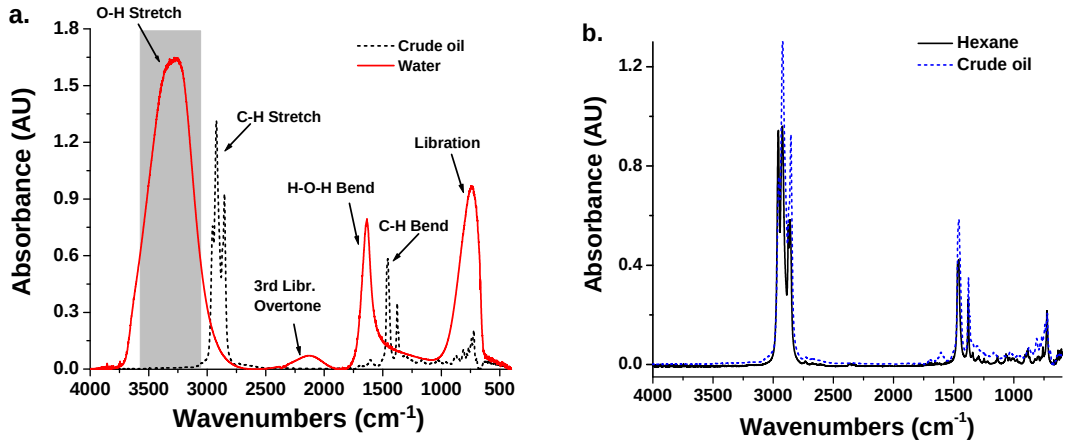

Figure 6.3: Overlap of IR-ATR spectra of (a.) water and crude oil, (b.) hexane and crude oil.

6.4.1 Unmodified fiber

First, an experiment using unmodified AgX fibers was conducted to detect how an increase in water concentration in hexane affects the IR signature of the emulsion**.** Water from 0-0.1% was added to the constantly stirred hexane matrix while the IR spectra were continuously acquired (**Figure 6.4a, Table 6.1**). Note that the size of the liquid droplets in the emulsions was shown not to vary at low concentrations of the dispersed phase, if the stirring parameters were kept constant [23, 26, 27]. Therefore, changes in the IR spectra (as the concentration of water is increased) cannot be associated with changes in diameter of the water droplets.

As illustrated by the arrows in **Figures 6.4a and b,** the absorbance intensity of water increases with water addition. The obtained results (**Figure 6.4c**) also demonstrate that water apparently replaces hexane from the sensing region at the fiber surface (i.e., the evanescent field). Once the water content in the system reaches 0.1%, the absorbance

intensity remains the same as for 0.8% (**Figure 6.4b**). This indicates that at these relatively higher concentrations additional water molecules are apparently not detected within the evanescent field of the AgX fiber. In fact, it can be estimated from **Figure 6.4b** that the absorbance intensity stops increasing at ~ 0.06%, as shown in **Figure 6.4b, d**. This indicates that above this concentration additional water molecules are not detected anymore by the evanescent field, as the entire fiber is covered with a layer of water. The thickness of the water layer can be estimated to be much higher than the evanescent filed of the optical fiber, since as mentioned previously formed water droplets are on the range of 1 to 10 μm in diameter.

Figure 6.4e yet demonstrates that concentrations from 0 to 0.06% follow a linear trend; thus, a first order linear calibration curve was established for this concentration regime (**Figure 6.4e)**. Note that for water concentrations below 0.02% (e.g., 0.01%), a very low water IR signal was observed, which did not allow reasonable quantification. Therefore, the unmodified optical fiber enabled the quantitative detection of water in the hexane matrix in the range of concentrations between 0.02 and 0.06% (200-600 ppm).

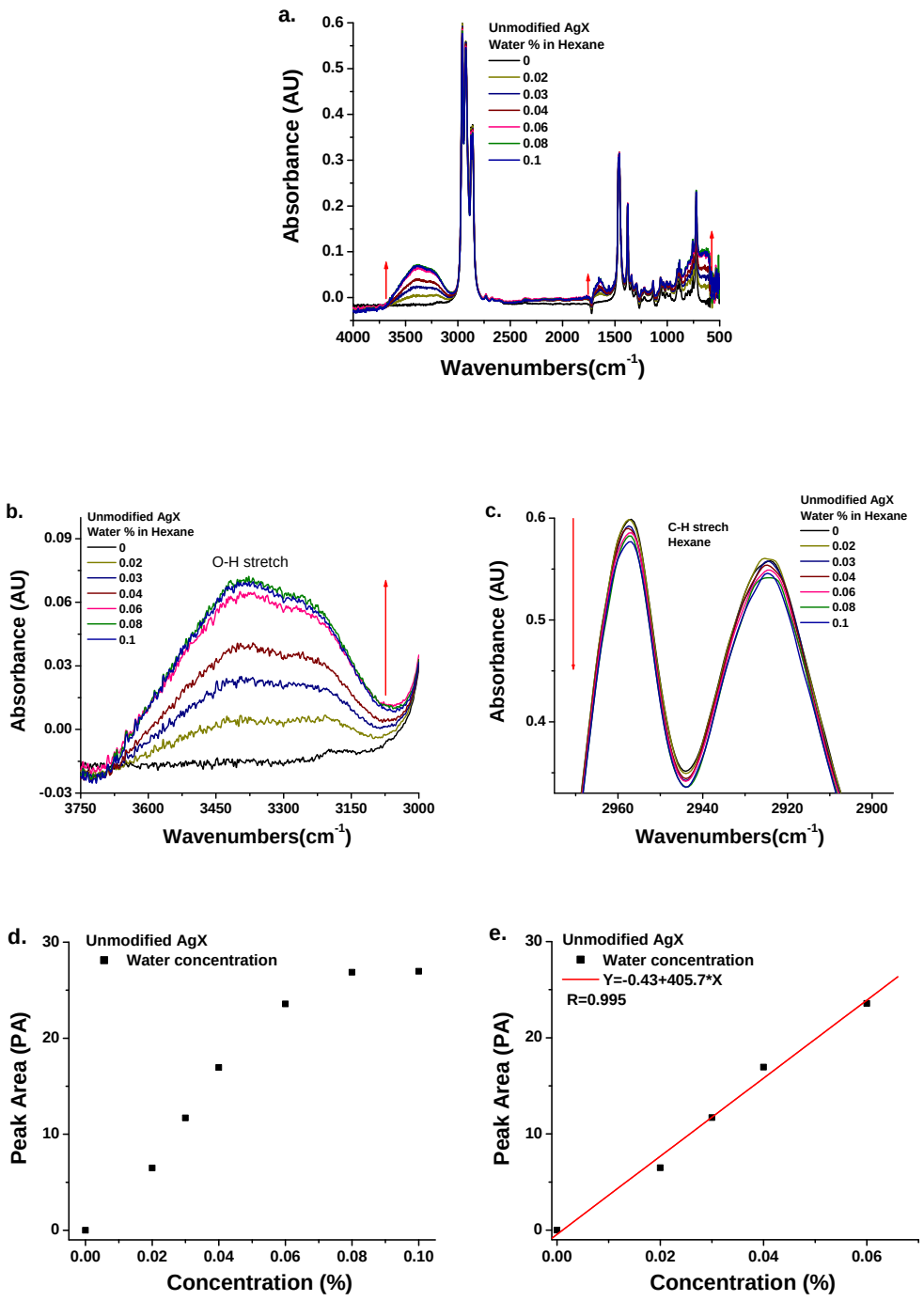

Figure 6.4: (a) IR-ATR spectra of 0-0.1% water in hexane using AgX fiber with no polymer coating, (b) enlarged region of O-H stretch of water, (c) enlarged region of C-H stretch of hexane, (d) PA of O-H stretch, (e) first order linear calibration function.

Table 6.1: Parameters for establishing calibration curves (± number represents standard deviation).

Concentration (%)	Concentration (ppm)	Peak Area (AU)
Unmodified AgX fiber (Range 0-600 ppm)		
0	0	0
0.02	200	6.49
0.03	300	11.69
0.04	400	16.94
0.06	600	23.56
y=-0.43+405.7*x, R=0.995		
PAA modified AgX fiber (Range 0-1000 ppm)		
0	0	0
0.01	100	3.85
0.02	200	22.23
0.03	300	30.42
0.04	400	33.74
0.06	600	44.89
0.08	800	51.26
0.1	1000	59.63
y=93.78(15.65*x)/(1+15.65*x)		
PAA-Sn modified AgX fiber (Range 0-1000 ppm)		
0	0	0±2.4
0.00007	0.7	0.73±1.06
0.00014	1.4	0.96±1.06
0.001	10	2.56±1.36
0.003	30	3.17±2.07
0.005	50	3.61±0.8
0.01	100	10.38±0.33
0.02	200	16.88±1.39
0.03	300	22.67±2.1
0.04	400	30.31±5.28
0.06	600	38.13±2.98
0.08	800	47.90±1.85
0.10	1000	51.64±5.56
y=88.35(12.84*x)/(1+12.84*x) LOD 76 ppm & LOQ 170 ppm Threshold sensitivity 10 ppm		

The IR response from water is apparently associated with water droplets accumulating at the fiber surface (**Figure 6.5)**.

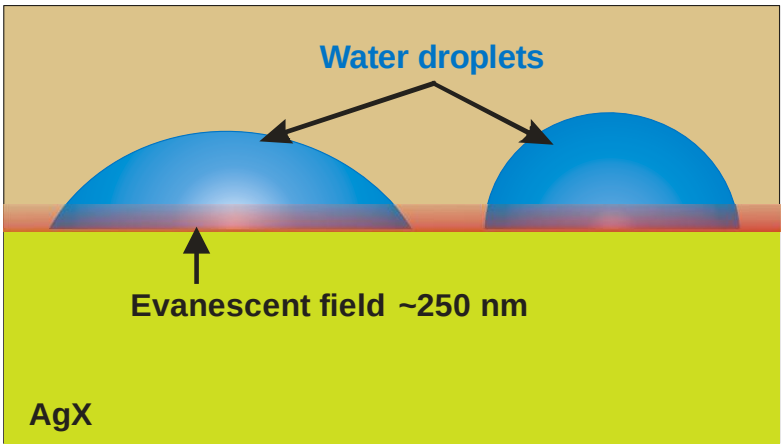

Figure 6.5: Accumulation of water droplets at the PAA-Sn modified (left) and unmodified (right) AgX fiber surface (figure is not to scale).

Once a droplet is interacting with the fiber surface, two scenarios may be occurring. In the first scenario, the droplet spreads across the fiber surface to maximize the contact area with the surface. The tendency of a material to spread across a surface in a matrix of another material is described via the spreading coefficient [28, 29]:

$$\lambda_{31} = \gamma_{12} - \gamma_{32} - \gamma_{13} \ , \qquad \text{Equation 6.1}$$

where γ_{12}, γ_{32} and γ_{13} are the interfacial energies (tensions) for each component pair. In our case, λ_{31} is the spreading coefficient of water (component 3) at the fiber (component 1). Index 2 refers to the hexane matrix. λ_{31} must be positive for matrix 3 (water) to spread across matrix 1 (fiber) in the presence of matrix 2 (hexane). If λ_{31} is

negative, the second possible scenario is in effect—the droplet of water in contact with the fiber surface will reveal a certain value of a contact angle (θ), which can be estimated from the following equation [30]:

$$Cos\theta = \frac{\gamma_{12} - \gamma_{13}}{\gamma_{32}} \qquad \text{Equation 6.2}$$

The spreading of the water layer across the fiber surface in principle should provide the optimum sensitivity of this IR method for the water detection, since maximum amount of material would be located within an evanescence wave region (~250 nm from the fiber surface [16]). The maximum sensitivity for the detection of water for the contact angle scenario will depend on the value of the angle. Indeed, from straightforward geometric considerations it is evident that at lower values of the contact angle more water molecules contained within the droplet would be located within the evanescent field **(Figure 6.5)**. To differentiate between the scenarios, the interfacial energies for each component pair were estimated from the following equation [31]:

$$\gamma_{ab} = \gamma_a + \gamma_b - \frac{4.\gamma_a^d.\gamma_b^d}{\gamma_a^d + \gamma_b^d} - \frac{4.\gamma_a^p.\gamma_b^p}{\gamma_a^p + \gamma_b^p}, \qquad \text{Equation 6.3}$$

where subscripts *a* and *b* represent components, and superscripts *d* and *p* refer to the dispersive and polar contributions to the surface energy γ, respectively. The dispersive and polar contributions to the surface energy can be obtained from contact angle measurements using the following expressions [32]:

$$\gamma = \gamma^d + \gamma^p \qquad \text{Equation 6.4}$$

$$1+Cos\theta \approx 2\left[\frac{(\gamma_S^d)^{0.5}(\gamma_L^d)^{0.5}}{\gamma_L}+\frac{(\gamma_S^p)^{0.5}(\gamma_L^p)^{0.5}}{\gamma_L}\right], \qquad \text{Equation 6.5}$$

where γ_S^d, γ_S^p and γ_L^d, γ_L^p are the dispersive and polar components for the surface energy of a solid (γ_S) and liquid (γ_L), respectively. These equations permit the derivation of γ_S, γ_S^d, and γ_S^p via measurements of the contact angles of two liquids if γ_L, γ_L^p, and γ_L^d for both liquids are known.

The contact angles at the optical fiber surface were determined for water and hexadecane in the course of this study, and the spreading coefficient and contact angle for the hexane/water/fiber system were estimated. The results of our evaluations (along with the parameters used) are presented in **Tables 6.2 and 6.3**. Thermodynamics indicate ($\lambda_{31} < 0$) that there is no spreading of the water across the fiber surface in the hexane matrix. Conversely, a relatively high contact angle (82^o) is formed if a water droplet is in contact with the unmodified fiber surface. Therefore, the AgX waveguide-sensing platform may achieve a further increase in sensitivity and a better LOD of water in the hydrocarbon matrix via surface modification of the fiber surface. To conduct further experiments on detection and quantification of the water content in hexane at lower concentrations and over a more extended concentration range, the surface properties of the silver halide fiber were modified to make it more hydrophilic.

Table 6.2: Surface energies and contact angles for liquids and substrates.

Substance	γ, mJ/m^2	γ^d, mJ/m^2	γ^p, mJ/m^2	**Contact angle, degree**	
				Water	**Hexadecane**
original fiber	46.1	27.25	19.8	58	5
PAA-Sn film	63.10	26.25	36.85	32	5
PAA-Sn film swollen in water*	66.5	41.8	41.8	N/A	N/A
Water**	72.8	21.8	51	N/A	N/A
Hexadecane**	26.35	26.35	0	N/A	N/A
Hexane***	18.4	18.4	0	N/A	N/A

* Estimated from PAA-Sn and water values assuming parameters to vary linearly with the volume fraction of the components

*** from Ref. [32]

** From Ref.[33]

Table 6.3: Thermodynamic parameters for oil/water/fiber system

Parameter	**Unmodified fiber**	**Fiber modified with PAA-Sn**	**Fiber modified with PAA-Sn swollen in water**
γ_{12}, mJ/m^2	21.2	38.2	42.7
γ_{32}, mJ/m^2	51.3	51.3	51.3
γ_{13}, mJ/m^2	14.2	2.3	1.1
λ_{31}, mJ/m^2	-44.3	-15.7	-9.7
Contact angle*, degree	82	46	36
W_A, mJ/m^2	58.3	86.8	93

**Contact angle is calculated for water on fiber in hexane matrix*

6.4.2 Modified fiber

6.4.2.1 *PAA coating*

The silver halide fiber was modified with a coating comprising hydrophilic and water soluble polyacrylic acid (PAA) to increase the fiber surface hydrophilicity. Specifically, a thin layer of the polymer was deposited at the fiber surface by dip coating from ethanol solution followed by annealing. A layer of the same solution was likewise deposited at the surface of a silicon wafer. Ellipsometry performed for the film coated at the wafer indicated that a film of ~40 nm was achieved. **Figure 6.6** shows AFM images of the unmodified fiber along with the fiber modified with a PAA layer. The difference in surface morphologies indicates that the PAA layer was deposited at the fiber surface.

In addition, the solubility of the PAA film in hexane and water was tested. For this purpose, the wafers covered with the PAA layer were immersed in hexane and water for 30 minutes. Ellipsometric measurements revealed that hexane does not remove the layer from the surface. Conversely, treatment with water removed the film from the wafer surface leaving just 1-2 nm of adsorbed PAA layer as a residue. Nevertheless, IR measurements using the fiber modified with PAA film were performed on the presumption that an abundance of hexane in the system prevents PAA removal.

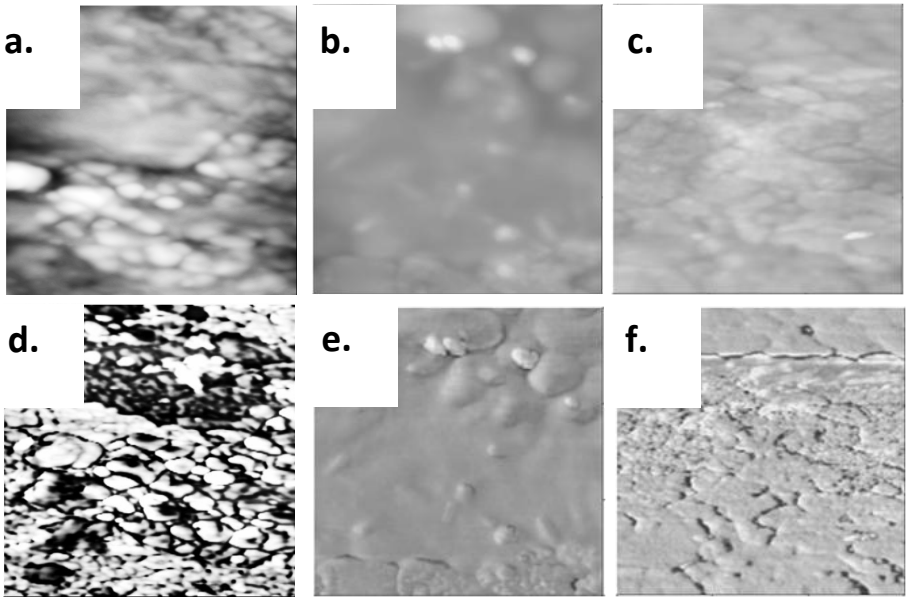

Figure 6.6: AFM topographical (a.-c.) and phase (d.-f.) 1.5 x1.5 μm images of: (a and d) unmodified fiber; (b. and e.) fiber modified with PAA layer; (c. and f.) fiber modified with PAA-Sn layer. For topography images the vertical scale is 200 nm. For the phase images the vertical scale is 100 degrees.

In the experiments involving the modified fiber, the water concentration in the hexane matrix was varied from 0 to 0.35% (**Figures 6.7a-c)**. The spectroscopic data demonstrate that the absorbance associated with the O-H stretch increases with increasing water content. The absorbance also shows a higher intensity than that observed for the unmodified fiber for the same water content (**Figures 6.4 and 6.7**). This indicates that water interacts more intensly with the modified surface. Once the water concentration reaches 0.25%, the signal associated with water does not increase any further. From **Figures 6.7b and c** it is evident that water at 0.02% in hexane may be detected, which is similar to the experiment using no PAA film. The plot in **Figure 6.7c** may be described by a Langmuir-type equation for surface coverage [34]:

$$A = \frac{A_{max}(K \times c)}{1 + K \times c}, \qquad \text{Equation 6.6}$$

where A is the absorbance intensity, K is the effective equilibrium constant, and c represents the concentration (the parameters used can be found in Table 6.1.). However, reproducing this data was challenging, as there were large deviations and a drop in sensitivity observed. The explanation for this was the partial dissolution of the PAA layer by the thin water film attracted to the surface. It is important to note in **Figure 6.7a** that with time there is a decrease in the absorbance intensity observed for the peaks at ~1720 cm^{-1} and 1300-1200 cm^{-1}, which are representative absorption features of the PAA film (IR spectra of PAA, **Figure A-2.2**). The absorbance intensity of these peaks is decreasing (becomes negative) as the water concentration increases in the solution. Even though we were able to establish a quantitative trend in **Figure 6.7c**, the obtained data is

not sufficiently reproducible and thus of limited practical utility due to the instability of the polymer coating over time.

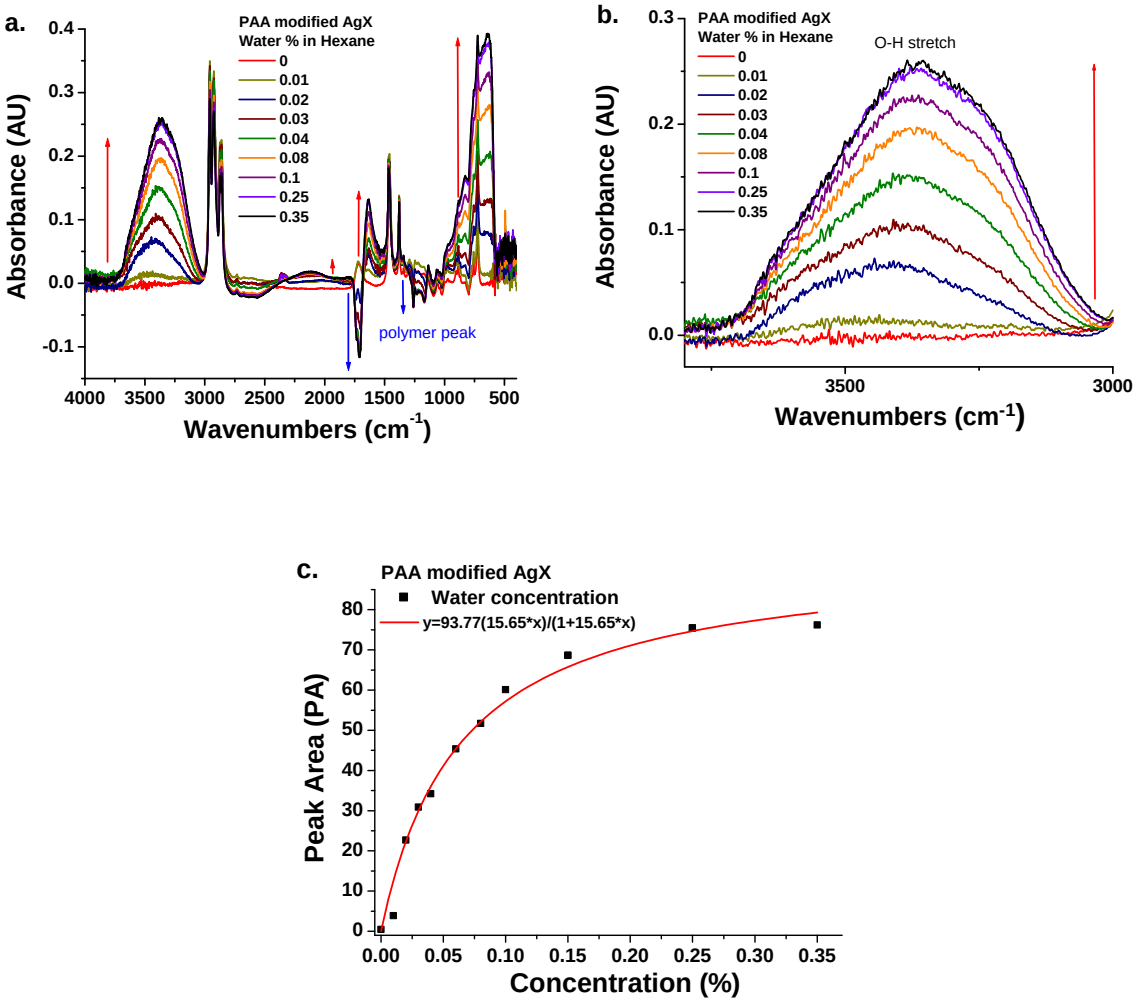

Figure 6.7: (a.) IR-ATR spectra of 0-0.55% water in hexane using AgX fiber coated with 40 nm thick PAA polymer film, (b.) enlarged region of O-H stretch of water, (c.) best fit calibration curve based on a Langmuir-type surface coverage.

6.4.2.2 PAA-Sn cross-linked coating

The next step in this study was to improve the stability of the PAA coating to prevent its removal from the fiber surface upon the addition of water. Specifically, to stabilize the hydrophilic film the PAA layer was cross-linked after deposition. It is well-known that increasingly cross-linked polymers are less soluble [35]. PAA was crosslinked with tin ions, which are insoluble in water PAA-Sn salt. The cross-linking mechanism is shown in **Figure 6.8** (the detailed procedure has been described in the experimental section). AFM and ellipsometry studies using silicon wafers as a substrate have confirmed that the cross-linked polymer layer remains stable in water and hexane. Next, the AgX fiber was coated with ~90 nm of the PAA-Sn film. The thickness of the coating was determined using ellipsometry at the model substrate (the silicon wafer). Again, AFM imaging confirmed the deposition of the coating at the fiber surface (**Figures 6.6c and f**).

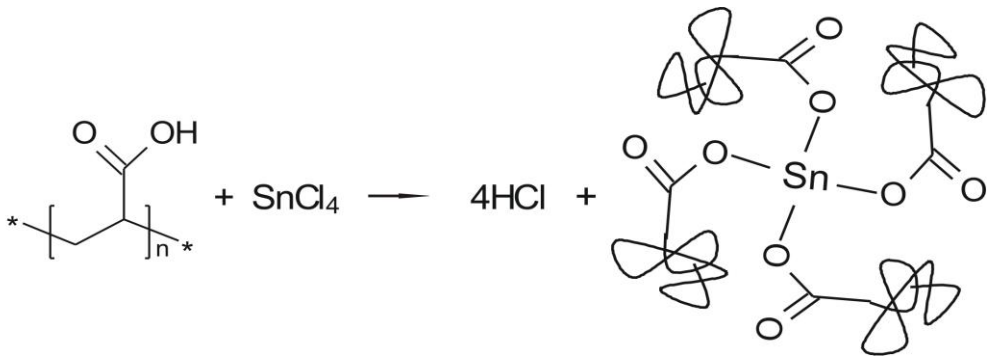

Figure 6.8: Schematic of PAA cross-linking using $SnCl_4$.

The sensing performance of the AgX fiber coated with the PAA cross-linked film was tested with the stirring cell setup. Water was added to hexane starting from 0 to

0.15% (**Figure 6.9)**. As illustrated by arrows in **Figures 6.9a and b,** the absorbance intensity of water increases with the addition of water. The obtained results (**Figure 6.9c**) also demonstrate that the water replaces hexane from the sensing region of the fiber (evanescent field). The absence of the negative peak associated with the removal of PAA from the surface confirmed the stability of the coating. In general, the water absorbance peaks give higher intensity than those observed for the unmodified fiber for the same water content (**Figures 6.4 and 6.9**). This indicates that water interacts stronger with the modified surface.

Figure 6.9b clearly shows that at 0.001% (10 ppm) of water in hexane the O-H peak remains clearly detectable in the IR spectra. (Note that this experiment was reproduced three times.) The peak area (PA) of each O-H absorption feature was integrated to establish a calibration function to correlate absorbance vs. concentration of water in hexane from 0.00007 to 0.16% (saturation limit of the polymer film), as shown in **Figure 6.9d**. The error bars represent the standard deviation (calculated from consecutive three measurements). **Table 6.1** summarizes the fit parameters for the calibration equation. The fit equation again follows a Langmuir-type equation (Equation 6.6) for surface coverage. A LOD of 76 ppm and a LOQ of 170 ppm of water in hexane were extracted from the calibration plot.

To estimate the threshold sensitivity of the system the concentration range < 0.01% water in hexane was enlarged, as shown in **Figure 6.9e**. At 0.0001% (1 ppm) water in hexane, the PA values are slightly higher compared to 0% water; however, these changes are very small and do not facilitate a quantitative evaluation. The PA value of 0.001% (10 ppm) is considerably higher than 0% and is clearly discernable (**Figures 6.7b**

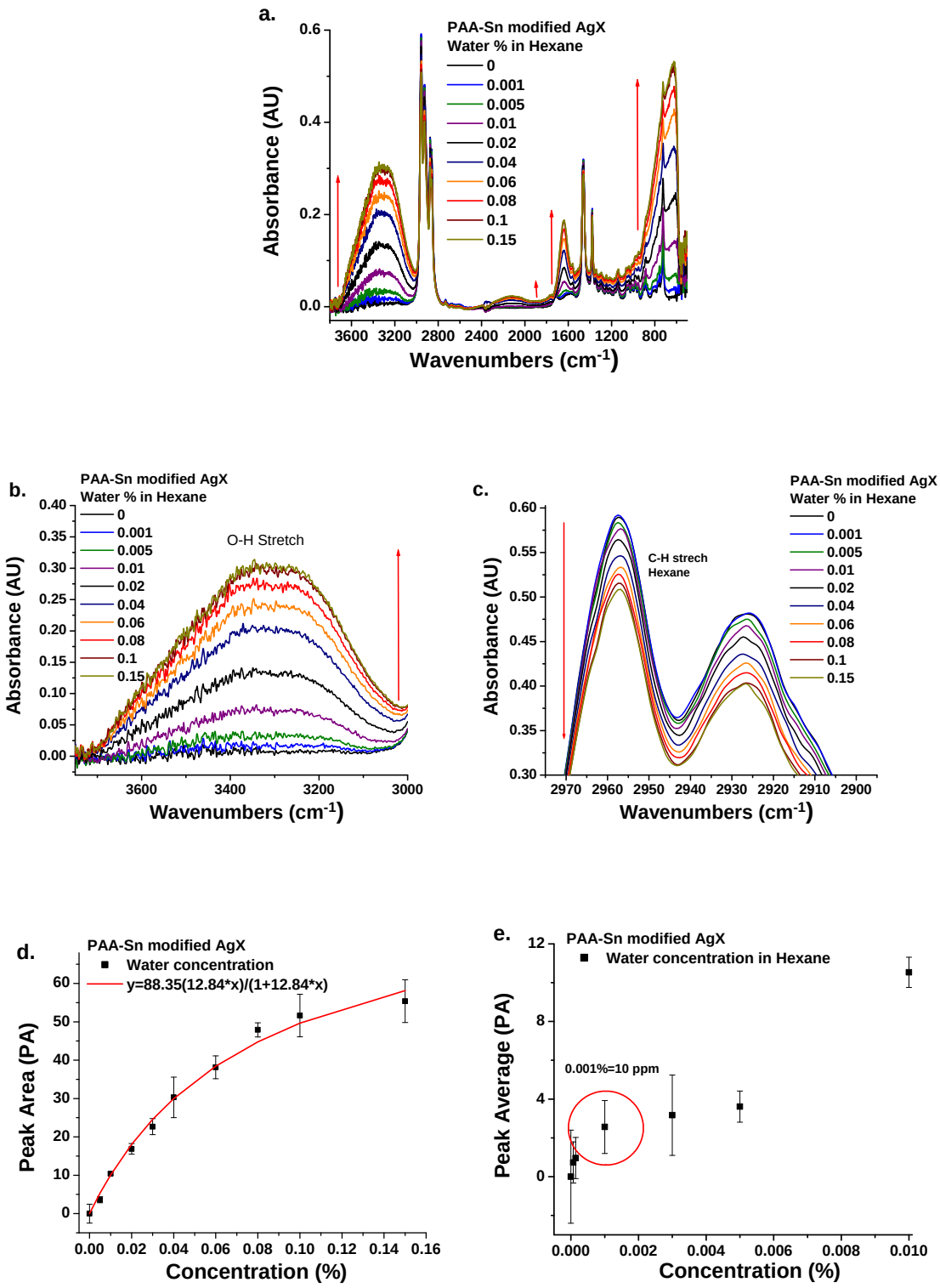

Figure 6.9: (a) IR-ATR spectra of 0-0.15 % water in hexane, **(b)** enlarged O-H stretch of water, **(c)** enlarged C-H stretch of hexane **, (d)** best fit calibration curve (Langmuir type), **(e)** PA of water (0-0.01 %) in hexane.

and e). These findings indicate that our experimental setup may detect 10 ppm of water in hexane; to the best of our knowledge, these are the lowest values reported for comparable IR techniques, and even for other sensing strategies.

The obtained results demonstrate that with the application of a stable polymer layer at the waveguide surface the sensitivity was significantly improved. We explain this improvement with the thermodynamically more favorable interaction between water and the fiber surface in the hexane matrix. Thermodynamic calculations (using **Eqs. 6.1-5, Table 6.3**) revealed that the surface modification of the fiber with the hydrophilic polymer does not cause spreading of the water at the modified fiber surface in the hexane matrix ($\lambda_{31} < 0$). However, the contact angle of water at the fiber for the hexane/water/fiber system decreases significantly—from 82 to 46 ^{o} (**Figure 6.4,** right and left, respectively). Therefore, the amount of water contributing to the IR signal increases, since more molecules per (1-10 μm) droplet are sensed by the evanescence field (propagating up to ~250 nm above the fiber surface). In fact, one can estimate (calculations in appendix A-2) that the contact area for a water droplet increases approx. 2 times, if the contact angle decreases from 82^{o} (unmodified fiber) to 46^{o} (PAA-Sn modified fiber). Note that at concentrations below the saturation limit the IR signal is approx. 1.5 times stronger for the modified fiber than for the unmodified one (**Figures 6.4d and 6.9d**). This observation is in accordance with the contact angle estimations.

Another important factor for practical applications is the swellability of the PAA-Sn film in water, which may contribute via enrichment to the obtained signal. To this end, swelling studies at these films in the presence of water and hexane vapors were performed using ellipsometry. The layer demonstrated a relatively high affinity to water

(35% swelling, the polymer layer thickness increased to approx. 120 nm), and a low affinity to hexane (0.5% swelling). The swellability results demonstrated that at low concentrations the sensitivity is further promoted by the penetration of water into the PAA-Sn film acting as an enrichment layer. Therefore, the wettability parameters were reevaluated taking swelling into account. Specifically, the surface energy of the swollen polymer film was assumed to vary linearly with the volume fraction of the constitutive PAA-Sn and water components (**Table 6.2**). These thermodynamic calculations (**Table 6.3**) indicate that even for the swollen film there is no spreading of water across the fiber in hexane ($\lambda_{31} < 0$). In fact, the contact angle of water on the fiber covered with the swollen PAA-Sn film for the hexane/water/fiber system decreases from 46 to 36 ^{o}.

Besides the difference in the extent of water-fiber contact area, the improved performance of the coated fiber can be explained by the increased adhesion between the water droplet and fiber surface for the modified fiber. The level of adhesion may be approximated via the work of adhesion, W_A, defined as the reversible work required to separate a unit area of liquid from a substrate [29, 36]. In the case of the hexane/water/fiber system considered in this work, the work of adhesion is defined as:

$$W_A = \gamma_{12} + \gamma_{32} - \gamma_{13} \qquad \text{Equation 6.7}$$

The higher the resulting value of W_A, the stronger the adhesion between the water droplet and the fiber surface. Calculations of W_A for the modified and unmodified fibers are reported in **Table 6.3**. The work of adhesion is approximately 30% higher for the surface modified with the PAA-Sn layer. Additionally, taking into the account the extent of surface contact between the water droplet and the AgX fiber, which is approx. 2 times

higher for the modified fiber (see calculations in **Appendix Section A-2.3**), the work of adhesion per droplet becomes approximately 60% higher for the PAA-Sn modified AgX fiber. Therefore, in the constantly stirred hexane matrix, the probability of attachment of a water droplet to the fiber surface is higher for the modified fiber. In analogy, the probability of detachment of an already attached droplet is lower for the modified fiber.

6.5 CONCLUSIONS

In this study, MIR evanescent field absorption spectroscopy was used to detect and quantify the concentration of water in hexane. An unmodified fiber enabled the detection of the presence of water in hexane to a level 0.02% (200 ppm) water in hexane. The application of a PAA-Sn polymer layer at the silver halide fiber surface enabled the on-line MIR detection of water in hexane to a level of10 ppm. To the best of our knowledge, this is the only IR-based sensing technique detecting such low concentrations of water in an organic matrix. It is hypothesized that the enhanced performance of the modified fiber is associated with an increased level of water/fiber wettability, and increased water/fiber adhesive interactions for the fiber covered with the PAA-Sn layer. Additionally, the swellability of the PAA-Sn film in water may add to the increase in sensitivity by enrichment effects.

6.6 OUTLOOK

This chapter represents an advance toward utilizing MIR fiber-optic evanescent field sensors with appropriate polymer modified waveguides for in-situ low level

detection of trace amounts of water in petroleum products and industrial oils. The determined LOD and LOQ are competitive with other laboratory methods and with commercially available techniques; however the reproducibility must be improved, especially at low ppm levels. Construction of a modified stirring cell is suggested with an optimized alignment of the optical elements and the fiber enabling to eliminate the realignment procedure for every new measurement, which adds to the variance. Additionally, the stirring cell should provide flow-through capabilities, which will enable more flexibility for measuring different concentrations. A precisely controlled stirring system should be added to the modified stirring cell.

Furthermore, the length, diameter, and shape of the AgX fiber may be further optimized. An enhancement of the evanescent field sensitivity could be achieved by tapering the fiber within the measurement region, as previously shown [16]. In addition, MCT detectors with higher sensitivity in the 3-5 μm region (water absorption region) could be applied, which would further improve the sensitivity for the detection of water.

6.7 REFERENCES:

(1) Van De Voort, F. R.; Sedman, J.; Cocciardi, R.; Juneau, S. "An automated FTIR method for the routine quantitative determination of moisture in lubricants: An alternative to Karl Fischer titration" *Talanta* **2007**, *72*, 289-295.

(2) Shishigin, A. A.; Bel'ganovich, V. I. "Change in engine oil quality due to water contamination " *Chemistry and Technology of Fuels and Oils* **1976**, *12*, 147-150.

(3) Duncanson, M., Tulsa, OK 2005; Noria Corporation.

(4) Araujo, A. M.; Santos, L. M.; Fortuny, M.; Melo, R.; Coutinho, R. C. C.; Santos, A. F. "Evaluation of water content and average droplet size in water-in-crude oil emulsions by means of near-infrared spectroscopy" *Energy & Fuels* **2008**, *22*, 3450-3458.

(5) Young, W. C.; Roberton, R. S. *Turbine oil monitoring* Baltimore, MD, 1989.

(6) Foster, N. S.; Amonette, J. E.; Autrey, T.; Ho, J. T. "Detection of trace levels of water in oil by photoacoustic spectroscopy" *Sensors and Actuators B-Chemical* **2001**, *77*, 620-624.

(7) Higgins, F.; Seelenbinder, J.; Analytical Instrumentation, FT-IR spotlight, September/August 2008.

(8) ASTM D6304: Standard Test Method for Determination of Water in Petroleum Products, L. O., and Additives by Coulometric Karl Fischer Titration, ASTM International Standards.

(9) Van De Voort, F. R.; Sedman, J.; Yaylayan, V.; Saint Laurent, C.; Mucciardi, C. "Quantitative determination of moisture in lubricants by Fourier transform infrared spectroscopy" *Applied Spectroscopy* **2004**, *58*, 193-198.

(10) Blanco, M.; Coello, J.; Iturriaga, H.; Maspoch, S.; Gonzalez, R. "Determination of water in lubricating oils by mid- and near-infrared spectroscopy" *Mikrochimica Acta* **1998**, *128*, 235-239.

(11) Borin, A.; Poppi, R. J. "Application of mid infrared spectroscopy and iPLS for the quantification of contaminants in lubricating oil" *Vibrational Spectroscopy* **2005**, *37*, 27.

(12) Zhao, Y.; Yang, J.; Wang, J. Q.; Gui, F. X. "High-accuracy low-water-content measurement of crude oil based on a near-infrared spectral absorption method" *Optical Engineering* **2004**, *43*, 2216-2217.

(13) Toms, L. A. In *Machinery Oil Analysis: Methods, Automation and Benefit,Coastal Skills Training*, 2nd ed.: Virginia Beach, 1998.

(14) Minty, B.; Ramsey, E. D.; Davies, I. "Development of an automated method for determining oil in water by direct aqueous supercritical fluid extraction coupled on-line with infrared spectroscopy" *Analyst* **2000**, *125*, 2356-2363.

(15) Mizaikoff, B. "Mid-infrared evanescent wave sensors - a novel approach for subsea monitoring" *Meas. Sci. Technol.* **1999**, *10*, 1185-1194.

(16) Mizaikoff, B. "Mid-IR Fiber-optic Sensors" *Analytical Chemistry* **2003**, *75*, 258A-267A.

(17) Mizaikoff, B.; Jakusch, M.; Kraft, M. "Infrared fiber-optic sensors - Versatile tool for water monitoring - Optical chemical sensors gain importance in environmental monitoring, process analysis/control; Now complement separation techniques and spectroscopy" *Sea Technol.* **1999**, *40*, 25.

(18) Heinrich, P.; Wyzgol, R.; Schrader, B.; Hatzilazaru, A.; Luebbers, D. W. "Determination of organic compounds by IR/ATR spectroscopy with polymer-coated internal reflection elements" *Appl. Spectrosc.* **1990**, *44*, 1641-1646.
(19) Janotta, M.; Karlowatz, M.; Vogt, F.; Mizaikoff, B. "Sol-gel based mid-infrared evanescent wave sensors for detection of organophosphate pesticides in aqueous solution" *Analytica Chimica Acta* **2003**, *496*, 339-348.
(20) Karlowatz, M.; Kraft, M.; Mizaikoff, B. "Simultaneous quantitative determination of benzene, toluene, and xylenes in water using mid-infrared evanescent field spectroscopy" *Anal. Chem.* **2004**, *76*, 2643-2648.
(21) Dobbs, G. T.; Balu, B.; Young, C.; Kranz, C.; Hess, D. W.; Mizaikoff, B. "Mid-infrared chemical sensors utilizing plasma-deposited fluorocarbon membranes" *Analytical Chemistry* **2007**, *79*, 9566-9571.
(22) Eley, D. D.; Hey, M. J.; Symonds, J. D. "Emulsions of water in asphaltene-containing oils 1. Droplet size distribution and emulsification rates" *Colloids and Surfaces* **1988**, *32*, 87-101.
(23) Aske, N.; Kallevik, H.; Sjoblom, J. "Determination of Saturate, Aromatic, Resin, and Asphaltenic (SARA) Components in Crude Oils by Means of Infrared and Near-Infrared Spectroscopy" *Energy & Fuels* **2001**, *15*, 1304-1312.
(24) Bayly, J. G.; Kartha, V. B.; Stevens, W. H. "The absorption spectra of liquid phase H2O, hdo and D2O from 0.7 mu-m to 10 mu-m" *Infrared Physics* **1963**, *3*, 211-222.
(25) Romero, M. T.; Ferrer, N. "Determination of oil and grease by solid phase extraction and infrared spectroscopy" *Anal. Chim. Acta* **1999**, *395*, 77-84.
(26) Mlynek, Y.; Resnick, W. "Drop sizes in an agitated liquid-liquid system" *AlChe Journal* **1972**, *18*, 122-127.
(27) Church, J.; Shinnar, R. "Stabilizing Liquid-Liquid Dispersions by Agitation" *Industrial & Engineering Chemistry* **1961**, *53*, 479-484.
(28) Luzinov, I.; Xi, K.; Pagnoulle, C.; Huynh-Ba, G.; Jerome, R. "Composition effect on the core-shell morphology and mechanical properties of ternary polystyrene/styrene butadiene rubber polyethylene blends" *Polymer* **1999**, *40*, 2511-2520.
(29) Sperling, L. H. *Polymeric Multicomponent Materials*; Wiley-Interscience New York, 1998.
(30) Jung, Y. C.; Bhushan, B. "Wetting Behavior of Water and Oil Droplets in Three-Phase Interfaces for Hydrophobicity/philicity and Oleophobicity/philicity" *Langmuir* **2009**, *25*, 14165-14173.
(31) Hobbs, S. Y.; Dekkers, M. E. J.; Watkins, V. H. "Effect of interfacial forces on polymer blend morphologies" *Polymer* **1988**, *29*, 1598-1602.
(32) Van Krevelen, D. W. *Properties of Polymers*, 3-rd ed.; Elsevier Amsterdam, 1997.
(33) Janczuk, B.; Wojcik, W.; Zdziennicka, A.; Bruque, J. M. "Components of the surface free energy of low rank coals in the presence of n-alkanes" *Powder Technology* **1996**, *86*, 229-238.
(34) Atkins, P., de Paula, J. *Physical Chemistry*, Seventh ed.; W.H. Freeman, 2002.
(35) Sperling, L. H. *Introduction to Physical Polymer Science*, Fourth ed.; Wiley-Interscience Hoboken, New Jersey, 2006.

(36) Cambiella, A.; Benito, J. M.; Pazos, C.; Coca, J.; Ratoi, M.; Spikes, H. A. "The effect of emulsifier concentration on the lubricating properties of oil-in-water emulsions" *Tribology Letters* **2006**, *22*, 53-65

CHAPTER 7

In-situ Analysis of Crude Oil in Water at ppb Concentrations Using Mid-infrared Fiberoptic Evanescent Field Spectroscopy

This chapter focuses on quantifying trace amounts of oil in water using mid-infrared (MIR) evanescent field absorption spectroscopy. Silver halide fibers were utilized as MIR waveguides to spectroscopically interrogate oil-in-water emulsions. Either unmodified fibers or fibers modified with grafted epoxidized polybutadiene layers were used for these studies. While unmodified fibers provided detection levels of oil at the ppm level, the surface modification of the fiber enabled the on-line MIR analysis of crude oil in water at ppb levels. Specifically, crude oil IR absorption signatures at levels of 46 ppb were still quantified. The proposed sensor system requires no sample preparation, and is based on a single measurement that can may be completed in a matter of few seconds.

7.1 MOTIVATION

Oil spills occur every day worldwide [1]. Large spills may cause extensive damage to marine life, terrestrial life, human health, and natural resources [1, 2]. Oil that enters the ocean comes from many sources, some being natural seepage, some being accidental spills or leaks, and some being the result of chronic and careless habits in the use of oil and oil products. The global volume of the natural seepage of petroleum is difficult to determine, but the best estimates are of the order of ~180 million gallons per year [3].

Additionally, a historical review and analysis of reported oil spills exceeding 10,000 gallons in the International Oil Spill Database [4] shows that since the early 1960s nearly 300 million gallons of oil have spilled into US marine waters, and approx. 200 million gallons of oil on US soil originates from land pipeline leaks [1, 5]. However, it is important to note that yearly consumption of petroleum products by US is approximately 7 billion gallons, thus comparatively only a very small fraction of oil is spilled [6]. Nevertheless, the impacts to the ecosystems, and the long-term effects of environmental pollution caused by oil contaminations are global concern [7]. Nowadays, oil spills along with their prevention, characterization, and remediation continue to be a widely researched topic of great concern in many countries. Therefore, early and unambiguous detection of trace amounts of oil in water is important for monitoring the health of ecosystems [8].

In recent years, the detection of hydrocarbons spilled at sea has been significantly advanced [9, 10]. Wang and Fingas have reviewed frequently used methods based on gas chromatography (GC) or GC coupled with mass spectrometry (MS) for the detection and characterization of oil spills and environmental forensic investigations [1]. These methods provide low parts per billion (ppb) sensitivity for the detection of crude oil in water [11]. However, there are some particular drawbacks associated with these methods, such as laborious sample collection and preparation, and substantial time required to perform the analysis. Moreover, it is difficult to design in-situ sensors utilizing these techniques [2].

In this respect, spectral techniques such as infrared (IR) spectroscopy represents a reliable option for providing rapid results with no or minimal sample preparation [12]. Today, a number of portable sensing systems are based on diamond single-reflection and/or multiple-reflection horizontal attenuated total reflection (ATR) devices [2, 12].

Sensors utilizing IR-ATR induced evanescent field absorption spectroscopy provide the capability of evaluating both viscous and highly absorbing samples in aqueous environments [13-15]. Other portable systems use fiber-optic probes whose sensing tips are constituted to operate in reflection mode for the direct measurement of samples [2]. Additionally, mid-infrared (MIR) spectroscopy coupled with multivariate pattern-recognition methods has been successfully applied to characterize oil pollutions [16-19]. Moreover, a variety of portable, commercial, hand-held MIR analyzers have been reported in the last few years [20, 21].

Despite of significant research conducted on MIR based sensors; the limits of detection (LOD) and sensitivity of these sensors have not been comparable to GC-MS based techniques for analyzing trace amounts of oil in water. As of recently, the best limits of detection for IR based methods were reached by extraction of crude oil into a nonpolar, hydrocarbon-free solvent followed by measurement of the infrared absorption spectrum of the extract [12, 22-25]. Most of these methods use 1,1,2-trichloro-1,2,2-trifluoroethane (CFC-113), tetrachloromethane, or carbon tetrachloride; however, these solvents are known ozone-depleting compounds [26-28]. A commercially available device by PerkinElmer requires tetrachloroethylene-assisted oil extraction followed by MIR spectrometry achieving a limit of detection of 0.5 mg/L (500 ppb) [29]. Romero and Ferrer have developed a procedure using solid-phase extraction, thereby avoiding the use of any kind of solvent, with a detection limit of 0.034 mg/L (34 ppb) (n-hexadecane was used as a model for oil)[24]. The use of separation techniques or solvent extractions prior spectroscopic analysis significantly slows down the detection process and makes these techniques less timely for in-situ analysis [12, 23, 30, 31].

Therefore, it is vital to develop straightforward-to-use, sensitive, cost-effective, rapid, and miniaturizable sensing techniques for on-site and in-situ analysis of crude oil in water. To this end, this chapter reports on design, construction, and testing of a sensitive MIR evanescent field fiber-optic sensor for the detection of crude oil pollutants in water.

7.2 INTRODUCTION

The in-situ determination of trace amounts of oil in water is beneficial for environmental forensic analysis of oil spills and contaminations. To this end, the study presented in this chapter is focused on quantifying trace amounts of oil content in water using MIR evanescent field absorption spectroscopy. To increase the sensitivity and improve the limit of detection, a waveguide-based sensing platform utilizing silver halide fibers was coated with a layer of a hydrophobic polymer (epoxidized polybutadiene, EPB), which attracts crude oil into the evanescent field sensing region. Polymer or polymer-like films have widely been deposited onto waveguide surfaces for enhancing the detection of various compounds [32-35]. The MIR fiberoptic sensing method developed herein provides a threshold sensitivity of 46 ppb of crude oil in water. To the best of our knowledge, this is the smallest amount of crude oil detected with MIR based technique without prior separation or solvent extraction reported in the open literature.

7.3 MATERIALS AND METHODS

7.3.1 Reagents and solution preparation

Natural crude oil supplied by ExxonMobil Research and Engineering Company (Annandale, NJ) was added to deionized (DI) water (R = 18.2 MΩ·cm at 25 °C). The mass of crude oil was determined using a GR-200 analytical mass balance (A&D Company, engineering Milpitas, CA). Since the amount of 0.0001 g is the smallest value possible to be measured with the GR-200 analytical mass balance, smaller concentrations were prepared by diluting 0.0006 g of oil in 10 mL of water. The volume of water used for dilution crude oil samples (<0.0006 g of crude oil) was measured using a 100–1000 μL Eppendorf pipette (Eppendorf North America Inc., New York, NY).

Polybutadiene (M_w = 424,540 g/mol, PDI 2.93 (GPC)) from Aldrich was epoxidized in $CHCl_3$ solution in the presence of stoichiometric (to double bonds) amounts of formic acid and 30% hydrogen peroxide [36]. The reaction was perfromed at room temperature for 4 hours. The degree of epoxidation was estimated from ^1H NMR studies [37]. The vinyl proton signal was used to monitor the extent of the reaction. The epoxidation yielded EPB with 60% molar content of epoxy groups. The epoxidation was conducted in collaboration with Dr. Zdyrko at Clemson University.

7.3.2 EPB layer deposition

Core-only silver halide fibers (AgX, X = $Cl_{0.3-0.4}Br_{0.7-0.6}$) purchased from JT Ingram Technologies Inc. were coated with an EPB layer by a dip-coating method (using DC Mono 160 dip-coater from NIMA Technologies Ltd.). This technique involved

dipping the fiber clamped at one end into a polymer solution (0.5% of EPB in chloroform from Spectrum). Prior to the deposition, the fiber was rinsed with methylethylketone (Spectrum) to remove possible contaminations. The coated fiber (protected from light) was allowed to dry in ambient air followed by annealing at 70^{o}C for two hours in an oven. The fiber was rinsed with chloroform to remove any ungrafted EPB macromolecules. The same experiment was conducted at a silicon wafer (Semiconductor Processing Co.) surface to determine the thickness and swellability of the grafted EPB layer via ellipsometry. The morphology of the EPB film was studied with atomic force microscopy (AFM).

7.3.3 Instrumentation and experimental setup

A detailed description of the instrumentation and characterization techniques used in this chapter can be found in **Section 6.3.3**. A block diagram and a description of the experimental setup can be found in section 6.3.4 (**Figure 6.1).**

7.3.4 Spectral data analysis

Each experiment using one AgX fiber was performed in triplicate. For all experiments reported in this chapter, five spectra were acquired for each sample concentration averaging 250 scans each in 80 s intervals at 2 cm^{-1} spectral resolution, thus measuring each concentration for the time period of approximately 6 minutes.

Using the OPUS software (Bruker Optics Inc., Billerica, MA), infrared absorption features of crude oil were evaluated by peak area analysis. Peak areas underneath the CH stretch feature at 2940 to 2880 cm^{-1} were integrated. Peak areas from each spectral

region collected during replicated measurements were averaged and used for further calculations. Consequently, from here on the three averaged peak areas for a given spectral region and respective sample mixture will be indicated as PA.

To establish quantitative calibration functions for analyzing crude oil in water, the PAs were plotted versus the amount of crude oil added to water in parts per million (ppm). The calculated limits of detection (LOD) and limits of quantification (LOQ) of oil in water were extracted from the calibration plot (LOD: 3σ concentration determination from the regression fit using the criterion of 3 times the noise of a blank sample. LOQ: 6σ concentration determination from the regression fit using the criterion of 6 times the noise of a blank sample).

7.4 RESULTS AND DISCUSSION

In order to model real-world conditions where oil is emulsified in water, an optical fiber was immersed into an oil-in-water mixture placed into a blender. Continuous turbulent stirring of the mixture (at 3000 RPM) caused the formation of an oil-in-water emulsion. This emulsion was created without any addition of surfactant, and is representative for macroemulsions with the size of droplets at the level of several micrometers [38]. Specifically, published results indicate that the size of the oil droplets in such emulsions is on the order of 10 to 100 microns [39-42]. From initial trials it was evident that the experimental setup allows spectroscopically monitoring the components of the mixture (**Figure 7.1**). Crude oil revealed strong signatures at 2940-2880 cm^{-1} (CH stretch) and 1500-1350 cm^{-1} (CH bending vibrations) [24]. In this study, the CH stretch region has been selected for quantitative due to the most intense absorption features of

hydrocarbons. The CH stretch overlaps with the OH stretch absorption feature of water (3750-2750 cm^{-1}) [43] (**Figure 7.1**). However, practically no interference with the measurements was observed, as the CH stretch is clearly detected on the shoulder of the OH stretch, therefore rendering the detection of crude oil straightforward. In future, multivariate calibration techniques may further enhance the sensitivity of such measurements by more elaborate quantification algorithms.

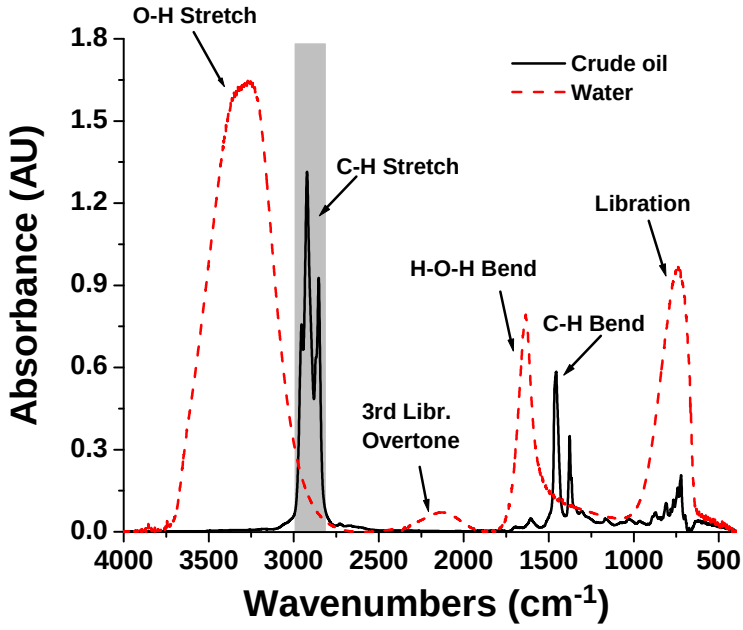

Figure 7.1: Overlay of the IR-ATR spectra of water and crude oil.

7.4.1 Unmodified fiber

Experiments using unmodified AgX fibers were conducted to detect how an increase of crude oil concentration in water affects the IR signature of the emulsion**.** Crude oil from 0 to 1022 ppm was added to constantly stirred water solutions, and IR

spectra were continuously acquired. It is necessary to highlight that the size of the oil droplets was shown not to vary at this low level of oil content, if the stirring parameters were kept constant [42]. Therefore, changes in the IR spectra (as the concentration of oil is increased) are not resulting from changes in the diameter of the oil droplets.

Figure 7.2a presents IR spectra of oil in water, as the oil concentration was increased from 0 to 1022 ppm. As illustrated by the arrows in **Figure 7.2a**, the absorbance intensity of the CH stretch increases as the crude oil concentration increases, and the absorbance intensity of the OH stretch associated with water decreases. The obtained result demonstrates that crude oil displaces water from the sensing region at the fiber surface (i.e., the evanescent field of the fiber). It is necessary to highlight that visual inspection of the fiber after a measurement confirmed that oil is present at the fiber surface. Once the oil content in the system reached 1022 ppm, the absorbance intensity remained similar to the signal obtained at 511 ppm (**Figure 7.2b**). These results indicate that at these relatively high concentrations additional oil is not detected anymore, as the AgX fiber is apparently fully covered with crude oil extending beyond the penetration depth of the evanescent field. In fact, it was estimated that the absorbance intensity stops increasing at approximately 283 ppm (**Figure 7.2c**).

The peak area (PA) of each CH absorption feature was integrated for three parallel measurements for establishing a calibration function to correlate absorbance versus concentration of crude oil in water from 0 to 1022 ppm. **Table 7.1** summarizes the fit parameters for establishing the calibration functions.

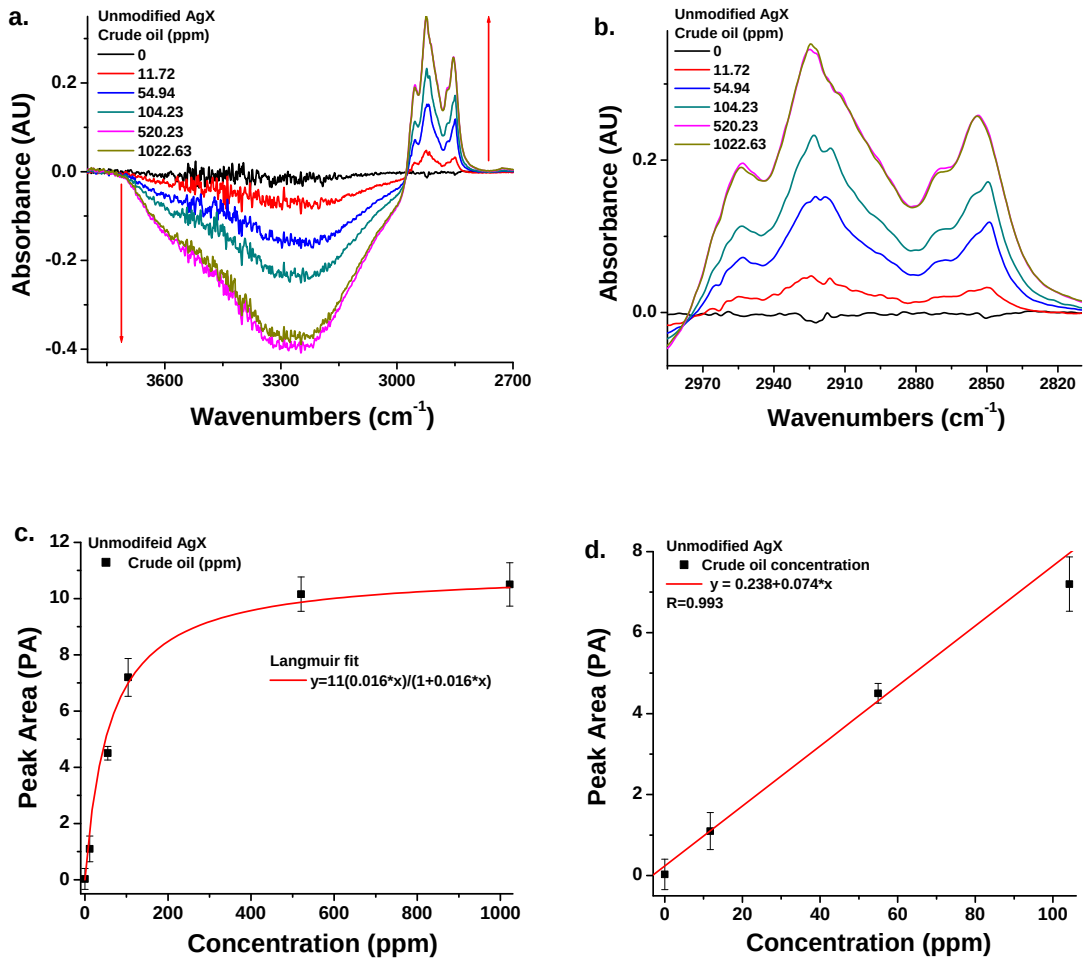

Figure 7.2: Unmodified fiber. (a.) IR spectra of crude oil content in water as oil concentration increases from 0-1022 ppm, (b.) enlarged region of C-H stretch of crude oil, (c.) Langmuir-type fit, (d.) first order liner calibration curve.

Table 7.1: Parameters for establishing calibration curves (± number represents standard deviation).

Concentration (mg)	Concentration (ppm)	Peak Area (AU)	Standard deviation
Unmodified AgX fiber (Range 0-1023 ppm)			
0	0.00	0.029	0.375
8.2	11.71	1.099	0.456
38.46	54.94	4.501	0.244
72.98	104.26	7.199	0.671
364.16	520.23	10.160	0.613
715.84	1022.63	10.504	0.770
Langmuir like fit: yy=11(0.016*x)/(1+0.016*x) LOD 7 ppm & LOQ 16 ppm		First order linear: y = 0.238+0.074*x, R=0.99 LOD 12 ppm & LOQ 27 ppm	
EPB modified AgX (Range 0-215 ppm)			
0	0.00	0.061	0.066
0.6	0.86	2.128	0.188
1.68	2.40	3.345	0.269
6.21	8.87	4.896	1.210
18.21	26.01	7.478	1.921
38.88	55.54	10.050	1.915
88.87	126.96	13.003	2.528
150.33	214.76	14.028	2.431
Langmuir type fit : y=14.81(0.05*x)/(1+0.05*x)			
Range 0-1 ppm			
0	0.00	0.000	0.066
0.0325	0.05	0.176	0.006
0.065	0.09	0.306	0.021
0.13	0.19	0.495	0.114
0.325	0.464	0.812	0.241
0.650	0.929	1.199	0.146
Langmuir type fit : y=1.82(1.94*x)/(1+1.94*x) LOD 63 ppb & LOQ 140 ppb Threshold sensitivity 46 ppb			

Figure 7.2c illustrates a Langmuir-type fit (Equation 6.6) for the measurements presented in **Figure 7.2a**. The calibration plot indicates that it is possible to differentiate between the absence of oil in water and concentrations up to 11.3 ppm. However, at concentrations below 11.3 ppm, no significant IR signal from oil was detected anymore. The LOD and LOQ derived from the Langmuir fit was calculated to be 7 ppm and 16 ppm, respectively (**Table 7.1**).

In addition, **Figure 7.2c** demonstrates that concentrations from 0 to 104 ppm follow a linear trend, and thus a first-order linear calibration curve was established for this region (**Figure 7.2d**). Judging by the R-value (goodness of the fit) of 0.99, the data points clearly follow the linear trend. Using the linear calibration function, the LOD and LOQ were determined to be 12 ppm and 27 ppm, respectively, which is similar to the ones derived from the Langmuir-type fit (**Table 7.1**).

The IR signature from oil is associated with the attachment of oil droplets to the fiber surface, similar to the previously studied effects of water-in-oil at hydrophilic surfaces (**Figure 7.3**). Once a droplet is present at the fiber surface, there are two possible scenarios. According to the first one, the droplet spreads across the fiber to maximize its contact area with the surface. The tendency of one material to spread across a surface in a matrix of another material is described via the spreading coefficient (Equation 6.1) [44, 45]. In this case, λ_{31} is defined as the spreading coefficient for oil (component 3) at the fiber (component 1). The index 2 refers to the water matrix. λ_{31} must be positive for matrix 3 (oil) to spread over matrix 1 (fiber) in the presence of matrix 2 (water). If λ_{31} is negative, the second possible scenario is in effect. Namely,

the droplet of oil in contact with the fiber will demonstrate a certain value for the contact angle (θ), which can be estimated from Equation 6.2 [46].

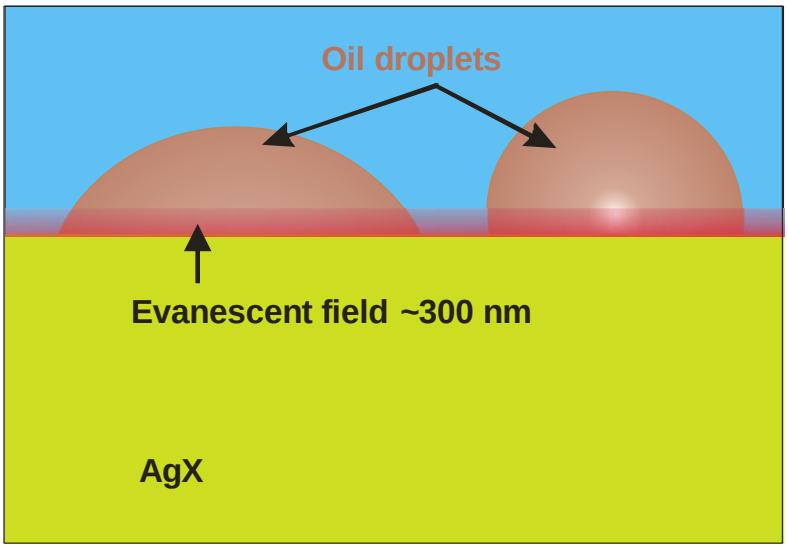

Figure 7.3: Presence of crude oil droplets at the EPB modified (left) and unmodified (right) AgX fiber (figure is not to scale).

Spreading of oil across the fiber should give rise to the highest achievable sensitivity of such IR sensors for the detection of oil, as more absorbing material is located within the evanescent field (extending ~300 nm from the fiber surface [14]). The highest sensitivity for oil in the contact angle scenario will depend on the value of the angle. Indeed, from straightforward geometrical considerations it is evident that at lower values of the contact angle more oil from the droplet will be located within the evanescence field **(Figure 7.3)**. To differentiate between the tow scenarios the interfacial energies for each component pair have been estimated using Equation 6.3 [47].

The contact angles at the optical fiber for water and hexadecane were measured, and the spreading coefficient and contact angle for the oil-water-fiber system were estimated. Results of these evaluations (along with the parameters used) are presented in **Tables 7.2 and 7.3**. (Hexadecane was used as surrogate for oil in these estimations.) The thermodynamics indicate ($\lambda_{31} < 0$) that there is no spreading of the oil across the fiber in the water matrix. Conversely, a relatively high contact angle (96^{o}) is obtained, if an oil droplet is in contact with the unmodified fiber surface. Therefore, further increase in sensitivity and better limit of detections for crude oil in water using the AgX waveguide sensing platform should be attained via appropriate surface modification of the fiber.

Table 7.2. Surface energies and contact angles for liquids and substrates.

Substance	**γ,** mJ/m^2	**γ^d,** mJ/m^2	**γ^p,** mJ/m^2	**Contact angle, degree**	
				water	**hexadecane**
Unmodified fiber	46.1	27.25	19.8	58	5
EPB film	32.74	26.25	6.5	81	5
Water*	72.8	21.8	51	N/A	N/A
Oil (hexadecane)*	26.35	26.35	0	N/A	N/A

* From Ref.[48]

Table 7.3. Thermodynamic parameters for oil/water/fiber system

Parameter[1]	**Unmodified fiber**	**Modified with EPB fiber**
γ_{12}, mJ/m^2	14.2	34.9
γ_{32}, mJ/m^2	51.4	51.4
γ_{13}, mJ/m^2	19.8	6.5
λ_{31}, mJ/m^2	-57.1	-21
Contact angle[2], *degree*	96	56.5
W_A, mJ/m^2	45.8	79.8

[1] *Hexadecane was used in calculations as an oil surrogate*

[2] *Contact angle is calculated for oil (hexadecane) on fiber in water matrix*

7.4.2 Modified fiber

In order to modify the fiber surface, a thin layer of epoxydized polybutadiene was deposited at the fiber surface by dip coating from chloroform solution followed by annealing. Using the same solution and experimental procedures, the layer was also deposited at the surface of a silicon wafer. Ellipsometry performed for the films deposited at the wafer indicated that a film of approximately 45 nm thickness was deposited at the substrate.

The selection of EPB was based on the inherent hydrophobicity of the polymer. In fact, the water contact angle for the EPB film deposited at the model silicon wafer substrate was approx. 82^o, which is significantly higher than the water contact angle of 58^o determined for the unmodified fiber **(Table 7.2)**. Thermodynamic calculations (using Equations 6.1–6.5**, Table 7.3**) revealed that surface modification of the fiber with the

hydrophobic polymer does not cause spreading of the oil across the modified fiber in the water matrix ($\lambda_{31} < 0$). However, the contact angle of oil at the fiber for the oil-water-fiber system decreased significantly from 96^{o} to 56.5^{o} (**Figure 7.3,** right and left respectively). Thus, the amount of oil contributing to the IR signal is increased, as more absorbing material per (10–100 μm) droplet can be sensed by the evanescence field (emanating up to ~300 nm above the fiber).

Another reason for selecting EPB is the reactivity of the polymer [49]. Epoxy functionalities of EPB are quite reactive and ensure adhesion of the EPB coating at the fiber surface. Additionally, the epoxy groups may react with each other at higher temperatures, and thus cause additional cross-linking of the deposited layer. Cross-linking further stabilizes the EPB film and prevents delamination during application in liquid media. In fact, the fiber and the wafer modified with the EPB layer were rinsed with chloroform (an excellent solvent for this polymer) several times without any indication of layer removal by the solvent treatment.

EPB films deposited at the model surface of the silicon wafer and at the AgX fiber were thoroughly characterized. **Figure 7.4** shows AFM images of the unmodified fiber along with the silicon wafer, and the fiber modified with an EPB layer. From a comparison of the surface morphologies, it is evident that the EPB layer was anchored to the fiber surface. AFM imaging after the wafer was covered with the EPB layer and exposed to a stirred water and (in a separate experiment) hexadecane environment for approximately 3 hours did not reveal any significant changes in surface morphology. Additionally, ellipsometry measurements showed no removal of the polymer layer after

the water and hexadecane treatment. Hexadecane was used as oil surrogate during these stability experiments.

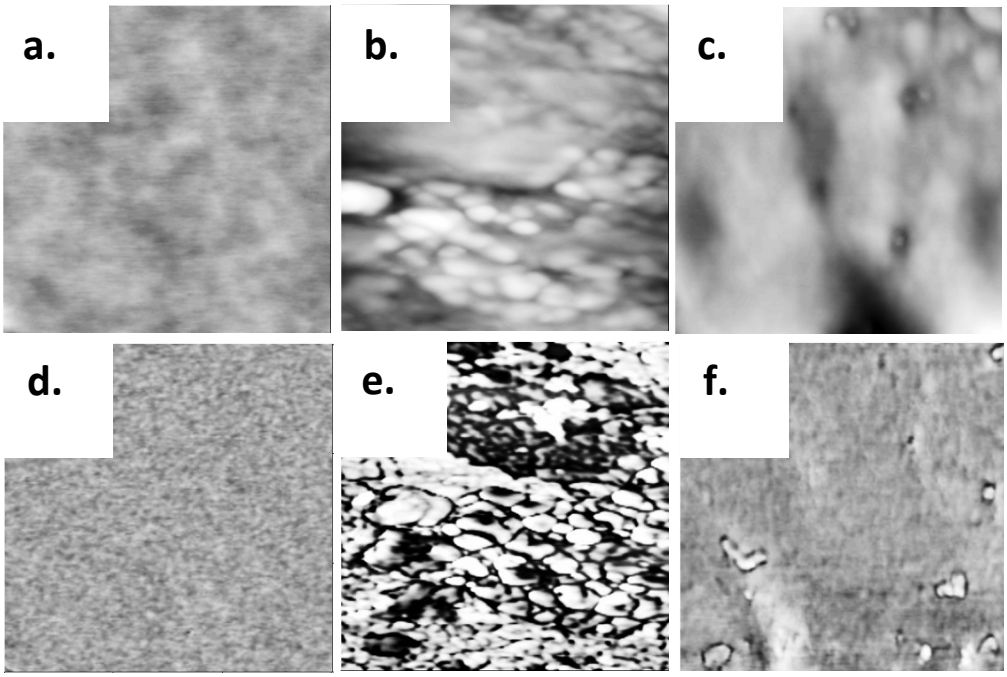

Figure 7.4: AFM topographical (a.-c.) and phase (d.-f.) 1.5 x1.5 μm images: (a. and d.) silicon wafer modified with EPB layer; (b. and e.) unmodified fiber; (c and f) fiber modified with EPB layer. For topography images the vertical scale is 20 nm (a.), 200 nm (b.), and 60 nm (c.). For the phase images the vertical scale is 100 degrees.

Finally, the level of interaction of hydrocarbons and water with the EPB layer was studied via ellipsometric measurements. Namely, the swelling of the film in the presence of water and hexane vapors was measured. The layer demonstrated a somewhat higher affinity to hexane (6% swelling) than to water (2% swelling). However, once for comparison the layer was exposed to the vapor of a solvent for this polymer (chloroform), the thickness of the EPB film was increased by more than 80%. The

swellability results demonstrated that only minute amounts of oil and water may be absorbed by the layer during IR measurement of oil-in-water emulsions.

Figures 7.5a and 7.5b present IR spectra of oil emulsion in water with increasing oil concentration from 0 to 214 ppm. The spectroscopic data demonstrate that the absorbance intensity of CH stretch increases, as the crude oil concentration increases. Simultaneously, a peak at (3750-2750 cm^{-1}) associated with water decreases. These results indicate that oil displaces water at the fiber surface. Once the oil concentration reached 114 ppm, the signal associated with oil did not increase any further indicating that the fiber is fully covered with crude oil within the evanescent field sensing region. This value is approx. 2.5 times lower than the saturation value of 283 ppm obtained for the unmodified fiber surface. This phenomenon was directly associated with the contact angle between the oil droplets and the fiber surface in the oil-water-fiber system. In fact, one can estimate (see calculations in **Appendix Section A-2.3**) that the contact area for an oil droplet approximately doubles, if the contact angle decreases from 96^{o} (unmodified fiber) to 56.5^{o} (EPB-modified fiber). It is necessary to highlight that at concentrations below the saturation limit, the IR signal is approx. 2 to 3 times stronger for the modified fiber compared to the unmodified one (**Figure 7.2c and 7.5c**). This observation is also in accordance with the contact angle estimations.

Figure 7.5c illustrates the PA of the CH stretch versus the concentration of crude oil. Additionally, a Langmuir-type curve (Equitation 6.6) was fitted to the calibration points in **Figure 7.5c.** It is evident from **Figures 7.5a–c** that it is possible to differentiate between 0 ppm oil in water and 1 ppm.

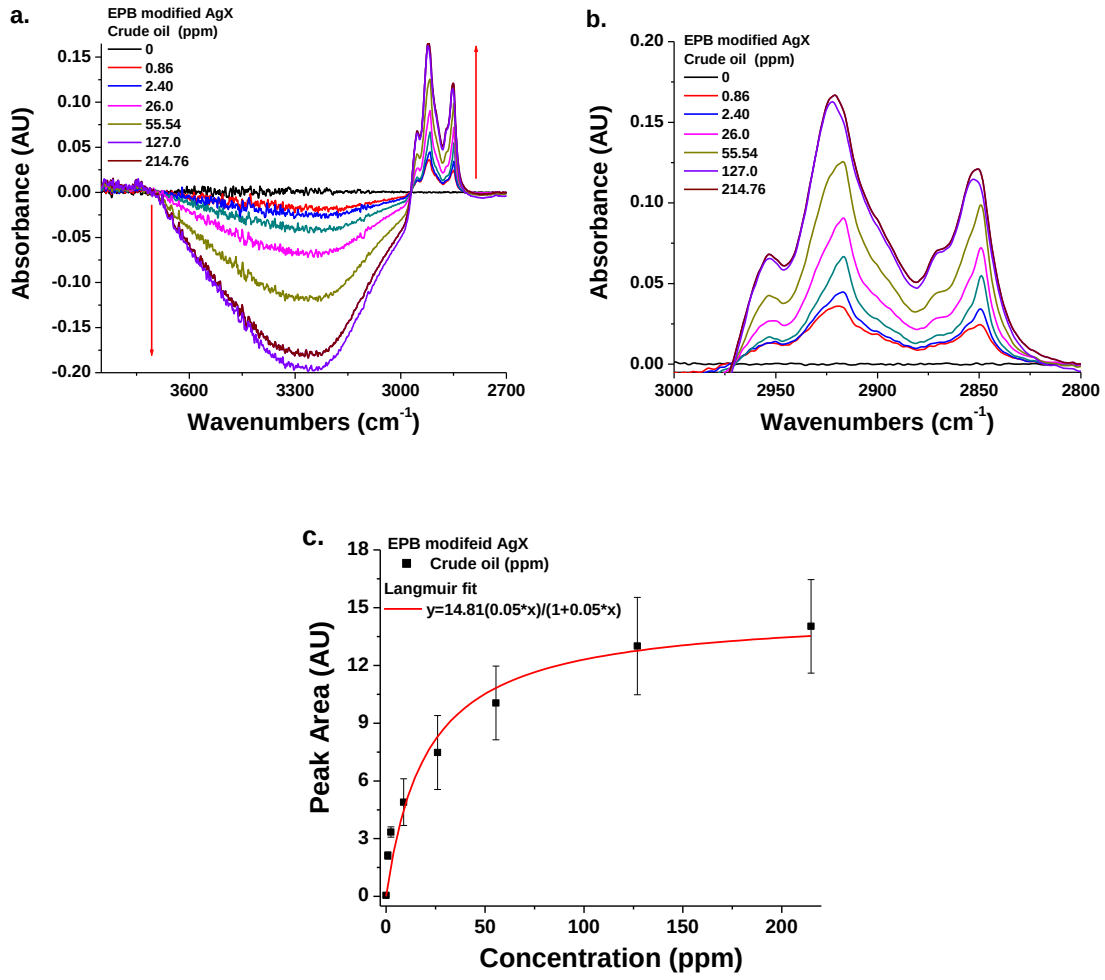

Figure 7.5: Modified with EPB layer fiber. (a.) IR spectra of crude oil content in water as oil concentration increases from 0-214 ppm, (b.) enlarged region of C-H stretch of crude oil, (c.) Langmuir-type fit.

The IR absorption signal associated with 1 ppm oil in water is relatively strong (**Figure 7.5a**), and thus measurements at lower concentrations were conducted to test the experimental setup at ppb levels of oil in water. **Figure 7.6a** presents IR spectra of oil in

water with oil concentrations increasing from 0 to 1 ppm. **Figure 7.6b** illustrates a Langmuir-type fit (Equation 6.6) for the PA versus crude oil concentrations. (Fitting parameters are given in **Table 7.1**.)

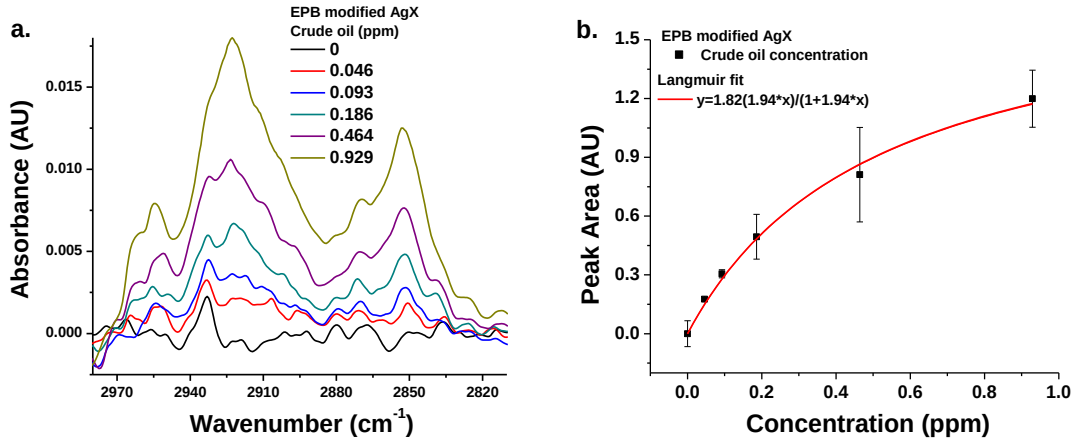

Figure 7.6: (a.) IR spectra of C-H stretch of crude oil content in water as oil concentration increases from 0-1 ppm, (b.) Langmuir-type fit.

The higher effective equilibrium constant (K) values were obtained for the lower concentrations of oil in water rather than for the higher concentrations, which is explained as follows. At low concentrations the probability that droplet arriving to the surface will land on the droplet which is already located on the fiber is low. Therefore, practically each arriving droplet contributes to the IR signal. This leads to the higher K values.

The data presented in **Figure 7.6b** indicate that it is possible to still differentiate between 0 ppb oil in water and 46 ppb. Thus, the threshold sensitivity of this experimental setup utilizing EPB-modified AgX fibers is 46 ppb of oil in water.

Calculated LODs and LOQs for the established calibration curve were determined at 63 ppb and 140 ppb, respectively (**Table 7.1**).

The obtained results demonstrate that by application of a polymer layer at the waveguide surface – here an AgX fiber - the LOD and LOQ of the experimental setup may be lowered by several orders of magnitude from approximately 12 and 27 ppm to 63 ppb and 140 ppb, respectively (**Table 7.1**). Even more importantly, the spectral signatures of crude oil in water using polymer-modified fibers could still be observed at 46 ppb compared to 10000 ppb at unmodified fibers, which is a significant improvement.

Besides the difference in the extent of oil-fiber contact, the improved performance of coated fibers may be further explained by the fact that adhesion between the oil droplet and fiber surface is higher for the modified fiber. The level of adhesion can be approximated via the work of adhesion (W_A), defined as the reversible work required to separate a unit area of liquid from a substrate [45, 50]. In the case of the oil-water-fiber system considered in this study, the work of adhesion is defined by Equation 6.7. The higher the resulting value of W_A, the stronger the adhesion between the oil droplet and the fiber surface. Calculations of W_A for the modified and unmodified fibers are reported in **Table 7.3**. The work of adhesion is approximately two times higher for the EPB-modified surface. Additionally, taking into account the extent of surface contact between the oil droplet and the AgX fiber, which is approximately 2 times higher for EPB-modified fiber, the work of adhesion per droplet is approximately 3.5 times higher for the EPB-modified AgX. Therefore, in the constantly stirred water matrix, the probability of an oil droplet attaching to the fiber is higher for the modified fiber. Likewise, the probability of detachment of the already attached droplet is lower for the modified fiber.

7.5 CONCLUSIONS

In this chapter, MIR evanescent field absorption spectroscopy was used without prior separation techniques or solvent extraction to detect and quantify the amount of crude oil in an oil-in-water emulsion. The unmodified fiber enabled the detection of the presence of oil in water at levels of 11 ppm. The application of an EPB polymer layer at the silver halide fiber surface has enabled the on-line MIR detection of crude oil in water at low ppb levels. Using this experimental setup, crude oil IR absorption signatures can be identified at concentration levels as low as 46 ppb. To the best of our knowledge, this is the only IR-based sensing technique facilitating ppb-level direct detection of oil in water at such low concentrations. The obtained characterization results suggest that the enhanced performance of the EPB-modified fiber is associated with a higher level of oil-fiber wettability, and adhesive oil-fiber interaction.

7.6 OUTLOOK

This chapter describes the application of MIR fiber-optic evanescent field spectroscopy utilizing polymer-modified waveguides for the in-situ detection of low-level oil concentrations in water. The LOD and LOQ of this method are competitive with current laboratory techniques and commercially available methods. However, the reproducibility needs to be further improved. To this end, a more robust experimental setup needs to be constructed, as already argued in the outlook of **Section 6.6**.

7.7 REFERENCES:

(1) Wang, Z. D.; Fingas, M. F. "Development of oil hydrocarbon fingerprinting and identification techniques", *Marine Pollution Bulletin* **2003**, *47*, 423-452.

(2) Perez-Caballero, G.; Andrade, J. M.; Muniategui, S.; Prada, D. "Comparison of single-reflection near-infrared and attenuated total reflection mid-infrared spectroscopies to identify and monitor hydrocarbons spilled in the marine environment", *Analytical and Bioanalytical Chemistry* **2009**, *395*, 2335-2347.

(3) National Research Council (2003) Oil in the Sea III: Inputs, F., and Effects III. National Academies Press. p. 192. http://www.nap.edu/openbook.php?record_id=10388&page=191, **May 2010**

(4) Etkin, D. S., Ed. *Oil Spill Intelligence Report's White Paper Series*; Cutter Information Corp. , 1998.

(5) Tanobe, V. O. A.; Sydenstricker, T. H. D.; Amico, S. C.; Vargas, J. V. C.; Zawadzki, S. F. "Evaluation of Flexible Postconsumed Polyurethane Foams Modified by Polystyrene Grafting as Sorbent Material for Oil Spills", *Journal of Applied Polymer Science* **2009**, *111*, 1842-1849.

(6) http://www.eia.gov/energyexplained/index.cfm?page=oil_use, June 2010.

(7) Fingas, M. F.; Brown, C. E. "Review of oil spill remote sensing", *Spill Science & Technology Bulletin* **1997**, *4*, 199-208.

(8) Begak, O. Y.; Syroezhko, A. M. "Monitoring of the sources of environmental pollution with crude oil", *Russian Journal of Applied Chemistry* **2001**, *74*, 636-639.

(9) Stenstrom, M. K.; Fam, S.; Silverman, G. S. "analytical methods for quantitative and qualitative determination of hydrocarbons and oil and grease in water and waste-water", *Environmental Technology Letters* **1986**, *7*, 625-636.

(10) Nemirovskaya, I. A.; Anikiev, V. V.; Theobald, N.; Rave, A. "Identification of oil hydrocarbons in seawater using different analytical methods", *Journal of Analytical Chemistry* **1997**, *52*, 349-353.

(11) Wang, Z. D.; Fingas, M. "Developments in the analysis of petroleum hydrocarbons in oils, petroleum products and oil-spill-related environmental samples by gas chromatography", *Journal of Chromatography A* **1997**, *774*, 51-78.

(12) Minty, B.; Ramsey, E. D.; Davies, I. "Development of an automated method for determining oil in water by direct aqueous supercritical fluid extraction coupled on-line with infrared spectroscopy", *Analyst* **2000**, *125*, 2356-2363.

(13) Mizaikoff, B. "Mid-infrared evanescent wave sensors - a novel approach for subsea monitoring", *Measurement Science & Technology* **1999**, *10*, 1185-1194.

(14) Mizaikoff, B. "Mid-IR Fiber-optic Sensors", *Analytical Chemistry* **2003**, *75*, 258A-267A.

(15) Mizaikoff, B.; Jakusch, M.; Kraft, M. "Infrared fiber-optic sensors - Versatile tool for water monitoring - Optical chemical sensors gain importance in environmental monitoring, process analysis/control; Now complement separation techniques and spectroscopy", *Sea Technology* **1999**, *40*, 25-+.

(16) Fernandez-Varela, R.; Andrade, J. M.; Muniategui, S.; Prada, D.; Ramirez-Villalobos, F. "Identification of fuel samples from the Prestige wreckage by pattern recognition methods", *Marine Pollution Bulletin* **2008**, *56*, 335-347.
(17) Fresco-Rivera, P.; Fernandez-Varela, R.; Gomez-Carracedo, M. P.; Ramirez-Villalobos, F.; Prada, D.; Muniategui, S.; Andrade, J. M. "Development of a fast analytical tool to identify oil spillages employing infrared spectral indexes and pattern recognition techniques", *Talanta* **2007**, *74*, 163-175.
(18) Staniloac, D.; Petrescu, B.; Patroeseu, C. "Pattern recognition based software for oil spills identification by gas-chromatography and IR spectrophotometry", *Environmental Forensics* **2001**, *2*, 363-366.
(19) Ruyken, M. M. A.; Pijpers, F. W. "Identification of oil-spills in harbors by means of pattern-recognition", *Analytica Chimica Acta* **1987**, *194*, 25-35.
(20) S. Rotteri, H. B., J. P. Dubreuil, J. Evers, J. Ilsbroux, H. G. Remstedt, H. J. Somerville and H. Van Strien In *Concawe Report* The Hague, 1984.
(21) Method, P. *Standard Methods for Analysis and Testing of Petroleum and Petroleum Related Products*; Wiley, : New York, 1995.
(22) Daghbouche, Y.; Garrigues, S.; MoralesRubio, A.; delaGuardia, M. "Evaluation of extraction alternatives for Fourier transform infrared spectrometric determination of oil and greases in water", *Analytica Chimica Acta* **1997**, *345*, 161-171.
(23) Minty, B.; Ramsey, E. D.; Davies, I.; James, D. I.; O'Brien, P. M.; Littlewood, M. I. "Analysis of oil in water at the low ppm level using direct supercritical fluid extraction coupled on-line with infrared spectroscopy", *Analytical Communications* **1998**, *35*, 277-280.
(24) Romero, M. T.; Ferrer, N. "Determination of oil and grease by solid phase extraction and infrared spectroscopy", *Analytica Chimica Acta* **1999**, *395*, 77-84.
(25) Wells, M. J. M.; Ferguson, D. M.; Green, J. C. "Determination of oil and grease in waste-water by solid-phase extraction", *Analyst* **1995**, *120*, 1715-1721.
(26) Noble, D. "Here today, gone tomorrow - halogenated solvents in analytical-chemistry", *Analytical Chemistry* **1993**, *65*, A693-A695.
(27) McCrum, W. A.; Whittle, P. J. "Infrared determination of petroleum oil .2. extraction from water and removal of interferences", *Analyst* **1982**, *107*, 1081-1085.
(28) Whittle, P. J.; McCrum, W. A.; Horne, M. W. "Infrared determination of petroleum oil - new approaches to the calculation", *Analyst* **1980**, *105*, 679-684.
(29) http://www.perkinelmer.com/, **May 2010**
(30) Ramsey, E. D. "Determination of oil-in-water using automated direct aqueous supercritical fluid extraction interfaced to infrared spectroscopy", *Journal of Supercritical Fluids* **2008**, *44*, 201-210.
(31) Ramsey, E. D.; Wei, G. "Oil-in-water analysis using supercritical fluid extraction interfaced with fixed wavelength infrared detection", *International Journal of Environmental Analytical Chemistry* **2008**, *88*, 957-968.
(32) Heinrich, P.; Wyzgol, R.; Schrader, B.; Hatzilazaru, A.; Luebbers, D. W. "Determination of organic compounds by IR/ATR spectroscopy with polymer-coated internal reflection elements", *Applied Spectroscopy* **1990**, *44*, 1641-1646.

(33) Janotta, M.; Karlowatz, M.; Vogt, F.; Mizaikoff, B. "Sol-gel based mid-infrared evanescent wave sensors for detection of organophosphate pesticides in aqueous solution", *Analytica Chimica Acta* **2003**, *496*, 339-348.
(34) Karlowatz, M.; Kraft, M.; Mizaikoff, B. "Simultaneous quantitative determination of benzene, toluene, and xylenes in water using mid-infrared evanescent field spectroscopy", *Analytical Chemistry* **2004**, *76*, 2643-2648.
(35) Dobbs, G. T.; Balu, B.; Young, C.; Kranz, C.; Hess, D. W.; Mizaikoff, B. "Mid-infrared chemical sensors utilizing plasma-deposited fluorocarbon membranes", *Analytical Chemistry* **2007**, *79*, 9566-9571.
(36) Kurusu, Y.; Masuyama, Y.; Yanagi, K.; Morinaga, H.; Yamamoto, S.; Makanishi, M. "Epoxidation of polyolefin by peroxy acid generated insitu", *Bulletin of the Chemical Society of Japan* **1993**, *66*, 673-675.
(37) Derouet, D.; Morvan, F.; Brosse, J. C. "Chemical modification of 1,4-polydienes by di(alkyl or aryl)phosphates", *European Polymer Journal* **2001**, *37*, 1297-1313.
(38) Ouyang, Y.; Mansell, R. S.; Rhue, R. D. "Flow of gasoline-in-water microemulsion through water-saturated soil columns", *Ground Water* **1995**, *33*, 399-406.
(39) Sprow, F. B. "Drop size distributions in strongly coalescing agitated liquid-liquid systems", *AlChe Journal* **1967**, *13*, 995-998.
(40) Peralta-Martinez, M. V.; Arriola-Medellin, A.; Manzanares-Papayanopoulos, E.; Sanchez-Sanchez, R.; Palacios-Lozano, E. M. "Influence of the speed mixing-on viscosity and droplet size of oil in water emulsions", *Petroleum Science and Technology* **2004**, *22*, 1035-1043.
(41) Ramirez, M.; Bullon, J.; Anderez, J.; Mira, I.; Salager, J. L. "Drop size distribution bimodality and its effect on O/W emulsion viscosity", *Journal of Dispersion Science and Technology* **2002**, *23*, 309-321.
(42) Mlynek, Y.; Resnick, W. "Drop sizes in an agitated liquid-liquid system", *AlChe Journal* **1972**, *18*, 122-127.
(43) Marechal, Y. "Infrared-spectra of water .1. effect of temperature and of h/d isotopic dilution", *Journal of Chemical Physics* **1991**, *95*, 5565-5573.
(44) Luzinov, I.; Xi, K.; Pagnoulle, C.; Huynh-Ba, G.; Jerome, R. "Composition effect on the core-shell morphology and mechanical properties of ternary polystyrene/styrene butadiene rubber polyethylene blends", *Polymer* **1999**, *40*, 2511-2520.
(45) Sperling, L. H. *Polymeric Multicomponent Materials*; Wiley-Interscience New York, 1998.
(46) Jung, Y. C.; Bhushan, B. "Wetting Behavior of Water and Oil Droplets in Three-Phase Interfaces for Hydrophobicity/philicity and Oleophobicity/philicity", *Langmuir* **2009**, *25*, 14165-14173.
(47) Hobbs, S. Y.; Dekkers, M. E. J.; Watkins, V. H. "Effect of interfacial forces on polymer blend morphologies", *Polymer* **1988**, *29*, 1598-1602.
(48) Janczuk, B.; Wojcik, W.; Zdziennicka, A.; Bruque, J. M. "Components of the surface free energy of low rank coals in the presence of n-alkanes", *Powder Technology* **1996**, *86*, 229-238.
(49) Zdyrko, B.; Iyer, K. S.; Luzinov, I. "Macromolecular anchoring layers for polymer grafting: comparative study", *Polymer* **2006**, *47*, 272-279.

(50) Cambiella, A.; Benito, J. M.; Pazos, C.; Coca, J.; Ratoi, M.; Spikes, H. A. "The effect of emulsifier concentration on the lubricating properties of oil-in-water emulsions", *Tribology Letters* **2006**, *22*, 53-65.

CHAPTER 8

CONCLUSIONS AND OUTLOOK

The objective of this thesis was the design and application of mid-infrared (MIR) sensor platforms facilitating the analysis of hydrocarbon containing systems at extreme conditions. Specifically, the focus was on the potential of MIR spectroscopy toward studying hydrocarbon seep ecosystems, and for measurement scenarios associated with oil/gas production, storage, and transportation. As a result of these studies, it was established that MIR sensors based on evanescence field absorption spectroscopy are an effective measurment platform for analyzing and monitoring target constituents at such conditions. It is expected that the developed sensing approaches will be utilized for design of fieldable MIR sensor prototypes in the near future.

In particular, the quantitative determination of diamondoid compounds (adamantane) in organic and hydrocarbon media is enabled utilizing IR-ATR spectroscopy. LODs and LOQs along with solubility limits of adamantane in dichloromethane, hexane, carbon tetrachloride, and standard crude oil were determined. In addition, the developed analytical strategy enabled the detection of adamantane in a real world crude oil matrix. The presented efforts thus provide a sensing platform for the detection and monitoring of diamondoid constituents in naturally occurring crudes and petroleum samples.

Next, IR-ATR spectroscopy was utilized for evaluating and characterizing distribution, variations, and origin of carbonate minerals within sediment formations surrounding a hydrocarbon seep site - MC 118 in the Gulf of Mexico. IR-ATR

spectroscopic studies revealed that carbonates formed from different sources of HCO_3^- may be identified by diverse infrared (IR) spectroscopic absorption profiles of the ν_3 asymmetric carbonate stretching vibration. Furthermore, these profiles have been utilized for establishing an analytical model to directly detect and classify ^{13}C-depleted authigenic carbonates associated with cold seep ecosystems. It was demonstrated that IR-ATR spectroscopy may in future be implemented as a direct on-ship – and potentially in future in-situ - analytical tool for characterizing hydrocarbon seep sites, thereby facilitating advances in the rapid spatiotemporal characterization of cold seep ecosystems.

MIR evanescent field absorption spectroscopy was also utilized to expand the understanding on the role of surfactants during hydrocarbon gas hydrate formation at surfaces. This experimental method allowed detailed spectroscopic observations of detergent-related surface processes during SDS-mediated propane hydrate formation. The obtained IR data enabled deriving a potential mechanism how SDS decreases the induction time for hydrate nucleation, and promotes hydrate formation. These studies thus demonstrated the potential of MIR fiberoptic evanescent field sensors for in-depth investigations on surface related phenomena to elucidate the molecular mechanisms involved in promoting gas hydrate nucleation and growth.

In addition, this thesis demonstrated the quantification of trace amounts of water in hydrocarbon matrices (hexane) using MIR fiberoptic evanescent field absorption spectroscopy. The sensitivity and limit of detection were significantly improved by coating the fiberoptic waveguide-based sensing platform with a layer of hydrophilic polymer (tin crosslinked polyacrylic acid). Specifically, the application of this polymer layer has enabled the on-line IR detection of water concentrations in hexane as low as 10

ppm. These results indicate that MIR evanescent filed sensing has a significant potential for in-situ detection and monitoring of water in industrial oils and petroleum products.

Finally, the quantification of trace amounts of oil in water using MIR evanescent field sensing was demonstrated. Unmodified and polymer-modified waveguides using grafted epoxidized polybutadiene layers were utilized during these studies. The surface modification of the fiber enabled the MIR analysis of crude oil in water at low ppb concentration levels, which are to the best of our knowledge the lowest directly detected concentration levels of oil in water reported to date for IR-based sensing techniques. Therefore, MIR fiberoptic evanescent field spectroscopy using polymer-modified waveguides may be applied for in-situ low level detection of oil and petroleum in water.

APPENDIX

A-1 IR-ATR spectroscopy analysis of marine sediments

Table A-1.1: Core numbers, water depth, core depth, latitude and longitude.

Core #	Water depth (m)	Core depth (cm)	Latitude	Longitude
4414	966	25	28º51.132	88º29.550
1	903	211	28º51.264	88º29.952
2	895	151	28º51.337	88º29.634
4	894.6	154	28º51.461	88º29.490
5	887	191	28º51.482	88º29.470
7	895.3	205	28º51.342	88º29.574
8	894	121	28º51.353	88º29.586
9	877	450	28º51.448	88º29.503
21	894	122	28º51.2498	88º29.5907
22	897	66	28º51.2400	88º29.5920
24	893	22	28º51.1388	88º29.5399
26	889	46	28º51.1551	88º29.4879
29	889	105	28º51.3293	88º29.4996
30	892	131	28º51.1402	88º29.1340
31	891	103	28º51.1438	88º29.3996
35	893	144	28º51.0388	88º29.3641

Table A-1.2: Characteristics of the sediment samples examined.

Core #	Depth (cmbsf)	Calcite %	Dolomite %	MgCalcite	Crude oil	$\delta^{13}C$ (‰)
			LMA			
	0-3	99	2			0.68
	8-10	99	1			
1	16-18	99	1			1.362
	90-93	76	24			
	210-213	54	46			0.99
	5-8	94	6			0.89
	28-31	99	1		X	0.75
	53-56	51	49			0.65
4	83-86	79	21			
	113-114	70	30			
	153-156	100	0			1.33
	0-2	94	6			1.17
	24-28	97	3			0.84
	40-43	94	6			0.32
5	70-73	67	33			
	110-113	80	20			
	150-153	95	5			
	190-193	88	12			-3.9
	0-4	96	4			0.15
	25-28	90	10			
	50-53	95	5			
35	75-78	74	26			
	100-103	58	42			
	130-134	38	62			0.28
			MMA			
	0-3	99	1			0.31
	15-18	88	12			-3.31
	30-33	65	35	X		-9.21
8	45-48			XX		
	75-78	51	49	X		
	100-103	56	44	X		
	120-123	51	49			-7.56
	0-3	97	3			0.99
	10-13	97	3			
	20-23	99	1			0.39
	60-63	56	44	X		-9.36
7	80-83			XX		
	100-103	45	55	X		
	150-153	39	61			
	200-203	54	46			-9.03

Core #	Depth (cmbsf)	Calcite %	Dolomite %	MgCalcite	Crude oil	δ13C (‰)
			MMA			
	0-3	86	14			-3.55
	5-6	81	19	X		
	6-7	71	29	X		
	7-8	60	40	X		-9.02
	8-9	61	39	X		
	9-10	57	43	X		
	10-12	56	44	X		
	12-14	58	42	X		
2	14-16	57	43	X		
	16-18			XX		
	25-28	52	46	X		
	50-53	61	39	X		
	75-78	54	46	X		
	100-103	68	32			
	125-128	66	34			
	150-153	59	41	X		
	170-175	51	49			-3.4
	0-3	98	2			0.96
	20-23	100	0			-4.67
29	40-43			XX		
	60-63	63	37	X		
	80-83	58	42			-8.87
	100-103	60	40			-5.5
	0-5	95	5			1.32
	30-33	98	2			
21	50-53	99	1			0.16
	88-91			XX		-18.8
	110-115			XX		-18.4
	0-4	100	0			0.73
22	20-24	98	2			0.81
	50-53			XX		-18.45
	60-63			XX		-16.65
	0-3			XX	XX	-7.96
24	6-9			XX	XX	
	12-15			XX	XX	-20.07
	15-18	93	7			-0.86
	30-33	95	5			-2.56
	45-48	95	5			
30	60-63	76	21			
	75-78	59	41			
	95-98	44	56			-1.4
	120-123	52	48			

Core #	Depth (cmbsf)	Calcite %	Dolomite %	MgCalcite	Crude oil	$\delta^{13}C$ (‰)
			HMA			
9	0-5	93	7			
	5-6			X		-9.69
	8-9			X		
	40-43			XX		
	120-123	87	13			-9.34
	233-236	36	64			
	328-331	45	55			0.79
	428-431	55	45			
26	0-3	98	2			0.82
	15-18	63	37			-7.31
	26-29	44	56			
	37-40	31	69			-13.79
	45-47	31	69			
4414	0-3	100	0	X		-9.9
	3-6	100	0	XX		
	6-9		0	XX	XX	
	.9-12		0	XX	XX	
	12-15		0	XX	XX	
	15-18		0	XXX	X	-23
	18-21		0	XX	X	
	21-24		0	XX	XXX	-19.02
31	0-3	100	0			-4.54
	17-20	73	27			-6.26
	40-43	84	16			
	80-83	72	28			
	60-63	56	44			
	100-103	41	59	X		
	110-113			XX	X	
	120-123			XX	X	-33.28

*X – weak intensity IR signatures seen for this compound

XX-medium intensity IR signatures

XXX-strong intensity IR signatures

Figure A-1.1: IR-ATR spectra of v_3 and v_4 regions for the sediment samples analyzed.

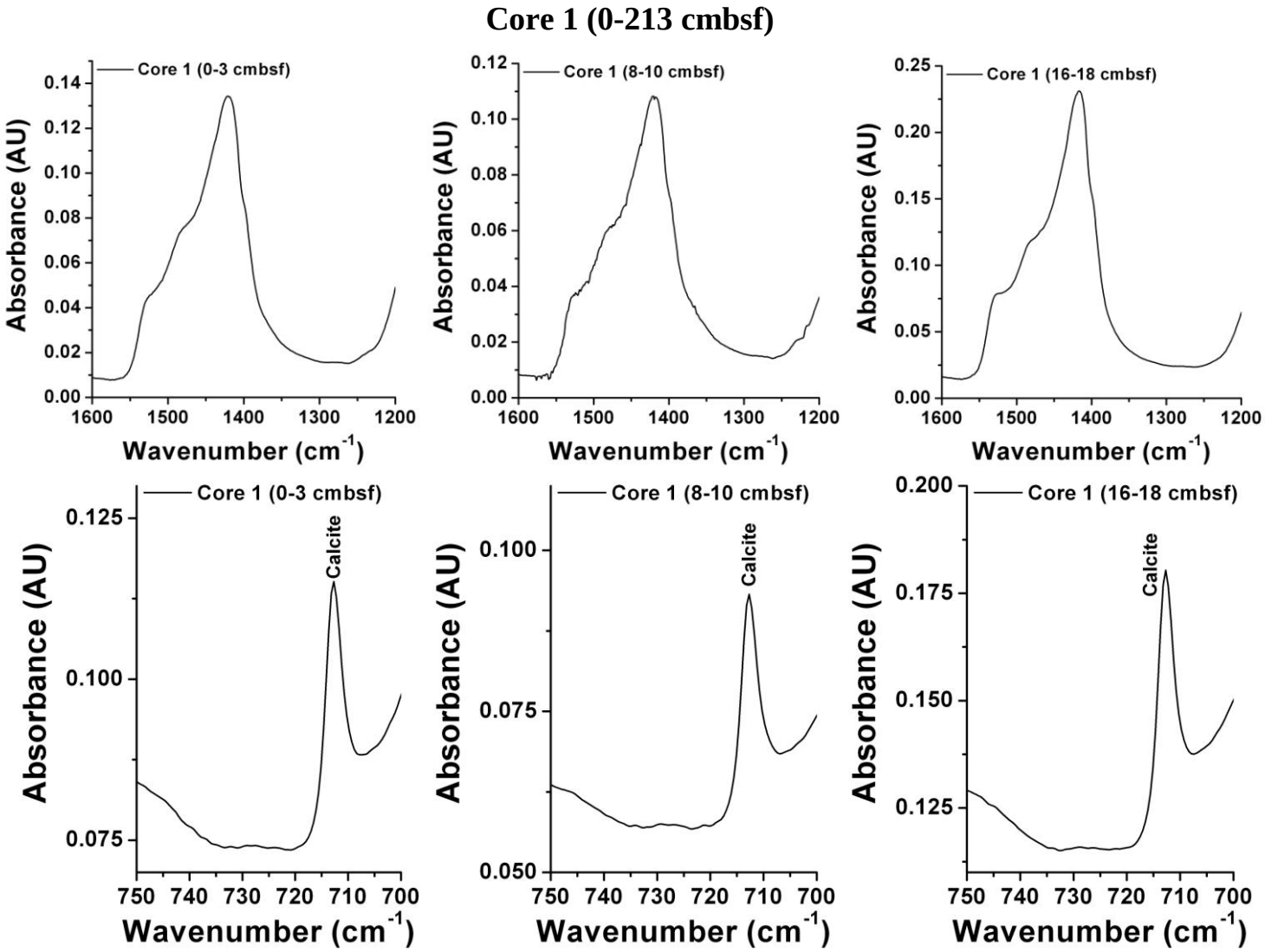

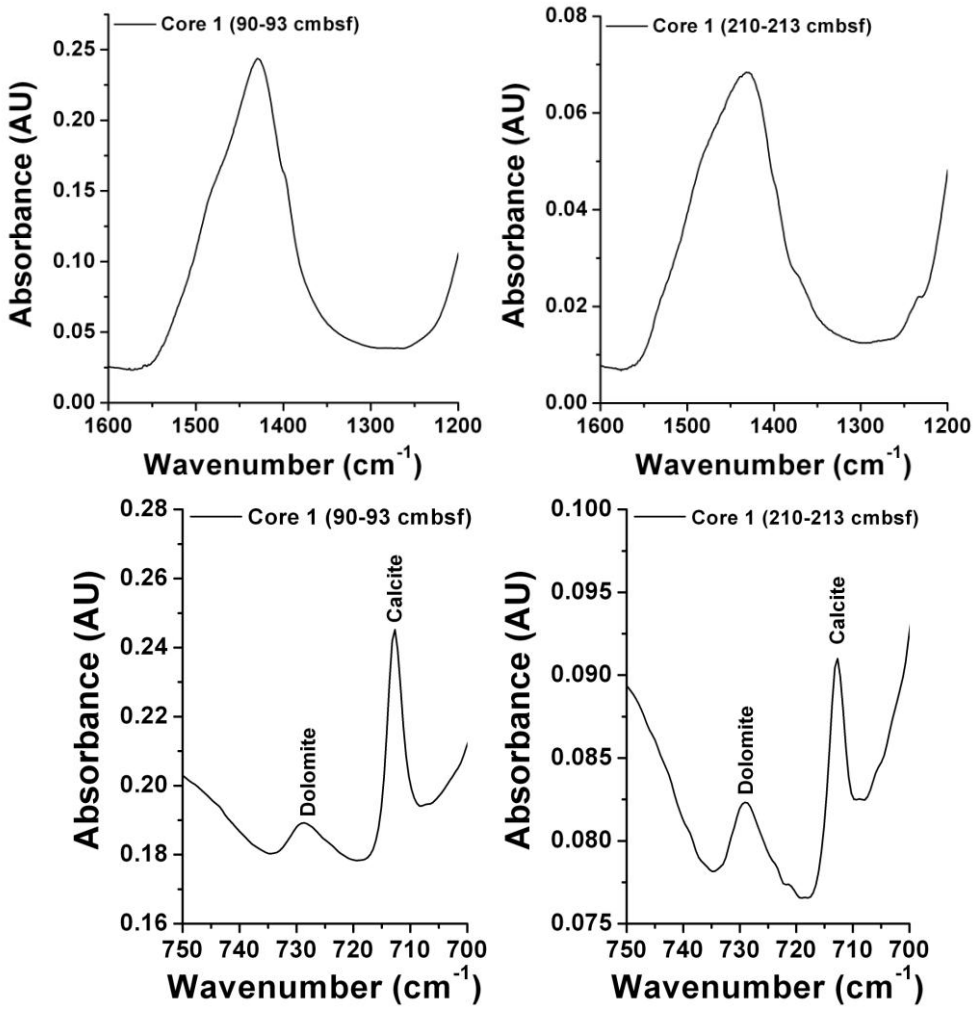
Core 1 (90-93 cmbsf)
Absorbance (AU)
Wavenumber (cm-1)
Core 1 (210-213 cmbsf)
Absorbance (AU)
Wavenumber (cm-1)
Core 1 (90-93 cmbsf)
Dolomite
Calcite
Absorbance (AU)
Wavenumber (cm-1)
Core 1 (210-213 cmbsf)
Dolomite
Calcite
Absorbance (AU)
Wavenumber (cm-1)

Core 2 (0-175 cmbsf)

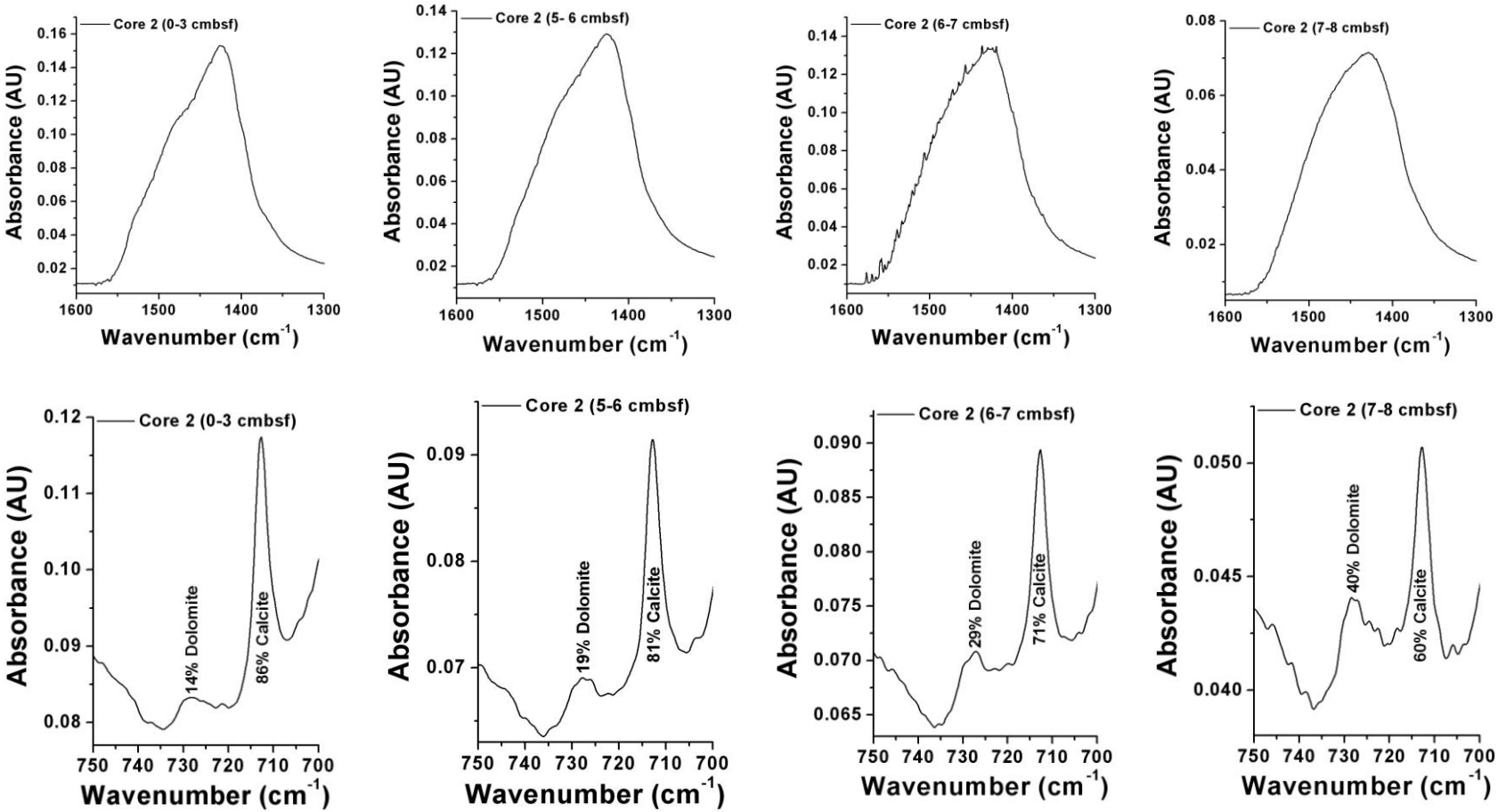

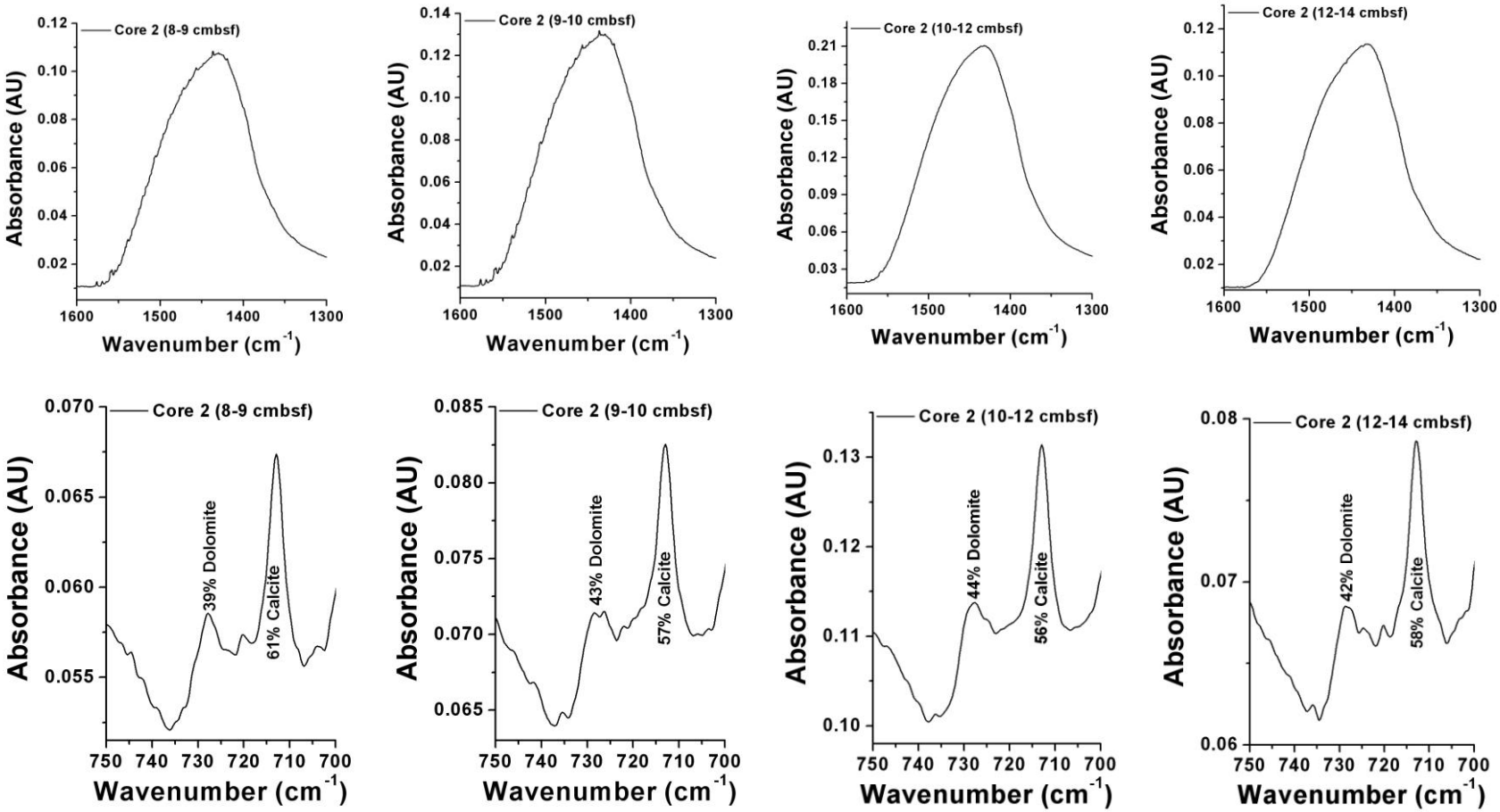
Core 2 (8-9 cmbsf)
Core 2 (9-10 cmbsf)
Core 2 (10-12 cmbsf)
Core 2 (12-14 cmbsf)
Absorbance (AU)
Wavenumber (cm-1)
39% Dolomite
61% Calcite
43% Dolomite
57% Calcite
44% Dolomite
56% Calcite
42% Dolomite
58% Calcite

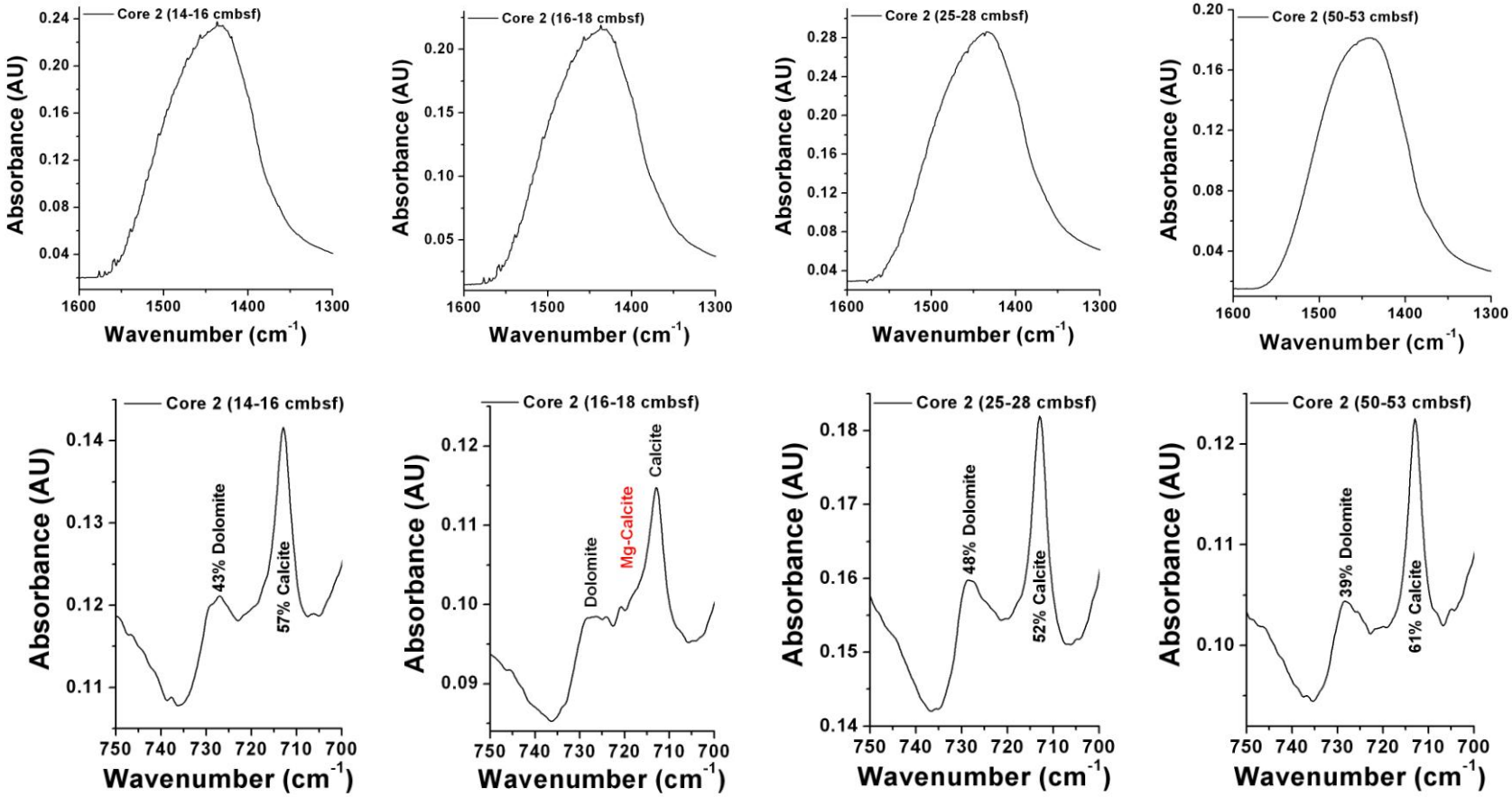
Core 2 (14-16 cmbsf)
Core 2 (16-18 cmbsf)
Core 2 (25-28 cmbsf)
Core 2 (50-53 cmbsf)
Absorbance (AU)
Wavenumber (cm-1)
43% Dolomite
57% Calcite
Dolomite
Mg-Calcite
Calcite
48% Dolomite
52% Calcite
39% Dolomite
61% Calcite

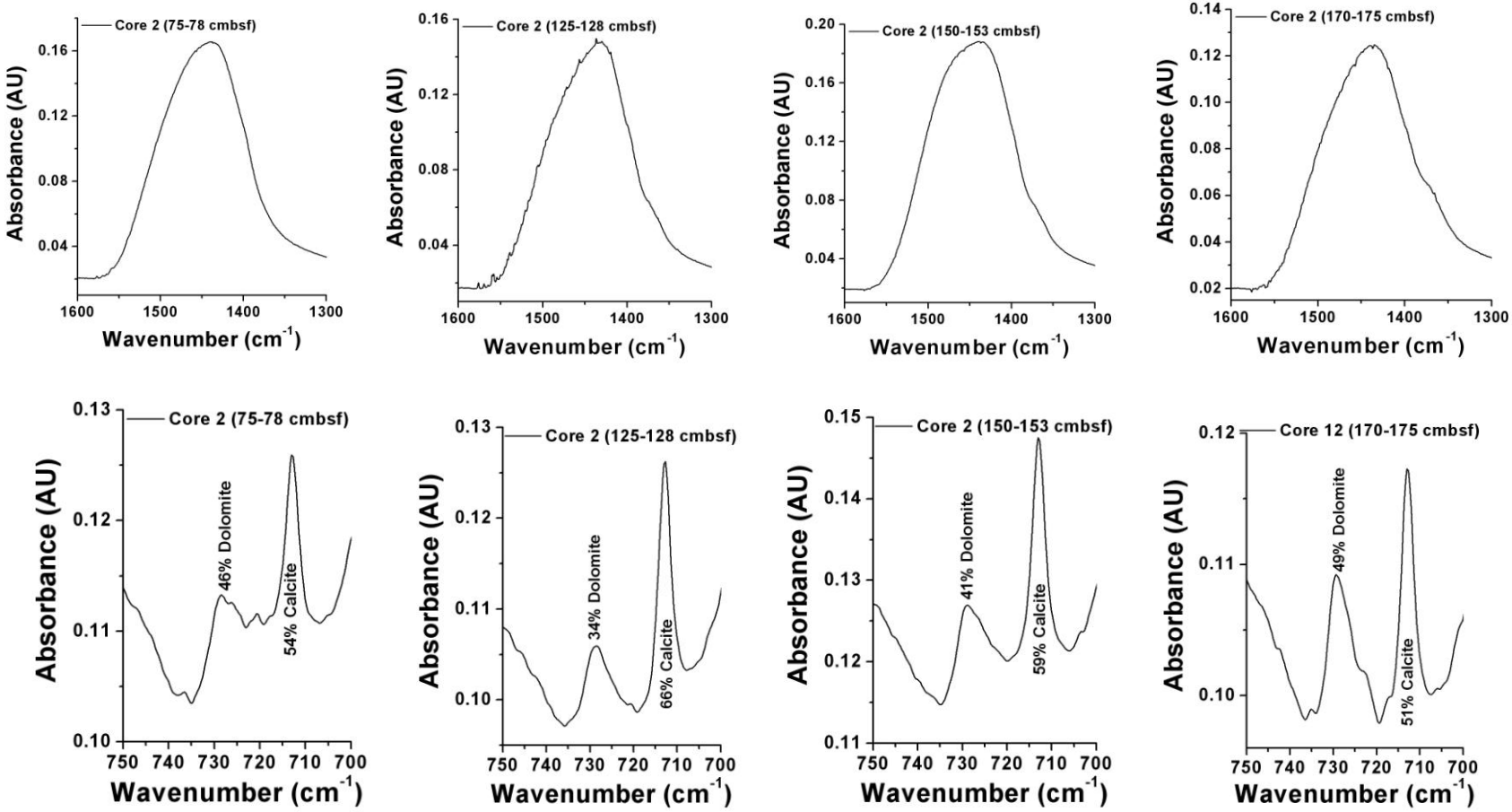
Core 2 (75-78 cmbsf)
Core 2 (125-128 cmbsf)
Core 2 (150-153 cmbsf)
Core 2 (170-175 cmbsf)
Absorbance (AU)
Wavenumber (cm-1)
Core 2 (75-78 cmbsf)
46% Dolomite
54% Calcite
Core 2 (125-128 cmbsf)
34% Dolomite
66% Calcite
Core 2 (150-153 cmbsf)
41% Dolomite
59% Calcite
Core 12 (170-175 cmbsf)
49% Dolomite
51% Calcite

Core 4 (5-156 cmbsf)

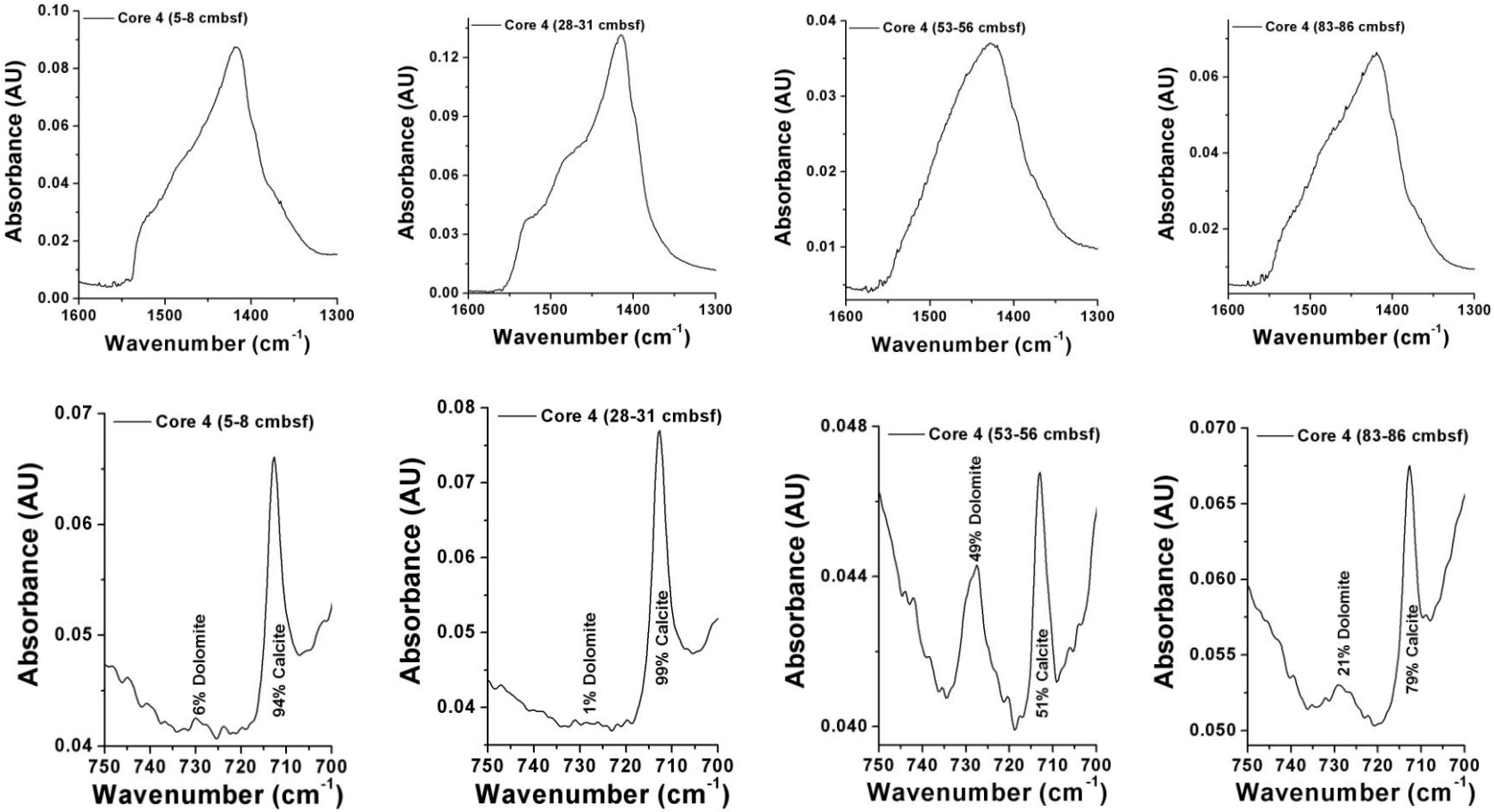

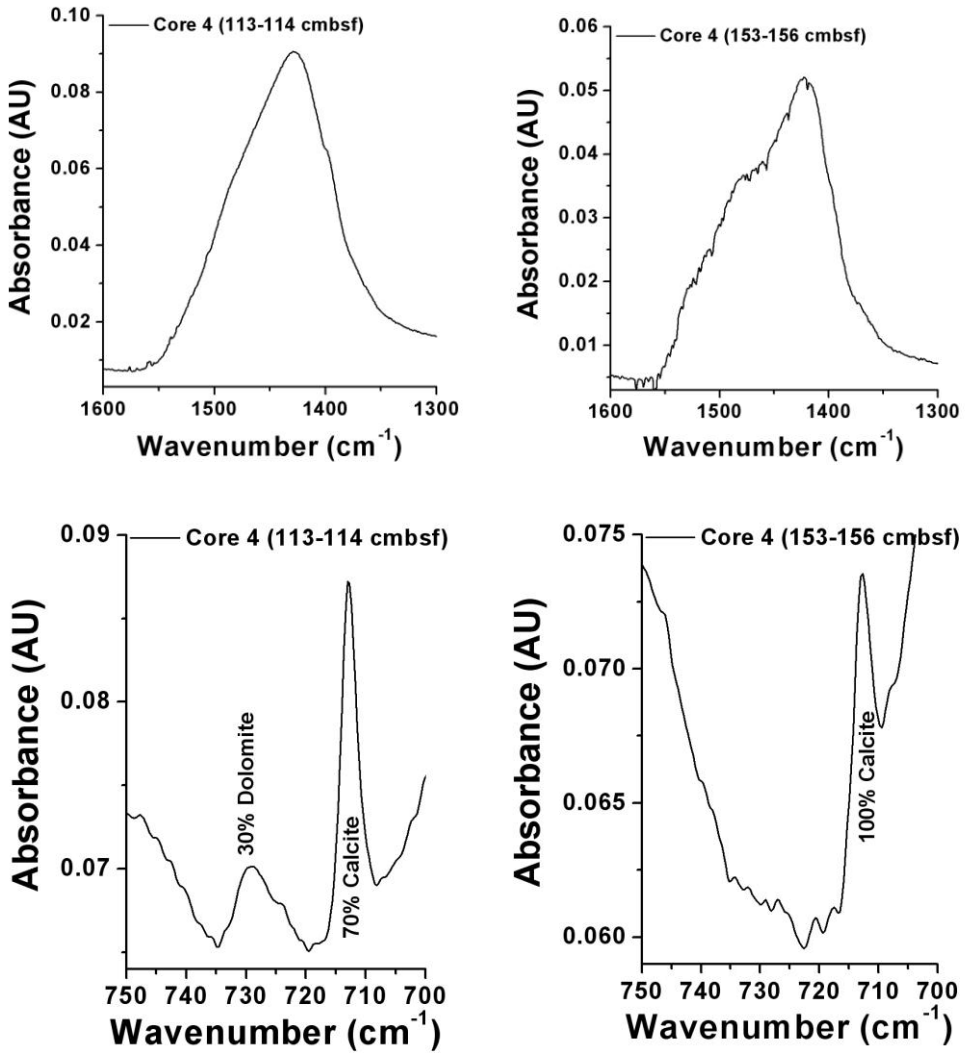
Core 4 (113-114 cmbsf)
Absorbance (AU)
Wavenumber (cm-1)
Core 4 (153-156 cmbsf)
Absorbance (AU)
Wavenumber (cm-1)
Core 4 (113-114 cmbsf)
30% Dolomite
70% Calcite
Absorbance (AU)
Wavenumber (cm-1)
Core 4 (153-156 cmbsf)
100% Calcite
Absorbance (AU)
Wavenumber (cm-1)

Core 5 (0-153 cmbsf)

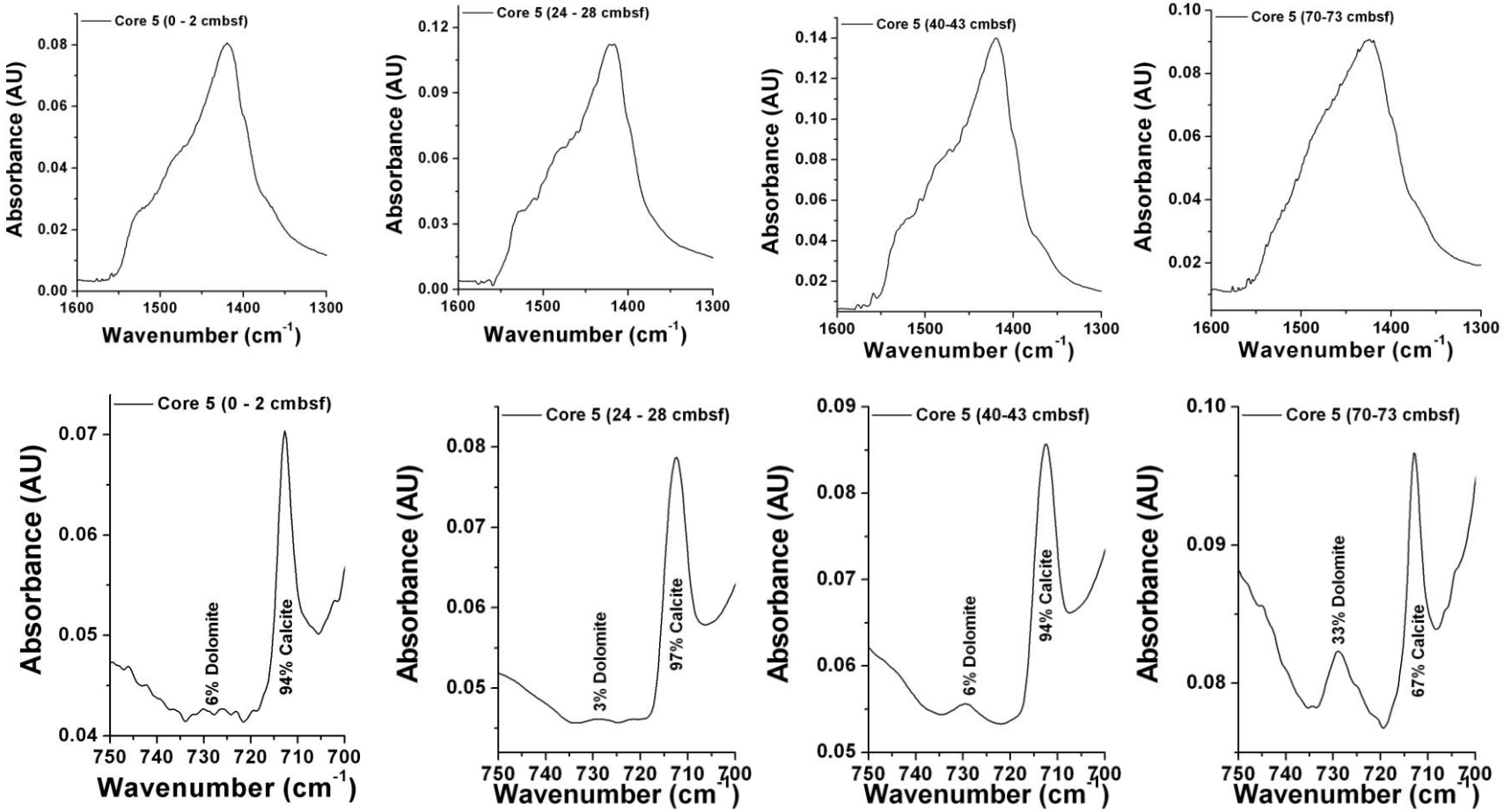

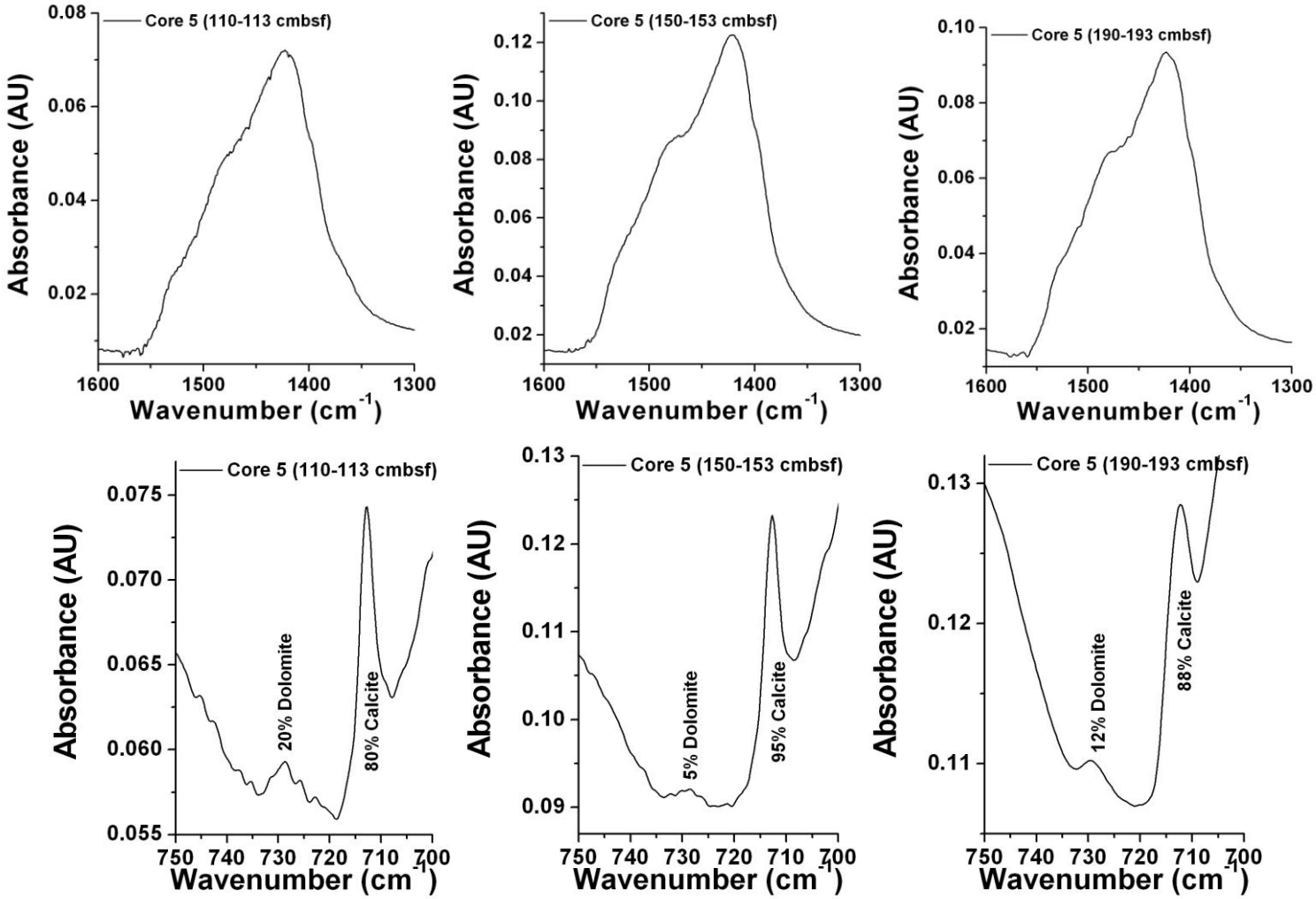
Core 5 (110-113 cmbsf)
Core 5 (150-153 cmbsf)
Core 5 (190-193 cmbsf)
Absorbance (AU)
Wavenumber (cm-1)
20% Dolomite
80% Calcite
5% Dolomite
95% Calcite
12% Dolomite
88% Calcite

Core 7 (0-203 cmbsf)

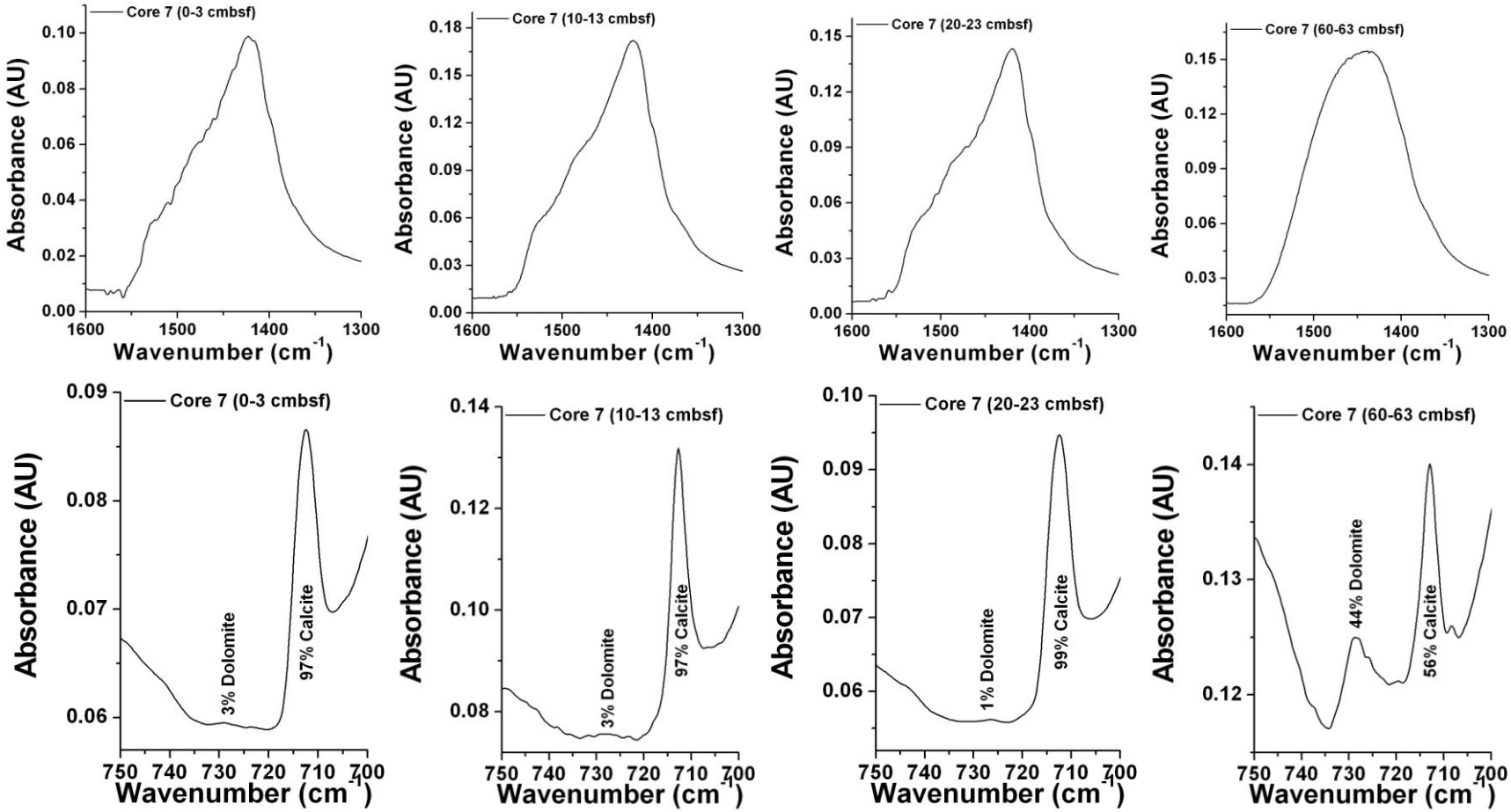

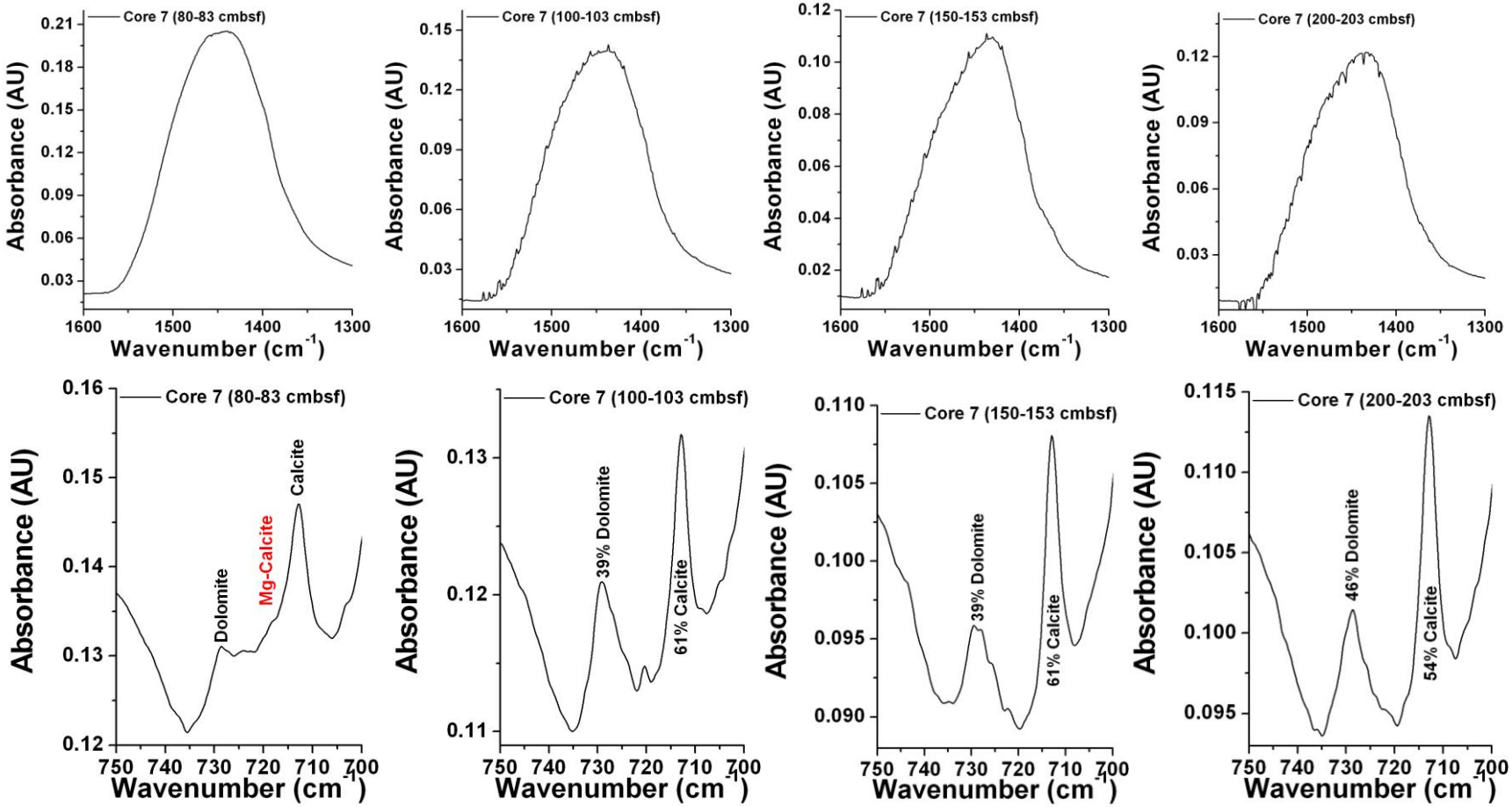
Core 7 (80-83 cmbsf)
Core 7 (100-103 cmbsf)
Core 7 (150-153 cmbsf)
Core 7 (200-203 cmbsf)
Absorbance (AU)
Wavenumber (cm-1)
Dolomite
Mg-Calcite
Calcite
39% Dolomite
61% Calcite
46% Dolomite
54% Calcite

Core 8 (0-123 cmbsf)

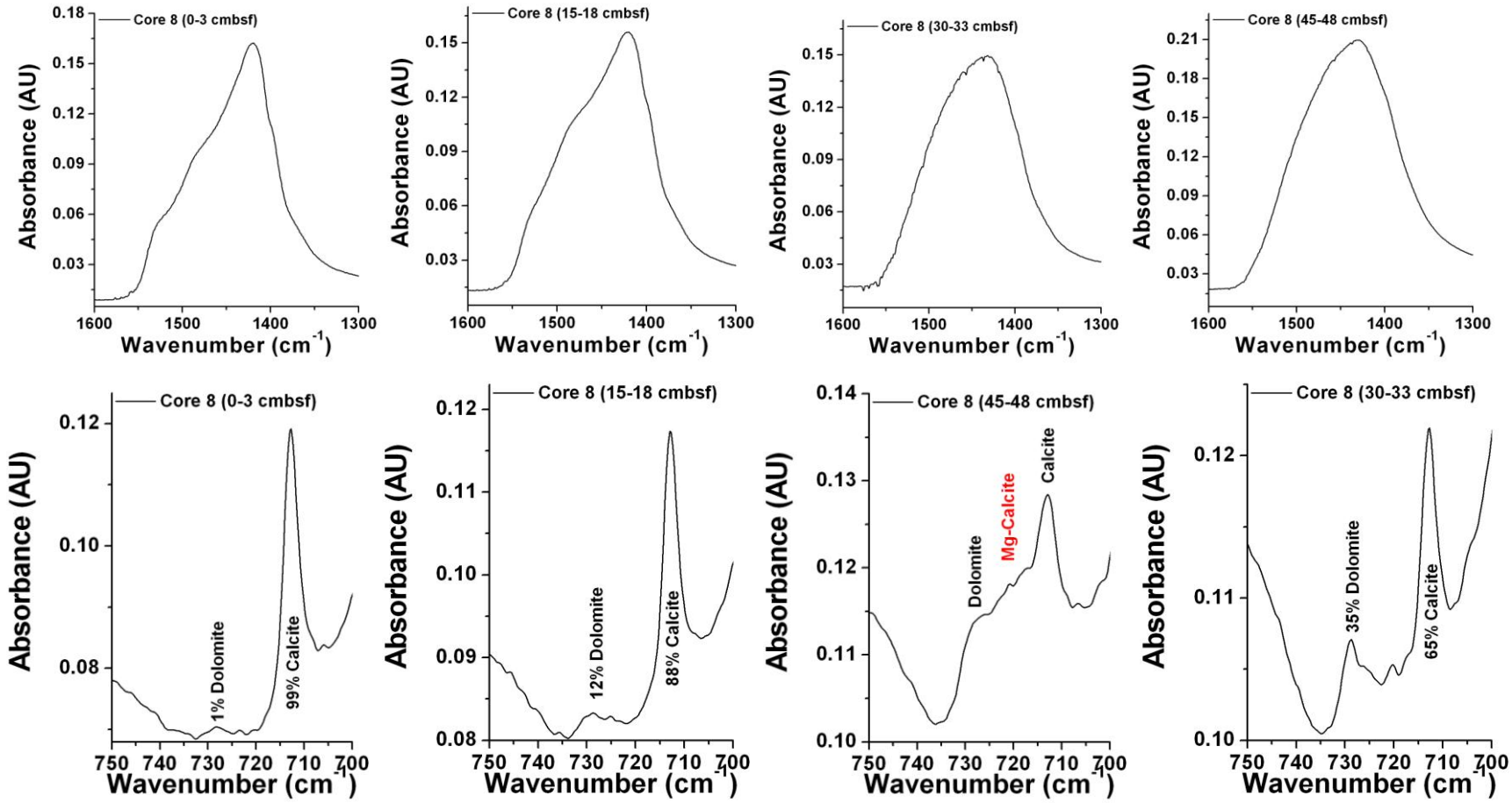

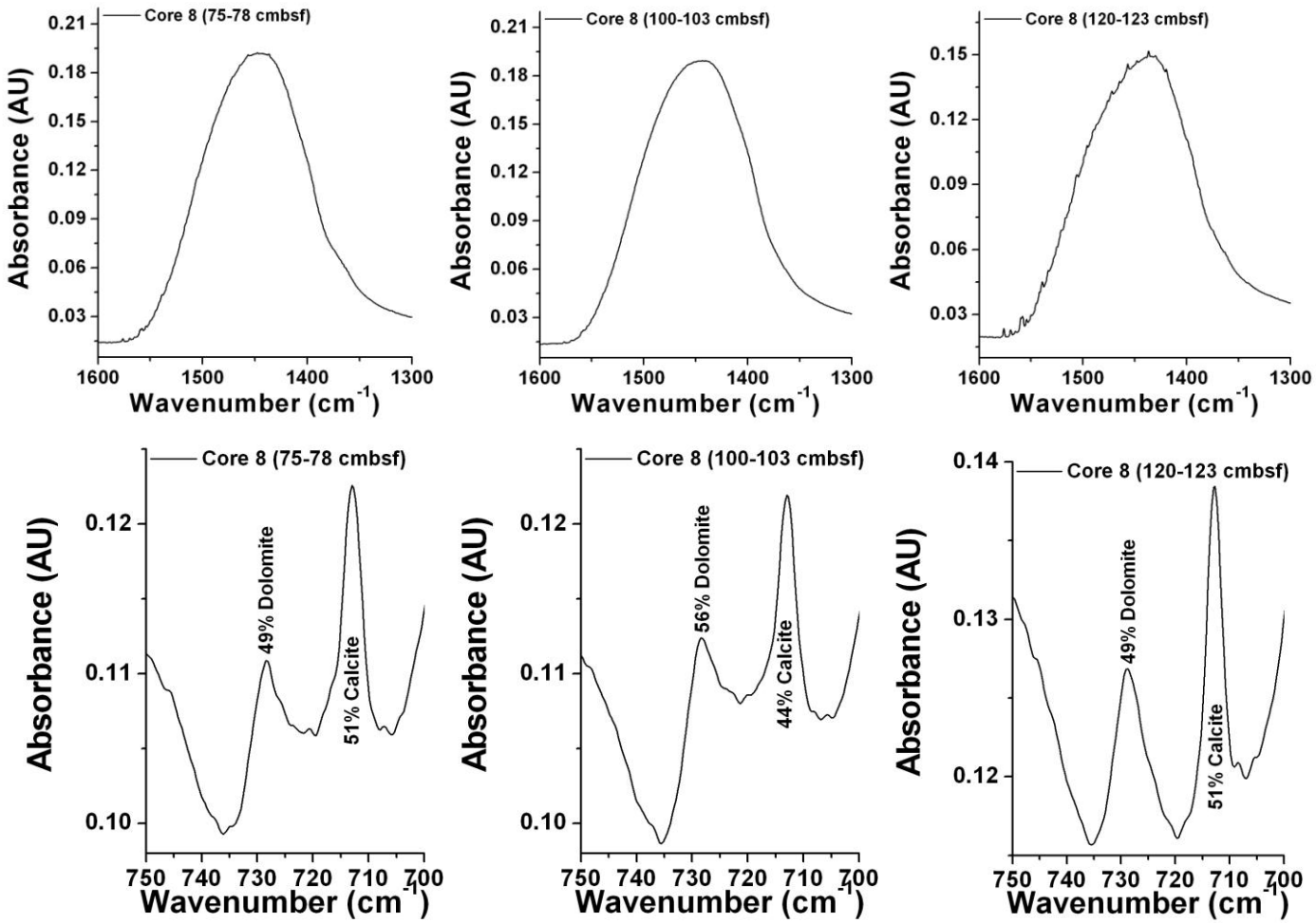
Core 8 (75-78 cmbsf)
Core 8 (100-103 cmbsf)
Core 8 (120-123 cmbsf)
Absorbance (AU)
Wavenumber (cm-1)
49% Dolomite
51% Calcite
56% Dolomite
44% Calcite

Core 9 (0-431 cmbsf)

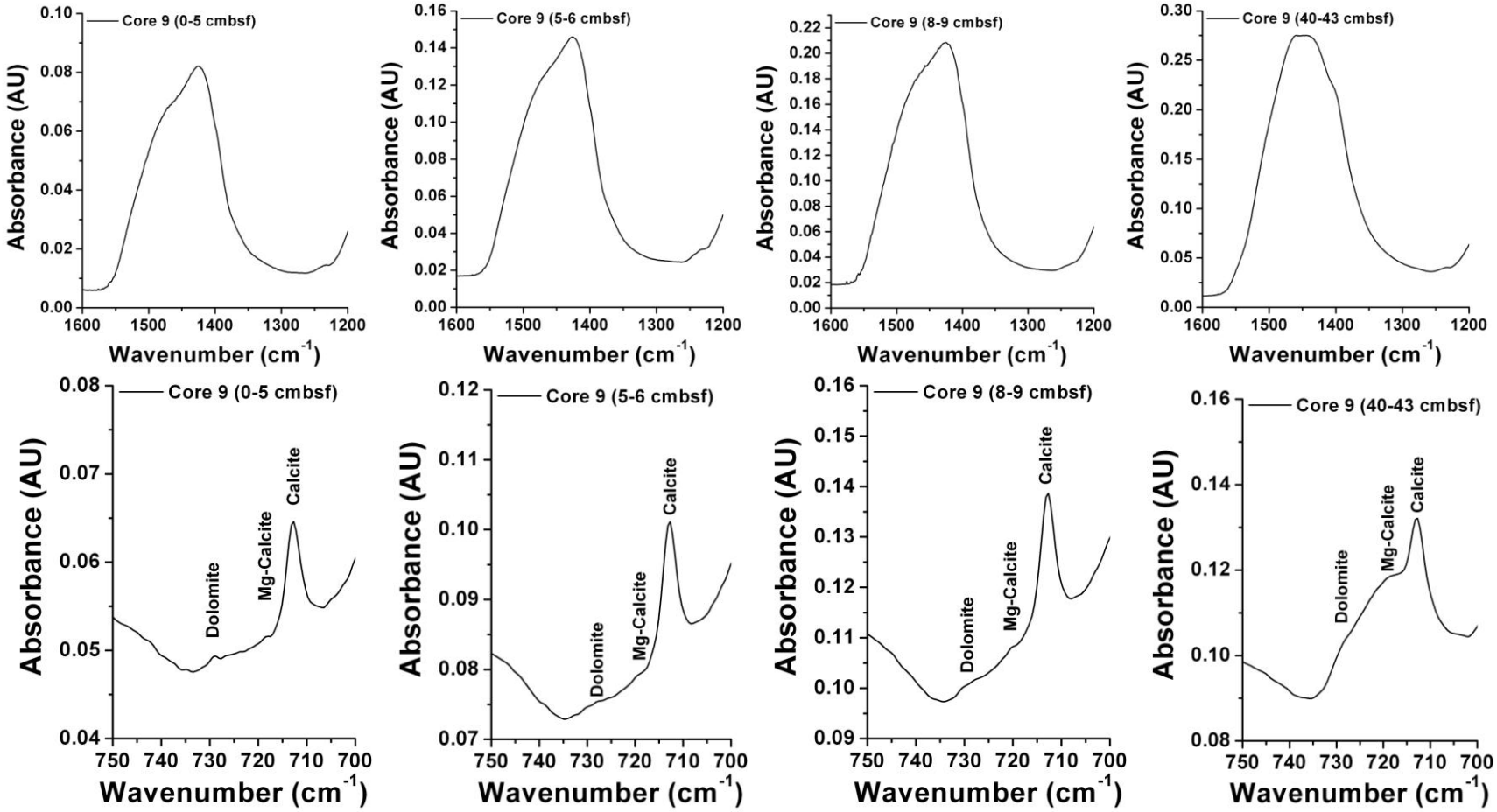

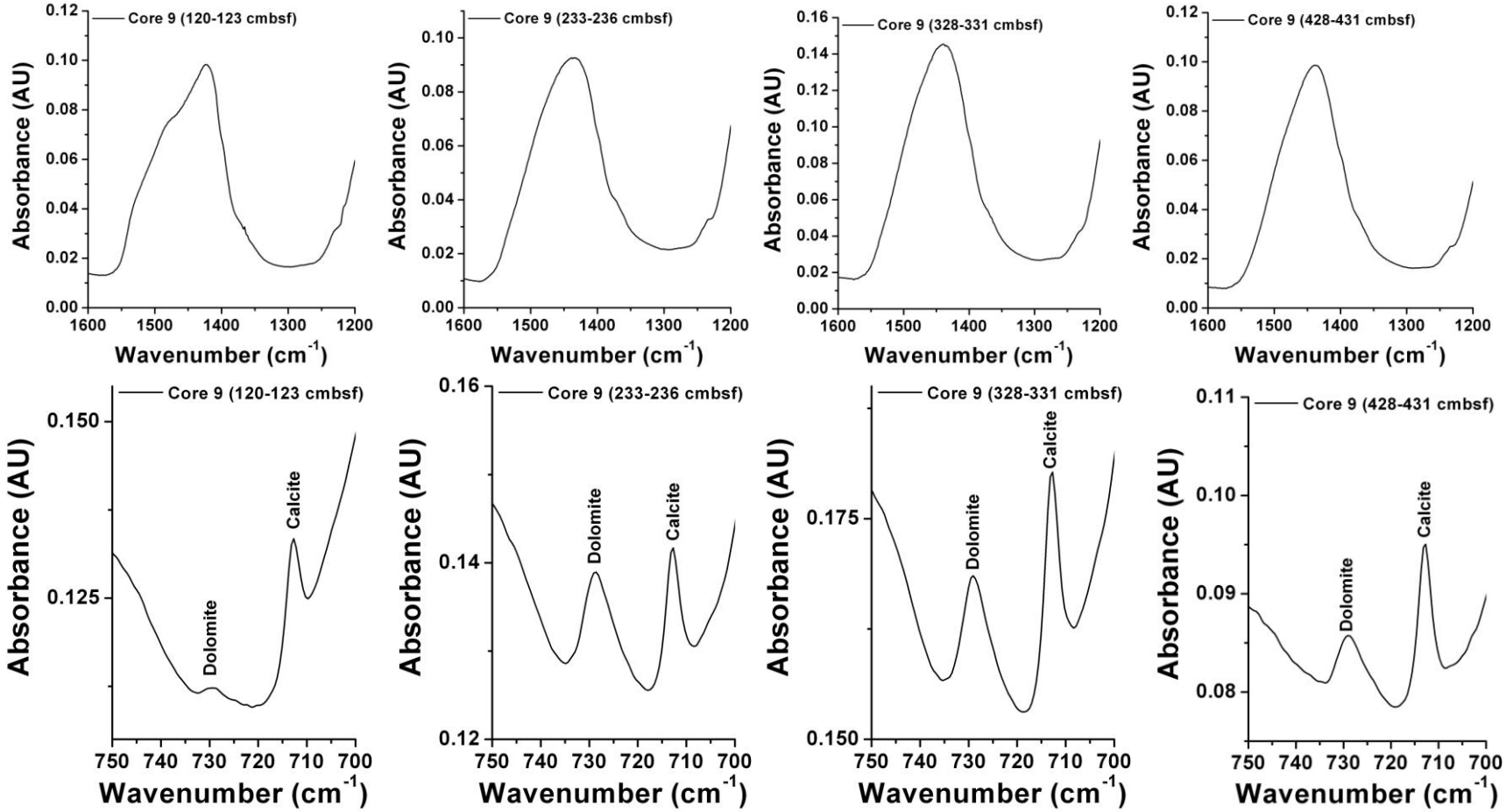
Core 9 (120-123 cmbsf)
Core 9 (233-236 cmbsf)
Core 9 (328-331 cmbsf)
Core 9 (428-431 cmbsf)
Absorbance (AU)
Wavenumber (cm-1)
Dolomite
Calcite

Core 21 (0-115 cmbsf)

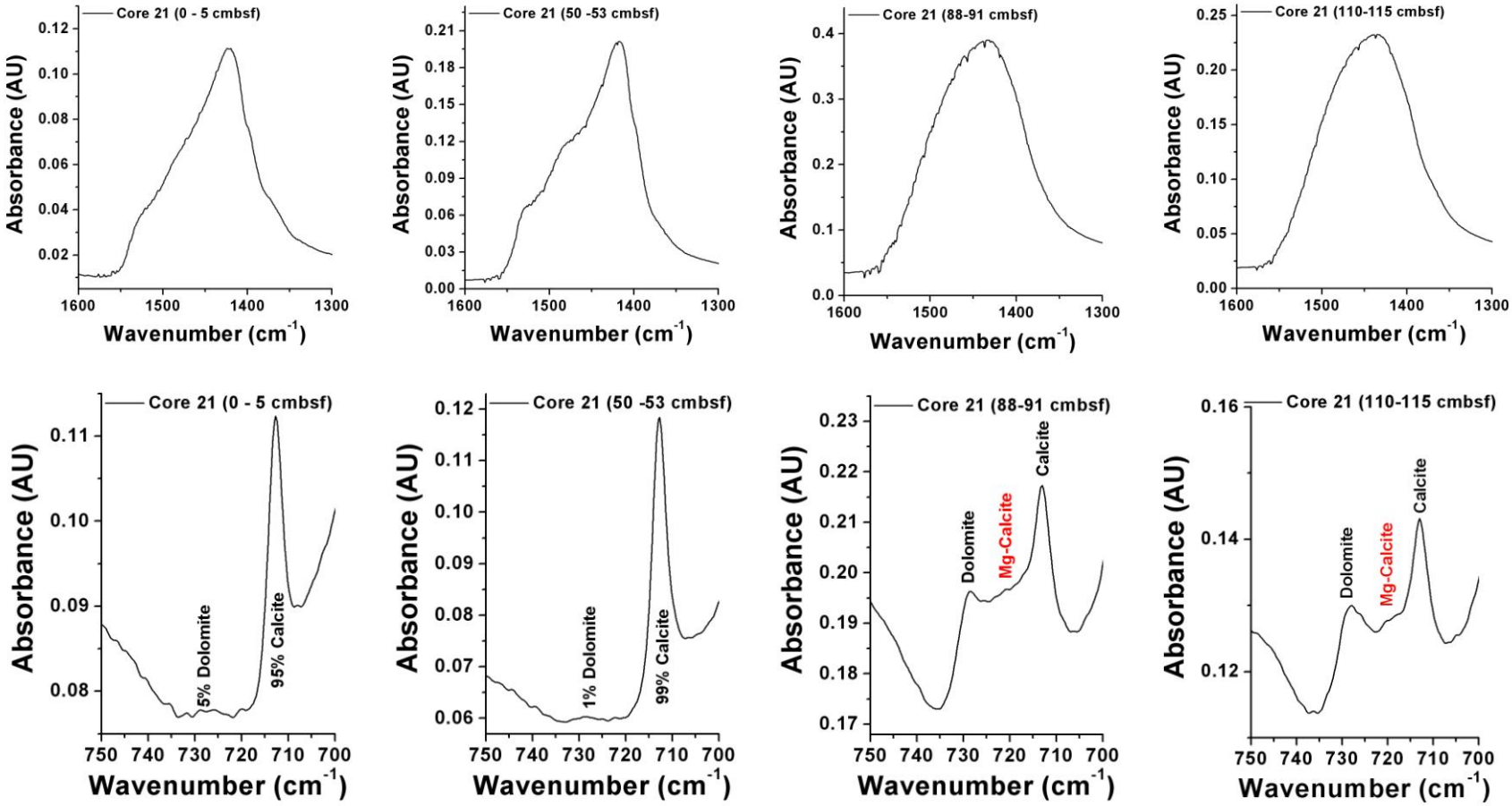

Core 22 (0-63 cmbsf)

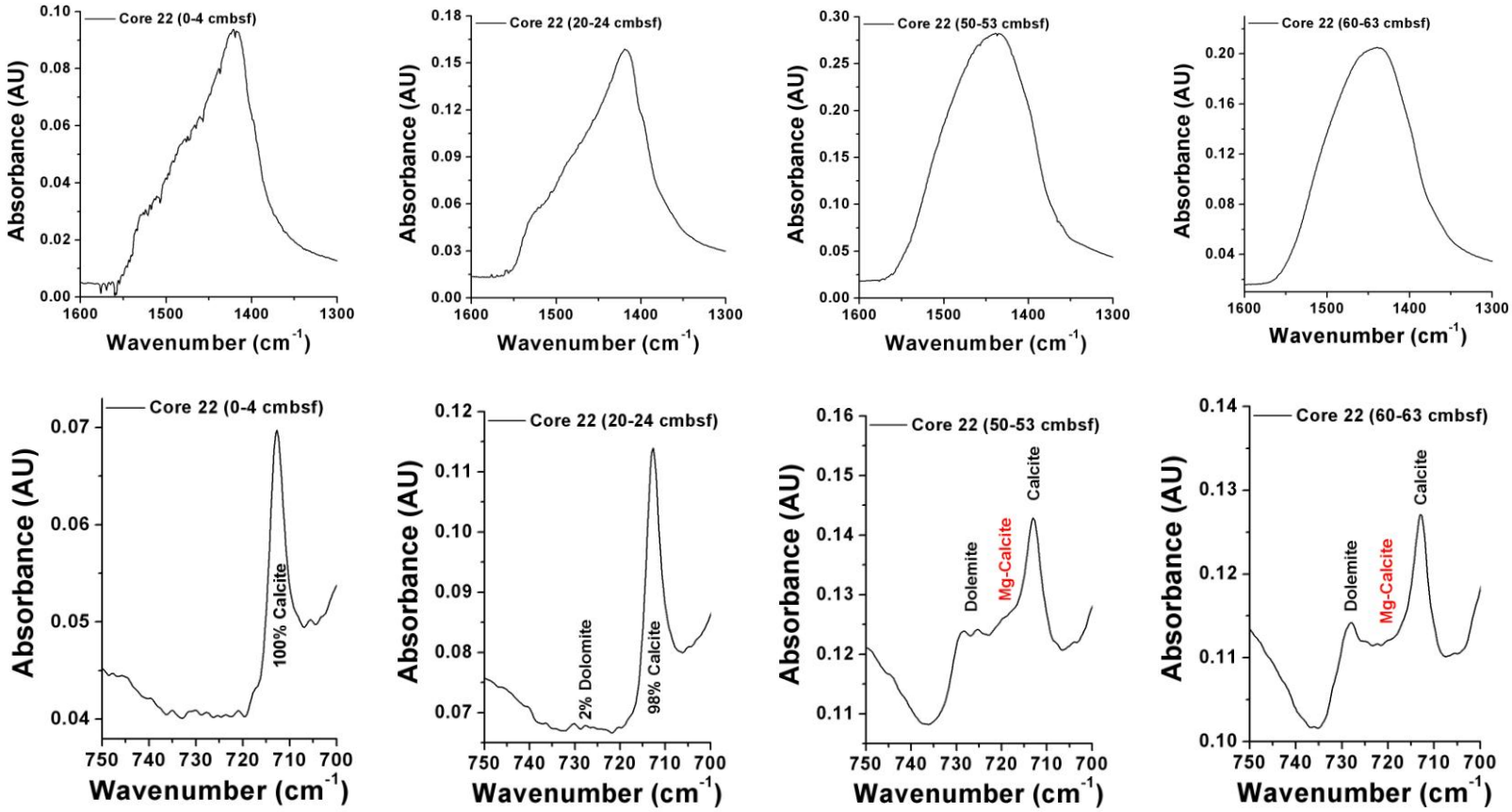

Core 24 (0-15 cmbsf)

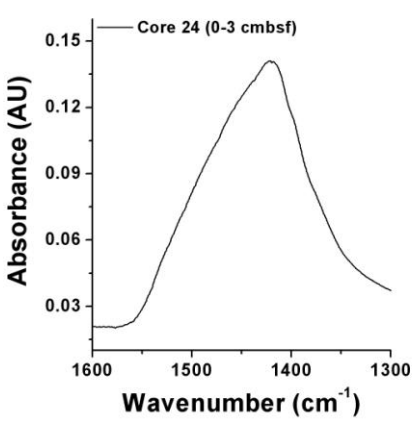

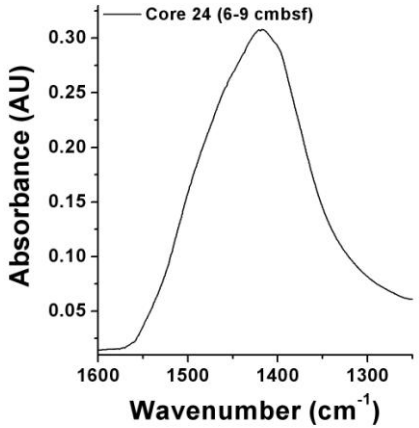

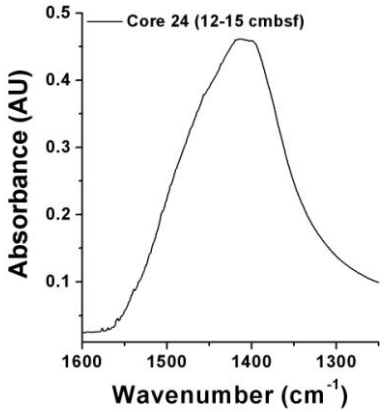

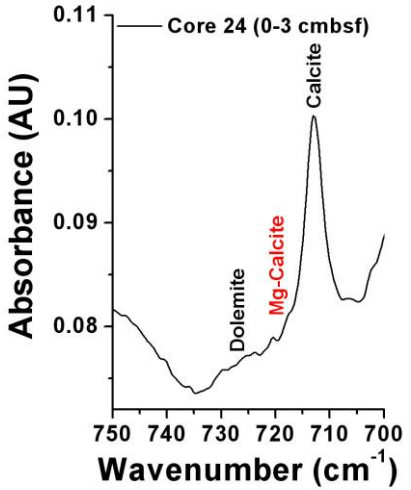

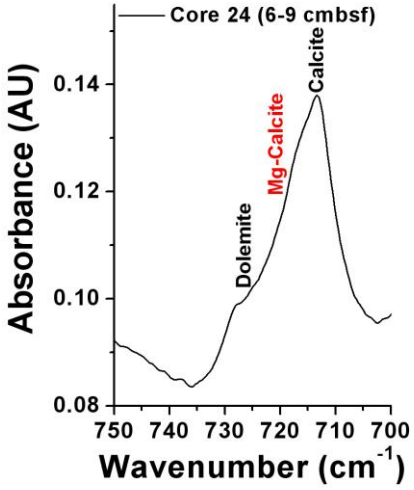

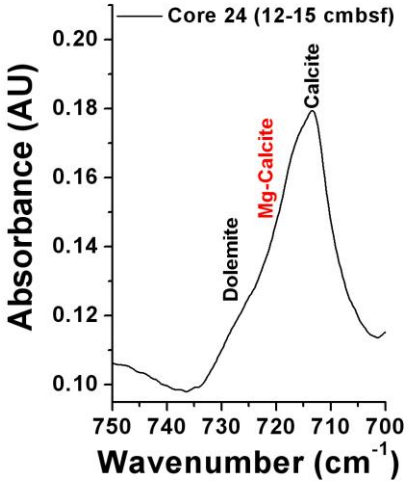

Core 26 (0-47 cmbsf)

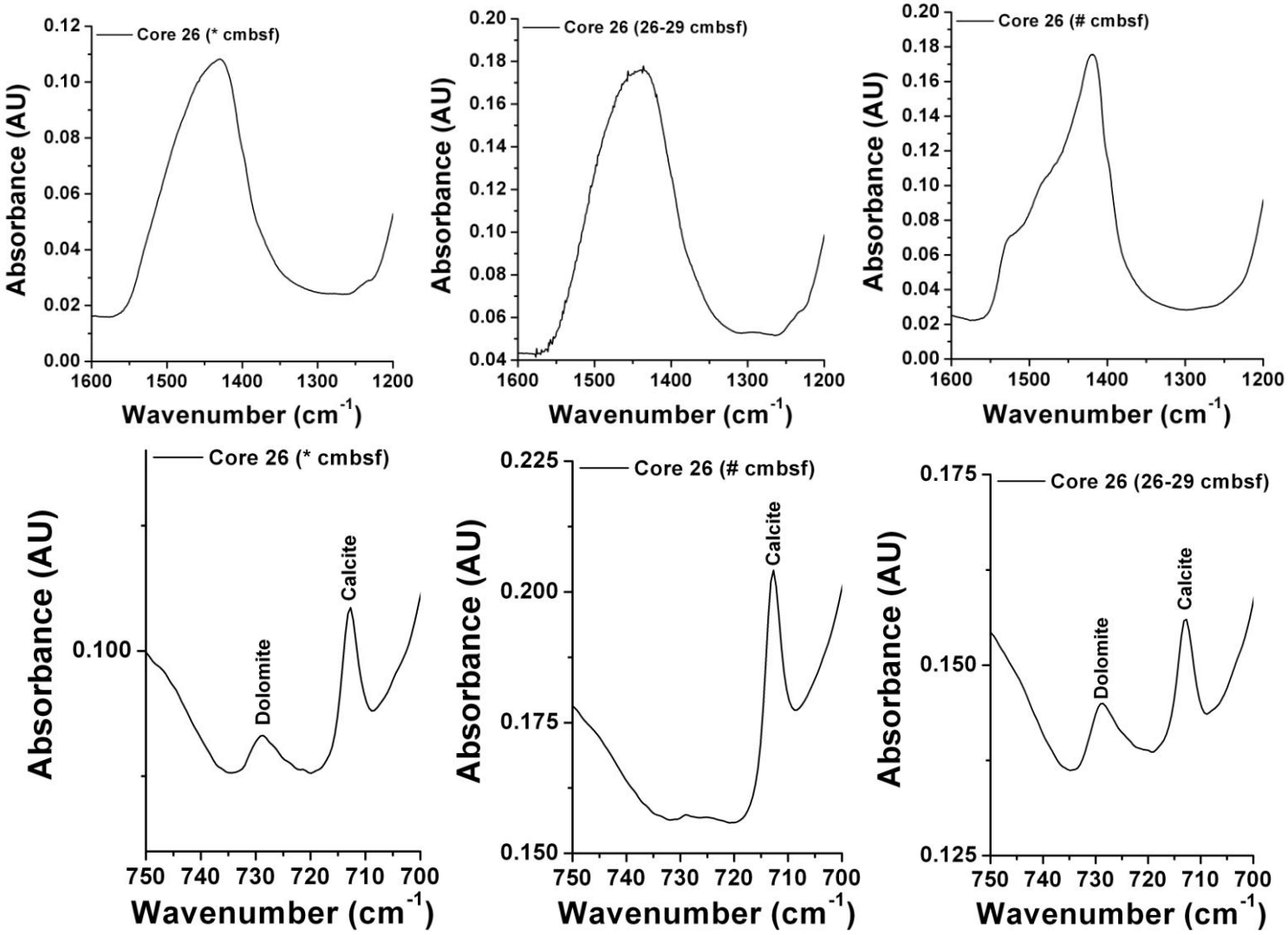

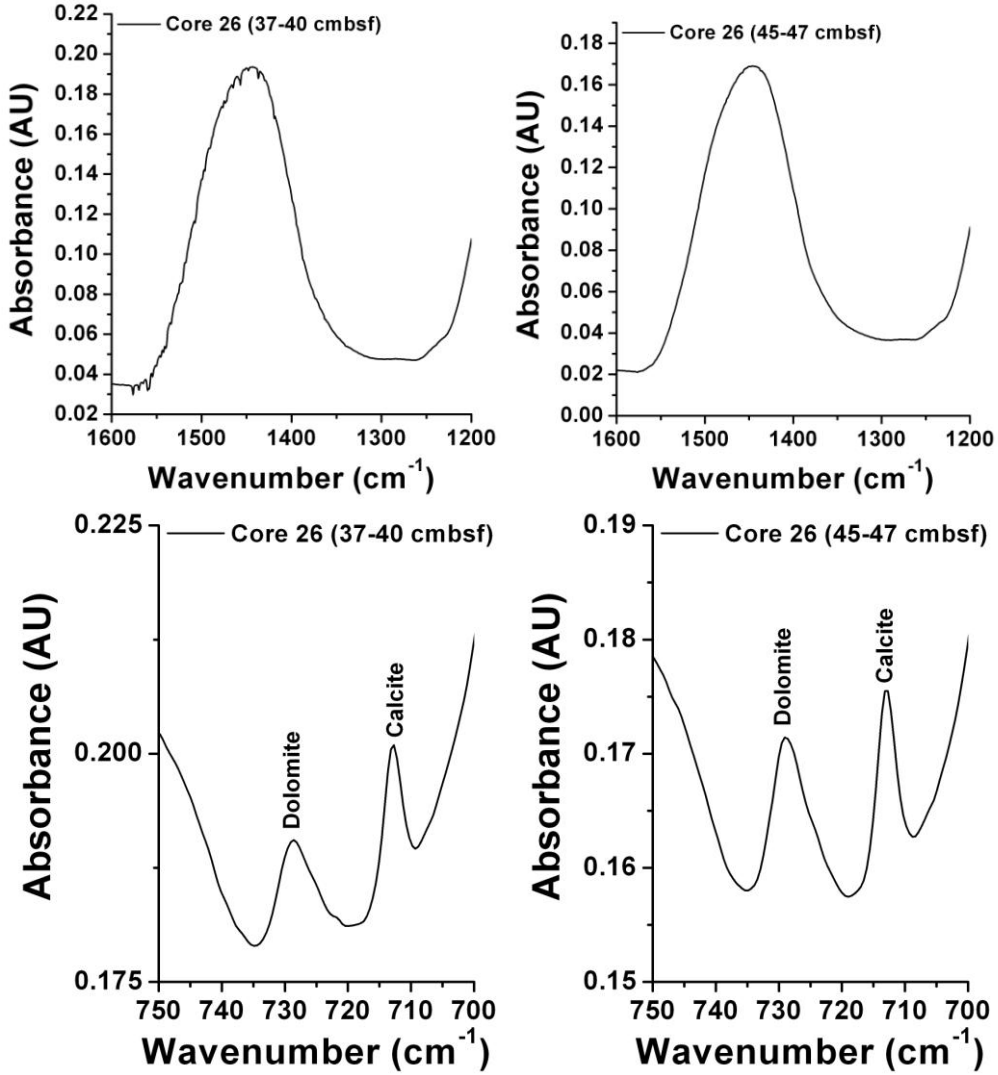
Core 26 (37-40 cmbsf)
Absorbance (AU)
Wavenumber (cm-1)
Core 26 (45-47 cmbsf)
Absorbance (AU)
Wavenumber (cm-1)
Core 26 (37-40 cmbsf)
Dolomite
Calcite
Absorbance (AU)
Wavenumber (cm-1)
Core 26 (45-47 cmbsf)
Dolomite
Calcite
Absorbance (AU)
Wavenumber (cm-1)

Core 29 (0-103 cmbsf)

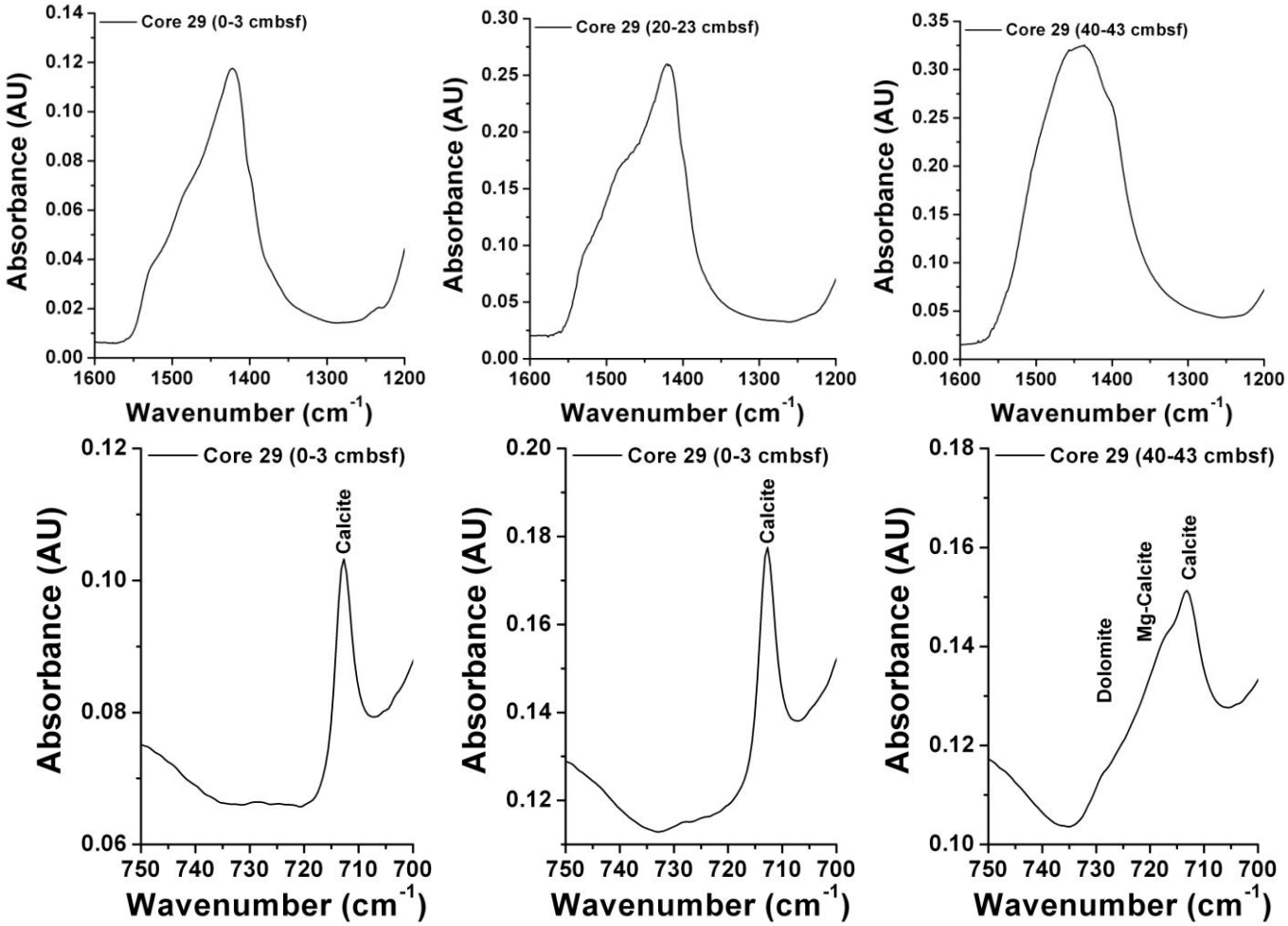

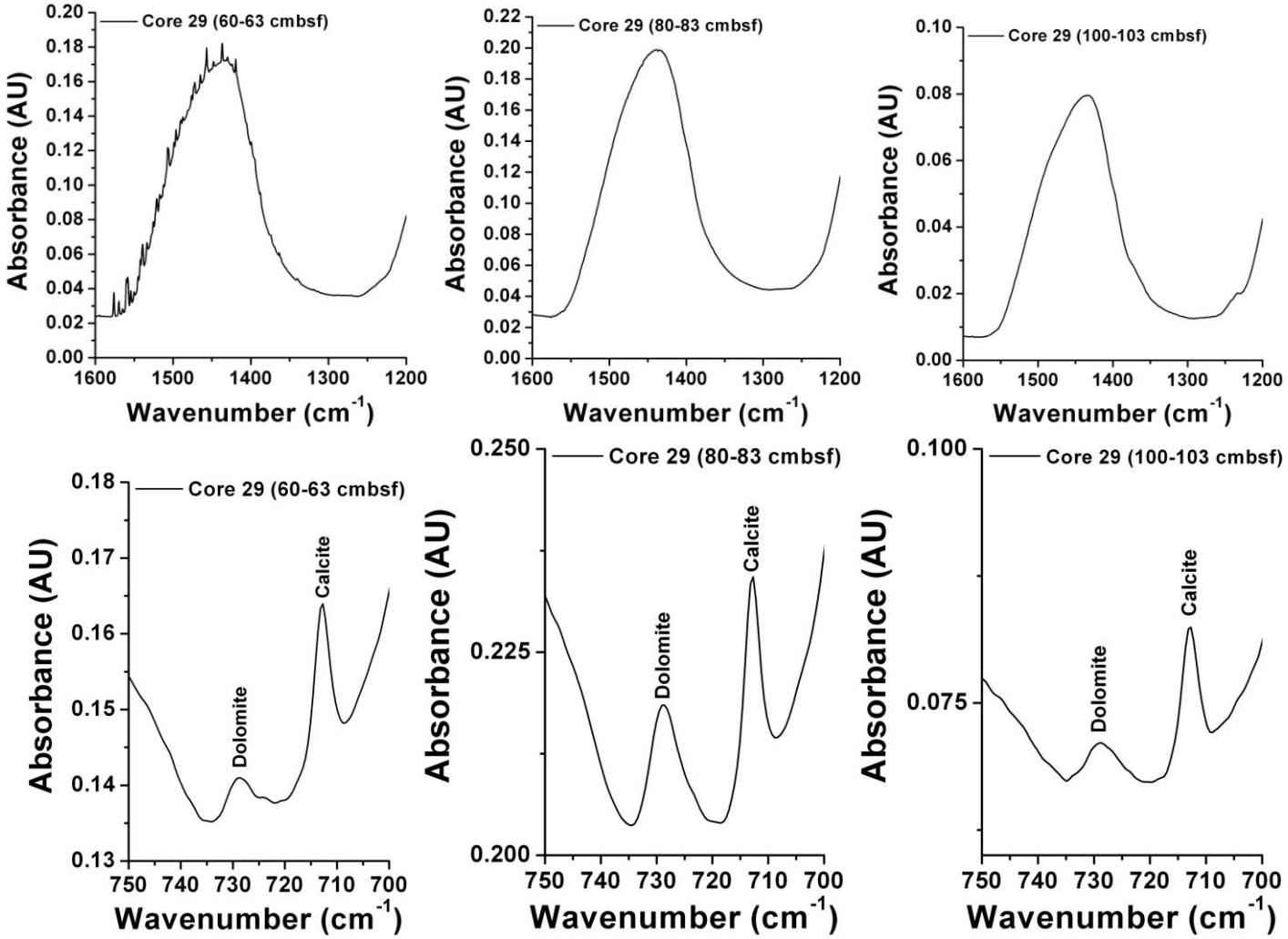
Core 29 (60-63 cmbsf)
Core 29 (80-83 cmbsf)
Core 29 (100-103 cmbsf)
Absorbance (AU)
Wavenumber (cm-1)
Dolomite
Calcite

Core 30 (15-123 cmbsf)

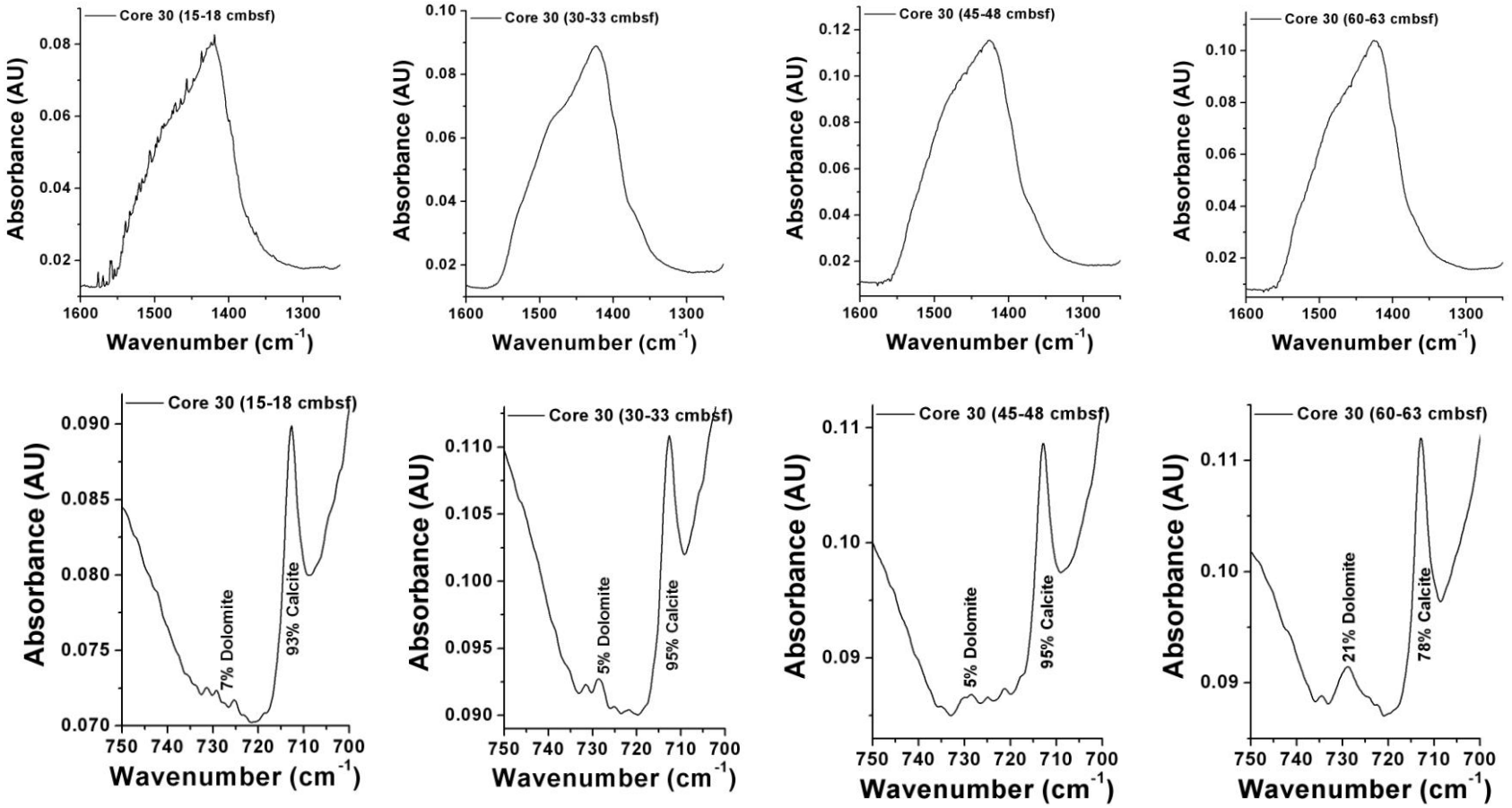

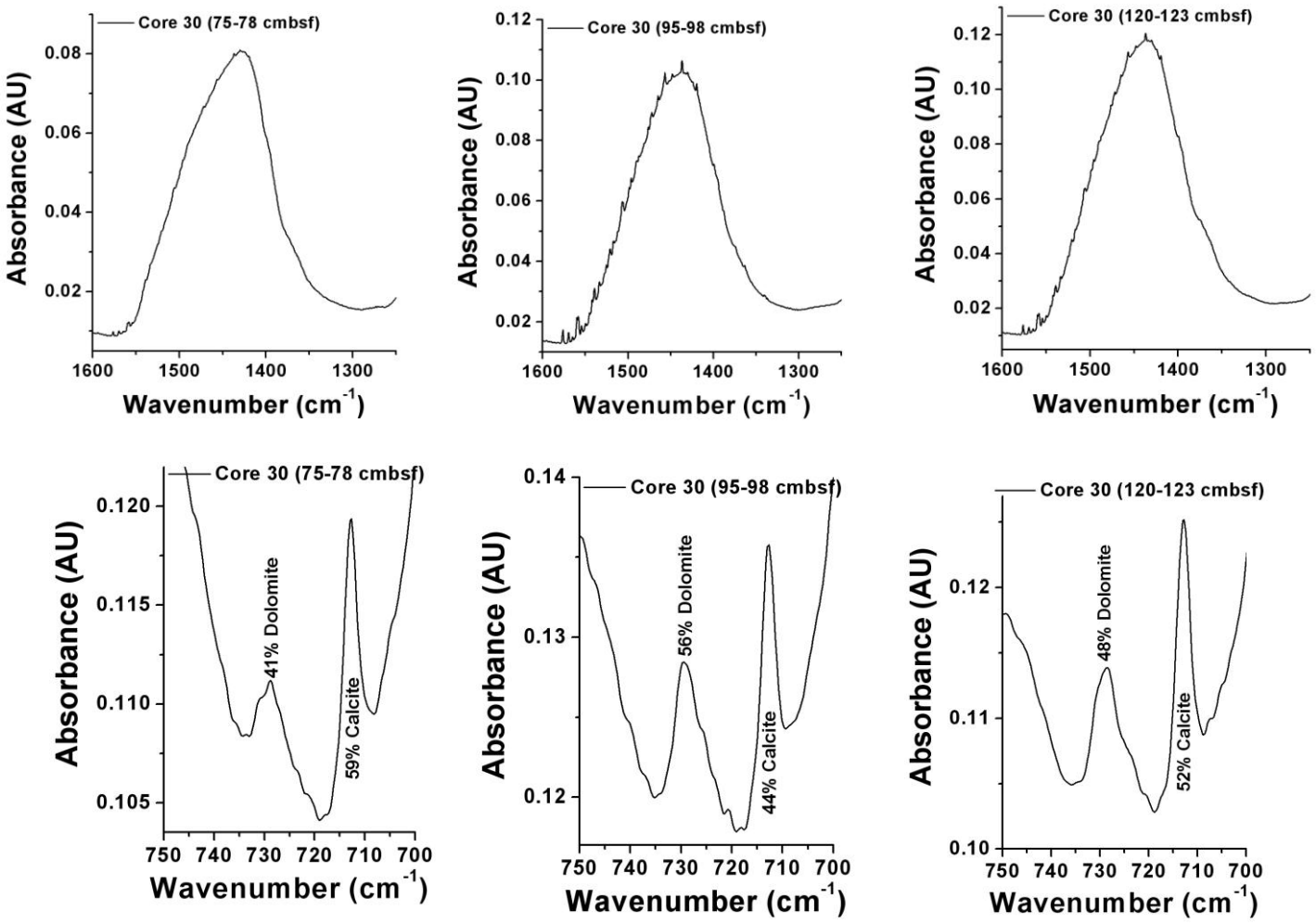
Core 30 (75-78 cmbsf)
Core 30 (95-98 cmbsf)
Core 30 (120-123 cmbsf)
Absorbance (AU)
Wavenumber (cm-1)
41% Dolomite
59% Calcite
56% Dolomite
44% Calcite
48% Dolomite
52% Calcite

Core 31 (0-123 cmbsf)

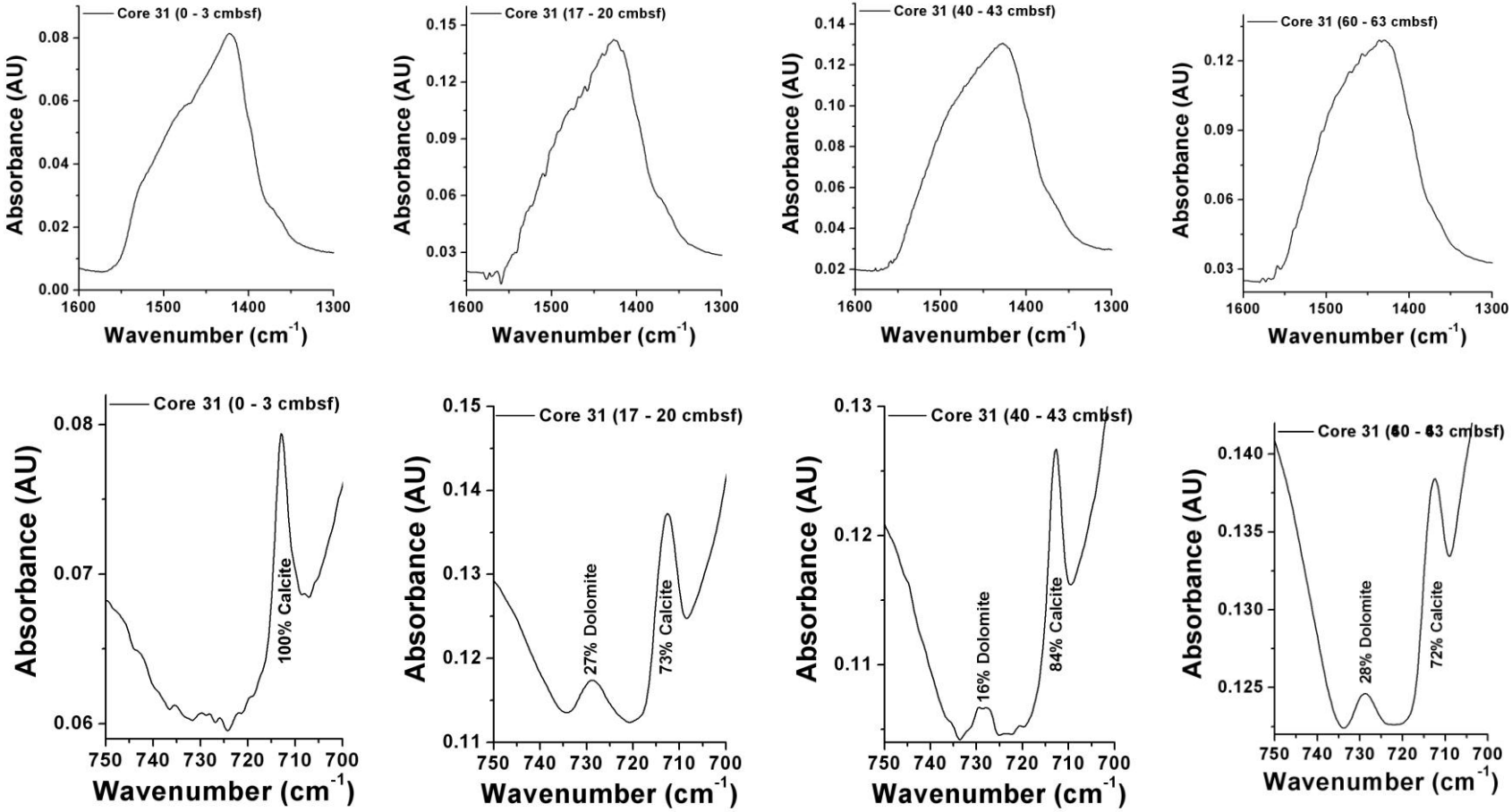

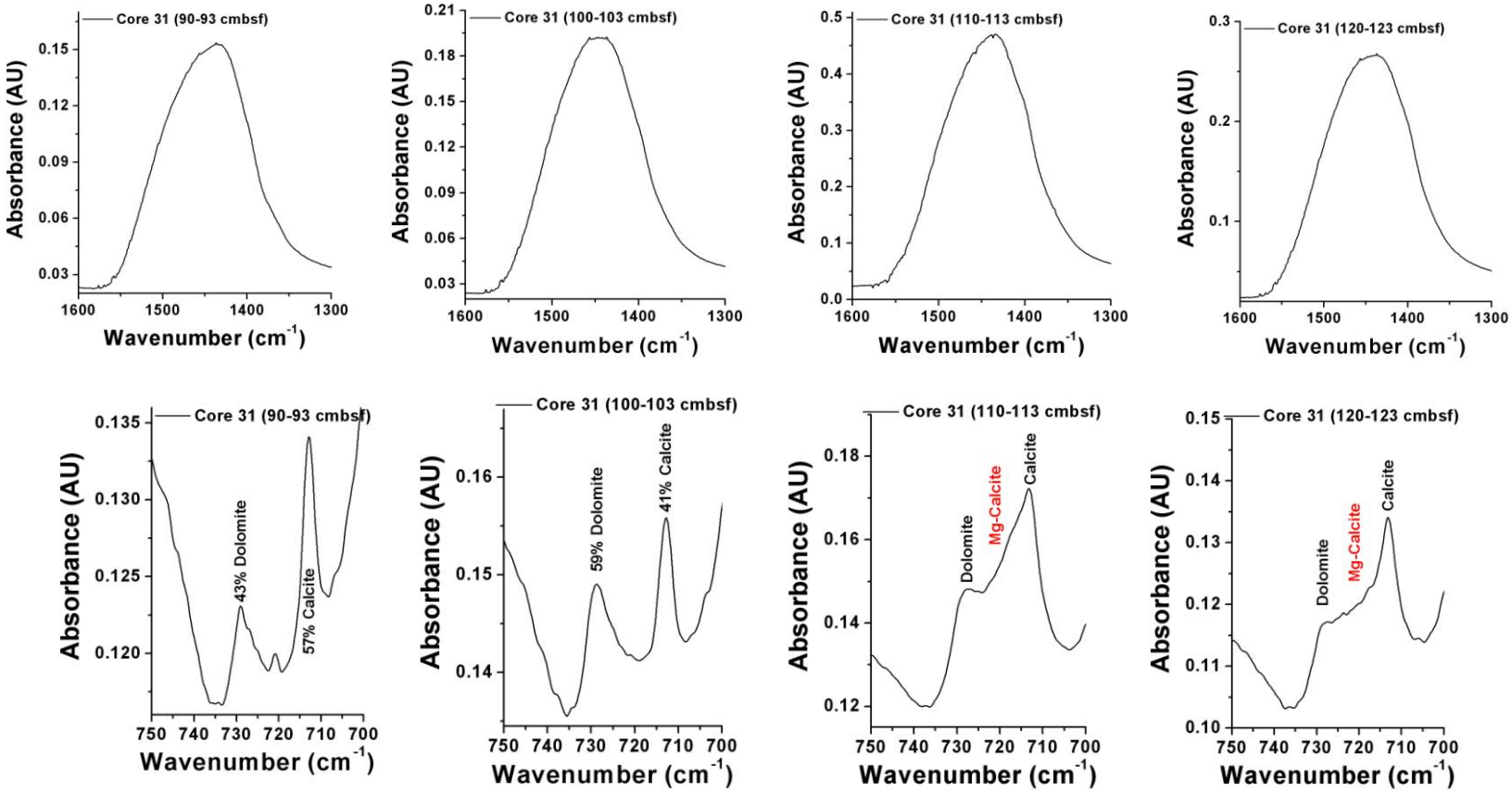
Core 31 (90-93 cmbsf)
Core 31 (100-103 cmbsf)
Core 31 (110-113 cmbsf)
Core 31 (120-123 cmbsf)
Absorbance (AU)
Wavenumber (cm-1)
43% Dolomite
57% Calcite
59% Dolomite
41% Calcite
Dolomite
Mg-Calcite
Calcite

Core 35 (0-134 cmbsf)

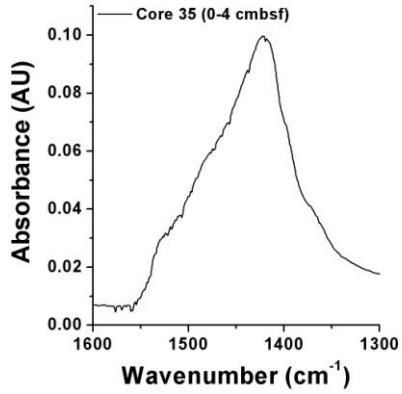

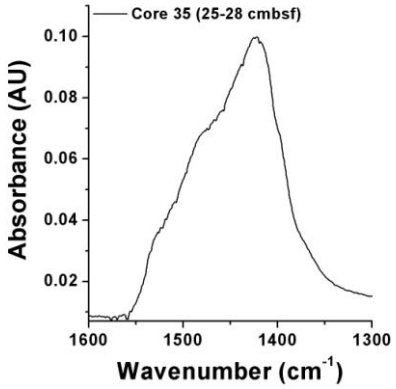

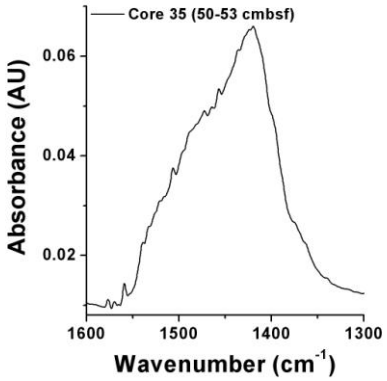

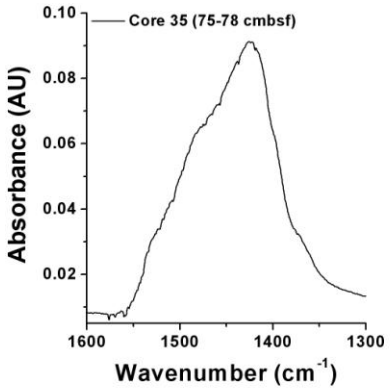

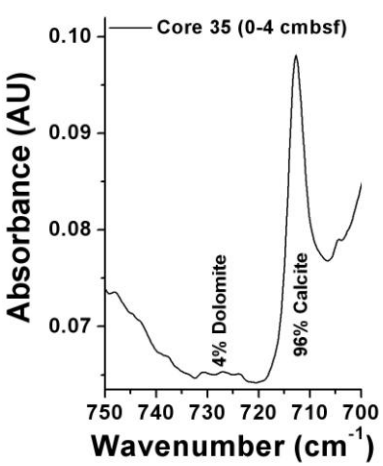

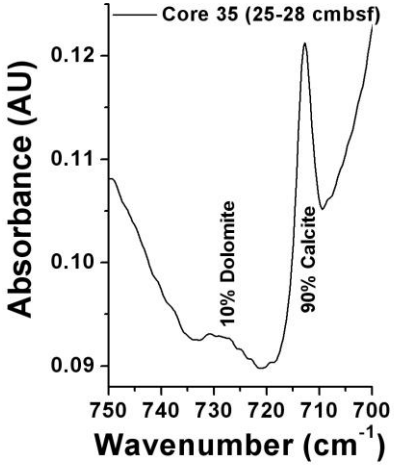

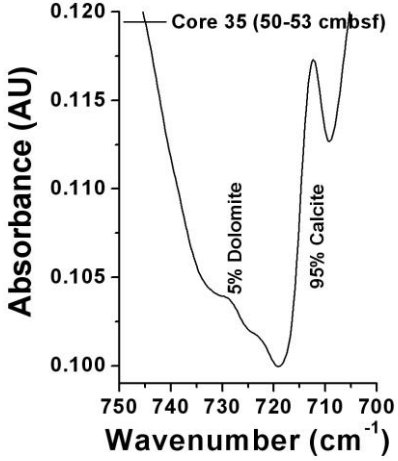

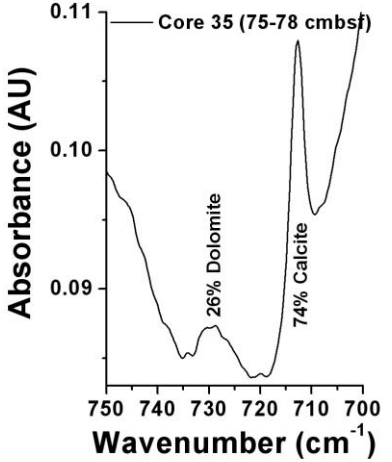

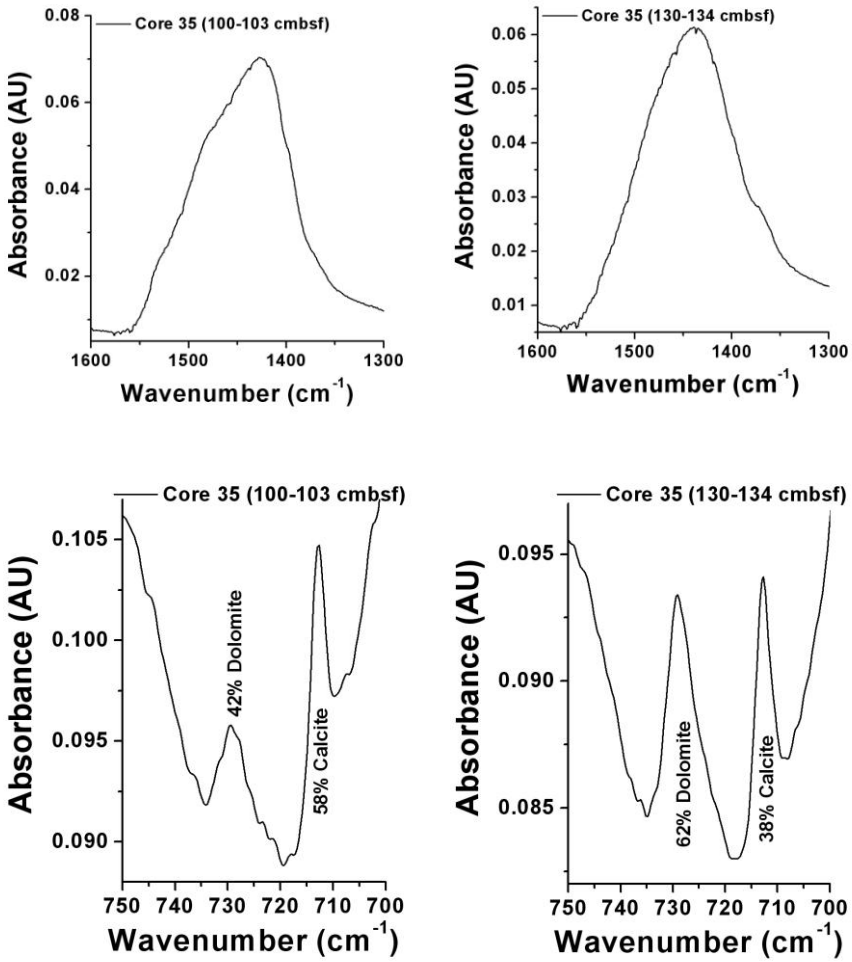
Core 35 (100-103 cmbsf)
Absorbance (AU)
Wavenumber (cm-1)
Core 35 (130-134 cmbsf)
Absorbance (AU)
Wavenumber (cm-1)
Core 35 (100-103 cmbsf)
42% Dolomite
58% Calcite
Absorbance (AU)
Wavenumber (cm-1)
Core 35 (130-134 cmbsf)
62% Dolomite
38% Calcite
Absorbance (AU)
Wavenumber (cm-1)

Core 4414 (0-134 cmbsf)

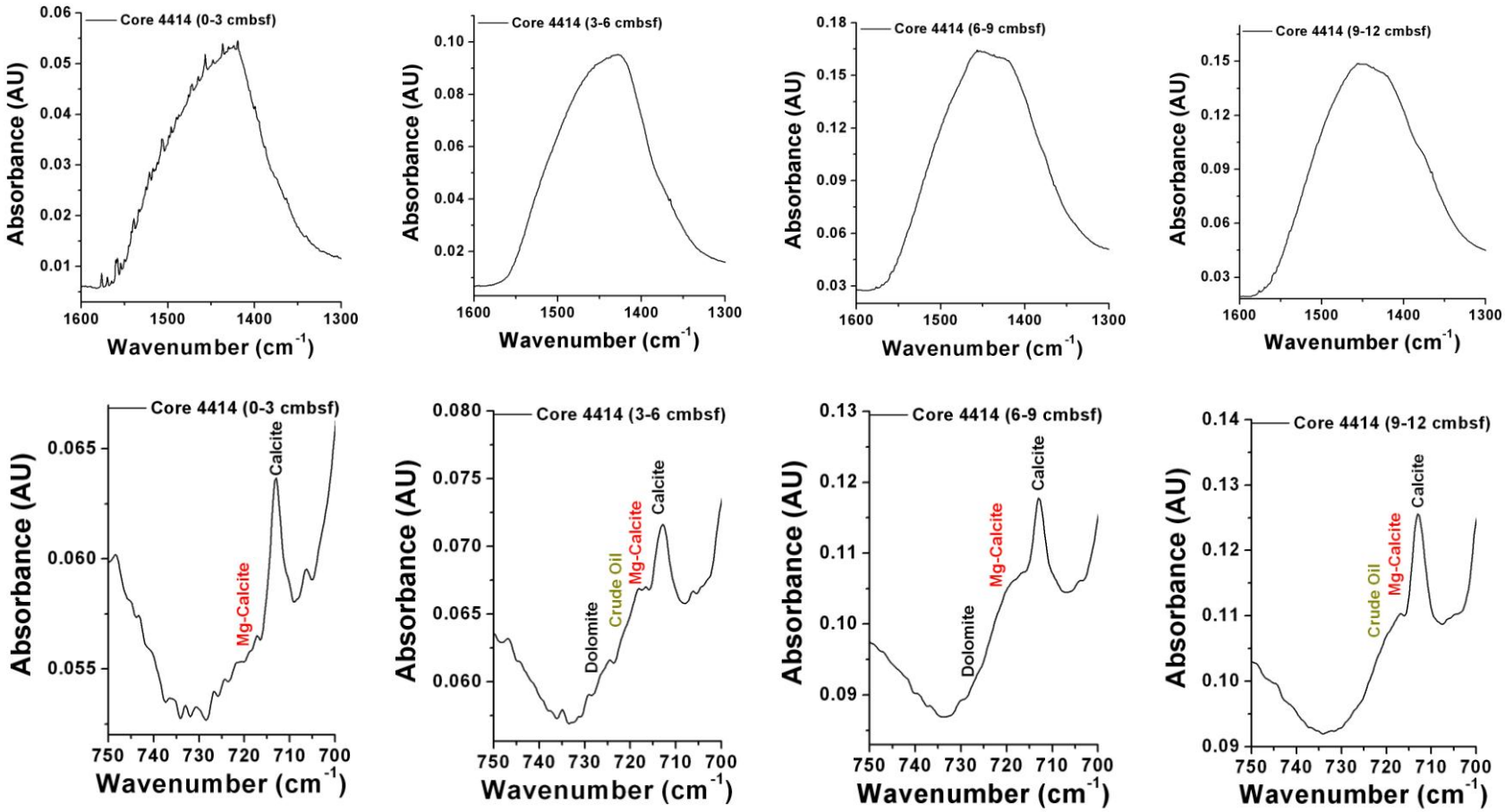

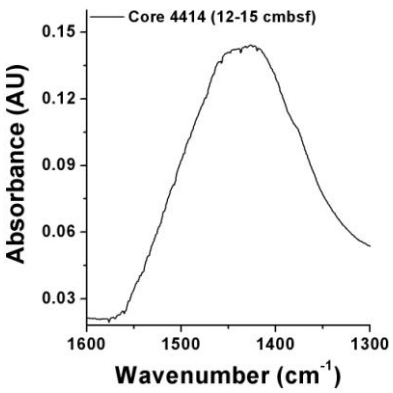
Core 4414 (12-15 cmbsf)
Absorbance (AU)
0.15
0.12
0.09
0.06
0.03
1600
1500
1400
1300
Wavenumber (cm-1)

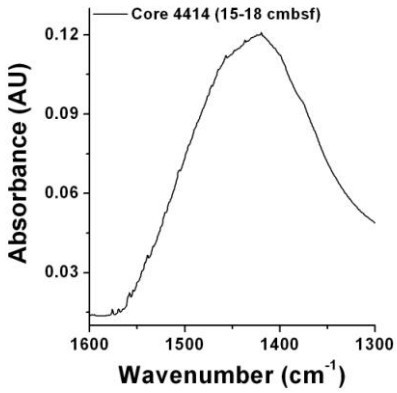
Core 4414 (15-18 cmbsf)
Absorbance (AU)
0.12
0.09
0.06
0.03
1600
1500
1400
1300
Wavenumber (cm-1)

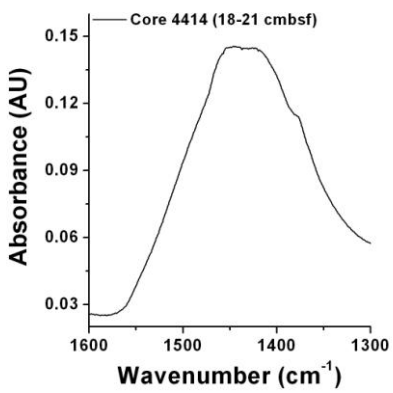
Core 4414 (18-21 cmbsf)
Absorbance (AU)
0.15
0.12
0.09
0.06
0.03
1600
1500
1400
1300
Wavenumber (cm-1)

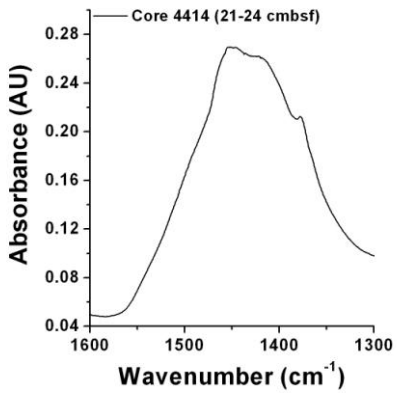
Core 4414 (21-24 cmbsf)
Absorbance (AU)
0.28
0.24
0.20
0.16
0.12
0.08
0.04
1600
1500
1400
1300
Wavenumber (cm-1)

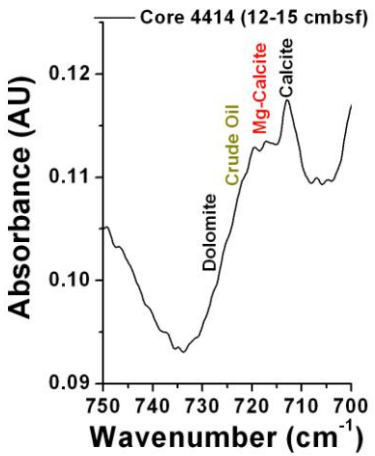
Core 4414 (12-15 cmbsf)
Absorbance (AU)
0.12
0.11
0.10
0.09
Dolomite
Crude Oil
Mg-Calcite
Calcite
750 740 730 720 710 700
Wavenumber (cm-1)

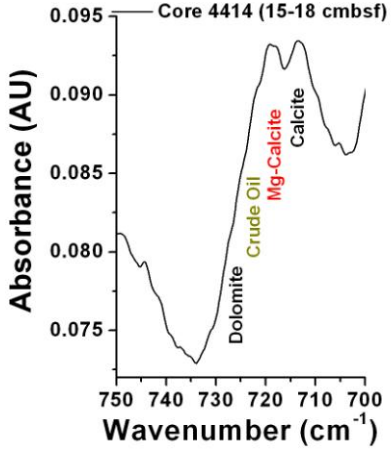
Core 4414 (15-18 cmbsf)
Absorbance (AU)
0.095
0.090
0.085
0.080
0.075
Dolomite
Crude Oil
Mg-Calcite
Calcite
750 740 730 720 710 700
Wavenumber (cm-1)

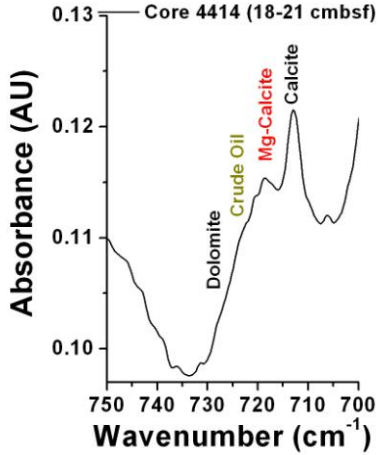
Core 4414 (18-21 cmbsf)
Absorbance (AU)
0.13
0.12
0.11
0.10
Dolomite
Crude Oil
Mg-Calcite
Calcite
750 740 730 720 710 700
Wavenumber (cm-1)

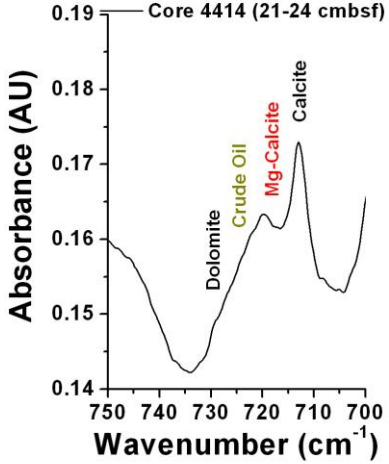
Core 4414 (21-24 cmbsf)
Absorbance (AU)
0.19
0.18
0.17
0.16
0.15
0.14
Dolomite
Crude Oil
Mg-Calcite
Calcite
750 740 730 720 710 700
Wavenumber (cm-1)

A-2 MIR Fiberoptic evanescent field spectroscopy for the analysis of water/hydrocarbon emulsions

A-2.1 Polishing of of the facets of AgX fibers

To achieve sufficient optical quality for high coupling efficiencies of the silver halide waveguide, the ends of the fiber were cut with a sharp blade followed by sequential polishing with diamond slurries with 3, 1, and 0.5 μm grain size (results shown in **Figure A-2.1**).

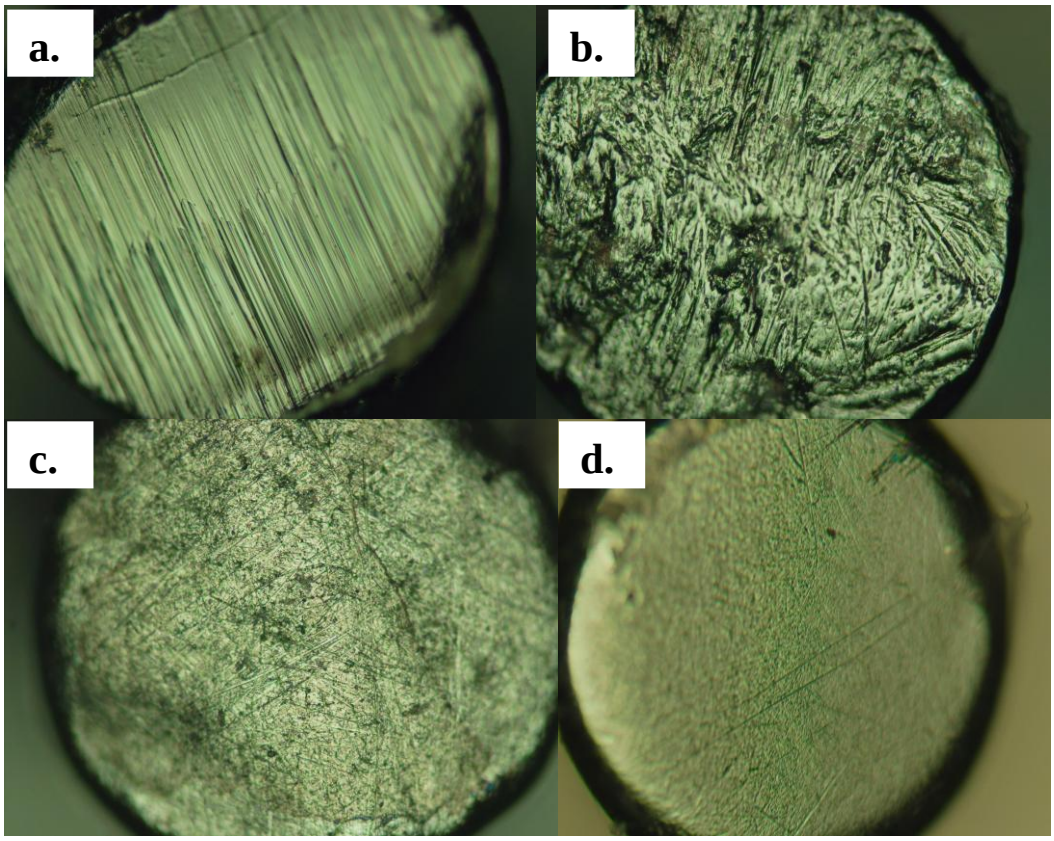

Figure A-2.1: Silver halide fiber after (a.) cutting, polishing with (b.) 3 μm, (c.) 1 μm, and (d.) 0.5 μm diamond slurries.

A-2.2 Polyacrylic acid polymer

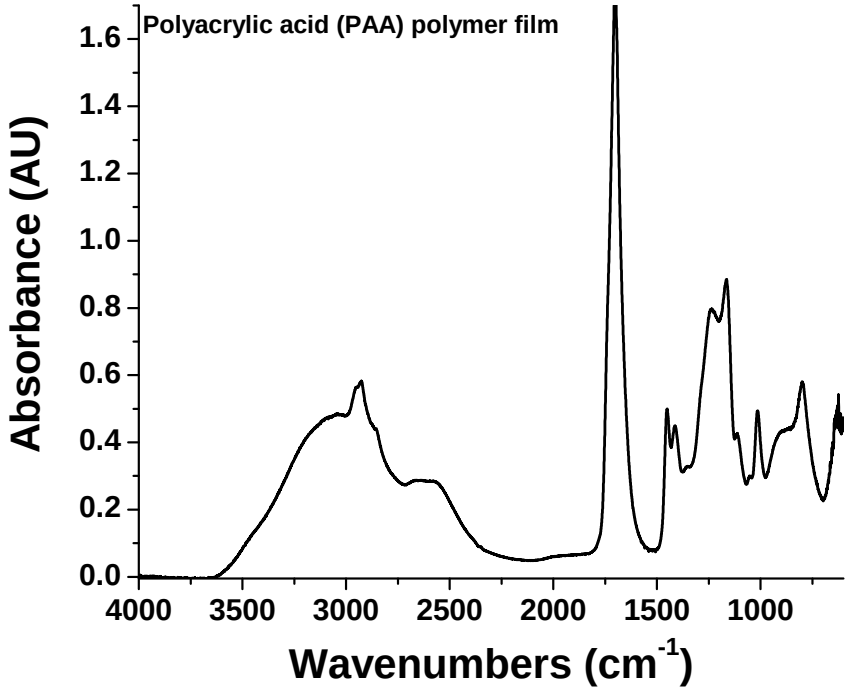

Figure A-2.2: IR-ATR spectrum of a polyacrylic acid film

A-2. 3 Calculations for the droplet contact area estimation

In collaboration with Dr. Zdyrko, Clemson University

To estimate the contact area of a droplet with constant volume but different contact angle following considerations were applied. The droplet of the liquid (grayed in **Figure A-2.3-1**) was enclosed by a sphere of arbitrary radius R. The radius of the droplet circle contact with the surface, r, and height of the droplet h or h+h1 was expresses via the contact angle Θ, and the radius R of the enclosing sphere around the droplet.

For contact angle values < 90^o, r and h are equal to:

$r=R*\cos(90-\Theta)$; $h=R*(1-\sin(90-\Theta))$.

For contact angle values > 90^o, r and h are equal to:

$r=R*\cos(\Theta-90)$; $h=R*\sin(\Theta-90)$.

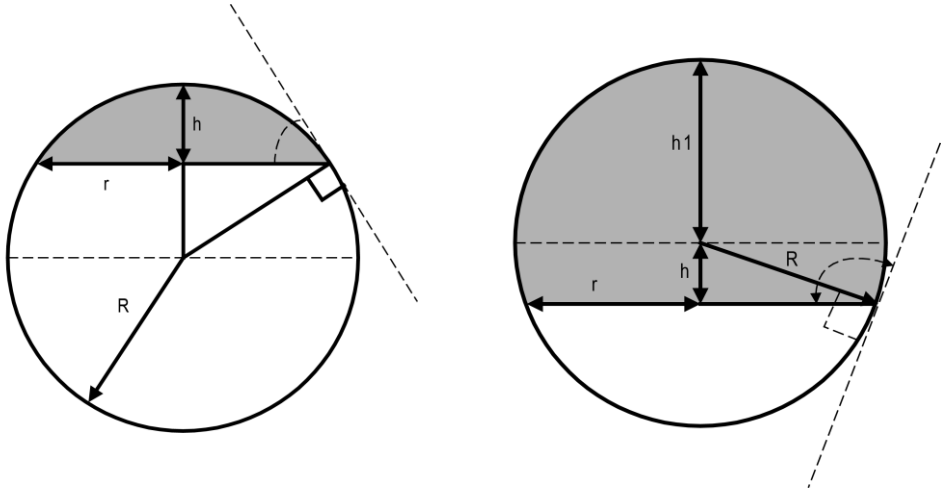

Figure A-2.3-1. Schematic representation of the liquid droplet (gray color) at different wetting angles at the surface.

Knowing h and r as function of R, the volume of the droplet may be expresses solely in terms of R and the contact angle value.

For contact angle values < 90^o, the volume of the droplet equals to:

$$V(\theta < 90) = \frac{1}{6}\pi h(3r^2 + h^2) = \frac{1}{6}\pi h\{3[Rcos(90 - \theta)]^2 + [R(1 - \sin(90 - \theta))]^2\}$$

For contact angle values > 90^o, the volume of the droplet equals to:

$$V(\theta > 90) = \frac{1}{6}\pi h(3R^2 + 3r^2 + h^2) + \frac{4}{6}\pi R^3$$
$$= \frac{1}{6}\pi h\{3R^2 + 3[Rcos(\theta - 90)]^2 + [Rsin(\theta - 90)]^2\} + \frac{4}{6}\pi R^3$$

Setting the volume of the droplet to be V=1 for known contract angles, the corresponding radii of the enclosed sphere can be readily determined (using Excel Solver). Thus, the corresponding radii of the droplet contact circles may be derived.